

Doctoral thesis

Doctoral theses at NTNU, 2023:19

Frode Håskjold Fagerli

A study on multilayered MXenes for rechargeable battery electrodes through surface termination control

NTNU
Norwegian University of Science and Technology
Thesis for the Degree of
Philosophiae Doctor
Faculty of Natural Sciences
Department of Materials Science and
Engineering



Norwegian University of
Science and Technology

Frode Håskjold Fagerli

A study on multilayered MXenes for rechargeable battery electrodes through surface termination control

Thesis for the Degree of Philosophiae Doctor

Trondheim, January 2023

Norwegian University of Science and Technology
Faculty of Natural Sciences
Department of Materials Science and Engineering



Norwegian University of
Science and Technology

NTNU

Norwegian University of Science and Technology

Thesis for the Degree of Philosophiae Doctor

Faculty of Natural Sciences

Department of Materials Science and Engineering

© Frode Håskjold Fagerli

ISBN 978-82-326-5567-0 (printed ver.)

ISBN 978-82-326-6548-8 (electronic ver.)

ISSN 1503-8181 (printed ver.)

ISSN 2703-8084 (online ver.)

Doctoral theses at NTNU, 2023:19

Printed by NTNU Grafisk senter

Preface

This dissertation has been submitted to the Norwegian University of Science and Technology (NTNU) in partial fulfillment of the requirements for the academic Philosophiae Doctor (Ph.D.). The work is mainly based on three manuscripts, where two have been published and the third is currently under review.

The doctoral studies were performed at the Functional Materials and Materials Chemistry Research Group (FACET), under the Department of Materials Science and Engineering, NTNU, Trondheim, Norway. The supervision of the work was led by Associate Professor Fride Vullum-Bruer from September 2018 to April 2019, by Professor Kjell Wiik from April 2019 to October 2022, and by Associate Professor Nils Peter Wagner from October 2022. The co-supervisors were Associate Professor Zhaohui Wang and Professor Sverre M. Selbach from September 2018, in addition to Associate Professor Nils Peter Wagner and Professor Tor Grande from April 2019, and Professor Kjell Wiik from October 2022.

This project has been funded by the Research Council of Norway, through the FRINATEK project "2D-Mg" with project number 275810.

Frode Håskjold Fagerli

Trondheim, January 2023

Acknowledgments

This work could not have been completed without the professional and non-professional assistance of others. I would therefore like to express my sincere gratitude to all who have made it possible, and to those who have made the journey worthwhile.

To begin with, I wish to express my appreciation for the Norwegian welfare society, as it has allowed me to get this far without any notable economical concerns.

Then, I would like to thank all my knowledgeable and supporting supervisors, who have safely guided me through this project. I wish to thank my first main supervisor, Frida Vullum-Bruer, for giving me the chance to work on batteries and for believing in me as a PhD candidate. A special thanks goes to my second main supervisor, Kjell Wiik, who accepted the responsibility for this uncertain project at a critical time. Thank you for your steadfast supervision and for learning me how to write like a professional academic. I also want to express my sincere gratitude to Nils Peter Wagner, who joined as a co-supervisor 8 months in the project and ended up as my main supervisor for the last months. Thank you for assisting me with your expertise on batteries, and for engaging discussions on how to portray their chemistries. I am looking forward to more discussions at SINTEF. Moreover, I want to thank my co-supervisors Zhaohui Wang, Sverre M. Selbach and Tor Grande for their help on navigating this project towards something worth publishing. Specifically, Tor Grande's suggestion to work on gas hydrolysis is acknowledged, as it resulted in two of my three manuscripts.

Additionally, all the work on MXenes would not have been possible, and not nearly as fun, without my MXene companions Henning Kaland and Jacob Hadler-Jacobsen. I am really glad we were on this MXene adventure together, and that we could share all ups and downs that the MXene research has led to. I also would not have come far without the assistance of all my helpful colleagues at the department. I would therefore like to thank the FACET research group, and all who have been part of the weekly battery meetings. I am very thankful for all the feedback I have received on my work, and I

am also exceptionally grateful for the opportunity to ask and discuss all kinds of battery-related questions in this open forum. A special thanks also goes to the engineers who have kept the labs up and running, and helped me complete all the experimental work I have done.

With four years swiftly passing by, I also have to thank all my colleagues for making this a joyful and interesting experience. To Heidi and Mohadese, for enduring me as an office mate with many questions. To the "K2 gang", and especially Harald, Vilde and Frida, for a lot of interesting lunches, discussing an extensive range of topics. Thanks also to the people in K1, for the friendly rivalry regarding which block is the best. Moreover, I would like to express my gratitude to the international students at the department, for all the cultural exchange I have experienced even though I have remained in Trondheim the whole period. I also wish to thank all my friends outside work for helping me focus on other things than the PhD. A special thanks goes to the people in TSS and Pirum, for learning me the true joy of singing and entertaining, and for turning me into one of "livets glade gutter".

Finally, I should like to thank my friends and family for the support. To my parents, Sissel and Bård, for the genes and for a safe upbringing, and to my big brother, Ruben, for having someone to look up to. Last but not least, I wish to thank my best friend and the love of my life, Isa-Lill, who has been my main supporter and personal psychologist throughout our years together. Thank you for being a wonderful human being!

The author's contribution

This dissertation comprise three papers of which two have been published and one is submitted. All three papers are provided in the appendix of this thesis.

1. H. Kaland, J. Hadler-Jacobsen, **F. H. Fagerli**, N. P. Wagner, Z. Wang, S. M. Selbach, F. Vullum-Bruer, K. Wiik and S. K. Schnell

Are MXenes Suitable as Cathode Material for Rechargeable Mg Batteries?

Sustainable Energy & Fuels **4**, 6, 2956-2966 (2020). DOI: [10.1039/D0SE00087F](https://doi.org/10.1039/D0SE00087F)

Contributions: F.V.B conceived the original research idea. H.K. and F.H.F designed and conducted the experiments with inputs from N.P.W and K.W. and experimental assistance from L.A. Boge. L.A.B. performed the synthesis of the V₂AIC MAX phase and together with F.H.F. most of the MAX phase milling. The MAX phase etching and subsequent material characterization were done by H.K. and F.H.F. Cathode preparation was conducted by H.K, F.H.F. and L.A.B. Electrolyte preparation and verification was done by H.K. Electrochemical characterization and post mortem analysis were performed by H.K and F.H.F. All DFT calculations were carried out by J.H.J. with inputs from Z.W., S.K.S. and S.M.S. The data was analyzed by H.K., F.H.F., J.H.J., N.P.W. and K.W. H.K., J.H.J. and F.H.F. wrote the paper with feedback from all co-authors.

2. **F. H. Fagerli**, Z. Wang, T. Grande, H. Kaland, S. M. Selbach, N. P. Wagner and K. Wiik

Removing Fluoride-terminations from Multilayered V₂CT_x MXene by Gas Hydrolyzation

ACS Omega **7**, 27, 23790-23799 (2022). DOI: [10.1021/acsomega.2c02441](https://doi.org/10.1021/acsomega.2c02441)

Contributions: T.G. conceived the research idea. F.H.F designed and conducted the experiments, with inputs from H.K., N.P.W and K.W. Z.W. performed the DFT calculations with input from S.M.S. F.H.F., H.K., N.P.W. and K.W. interpreted the data. F.H.F. wrote the paper with feedback from all co-authors.

3. **F. H. Fagerli**, P. E. Vullum, Z. Wang, T. Grande, S. M. Selbach, N. P. Wagner and K. Wiik

Bulk substitution of F-terminations from $Ti_3C_2T_x$ MXene by cation pillaring and gas hydrolysis

Accepted for publication in the Elsevier journal FlatChem.

Contributions: T.G. and F.H.F. conceived the research idea. F.H.F designed and conducted the experiments, with inputs from P.E.V., N.P.W and K.W. P.E.V. performed the TEM characterisation. Z.W. performed the DFT calculations with input from S.M.S. F.H.F., N.P.W. and K.W. interpreted the data. F.H.F. wrote the paper with feedback from all co-authors.

The following scientific papers are not included in this thesis:

1. H. Kaland, J. Hadler-Jacobsen, **F. H. Fagerli**, N. P. Wagner, S. K. Schnell and K. Wiik

Dipentamethylene Thiuram Tetrasulfide-Based Cathodes for Rechargeable Magnesium Batteries

ACS Applied Energy Materials **3**, 11, 10600-10610 (2020). DOI: [10.1021/acsaem.0c01655](https://doi.org/10.1021/acsaem.0c01655)

Contributions: H.K. conceived the research idea, designed and conducted the experiments with inputs from F.H.F., N.P.W. and K.W. J.H.J. performed the DFT study. H.K., J.H.J., F.H.F., N.P.W., K.W. interpreted the data. H.K. wrote the paper with feedback from all co-authors.

2. H. Kaland, **F. H. Fagerli**, J. Hadler-Jacobsen, K. Wiik, Z. Zhao-Karger, M. Fichtner, N. P. Wagner

Performance Study of MXene/Carbon Nanotube Composites for Current Collector- and Binder-Free Mg-S Batteries

ChemSusChem **18**, 8, 1864-1873 (2021). DOI: [10.1002/cssc.202100173](https://doi.org/10.1002/cssc.202100173)

Contributions: H.K. conceived the research idea, designed and conducted the experiments with inputs from F.H.F., N.P.W. and K.W, except the $\text{Mg}[\text{B}(\text{hfp})_4]_2$ electrolyte salt that was synthesized by Z.Z.K. H.K., F.H.F., J.H.J., N.P.W., K.W. interpreted the data. H.K. wrote the paper with feedback from all co-authors.

3. J. Hadler-Jacobsen, **F. H. Fagerli**, H. Kaland and S. K. Schnell

Stacking Sequence, Interlayer Bonding, Termination Group Stability and Li/Na/Mg Diffusion in MXenes

ACS Materials Letters **3**, 9, 1369-1376 (2021). DOI: [10.1021/acsmaterialslett.1c00316](https://doi.org/10.1021/acsmaterialslett.1c00316)

Contributions: J.H. conceived the research idea together with S.K.S. J.H. designed and performed all DFT simulations with input from S.K.S. F.H.F. performed the experiments and wrote the experimental part with input from H.K. J.H. wrote the rest of the paper with feedback from all co-authors.

Summary

In the transition from fossil fuels to renewable energy sources, the demand for rechargeable batteries is rapidly increasing. To meet this demand, a diversification of battery chemistries will be essential, due to limited abundance of currently used battery materials. In addition to Li-ion batteries (LiBs), rechargeable Mg batteries (RMBs) stand out as a theoretically promising battery chemistry, with the potential to yield high energy batteries based on abundant materials. However, to enable practical RMBs, competitive cathode materials need to be established. Potential candidates may come from the family of two-dimensional transition metal carbides and nitrides known as MXenes, which due to their high electrical conductivity, chemical tunability and ion intercalating properties, have been predicted to yield high intercalation capacities for a range of cations, including Mg-ions. Hence, this study aimed towards evaluating the feasibility of MXenes for rechargeable battery electrodes, and in particular for RMBs.

In the first paper of this work, the feasibility of MXenes as an RMB cathode was investigated by using two different MXene compositions: V_2C and Ti_3C_2 . To ensure the possibility for Mg-ion desolvation and migration, these electrodes were galvanostatically cycled in cells with four different electrolytes, and at both low (20 °C) and high (60 °C) temperatures. Still, only minimal capacities were obtained, indicating insignificant reversible Mg-intercalation in the MXene particles. However, by including Li-salts to the electrolyte, significant reversible capacities were measured, demonstrating the functionality of the MXene electrodes. To explain this difference, density functional theory (DFT) calculations were implemented and showed that the migration barriers for Mg-ions were significantly higher than for Li-ions, and that the termination groups attached to the surface of the MXene sheets strongly influenced the intercalation voltages for Li- and Mg-ions. Denoted as "T" (i.e. V_2CT_x), these termination groups usually consist of a mixture of OH, O and F, and the DFT calculations showed that multilayered particles of O-terminated MXenes would be ideal for RMB cathodes. Hence, the focus of this

work was directed towards controlling the termination groups of MXenes, and especially towards substituting F- with O-terminations.

In the second and third paper of this work, gas hydrolysis was explored as a post-etching treatment to substitute F-terminations in multilayered V_2CT_x and $Ti_3C_2T_x$ MXenes, respectively. It was found that successful hydrolysis required a MXene structure with an expanded interlayer spacing, to allow the water molecules to penetrate in between the MXene sheets. For the V_2CT_x phase, this was achieved by intercalated water molecules from the HF etching step, whereas the $Ti_3C_2T_x$ phase required pre-intercalation of cations prior to hydrolysis. For both phases, a F-reduction around 70 % was achieved, demonstrating the greatest F-reduction in multilayered particles reported so far. However, due to challenges of quantifying the remaining terminations (O vs. OH vs. unterminated), the exact composition of the final MXenes remained unclear. Although the F-reduction was clear for both MXene phases, no increase in capacity was observed upon cycling in RMB coin cells. To investigate the termination group's influence on the electrochemical performance, MXene electrodes were thus cycled in LiBs. This resulted in dissimilar changes for the two MXene compositions. Where the hydrolysed V_2CT_x phase displayed an enhanced rate capability compared to the pristine MXene, the opposite was true for the $Ti_3C_2T_x$ MXene. The $Ti_3C_2T_x$ phase also showed increased average voltages and capacities after hydrolysis, which was not observed for the V_2CT_x phase. Based on these ambiguous changes in electrochemical performance, and the uncertain composition of the resultant termination mixtures, no clear conclusion on the effect of termination change could be drawn from this work. To ensure controlled formation of O-terminated MXenes, further refining of the hydrolysis method will be required, combined with enhanced termination characterisation.

In addition to the published results, the thesis includes new results on a F-free etching method based on hydrothermal treatment in concentrated NaOH solutions. These etching conditions allowed for F-free $Ti_3C_2T_x$ MXene, while the synthesis of other MXene compositions was not successful. Whereas all of the Ti_2AlC , Ti_2AlN , Ti_3AlCN , $TiMo_2AlC_2$, Nb_4AlC_3 , Nb_2AlC , V_2AlC and V_4AlC_3 MAX phase precursors demonstrated significant oxidation, the former three showed possible signs of some unordered MXene. Further investigation, with optimised etching conditions, is therefore required to conclude about this etching method's compatibility to form other MXene phases than $Ti_3C_2T_x$. Nevertheless, due to the mixture of O- and OH-terminations, this etching method is not ideal for optimal termination control. In comparison, a recently reported etching method, based on Lewis acid etching in molten salts, has enabled synthesis of homogeneously terminated MXenes from different precursors, and with various terminations.

Sammendrag

I overgangen fra fossile til fornybare energikilder øker etterspørselen etter oppladbare batterier raskt. For å kunne møte denne etterspørselen, vil det bli nødvendig å benytte ulike batterikjemier, på grunn av begrensede ressurser av dagens batterimaterialer. I tillegg til Li-ionebatterier (LiB), har oppladbare Mg batterier (RMB) stått frem som en lovende batterikjemi, med potensial for høyenergibatterier basert på rikelige materialer. For å muliggjøre praktiske RMBer, er man derimot avhengig av å finne konkurransedyktige katodematerialer. Potensielle kandidater kan finnes blant familien av todimensjonale overgangsmetallkarbider og -nitrider kjent som MXene, som basert på høy elektriske ledningsevne, kjemiske justeringsmuligheter og ioneinterkaleringsegenskaper, har blitt beregnet å kunne gi høy kapasitet for en rekke kationer, inkludert Mg. Denne studien har derfor hatt som mål å evaluere MXenes potensiale som oppladbare batterielektroder, og da spesielt i RMBer.

I den første artikkelen av dette arbeidet ble MXene testet som en RMB-katode ved bruk av to forskjellige MXene-sammensetninger: V_2C og Ti_3C_2 . For å forsikre sannsynlig Mg-ionedisosiasjon og -migrering, ble disse elektrodene syklet i celler med fire forskjellige elektrolytter, og ved både lave ($20\text{ }^\circ\text{C}$) og høye ($60\text{ }^\circ\text{C}$) temperaturer. Likevel ble kun minimale reversible kapasiteter oppnådd, noe som indikerer ubetydelig Mg-interkalering i MXene-partiklene. Ved å inkludere Li-salter i elektrolytten ble derimot betydelige kapasiteter målt, noe som demonstrerte funksjonaliteten til MXene-elektrodene. For å forklare denne forskjellen ble beregninger av tetthetsfunksjonalteori (DFT) implementert, hvilket viste at migrasjonsbarrierene for Mg-ioner var betydelig høyere enn for Li-ioner, og at interkaleringsegenskapene for både Li- og Mg-ioner var svært avhengige av termineringsgruppene på overflaten av MXene-lagene. Angitt som "T" (eks. V_2CT_x), består disse termineringsgruppene vanligvis av en blanding av OH, O og F, og basert på beregningene viste det seg at flerlagspartikler av O-terminerte MXener ville være ideelle for RMB-katoder. Følgelig ble fokuset i dette arbeidet rettet mot å kontrollere terminerings-

gruppene til MXenene, og spesielt mot å bytte ut F- med O-termineringer.

I den andre og tredje artikkelen av dette arbeidet ble gasshydrolyse testet som en post-etsingsmetode for å bytte ut F-termineringer i multilags V_2CT_x og $Ti_3C_2T_x$ MXene-partikler. Fra disse studiene kom det frem at vellykket hydrolyse var avhengig av MXene-strukturer med utvidet mellomlagsavstand, for å tillate vannmolekylene å trenge inn mellom MXene-lagene. For V_2CT_x -fasen ble dette oppnådd ved hjelp av interkalerte vannmolekyler fra syntesen, mens $Ti_3C_2T_x$ -fasen var avhengig av interkalering av kationer for å holde på mellomlagsavstanden. For begge MXenene førte hydrolysen til en F-reduksjon på rundt 70 %, noe som er den største F-reduksjonen i multilags MXene-partikler rapportert så langt. På grunn av utfordringer med å kvantifisere de gjenværende termineringsgruppene (O vs. OH vs. uterminert), forble imidlertid den nøyaktige sammensetningen av MXenene udefinert. Selv om F-reduksjonen var tydelig for begge MXene-fasene, ble ingen økning i kapasitet observert ved sykling i RMB-celler. For å undersøke termineringsgruppenes innflytelse på de elektrokjemiske egenskapene, ble MXene-elektroden syklet i LiBer. Dette resulterte i ulike endringer for de to MXenene. Der den hydrolyserte V_2CT_x -fasen viste en forbedret ytelse ved høyere effekt sammenlignet med den ubehandlede MXenen, var det motsatte tilfelle for $Ti_3C_2T_x$. $Ti_3C_2T_x$ -fasen viste derimot økte spenninger og kapasiteter etter hydrolysering, noe som ikke ble observert for V_2CT_x -fasen. Basert på disse avvikende endringene i elektrokjemisk ytelse, og den udefinerte sammensetningen av termineringer, kunne det derfor ikke trekkes noen tydelig konklusjon om effekten av termineringsendring fra dette arbeidet. For å sikre kontrollert dannelse av O-terminerte MXener vil ytterligere raffinering av hydrolysemetoden være nødvendig, kombinert med forbedret karakterisering av termineringene.

I tillegg til de publiserte resultatene, inkluderer oppgaven nye resultater om en F-fri etsetmetode basert på hydrotermisk behandling i konsentrerte NaOH-løsninger. Disse etseforholdene resulterte i F-fri $Ti_3C_2T_x$ MXene, mens syntesen av andre MXene-komposisjoner var mindre vellykket. Selv om alle Ti_2AlC , Ti_2AlN , Ti_3AlCN , $TiMo_2AlC_2$, Nb_4AlC_3 , Nb_2AlC , V_2AlC - og V_4AlC_3 forløperne viste betydelig oksidering, viste de tre førstnevnte mulige tegn på noe uordnet MXene. Ytterligere undersøkelser, med optimaliserte etseforhold, er derfor nødvendig for å konkludere om denne etset metodens kompatibilitet for å danne andre MXene-faser enn $Ti_3C_2T_x$. Uansett er ikke denne etsetmetoden ideell for optimal termineringskontroll, ettersom den resulterer i en blanding av O- og OH-termineringer. Til sammenligning har en nylig rapportert etsetmetode, basert på Lewis-syre-etsing i saltmelter, muliggjort syntese av homogent terminerte MXener fra forskjellige forløpere, og med ulike termineringer.

List of abbreviations

| | |
|------------------------|---|
| 2D | Two-dimensional |
| APC | All phenyl complex |
| AN | Acetonitrile |
| BMOC | Borate magnesium oxide complex |
| CTA⁺ | Cetyltrimethylammonium ion |
| CV | Cyclic voltammetry |
| DEC | Diethyl carbonate |
| DFT | Density functional theory |
| DMC | Dimethyl carbonate |
| DME | 1,2-dimethoxyethane |
| EC | Ethylene carbonate |
| EDS | Energy dispersive X-ray spectroscopy |
| EELS | Electron energy loss spectroscopy |
| EMC | Ethyl methyl carbonate |
| EV | Electric vehicle |
| FESEM | Field emission scanning electron microscopy |
| FIB | Focused ion beam |
| FTIR | Fourier-transform infrared spectroscopy |
| HAADF | High-angle annular dark-field |
| hcp | hexagonal close-packed |
| LCO | LiCoO ₂ |

| | |
|------------------------|---|
| LFP | LiFePO ₄ |
| LiB | Li-ion battery |
| LMO | LiMn ₂ O ₄ |
| LNMO | LiMn _{1.5} Ni _{0.5} O ₄ |
| LTO | Lithium titanium oxide (Li ₄ Ti ₅ O ₁₂) |
| MACC | Magnesium aluminium chloride complex |
| NEP | 1-ethyl-2-pyrrolidone |
| Ni-MH | Nickel metal hydride |
| NMC | LiNi _x Mn _y Co _z O ₂ |
| NMR | Nuclear magnetic resonance |
| NTO | Sodium titanates (Na _x Ti _y O _z) |
| PAQ | Polyanthraquinone |
| PC | Propylene carbonate |
| PiB | Potassium-ion battery |
| PVDF | Polyvinylidene fluoride |
| RMB | Rechargeable Mg battery |
| SEI | Solid electrolyte interphase |
| SEM | Scanning electron microscopy |
| SiB | Sodium-ion battery |
| SSE | Solid state electrolyte |
| STEM | Scanning transmission electron microscopy |
| TBA⁺ | Tetrabutylammonium-ion |
| TBAOH | Tetrabutylammonium hydroxide |
| TEM | Transmission electron microscopy |
| TFSI | Bis(trifluoromethanesulfonyl)imide |
| TGA | Thermogravimetric analysis |
| THF | Tetrahydrofuran |
| THFPB | Tris(2H-hexafluoroisopropyl) borate |
| XPS | X-ray photoelectron spectroscopy |
| XRD | X-ray diffraction |

Contents

| | |
|---|-------------|
| Preface | i |
| Acknowledgments | iii |
| The author's contribution | v |
| Summary | ix |
| Sammendrag | xi |
| List of abbreviations | xiii |
| 1 Introduction | 1 |
| 1.1 Background and motivation | 2 |
| 1.2 Aim of work | 4 |
| 2 Literature review | 7 |
| 2.1 Rechargeable batteries | 8 |
| 2.1.1 General introduction | 8 |
| 2.1.2 Lithium-ion batteries (LiBs) | 12 |
| 2.1.3 Rechargeable magnesium batteries (RMBs) | 19 |
| 2.2 MXenes | 28 |
| 2.2.1 Introduction | 28 |
| 2.2.2 Properties and applications | 32 |
| 2.2.3 MXenes for energy storage | 33 |
| 2.2.4 Termination control | 40 |
| 3 Methods | 49 |
| 3.1 Overview | 50 |

| | | |
|----------|--|-----------|
| 3.2 | MXene synthesis | 51 |
| 3.2.1 | MAX phase synthesis | 51 |
| 3.2.2 | HF etching | 51 |
| 3.2.3 | F-free alkaline etching | 52 |
| 3.3 | Post-etching treatments | 52 |
| 3.3.1 | Cation intercalation | 52 |
| 3.3.2 | Gas hydrolysis | 53 |
| 3.4 | Material characterisation | 54 |
| 3.4.1 | X-ray diffraction (XRD) | 54 |
| 3.4.2 | Scanning electron microscopy (SEM) | 54 |
| 3.4.3 | Energy-dispersive X-ray spectroscopy (EDS) | 54 |
| 3.4.4 | Laser diffraction | 55 |
| 3.4.5 | X-ray photoelectron spectroscopy (XPS) | 55 |
| 3.4.6 | Raman spectroscopy | 55 |
| 3.4.7 | Transmission electron microscopy (TEM) | 55 |
| 3.4.8 | Fourier-transform infrared spectroscopy (FTIR) | 56 |
| 3.4.9 | Thermogravimetric analysis (TGA) | 56 |
| 3.5 | Electrochemical characterisation | 56 |
| 3.5.1 | Electrode preparation | 56 |
| 3.5.2 | Electrolyte preparation | 57 |
| 3.5.3 | Coin cell assembly | 57 |
| 3.5.4 | Galvanostatic cycling | 58 |
| 3.6 | Density functional theory (DFT) calculations | 58 |
| 4 | Summary of results | 59 |
| 4.1 | Foreword | 60 |
| 4.2 | Paper I: MXenes as cathode material in RMBs | 60 |
| 4.2.1 | Overview | 60 |
| 4.2.2 | MXene synthesis | 60 |
| 4.2.3 | Electrochemical performance | 61 |
| 4.2.4 | DFT calculations and conclusion | 63 |
| 4.3 | Paper II: Gas hydrolysis of V_2CT_x | 65 |
| 4.3.1 | Overview | 65 |
| 4.3.2 | MXene synthesis | 65 |
| 4.3.3 | Gas hydrolysis | 66 |
| 4.3.4 | Electrochemical performance in LiBs | 68 |
| 4.4 | Paper III: Gas hydrolysis of $Ti_3C_2T_x$ | 69 |

| | | |
|----------|--|------------|
| 4.4.1 | Overview | 69 |
| 4.4.2 | MXene synthesis | 69 |
| 4.4.3 | Gas hydrolysis on pristine $\text{Ti}_3\text{C}_2\text{T}_x$ | 69 |
| 4.4.4 | Gas hydrolysis on pre-intercalated $\text{Ti}_3\text{C}_2\text{T}_x$ | 70 |
| 4.4.5 | Electrochemical evaluation of K- Ti_3C_2 electrodes in LiBs | 71 |
| 4.4.6 | Thermal stability of $\text{Ti}_3\text{C}_2\text{T}_x$ | 72 |
| 4.4.7 | Cycling results of oxidised $\text{Ti}_3\text{C}_2\text{T}_x$ MXene (not published) | 74 |
| 4.5 | F-free etching in alkaline solutions | 76 |
| 4.5.1 | Etching of the Ti_3AlC_2 MAX phase | 76 |
| 4.5.2 | Alkaline etching of other MAX phases | 80 |
| 4.5.3 | Summary of alkaline etching results | 84 |
| 5 | Conclusions and outlook | 85 |
| | Bibliography | 91 |
| | Appended papers | 111 |
| | Paper I: Are MXenes Suitable as Cathode Material for Rechargeable Mg Batteries? | 113 |
| | Paper 2: Removing Fluoride-terminations from Multilayered V_2CT_x MXene by Gas Hydrolyzation | 143 |
| | Paper 3: Bulk substitution of F-terminations from $\text{Ti}_3\text{C}_2\text{T}_x$ MXene by cation pillaring and gas hydrolysis | 167 |

1

Introduction

1.1 Background and motivation

As stated by the IPCC's Sixth Assessment Report on climate change, a transition from fossil fuels to renewable energy sources will be required to reduce the amount of human-emitted greenhouse gases and thereby avoid surpassing a 1.5 degree increase in global temperature.¹ However, as most of the renewable energy sources are based on intermittent weather phenomenon such as wind, rain and sunlight, energy storage methods will be required to enable energy supply regardless of weather. In recent months, security of energy supply has also become one of the most pressing topics in the European Union, as the transition from fossil based energy has been escalated by the political situation in the region.² To help mitigate these challenges, rechargeable batteries are envisioned to play a pivotal role in balancing the future energy supply.^{3,4} As batteries are also essential for the rise of electric vehicles (EVs), the market for rechargeable batteries are expected to grow exponentially in the upcoming decades, as illustrated in Figure 1.1.^{5,6}

To meet this immense demand for rechargeable batteries, most of the liability has been placed on the Li-ion battery (LiB) chemistry. This is based on the extensive advancements of the technology since it was commercialised in 1991.⁸ With a high energy density and energy efficiency, combined with a continuous reduction in production costs, LiBs have demonstrated their role as one of the most competitive methods for energy storage, and

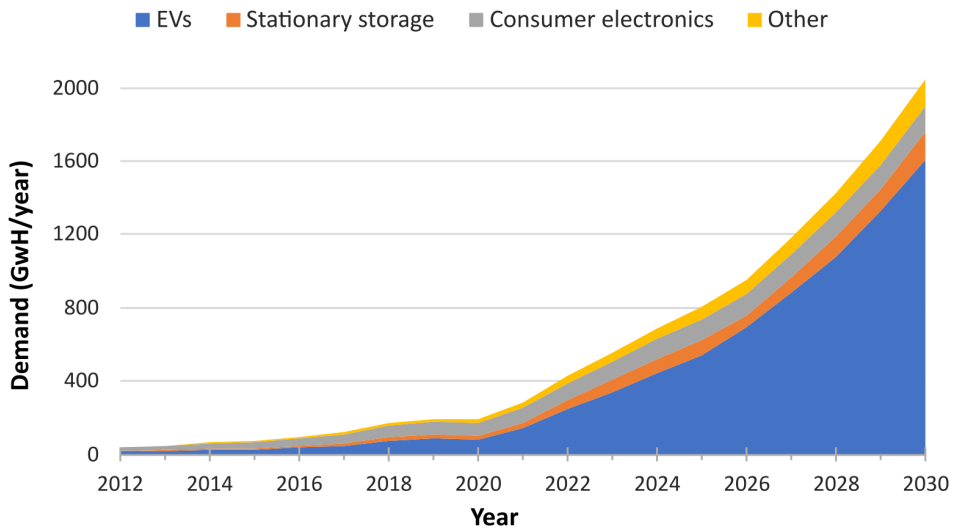


Figure 1.1: Historic and predicted demand for rechargeable batteries in the period 2012-2030, separated by application area. The data is obtained from BloombergNEF.⁷

are one of the main enablers for the growth of the EV market in recent years.⁹ The most significant change has been related to the price of the battery packs, which since 2010 has declined by 89 % to a price of \$132/kWh in 2021.^{10,11} However, with globally and regionally limited material reserves, this price reduction is expected to turn, as the demand for current LiB related materials now has surpassed the supply, causing the prices to skyrocket during the last year.¹² Due to the ethical concerns related to the extraction of Co,¹³ a key material in most LiB chemistries today, the sustainability of material production has also been questioned.^{14,15} Hence, alternative battery materials are necessary to ensure the high supply of batteries that are needed, and ideally from more sustainable battery chemistries. As the electrode materials constitute more than 30 % of the total cell production cost, and due to the scarcity of some of the currently used electrode materials, significant cost reductions can be achieved by a diversification of electrode chemistries.^{9,11,14,15}

In addition to continuous improvements in LiB technology, the high demand for rechargeable batteries may also necessitate the use of alternative battery chemistries based on Na, Mg, Zn, K, Ca or Al cations or on F or Cl anions.^{15,16} Due to higher abundance and easier accessibility of these materials compared to Li,¹⁷ these chemistries could potentially result in cheaper battery cells and be easier to scale up than today's LiBs. Moreover, by utilising several battery chemistries for various applications, the demand for LiB materials would be reduced, preventing unwanted increase in battery cell costs upon further growth of the rechargeable battery market. However, in order for these chemistries to deliver the necessary battery performance, further improvements of the state-of-the-art electrode materials may be needed.^{16,18}

A promising candidate for future electrode materials has been the family of two-dimensional materials known as MXenes, which was first synthesised by Naguib et al. in 2011.¹⁹ Based on properties such as high electrical conductivity, ion-storage possibility and chemical tunability,^{20,21} MXenes have attracted significant interest for a range of applications, including electrode materials for rechargeable batteries.²⁰ Initial experimental reports have demonstrated well performing MXene electrodes in several battery chemistries, such as LiBs^{22,23}, sodium-ion batteries (SiBs)²⁴, potassium-ion batteries (PiBs)²⁵ and rechargeable Al batteries²⁶, but they have yet to reach their theoretically calculated limits.²⁷⁻²⁹ To overcome this challenge, focus has been directed towards delamination of the MXene layers, to obtain higher capacities by increasing the surface area.^{30,31} However, in order to achieve competitive volumetric energy densities to today's state-of-the-art electrode materials, improved performance of multilayered MXene particles will be required. Therefore, control of the ion-intercalation environment

at the interface between the two dimensional MXene sheets is essential for commercial utilisation of MXene electrodes. This includes the chemical composition of the MXene, and specifically the surface terminations, the intercalation of other ions and the stacking of the MXene sheets (Figure 1.2). From density functional (DFT) calculations, these parameters have been demonstrated to significantly change the intercalating properties such as ion migration, voltage and obtainable capacities, in addition to the possible side reactions that might take place.^{28,32–34}

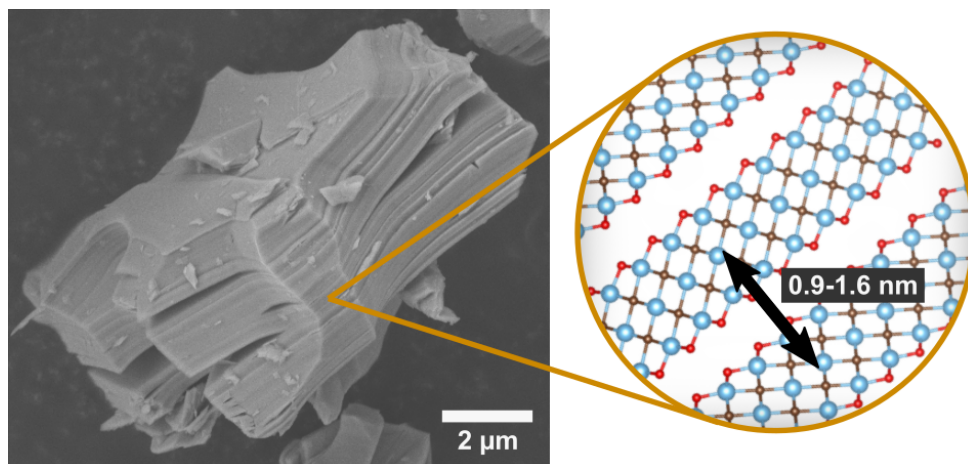


Figure 1.2: Scanning electron microscopy (SEM) micrograph of the most studied MXene composition, $\text{Ti}_3\text{C}_2\text{T}_x$ (T = termination group), with a schematic of its layered structure. The range of interlayer spacings illustrates the possibility for ion intercalation in between the MXene sheets. Reproduced from Ref.³⁵ with permission from the Royal Society of Chemistry.

1.2 Aim of work

The overall aim of this project has been to evaluate the feasibility of multilayered MXenes as electrode materials in rechargeable batteries. More specifically, the focus has been on the synthesis and surface termination modification of various multilayered MXene compositions, in order to control their ion-intercalating properties for both Mg- and Li-ions. The work is divided into four parts.

Initially, the goal of the project was to assess the feasibility of MXenes as potential cathode materials in rechargeable Mg batteries (RMBs). This was based on theoretically predicted high capacities for MXene electrodes in RMBs,^{27,28} and a previous report that demonstrated a functioning Mg/Li hybrid battery using a titanium carbide MXene electrode.³⁶ During the work, several reports on Mg-intercalation were published,^{37–39} but

similar to most of the research on MXene electrodes, these reports utilised delaminated MXenes electrodes with high porosity. Our work therefore aimed to answer whether or not reversible Mg-ion intercalation would be possible in multilayered MXene particles, with the use of V_2CT_x and $Ti_3C_2T_x$ MXene, where "T" represents the surface terminations. The main findings from this work are included in Paper I.

As the conclusion from the first paper was that Mg-ion intercalation strongly depend on the MXene chemistry, and that O-terminated V_2CO_2 stood out as the ideal composition, further work was aimed at controlling the mixture of these terminations and especially reducing the amount of F-terminations on V_2CT_x MXene. Although several post-etching methods had previously been reported, such as alkali treatment^{40,41} and annealing in various atmospheres,⁴²⁻⁴⁴ none of these had demonstrated controlled removal of F-terminations from multilayered MXene particles. Due to its theoretical promise, gas hydrolysis was chosen as a novel method to be assessed. Hence, the second part of this project was aimed at substituting F-terminations from HF-etched V_2CT_x MXene by gas hydrolysis, and subsequently examine its effect on the ion-intercalation properties of the MXene. The main results related to this part are included in Paper II.

After the successful F removal from the V_2CT_x MXene, the next goal was to explore gas hydrolysis on other MXene compositions. Therefore, gas hydrolysis was also performed on the most studied $Ti_3C_2T_x$ MXene, to investigate if similar termination changes could be obtained for this MXene phase, and how potential changes would change its electrochemical performance. The results from this work are summarised in Paper III.

At last, in addition to the post-etching method of gas hydrolysis, a F-free etching method was also investigated to completely avoid the formation of F-terminations. This was based on the work by Li et al.,⁴⁵ and consisted of hydrothermal etching in concentrated NaOH solutions. In addition to reproducing Li's results on $Ti_3C_2T_x$ MXene, our investigation was expanded to study hydrothermal etching of a number of different MAX phases. The main findings from this work are presented in Section 4.5.

2

Literature review

2.1 Rechargeable batteries

2.1.1 General introduction

Working principles

Battery cells comprise of several different components, as illustrated in Figure 2.1.⁴⁶ It consists of two electrodes (anode and cathode) that may store cations at different electrochemical potentials, an electronically insulating electrolyte to transfer only the cations between the electrodes and an outer electric circuit to transport electrons in the same direction. The separator is required to prevent contact between the electrodes, as it would short circuit the cell. Additionally, current collectors are normally employed as a substrate for the electrode materials to ensure mechanical stability of the electrodes and improve electrical contact between the electrochemical reactions in the electrodes and the outer circuit. The electrodes usually comprise of three different components, the active electrode material, a carbon conductive additive and a binder material to ensure good contact between the different particles and to the current collector.

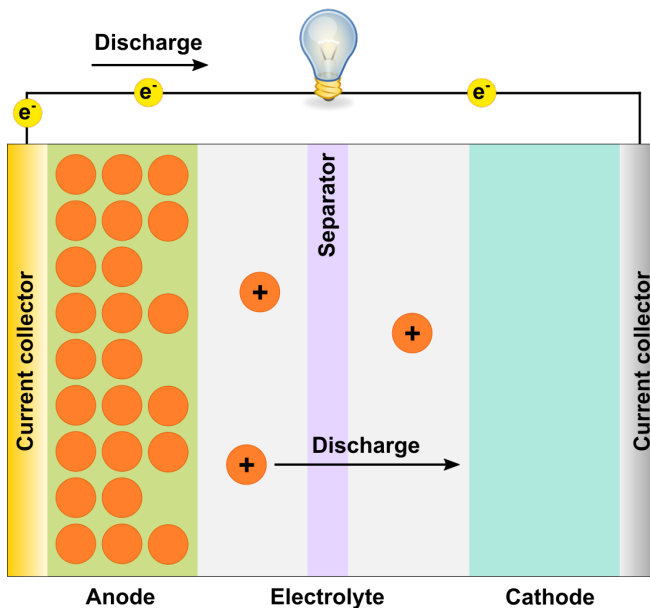


Figure 2.1: Schematic of a charged battery cell demonstrating the transportation of cations and electrons from the anode to the cathode through the electrolyte and an electrical circuit, respectively, upon discharge.

Although all these components are important for the total electrochemical performance of the cell, the main components governing the cell's energy storage are the active electrode materials and the electrolyte. The energy stored is a product of the charges transferred between the electrodes and the voltage at which these charges are being transported, where the total charge that can be stored in each electrode is denoted as the electrodes capacities. As illustrated in Figure 2.2, the open circuit voltage for this charge transfer is given by the difference in the electrons electrochemical potentials at the two electrodes, and the greater the separation of the potentials, the higher operating voltage of the cell. However, in order to prevent unwanted reactions with the electrolyte, it is also necessary to maintain the electrochemical potentials within the electrolytes stability window. If not, electrons from the anode would be able to reduce the electrolyte, or the lower potential at the cathode would cause an oxidation of the electrolyte.⁴⁷ To maximise the operating voltage of a battery cell one would therefore need an electrolyte with a high stability window, combined with two electrode materials that fully exploits this large stability window. To further maximise the energy density of the cell, the gravimetric and volumetric capacities (mAh/kg and mAh/L) of the electrode materials must be maximised, in addition to minimising the mass and volume of all the additional cell components.

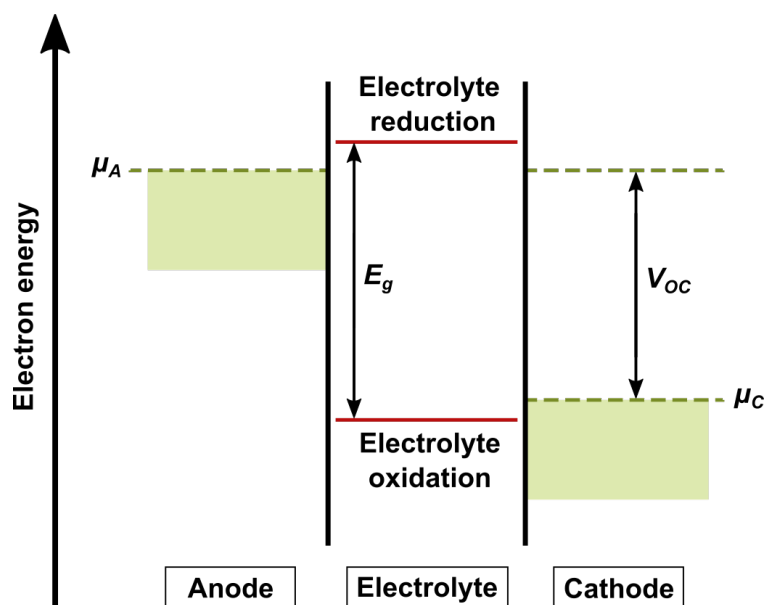


Figure 2.2: Schematic of the electrochemical potentials of electrons in the anode (μ_A) and the cathode (μ_C) resulting in the open circuit voltage of the cell (V_{OC}), in addition to the stability window of the electrolyte (E_g).

What distinguishes rechargeable batteries from their non-rechargeable counterparts is the possibility of reversing the electrochemical reactions by applying a reversed voltage. By forcing the electrons and cations back to the anode, and to a higher electrochemical potential, one can restore the initial energy in the battery. As small overpotentials are required for the electrochemical reactions to occur, the energy required to charge a battery is always higher than the energy that can be withdrawn upon discharge. These overpotentials also relate to the power densities of the cells, as high overpotentials can cause reduced operating voltages and/or unwanted side reactions with the electrolyte. Furthermore, if these reactions were to be 100 % reversible and no side reactions were to occur, these cells would be able to cycle endlessly. However, as this is usually not the case, most cells have a limited cycle life. Due to degradation without cycling as well, batteries also have a limited calendar life.

In addition to the already mentioned battery performance parameters, there are several more factors that are important when evaluating battery cells. One of the most important specifications in our market based economy is related to the cost of the cells, which is usually given in \$/kWh. Moreover, with an increased focus on sustainability in today's society, the use of environmentally benign and recyclable materials is highly sought. Regarding sustainability, there is also a need for increased safety, both during production of the battery cells, as well as upon utilisation. One of the most relevant examples is the challenge of most electrolytes for high energy battery chemistries being highly flammable, making these cells inapplicable for various applications. A summary of the most important parameters for battery cell evaluation is given in the list below.

1. Energy density (Wh/L and Wh/kg)
2. Cost (\$/kWh)
3. Power density (W/L and W/kg)
4. Sustainability/recyclability
5. Safety
6. Cycle life and calendar life
7. Energy efficiency
8. Self discharge
9. Temperature stability

Historical development

Alessandro Volta demonstrated the first battery cell in 1800.⁴⁸ Since then, it took 59 years until Gaston Planté reported on the first rechargeable battery, which was based on a lead acid chemistry.⁴⁹ Even though being the oldest rechargeable battery chemistry, lead acid batteries have constituted more than half of the market for rechargeable batteries until 2018 as they have been used for start ignitions in cars, trucks and boats etc.⁵⁰ Nonetheless, although lead acid batteries perform well for a lot of the above-mentioned parameters, their energy density is too low for energy storage in a lot of portable applications. In 1899, Waldemar Jungner invented the nickel-cadmium battery, which resulted in significantly increased energy densities and would end up dominating the high energy-density market for almost a century. It was not until the introduction of nickel-metal hydride (Ni-MH) and LiBs around 1990, that a similar improvement in energy density was achieved.⁴⁹ Since then, these battery chemistries have been used for a range of different portable electronic applications. As LiBs have demonstrated the highest energy density of all battery chemistries so far, it has played a pivotal role in the development of EVs, and is now dominating the market for rechargeable batteries.^{8,50} A comparison of the energy densities from the different battery chemistries is illustrated in Figure 2.3.

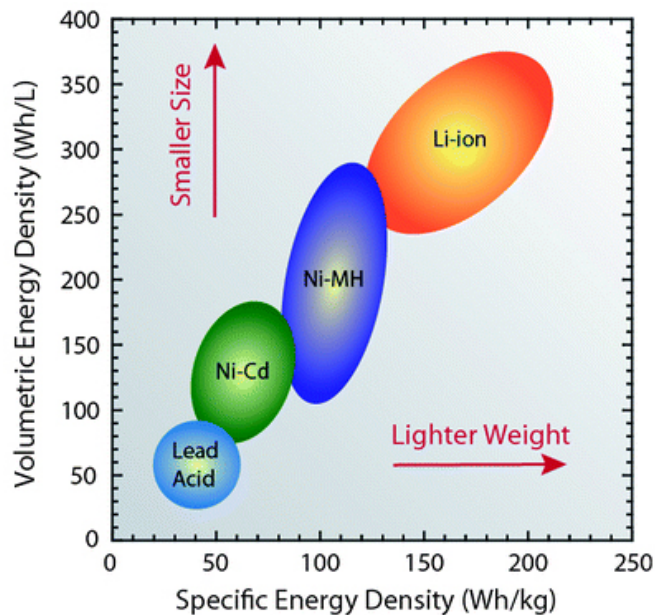


Figure 2.3: Comparison of cell energy densities for different rechargeable battery chemistries. Reproduced from Ref⁵¹.

2.1.2 Lithium-ion batteries (LiBs)

Introduction

Rechargeable Li batteries have always been an interesting chemistry for high energy applications, due to the low reduction potential and light weight of Li. However, due to the formation of detrimental morphologies upon plating and stripping of Li metal, alternative anode materials were required for the Li chemistry to work for prolonged cycling.⁸ As these electrode materials were based on the transfer of Li-ions, these chemistries were referred to as Li-ion batteries. Considering most electrolytes decompose in contact with electrodes operating at a similar potential as Li metal, LiBs faced severe challenges in its early stages. The commercialisation of the Li-ion battery therefore relied on the formation of a Li-permeable solid electrolyte interphase (SEI) with a low electronic conductivity, which then enabled continued cycling while preventing further decomposition of the electrolyte.⁸ The stable SEI layer formed by the reductive decomposition of ethylene carbonate (EC) based electrolytes also allowed the use of graphite anodes, as it prevented delamination of graphene flakes upon Li-intercalation, which was previously a problem for propylene carbonate (PC) based electrolytes.^{52,53} Although the combination of graphite anodes with high-voltage layered oxides have enabled the high energy density of LiBs, extensive research has been applied to further optimise the performance of LiBs.⁹ In the upcoming sections, short reviews of relevant electrolytes and electrode materials will be given, starting off with the anode and cathode materials. Before that, ideal properties for both electrode materials are summarised as follows:

1. Reversibly react with Li
2. Have high capacity for Li-ions
3. React with Li at a high/low voltage for cathode/anode
4. Show fast reactions with Li (for high power density)
5. Possess sufficiently high electrical conductivity
6. Remain structurally stable upon lithiation and delithiation
7. Based on low cost materials and scalable synthesis methods
8. Based on environmentally benign materials

Anode materials

As stated by Winter et al.,⁸ the "Holy Grail" of LiB research has been related to enabling the use of Li metal anodes, as it possesses the maximum capacity and minimum reduction potential possible for any LiB anode material. To overcome the challenges of dendritic growth upon cycling, a lot of research is directed towards the use of solid state electrolytes.⁵⁴ However, with the implementation of solid electrolytes, the immense volume change of the Li metal anode causes new challenges related to the contact between the anode and the electrolyte. For common electrolytes the volume change also causes an extended SEI formation, which leads to significant capacity decay.⁵⁵ Therefore, the quest for the "Holy Grail" still remains unsolved, causing the industry to utilise other anode materials that enable stable and safe cycling. In addition to the plating and stripping of Li metal, LiB electrode materials are usually classified into intercalation, alloying and conversion types based on their reaction mechanism.

After being one of the first commercial anode materials, intercalation based graphite still remains the most used anode material, due to its reliable insertion of Li-ions at a low voltage of 0.1 V and its reasonably high capacity of 372 mAh/g.^{8,52} Combined with the commonly lithiated cathode materials, graphite can be implemented in its delithiated state, which also simplifies the production of the cells. However, in search for higher energy densities and more stable performance, other anode materials are also being investigated.

In Table 2.1, a comparison of relevant properties for some of the most studied anode materials is presented. Although other alloying materials (e.g. SiO_x, Sn, and Ge) have shown promising results,⁶¹ Si has received most attention due to its high theoretical capacity, relatively low delithiation voltage, high chemical stability and natural abundance.^{57,59,61} Although the delithiated specific capacity of 3579 mAh/g makes it comparable to the metal anode, this is somewhat misleading, as the theoretical capacity of metal anodes is

Table 2.1: Properties for common anode materials for Li-ion batteries. The theoretical specific capacities and volume changes are based on the mass and volume of delithiated non-metal electrode materials. For Li metal, it is based on a lithiated electrode with zero excess Li.

| Anode material | Type | Lithiated comp. | Voltage [V vs. Li/Li ⁺] | Capacity [mAh/g] | Volume change [%] |
|---------------------------|-----------------------|---|-------------------------------------|------------------|-------------------|
| Li metal ⁵⁶ | Plating and Stripping | Li | 0 | 3861 | 100 |
| Graphite ^{52,57} | Intercalation | LiC ₆ | 0.1 | 372 | 10 |
| Si ⁵⁷⁻⁵⁹ | Alloying | Li ₁₅ Si ₄ | 0.4 | 3579 | 270 |
| LTO ^{57,60} | Intercalation | Li ₇ Ti ₅ O ₁₂ | 1.6 | 175 | 0.2 |

usually referred to its lithiated state, or by utilisation of 100 % excess Li. Nonetheless, even with a lithiated specific capacity of 1857 mAh/g, Si anodes still demonstrate more than a 5 times increase compared to graphite, and almost half of the optimal Li metal anode. Even though the voltage is slightly higher than for graphite (0.4 V vs. 0.1 V), the high capacity of Si has the potential to significantly increase the energy density of LiBs. The major problem hampering the implementation of Si anodes relates to the enormous volume change during lithiation (270 %), that leads to particle pulverisation, disintegration of the electrode, increased SEI formation and loss of electrical contact, which again limits the cycle life of LiBs with Si anodes.^{58,59} To restrict this volume change, utilisation of a graphite/Si mixture is one of the most likely improvements for near future high energy LiBs.^{9,62}

Another interesting anode material is the intercalation-based $\text{Li}_4\text{Ti}_5\text{O}_{12}$ (LTO) spinel structure. Compared to the other materials, the main advantages of LTOs are increased cycle life and thermal stability, in addition to higher energy efficiency and rate-capability (faster reactions with Li).^{57,60,63} These improvements mostly originates from the "zero-strain" intercalation, as demonstrated by the 0.2 % volume change, and the lack of SEI formation upon reacting at a voltage within the stability window of normal electrolytes (1.6 V). However, due to this high operating voltage and the low capacity of 175 mAh/g, LTO anodes result in the lowest energy density of these electrode materials.

Cathode materials

Compared to the anodes, there has been a larger variation in utilised cathode materials over the last 30 years, where some of the most important ones are listed in Table 2.2.^{8,57,64} Since Goodenough demonstrated the high voltages of layered oxides in 1980 (Figure 2.4a),⁶⁵ LiCoO_2 (LCO) has remained as one of the best performing cathode materials for high energy LiBs, with an operating voltage of 4.0 V and a practical capacity of around 140 mAh/g.^{62,66} Still, as only ~50 % of the theoretical capacity of 274 mAh/g can be reversibly intercalated without structural instability,⁶⁶ other cathode materials with higher capacities have enabled further improvement in the energy density of modern LiBs. The transition away from LCO cathodes has also been linked with the political and economical challenges related to the use of Co.^{14,15} As an example, layered LiMn_2O_4 (LMO) has demonstrated similar performance to LCO, without the need for Co.⁶⁷ However, as LMO electrodes display no improvements in energy density and increased capacity fading upon cycling due to i.e. Mn dissolution in the electrolyte,^{57,67} other materials have attracted more attention in recent years.

Table 2.2: Overview of properties for a selection of relevant cathode materials for Li-ion batteries, including average voltages and commonly obtained specific capacities. Except for S, the specific capacities are based on the mass of lithiated compositions.

| Type | Abbreviation | Lithiated composition | Voltage [V vs. Li/Li ⁺] | Capacity [mAh/g] | Ref. |
|---------------|--------------|--|-------------------------------------|------------------|-------|
| Intercalation | LCO | LiCoO ₂ | 4.0 | ~140 | 57,66 |
| | LMO | LiMn ₂ O ₄ | 4.0 | ~130 | 57,67 |
| | NMC | LiNi _x Mn _y Co _z O ₂ | 3.9 | ~150-200 | 57,68 |
| | LFP | LiFePO ₄ | 3.5 | 170* | 57,69 |
| | LNMO | LiMn _{1.5} Ni _{0.5} O ₄ | 4.7 | 147* | 57,70 |
| Conversion | S | Li ₂ S | 2.2 | 1672* | 57,71 |

*Theoretical

One of the best-performing cathode materials today are the layered LiNi_xMn_yCo_zO₂ (NMC) structures that comprise a mixture of transition metals.^{9,68} The initial composition with a Ni:Mn:Co ratio of 1:1:1 (NMC111) was able to deliver a stable capacity of around 150 mAh/g at an average voltage of around 3.9 V.⁷² By increasing the Ni content, the capacity has been improved to around 200 mAh/g for NMC811 (80 % Ni), making it the ideal electrode for high-energy applications.^{9,62,73} Additionally, the increased Ni content reduces the need for Co. However, as the increased Ni content reduces the thermal and cycling stability of the cathodes, it is uncertain whether or not further Co reduction can be obtained for practical NMC cathodes.⁶⁸ To overcome this challenge and further improve the performance and cost of NMC cathodes, approaches such as doping are currently being investigated.^{74,75}

Similar to the anode materials, conversion cathodes may deliver capacities that greatly outperform the intercalation based materials. With a theoretical specific capacity of 1672 mAh/g, sulfur cathodes offer significantly increased capacities compared to the layered oxides, making Li-S batteries one of the most interesting battery chemistries for the future.^{71,76} Nonetheless, due to the low voltage of S relative to Li/Li⁺ (2.2 V), the realisation of high energy density requires the utilisation of a Li metal anode for a sufficiently high practical voltages. A Li metal anode would also ensure enough Li, as the S cathode is free of Li, unlike most other cathode materials. In addition to the already discussed challenges with Li metal anodes, Li-S batteries also struggle with the shuttling of polysulfides that are soluble in common electrolytes.⁷¹ If these challenges are overcome, Li-S batteries would be able to greatly improve the gravimetric energy density from current LiBs, with the use of abundant and cheap materials.

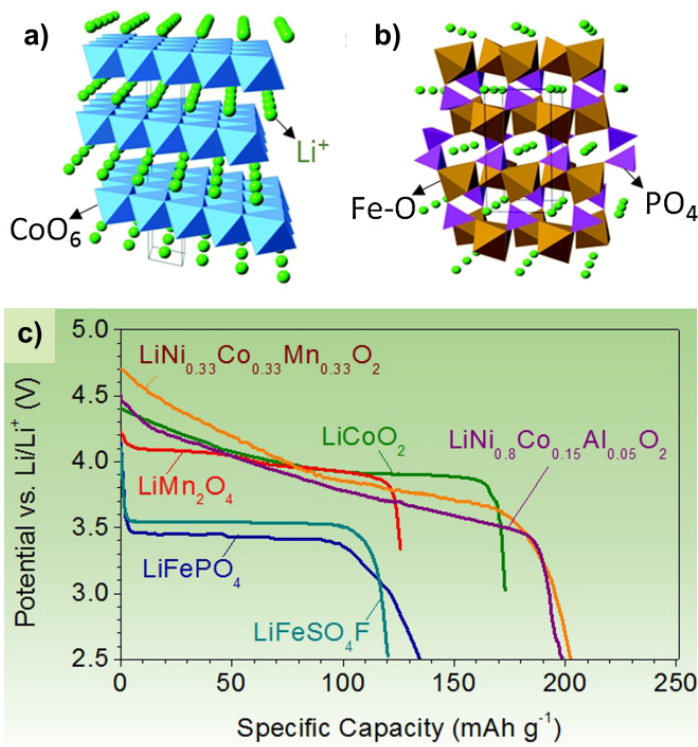


Figure 2.4: Crystal structures of layered LCO (a) and olivine LFP (b), together with common voltage profiles for several intercalation based cathode materials for LiBs. Adapted from Ref⁵⁷ under the Creative Commons Licence [CC BY-NC-ND 4.0](https://creativecommons.org/licenses/by-nc-nd/4.0/).

Another approach to improve the energy density of LiBs, is by increasing the intercalation voltage. Together with a Co free composition, increased voltage is one of the main advantages of the spinel LiMn_{1.5}Ni_{0.5}O₄ (LNMO) cathode, as it operates at almost 1 V higher than the layered oxides.^{57,70} However, the increased voltage also results in new challenges, as there are fewer electrolytes that are stable at such high potentials. This is illustrated in Figure 2.5, where the voltages of the mentioned electrode materials are marked together with the electrochemical stability window of two electrolyte solvents.⁸ In order for LNMO, or any other high-voltage cathode, to work at such high voltages either new electrolytes will be required, or an improved solid-electrolyte interphase to limit the electrolyte degradation.⁷⁷ Although the relatively low theoretical capacity of LNMO (< 150 mAh/g) results in a lower energy density than NMC811, the reduced materials cost and improved sustainability of this material has attracted attention from commercial companies.⁷⁸

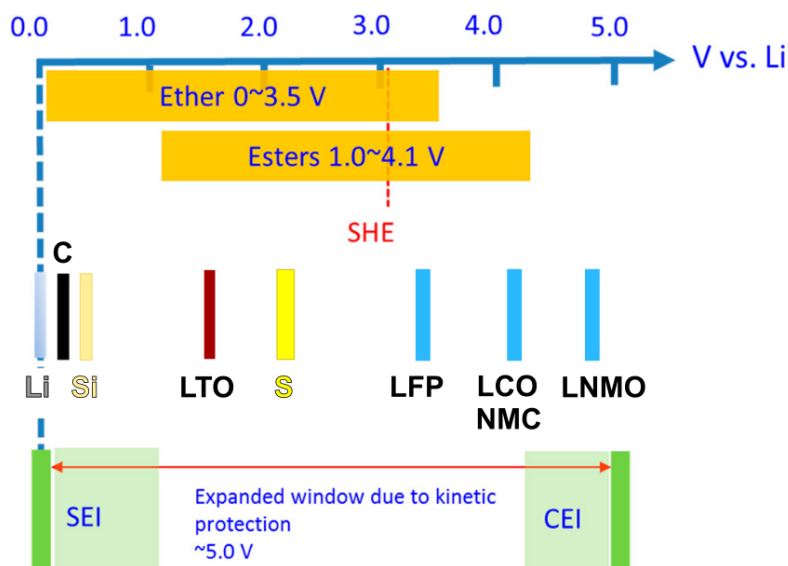


Figure 2.5: Schematic potential diagram illustrating the mismatch between the electrochemical stabilities of two electrolytes and the redox potentials of most cathode and anode materials used in modern LiBs. Adapted from Ref⁸. Copyright ©2018 American Chemical Society.

Considering the cathode material constitute around 20-40 % of the materials costs at cell level,⁹ significant savings can be achieved by utilising cheaper materials. This is one of the main reasons why car companies such as Tesla have switched to LFP cathodes for several of their car models.⁷⁹ LFP is based on an olivine structure of LiFePO_4 which comprise more cheap and abundant materials compared to Ni, Co and Mn, which again may enable a 10 % cost reduction of the batteries.^{15,80} Together with their high thermal stability, high rate capability and excellent cycling stability, this material has also proven applicable for other applications than EVs.^{57,69} The main drawback of LFP cathodes relates to the relatively low average voltage of 3.5 V and a poor electric and ionic conductivity, which causes the need for reduced particle sizes and carbon coatings. In total this results in a significantly lower energy density compared to the high energy NMC cathodes.⁶²

Electrolytes

Electrolytes are a key component for functional LiBs, as they govern the (de)solvation of Li-ions at both electrodes, the ionic transport between them, the electrochemical stability window and what side reactions that can occur.⁴⁶ An ideal electrolyte would therefore be able to hold significant amounts of Li, have a high ionic conductivity with a high cation

transference number, be electronically insulating, show good contact to the electrodes and be inert to the other cell components, in addition to remaining stable for a wide temperature range.^{81,82} Although lean amounts of electrolyte are required to achieve high energy densities,⁹ the use of sustainable, cheap and low flammable electrolytes would also be ideal properties for commercial LiBs. To achieve this, there are several approaches that have been explored.

The currently utilised electrolytes in commercial LiBs are based on dissolved Li-salts in liquid aprotic organic solvents.⁹ Although these electrolytes are unstable towards most of the cell components, a passivating SEI layer forms upon initial cycling, which prevents further decomposition and thus allows for continued cycling.⁸¹ These stable SEIs have enabled the utilisation of aprotic organic carbonate solvents such as the cyclic propylene carbonate (PC) and ethylene carbonate (EC), and the linear ethylmethyl carbonate (EMC), dimethyl carbonate (DMC) and diethyl carbonate (DEC), combined with a LiPF₆ salt to constitute the most common electrolytes in today's LiBs.⁸² Compared to the linear carbonates, cyclic carbonates generally possess the highest temperature stability and the highest dielectric constants (dissolving most Li salts), but also the highest viscosity, which leads to a poor ionic conductivity.^{81,83} To optimise the electrolyte properties for specific applications, a mixture of different carbonates is therefore commonly utilised.^{81,82}

For improved safety of LiBs and the possibility of enabling a Li metal anode, other electrolyte types have been investigated.^{54,84,85} These include ionic liquids, polymers, solid state electrolytes (SSE), and a combinations of these. However, although the promise of these electrolytes is great, they still face significant challenges to outperform current liquid electrolytes. Where high energy densities can be achieved through the utilisation of metal anodes, this may come at the expense of limited power densities, as high currents have been shown to result in dendrites even penetrating through inorganic solids.⁸⁶ In addition, these electrolytes face significant challenges related to poor ionic conductivity at low temperatures and bad contact between the electrodes and the electrolytes. Until these challenges are overcome, liquid organic electrolytes will continue to be used in most commercial LiBs.

2.1.3 Rechargeable magnesium batteries (RMBs)

The potential of RMBs

With the need for continued improvements of rechargeable batteries, as well as a diversification of battery chemistries to enable the extensive supply, several new chemistries stand out as interesting candidates. One of the most studied alternative chemistries to date are based on Mg-ions. In short, the main motivation for RMBs can be summarised in three points:

1. Possibility to use Mg metal anode
2. High gravimetric and volumetric capacities of Mg metal anode
3. Natural abundance and low cost of Mg

Although dendritic growth have been demonstrated in some uncommon electrolytes,^{87–89} Mg metal is generally known to plate in a non-detrimental way upon cycling.^{18,87} Unlike for LiBs, this allows for the use of ideal metal anodes in RMBs. Considering the low reduction potential of 2.7 V and the high capacity of the metal anode, this may allow for RMBs with competitive energy densities. As illustrated in Figure 2.6, the reduction potential of Mg metal anodes is close to the currently used graphite anodes in LiBs, while the gravimetric and volumetric capacities are around 8 times higher. Due to the small size of the Mg-ions, the volumetric capacity of Mg metal is even twice that of Li metal. Compared to other multivalent chemistries, Mg has an advantageous combination of reduction potential and capacity to facilitate high energy density batteries.

Another advantage is the natural abundance of Mg, which could enable the production of cheaper batteries than current LiBs. In numbers, the crustal abundance of Mg is around 1000 times higher compared to Li,¹⁷ and the seawater concentration of Mg lies at 1270 ppm (vs. 0.1 ppm for Li).⁹⁰ The high concentration makes Mg practically extractable from seawater, enabling global availability of the material, which again facilitates local security of supply. However, due to the strong dominance of China, that stand for 84 % of the total Mg production worldwide, Mg is currently considered a critical raw material within the EU and the US.^{91,92} Nonetheless, after a drastic cost increase since the start of 2021, lithium carbonate now costs around 70,000 \$/ton compared to around 3600 \$/ton for 99.9 % pure magnesium ingots.^{93,94} Even before the cost increase, the price of LiCO₃ precursor material was several times higher than for pure Mg metal, demonstrating how the Mg chemistry shows a great potential for cost reduction compared to current LiBs.

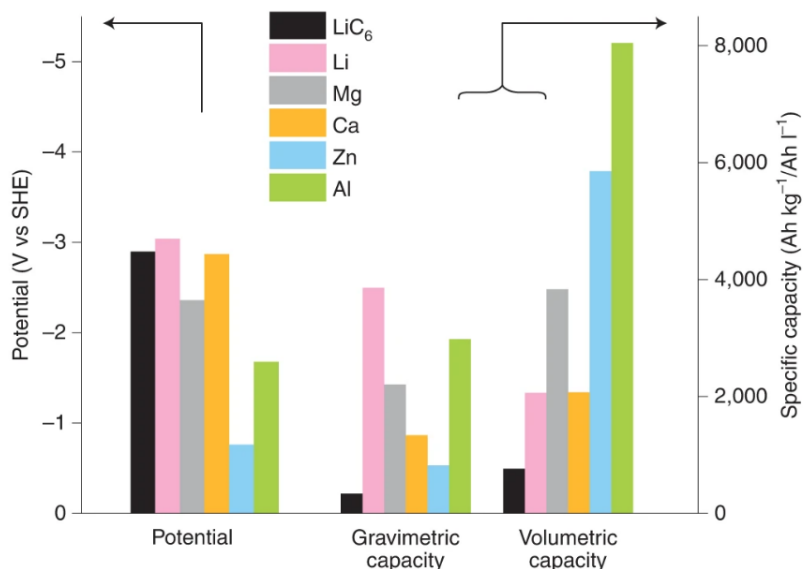


Figure 2.6: Comparison of the standard reduction potential and gravimetric and volumetric capacities of various anode materials. Adapted from Ref¹⁸ with permission from Nature Energy.

Current challenges

Although RMBs have the potential for high energy density batteries based on cheap materials, there are still several challenges that need to be faced before the technology can compete with current LiBs.¹⁸ The two most important challenges are listed here:

1. Mg impermeable SEIs → electrolyte must be stable towards Mg metal
2. Sluggish kinetics due to high charge density of divalent Mg-ions

Unlike for LiBs, the SEI film that is formed upon electrolyte decomposition of polar non-protonic solvents (carbonates, nitriles, esters etc.) does not allow the divalent Mg-ions to permeate through.⁹⁵ Hence, RMBs require different electrolytes that are stable against both the Mg metal anode and a cathode material, which greatly limits the number of suitable candidates.⁹⁶ In 1990, Gregory et al. pioneered the work on practical RMBs with their study on RMB electrolytes based on organomagnesium compounds in ethers and tertiary amines.⁸⁷ These electrolytes demonstrated reversible Mg plating and stripping, but the study also suggested that the plating compatibility of these electrolytes comes at the expense of poor Mg-ion dissolution at the cathode. Still, in 2000 Aurbach et al. were able to demonstrate a practical RMB using an intercalation based Mg_xMo₆S₈ chevrel phase cathode (0 < x < 2) and an electrolyte consisting of a Mg organohaloalu-

minate salt ($\text{Mg}(\text{AlCl}_2\text{BuEt})_2$) in tetrahydrofuran (THF) solvent, which demonstrated reversible capacities of above 50 mAh/g at a voltage of ~ 1.1 V for more than 500 cycles.⁹⁷ Several organomagnesium compounds, such as the all-phenyl complex (APC)⁹⁸ and the magnesium aluminium chloride complex (MACC)⁹⁹, have shown > 99 % reversibility when combined with solvents such as THF, acetonitrile (AN) and 1,2-dimethoxymethane (DME).⁹⁵ However, as the chloride salts results in poor electrochemical stability, due to corrosion, and high energy barriers for Mg^{2+} dissolution, other salts have also been investigated. One example is the halogen-free $\text{Mg}(\text{BH}_4)_2$ salt reported by Mohtadi et al., which shows an oxidative stability of around 2 V together with significantly lower Mg dissociation energies in a DME electrolyte.¹⁰⁰ Another example is the borate magnesium oxide complex (BMOC), which in DME has demonstrated an anodic stability of up to 4.2 V vs. Mg/Mg^{2+} and an electroactive species of solvated $[\text{Mg}(\text{DME})_n]^{2+}$.¹⁰¹ Still, the reversibility of these electrolytes remains relatively low, resulting in the need for further improvements of the electrochemical performance of RMB electrolytes.^{90,95} Moreover, the thermal stability and cost of these electrolytes will need to be addressed for use in commercial cells.

Although the divalency of the Mg-ions is often referred to as advantageous, due to the possibility of transferring twice the charge per ion, this is not without problems. With Mg-ions being of similar size to Li-ions (86 pm vs. 90 pm), their divalent nature results in more than a doubling of the charge density (120 vs. 54 C/mm³).¹⁰² This leads to sluggish kinetics and very slow migration of Mg-ions in insertion based cathode materials.¹⁰³ Hence, most of the commonly used LiB cathode materials remain inapplicable for RMBs, and the number of feasible intercalation based cathode materials are reduced. The slow solid-state diffusion of Mg-ions also makes it difficult to find suitable solid-state electrolytes for RMBs.⁹⁵ One way to reduce high migration barriers for Mg-ions has been the utilisation of open structures with the more polarisable sulfides and selenides compared to oxides.¹⁰⁴ However, this comes at the expense of a reduced cell potential, leading to a limited energy density with such cathode materials.^{104,105} As the intercalation of divalent cations may also require a double change in oxidation state of the host material, the number of relevant cathode materials are further reduced. As illustrated in Figure 2.7, one electron transfer is required for the intercalation in most oxide materials, where conversion reactions dominate for two electron transfer.¹⁰⁴ Although high voltages may be obtained, a one electron transfer greatly limits the achievable capacities through intercalation. For conversion reactions with Mg-ions, this often leads to kinetic hindrance from phase transformations, and for some materials even the formation of Mg-impermeable surfaces preventing continued cycling.¹⁰³

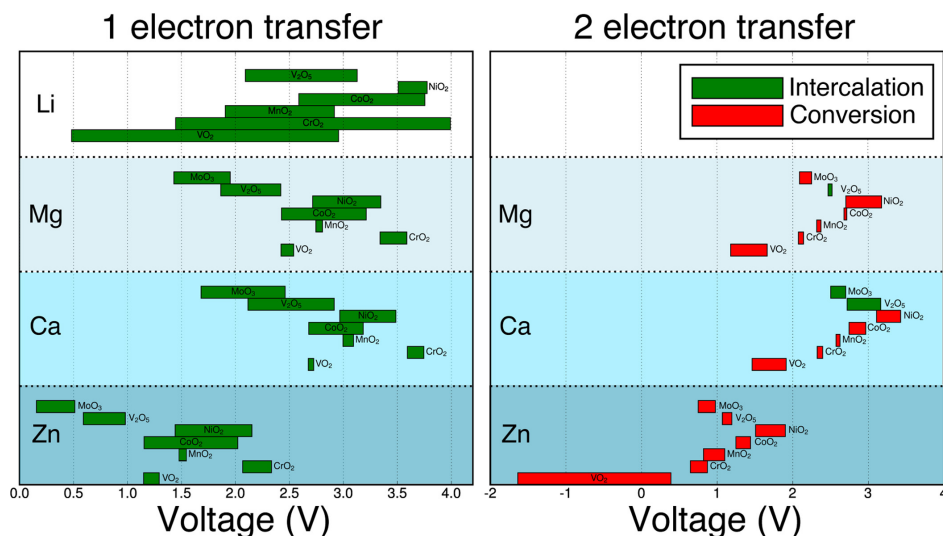


Figure 2.7: Competition between ion intercalation and conversion reactions for Li, Mg, Ca and Zn in various oxides, showing how two electron transfer intercalation is challenging. From the top: Mo_3 , V_2O_5 , NiO_2 , CoO_2 , MnO_2 , CrO_2 , VO_2 for each segment. Reproduced from Ref¹⁰⁴. Copyright ©2017 American Chemical Society.

Additionally, the high charge density of Mg-ions causes strong interactions both with electrolyte and electrode materials, leading to significant overpotentials required for successful desolvation and solid state diffusion.^{18,96} As an example, the cleavage of the Mg-Cl bond in THF solvents has been estimated to be > 3 eV.¹⁰⁶ This in turn limits the achievable current densities and leads to high voltage hysteresis and poor energy efficiencies of RMBs compared to modern LiBs. Utilisation of Mg alloy anodes (e.g. Mg_2Sn and Mg_3Bi_2) have shown to expand the number of applicable electrolytes for RMBs,¹⁰⁷ but they also come at the expense of reduced energy densities and the need for less abundant elements.⁹⁶ Although improvements of RMB electrolytes will be required for increased energy efficiency and cyclability of RMBs, the main limitation to RMBs energy density currently relates to finding suitable cathode materials that allow for stable Mg reactions at high voltages combined with high capacities.^{18,103,104} Hence, a short review of the state-of-the-art RMB cathode materials will be presented, sectioned by the reaction method: intercalation or conversion.

Intercalation-based cathode materials

In LiBs, intercalation compounds are utilised due to their topotactic intercalation reactions which maintains their structure upon cycling and thereby allows for fast Li-ion dif-

fusion and good cycling stability.⁶⁴ However, as already mentioned, the kinetics of Mg diffusion is significantly hampered by the strong interactions between the divalent Mg-ions and the host structure. Since the report of Aurbach et al. in 2000,⁹⁷ the $\text{Mg}_x\text{Mo}_6\text{S}_8$ chevrel phase ($0 < x < 2$) has remained as one of the best performing cathode materials due to its good reversibility and intercalation kinetics.^{103,104} Due to its 3D open structure, the polarisable S anions and the delocalised charges inside the S, and MO_6 clusters, the Mg-ion migration barrier has been estimated to 360 meV, which is among the lowest reported for all RMB cathodes.^{108,109} Additionally, it has been found that the presence of Mo atoms catalyses the desolvation of Mg^{2+} ions from the MgCl complex in the electrolyte, which further lowers the overpotential required for desolvation.¹⁰⁶ Still, although it is often reported that Mo_6S_8 cathodes can deliver thousands of charge-discharge cycles,^{95,104,110,111} only a maximum of 580 cycles has been demonstrated experimentally.⁹⁷ As illustrated in Figure 2.8, the phase holds two distinct sites at which Mg-ions can be located, which again results in two voltage plateaus upon cycling. Due to structural changes at low degree of magnesiation ($x < 1$), achieving the theoretical capacity of 122 mAh/g at room temperature has remained challenging.¹⁰⁴ Although extensive research has been directed towards overcoming this challenge, the operating voltage of ~ 1.1 V still limits the theoretical energy density to ~ 130 Wh/kg. Since this is significantly lower than most LiB chemistries and state-of-the-art SiBs (> 160 Wh/kg), it gives an explanation to why $\text{Mg}_x\text{Mo}_6\text{S}_8$ -based RMBs remain non commercialised.^{9,112}

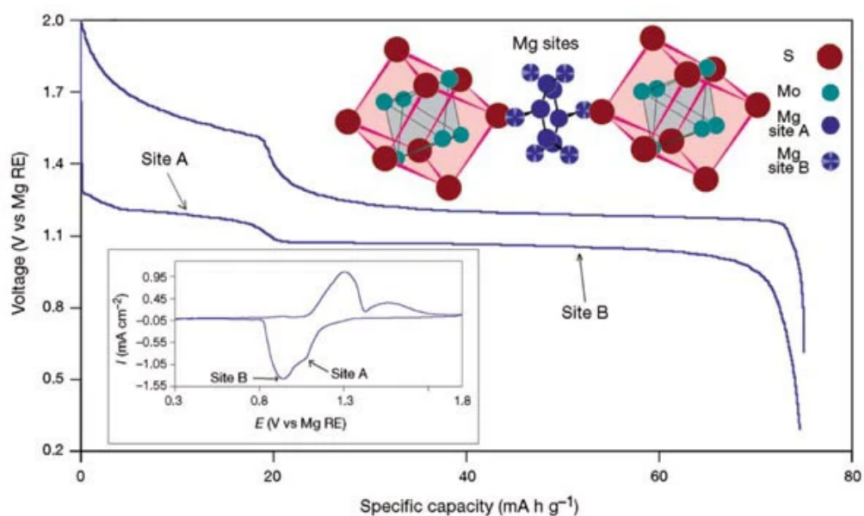


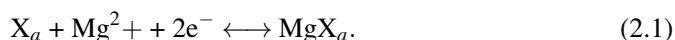
Figure 2.8: Illustration of possible Mg sites in the $\text{Mg}_x\text{Mo}_6\text{S}_8$ chevrel structure, $0 < x < 2$, in addition to common voltage profiles and cyclic voltammogram (CV) in the inset. Reproduced from Ref⁹⁷ with permission from Springer Nature.

Although high voltage oxide cathodes would be preferential for an optimal energy density, practical RMBs utilising such electrodes have yet to be demonstrated.^{104,105} This is mainly due to the higher migration barriers for Mg-diffusion,^{95,113} which entails the need for low current densities and high temperatures in order to achieve notable capacities.¹⁸ Additionally, irreversible phase transformations upon reacting with Mg have limited the reversibility of some oxide materials.^{114,115} Co-intercalation of electrolyte components, such as singly charged MgCl^+ or hydrated Mg^{2+} ions, have demonstrated improved kinetics in some oxides (e.g. layered V_2O_5 and MnO_2).^{103,116} However, as this either would necessitate larger amounts of electrolyte or going away from the Mg metal anode, co-intercalation is not relevant for practical batteries, as it would greatly limit the achievable energy density of RMBs.

The best performing intercalation-based cathodes so far therefore consist of the softer chalcogenides (e.g. S, Se and Te), as they allow for faster kinetics.¹⁰³ In addition to the Mo_6S_8 chevrel phase, 1D (VS_4 ^{117,118}), layered (TiS_2 ¹¹⁹, TiSe_2 ¹²⁰ and MoS_2 ¹²¹) and spinel (Ti_2S_4 ¹²²) structures have demonstrated reversible cycling in RMBs. Although the reported reversibility (< 100 cycles) and energy efficiency are often low, and the voltage usually is below 1.5 V, several of these materials have demonstrated significantly higher capacities than the Mo_6S_8 phase. Most notable are the VS_4 and MoS_2 phases demonstrating reversible capacities above 300 mAh/g and 160 mAh/g, at operating voltages around 1.1 V and 1.9 V, respectively.^{117,118,121} The VS_4 has even demonstrated > 100 mAh/g at a current density of 500 mA/g, demonstrating that its structure can overcome the challenges of sluggish Mg-ion kinetics. If the reversibility and energy efficiency of Mg cells using these electrodes can be further improved, they may even be able to result in a competitive RMB chemistry.

Conversion-based cathode materials

In order to avoid the challenges related to solid-state migration, significant interest has been directed towards conversion-based cathodes for RMBs.¹⁰² For the two electron transfer of Mg, conversion reactions are often thermodynamically favourable,^{102,104} which is previously demonstrated by the oxides in Figure 2.7. The most relevant type of conversion reaction usually includes a combination reaction of chalcogens (e.g. S¹²³, Se¹²⁴ and Te¹²⁵) or halogens (e.g. I₂¹²⁶), which here is denoted as "X". The general reaction can then be described as follows:¹⁰²



The most studied conversion material is sulfur, which, due to its high theoretical capacity (1675 mAh/g and 3459 mAh/cm³), safety and natural abundance, leaves it as a very promising candidate for high-energy battery applications.^{17,102,123,128} Combined with a metal anode, the Mg-S battery offers a theoretical voltage of 1.7 V, which leads to theoretical energy densities that outperforms state-of-the-art LiBs (1700 Wh/kg vs. ~700 Wh/kg, based on electrode materials).⁹ Nevertheless, there are still several obstacles that must be overcome for this battery chemistry to work satisfactory. One of the challenges with Mg-S batteries is the poor electronic conductivity of S ($\sim 5 \cdot 10^{-30}$ S/cm) and the practically insulating S and MgS phases towards ionic conduction of Mg-ions.^{129,130} Therefore, the S cathode requires a conductive network (usually carbon-based) to ensure good electronic contact and thereby utilisation of all the cathode material.¹²³ This results in additional "dead weight" that limits the practical capacity that can be achieved. Furthermore, a major challenge for Mg-S batteries relates to the shuttling of polysulfide intermediates and of the elemental sulfur cathode itself,¹³¹ causing a poor cycle life in current Mg-S batteries cells.¹²³ As illustrated in Figure 2.9, the transition from elemental S to fully magnesiated MgS occurs stepwise through a set of polysulfide chains that are soluble in common RMB solvents.¹²³ In order to prevent significant loss of active material, ways to prevent the polysulfide shuttling are necessary. An example is the use of S containing compounds, which has been able to mitigate the capacity loss upon cycling.¹³² In general, the development of improved RMB electrolytes that are compatible with both the Mg metal anode and the S cathode, will play an essential role.

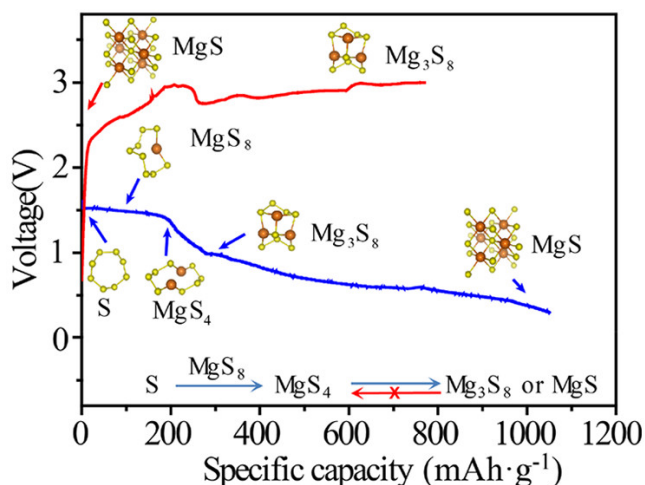


Figure 2.9: Schematic of common voltage profile for Mg-S battery, indicating the Mg_XS stages between elemental S and formation of MgS. Reproduced from Ref¹²⁷. Copyright ©2019 American Chemical Society.

Organic cathodes have also demonstrated interesting properties for RMBs.^{133–136} With flexible structures and rotational bonds, these compounds can facilitate for charge distribution and improved Mg migration pathways. While several of the organic compounds struggle with similar dissolution problems as the Mg-S batteries, Pan et al. reported on various polyanthraquinone-based (PAQ) cathodes with reduced solubility, enabling stable 1000 cycles with a capacity retention > 80 %.¹³⁵ When cycled with a current density of 130 mA/g, a capacity of ~ 110 mAh/g, at an average voltage of ~ 1.4 V, was demonstrated for the 1,4-polyanthraquinone (14PAQ) cathode. This is among the best performances of RMB cathodes so far, and even outperforms the Mo_6S_8 phase. Based on the higher theoretical voltages and capacities of other organic compounds,¹³³ the development of organic cathode materials will definitively be of interest for the future of RMBs.

Comparison

Dominko et al. have compared the theoretical energy densities that can be achieved for RMB cells with some of the most promising cathode materials to date, as illustrated in Figure 2.10.¹⁰⁵ In addition, they also included a hypothetical 3 V oxide cathode deliver-

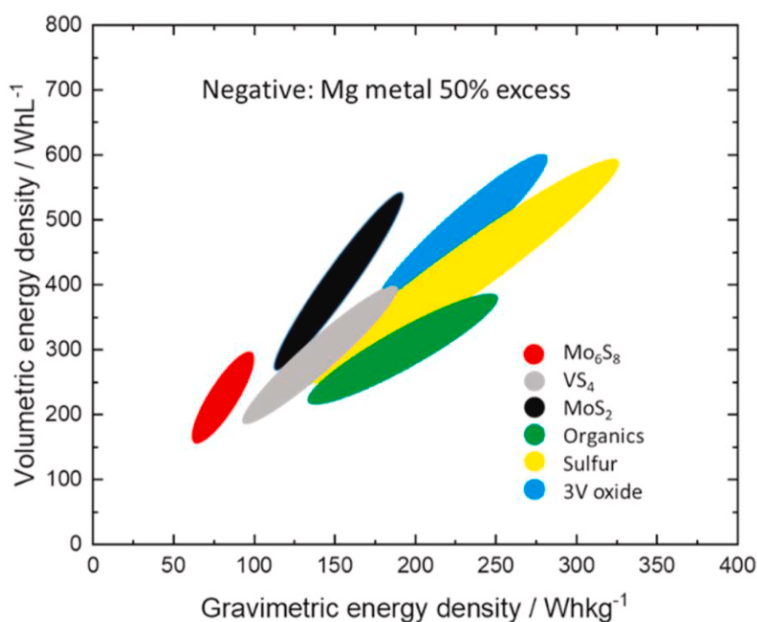


Figure 2.10: Prediction of potential energy densities that can be achieved at cell level by combining a Mg metal anode in 50 % excess with various cathode materials. Adapted from Ref¹⁰⁵ with permission from Elsevier.

ing a capacity of 150 mAh/g. The values are calculated based on a classical LiB pouch cell stack, where they have included the mass and volume of all cell components except the cell casing. They also utilised a 50 % excess of the Mg metal anode, as a security margin. The figure demonstrates how significant improvements in gravimetric and volumetric energy densities can be achieved for RMBs. This remaining potential justifies the interest in continued research on the RMB technology as it unequivocally has the potential to compete with the energy densities of current LiBs. Nonetheless, significant improvements on the reversibility of these cathode chemistries will be required before practical RMBs can be realised. Together with improved cathodes, the RMB technology also greatly relies on the development of suitable electrolytes that allow for reversible stripping/plating of Mg without any side-reactions, combined with low (de)solvation energies to minimise the energy loss upon cycling.

2.2 MXenes

2.2.1 Introduction

What are MXenes?

MXenes are a family of two-dimensional (2D) transition metal carbides and nitrides that are formed by the selective exfoliation of their layered precursor.¹³⁷ Their name originates from the parent MAX phase, which consists of transition metals (M) and carbon/nitrogen (X) in a layered structure, separated by layers of A-elements (e.g. Al, Si, Ga). Due to the weaker bond strength of A-M bonds compared to M-X bonds, selective removal of the A-layer can be achieved, leaving only the "MX" layers, as illustrated in Figure 2.11.¹³⁸ To emphasise the 2D nature resembling graphene, the family was therefore denoted as "MXenes" (pronounced "max-eens").^{139,140} Based on the chemical variability of MAX phases, as well as the successful synthesis from other precursor materials, more than 30 different MXene compositions have been experimentally verified so far,¹⁴¹ and many more are theoretically predicted.¹⁴² A summary of MXene structures and stoichiometries that have been experimentally verified is given in Figure 2.12.

Similar to the MAX phases, MXenes comprise a hexagonal close-packed (hcp) crystal structure with a $P6_3/mmc$ space group symmetry.²¹ As illustrated in Figure 2.12a, the M atoms are close-packed with the X atoms located in octahedral sites in between the atomic M planes. The MX-layer generally shows a stoichiometry of $M_{n+1}X_n$, where n can vary from 1 to 4, leading to MXene sheets of varying thickness (Figure 2.12b). Additionally, some ternary MXenes (denoted " $(M,M')_{n+1}X_n$ ") and transition metal deficient MXenes (" $M_{4/3}X_n$ ") have been successfully synthesised using precursors with mixed transition

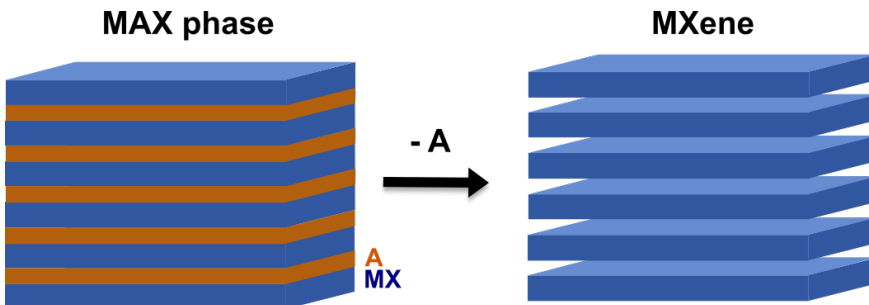


Figure 2.11: Schematic of the general synthesis of MXene from a parent MAX phase, highlighting the 2D nature of MXenes.

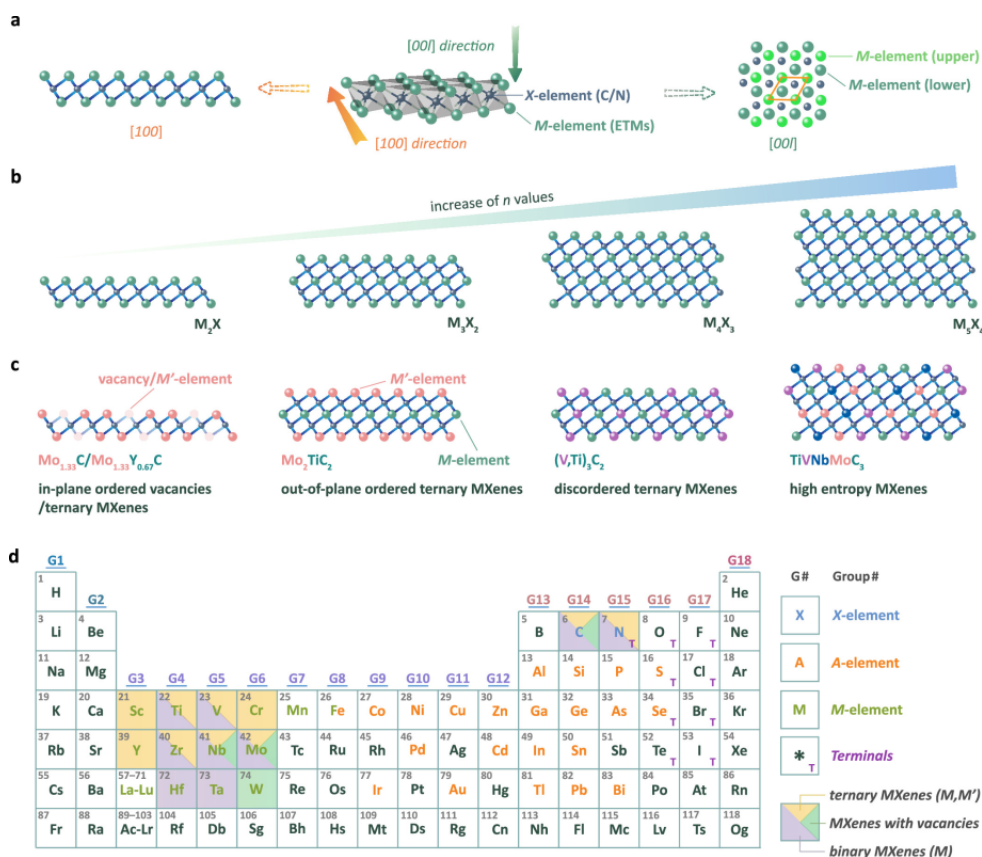


Figure 2.12: Diversity of MXene structures and compositions. (a) Projection representation of M_2X MXene from various crystallographic directions. (b) MXene thicknesses ($M_{n+1}X_n$) experimentally verified. (c) Mixed MXene structures including transition metal mixtures and vacancies. (d) Periodic table demonstrating the experimentally confirmed MXene compositions, including A-elements for MAX phases and termination groups (T) on the MXene surfaces. The termination groups are not included in the structural representation in (a-c). Reproduced with permission from Ref¹⁴³. Copyright ©2021 American Chemical Society.

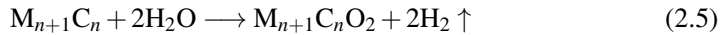
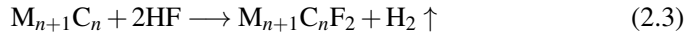
metals (Figure 2.12c).^{141,143} Combined with the formation of surface termination groups upon exfoliation, denoted "T" (usually O, OH, F, Cl), with a varying coverage "x", the possible compositional variations of $M_{n+1}X_nT_x$ MXene becomes substantial.¹⁴⁴ This is one of several reasons why the research field of MXenes has grown exponentially since its discovery in 2011.^{19,145}

Synthesis and delamination

To synthesise MXenes, the M-A bond has to be broken without damaging the M-X bond. Whereas mechanical exfoliation (e.g. scotch tape and ball milling) has been used to produce several other 2D materials, such as graphene,^{146,147} mechanical force has not been able to break the M-A bonds in MXenes.¹⁴⁸ Instead, MXenes are generally produced by a wet chemical etching method which selectively removes the layer of A-elements from the precursor material (Figure 2.11), where the most common A-element is Al.¹³⁸ So far, the most reported etching solutions are based on either aqueous HF solutions or acidic solutions of F-salts causing the formation of HF in-situ.^{149,150} Exfoliation has also been achieved by other etching methods, including electrochemical etching in basic¹⁵¹ and acidic¹⁵² solutions, anhydrous halogen solutions,¹⁵³ hydrothermal reaction in highly concentrated HCl and NaOH,^{45,154} and molten salt reactions in Lewis acids^{155,156}. However, the degree of experimental simplicity and MXene quality differs significantly between the different methods. While this section will focus on the HF-related etching methods, the latter two etching methods will be discussed further in Section 2.2.4. The general reaction describing the exfoliation from HF containing solutions is given by:¹³⁹



Furthermore, this etching method results in a mixture of surface terminations (O, OH and F), which are formed by the following reactions:



Even though the Al layer is removed upon etching MAX phases in HF acids, the particles generally remain in multilayered stacks, held together by weak van der Waals forces.¹⁴⁹ However, due to the volume expansion upon gas formation, some MXenes partly delaminate into accordion-like morphologies, as illustrated in Figure 2.13a. Figure 2.13a also demonstrates how the delamination of single-layered MXene sheets can be obtained by intercalation followed by shaking or similar force-inducing methods (e.g. sonication). Due to the negative surface potential of the MXene sheets,¹⁴¹ both small metal cations (e.g. Li⁺) and large organic cations (e.g. tetrabutylammonium/TBA⁺) have been

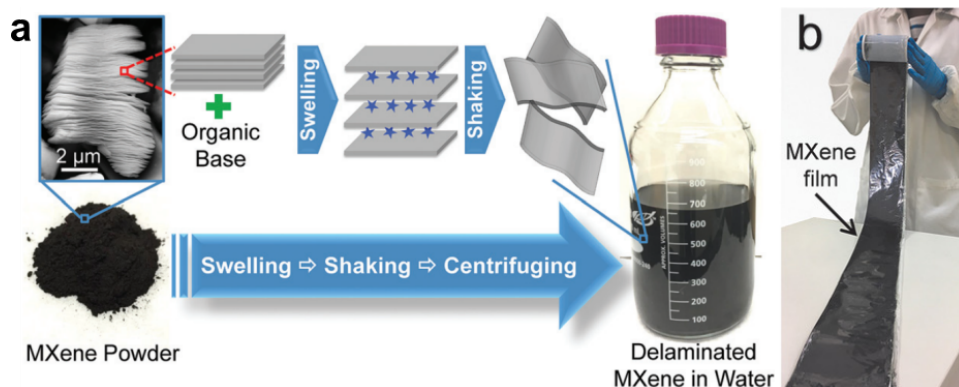


Figure 2.13: (a) Delamination process of MXenes, going from multilayered MXene powder to an aqueous dispersion of delaminated MXene flakes. Reproduced from Ref¹⁵⁹ with permission from the Royal Society of Chemistry. (b) Large-scale film of delaminated $\text{Ti}_3\text{C}_2\text{T}_x$ MXene. Adapted from Ref¹⁶⁶ with permission from John Wiley and Sons.

demonstrated to spontaneously intercalate the MXene sheets upon dispersion in aqueous solutions.¹⁴³ In addition, MXenes have been found to intercalate various amounts of water molecules,¹⁵⁷ which for some compositions has resulted in claylike rheological behaviour.¹⁵⁸ In total this intercalation causes a swelling of the MXene structure and a weakening of the van der Waals forces, which for some compositions is sufficient to result in delamination.³⁰ Due to the hydrophilic nature of the MXenes, colloidal solutions of delaminated MXene flakes remain stable in both aqueous and organic solvents, which greatly simplifies the processing possibilities.^{145,159,160} Upon vacuum filtration of these solutions, free-standing MXene films can be formed, and by various coating, casting and printing methods, films with controlled thicknesses can be produced.¹⁴¹

Although 2D materials are often described as "wonder materials", their commercial utilisation is usually restrained by the limited scalability of current synthesis methods.^{161,162} As the synthesis of MXene is based on a top-down approach through scalable methods, it potentially enables large-scale production.¹⁶³ Currently, large-scale synthesis of both the Ti_3AlC_2 MAX phase¹⁶⁴ and the $\text{Ti}_3\text{C}_2\text{T}_x$ MXene¹⁶⁵ have been demonstrated without affecting the properties of the products. Furthermore, large-scale MXene films have been demonstrated by blade coating, as shown in Figure 2.13b.¹⁶⁶ In total, this demonstrates the scalability potential of MXene synthesis, which again makes it a very promising 2D material for utilisation in commercial applications.

2.2.2 Properties and applications

General

In addition to the scalability potential of MXene synthesis, there are several properties that make this material family interesting for a range of different applications. In 2019, Anasori et al. summarised the research on MXenes in a pie chart based on number of publications for different applications (Figure 2.14).¹⁴⁵ The pie chart also indicates the approximate initiation of each MXene-application, demonstrating a continuous development of new application areas during the first 8 years of research on MXenes. Although

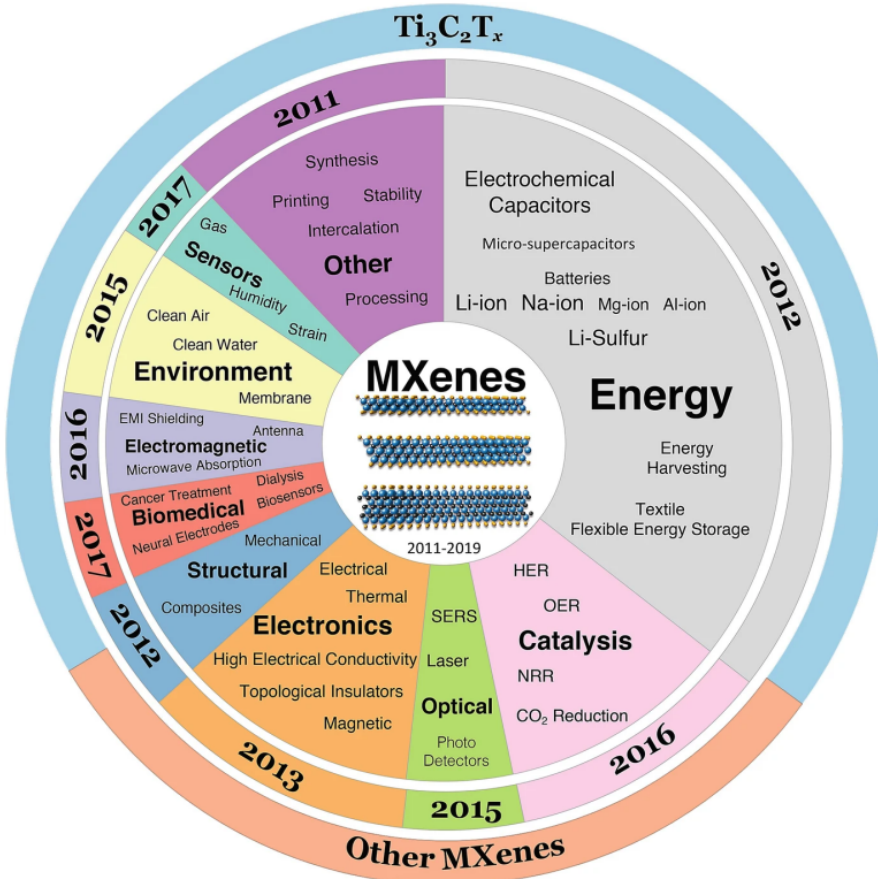


Figure 2.14: Explored properties and applications of MXenes until 2019. The centre pie chart indicates the ratio of total publications per topic, where the year roughly represents the time of initiation. The outer pie chart shows the ratio of publications on the Ti₃C₂T_x MXene versus all other compositions. Reprinted from Ref¹⁴⁵ with permission from Springer Nature ©(2019).

the pie chart may look different in 2022, after a doubling of MXene publications since then (from Web of science), the figure still gives a good indication on the many possibilities that MXenes have enabled.

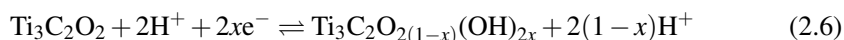
One of the reasons for the expanding research on MXene relates to the tunability of the MXenes, as most of their electrical, optical, thermal, (electro)chemical and mechanical properties greatly depend on the structure and composition of the MXene.^{141,167} For instance, whereas some MXene compositions (e.g. $\text{Ti}_3\text{C}_2\text{T}_x$) are found to be metallic, others (e.g. Mo_2CT_x and V_2CT_x) display a semiconductor-like behaviour.^{168,169} As the electronic properties also change with the presence of intercalants and the surface terminations of the MXenes,^{170,171} this demonstrates the great span of tunable factors. Generally, most MXenes demonstrate high electronic conductivities,¹⁷² where 20 000 S/cm for $\text{Ti}_3\text{C}_2\text{T}_x$ films is among the highest conductivities measured for solution-processed nanomaterials to date.¹⁷³ This has also proven MXenes as the best material for electromagnetic interference shielding and antenna applications.¹⁷⁴ Additionally, although the study of MXenes' mechanical properties is limited, single-layer $\text{Ti}_3\text{C}_2\text{T}_x$ has demonstrated a Young's modulus of 330 ± 30 GPa, making it one of the strongest 2D materials known to date.^{145,175}

While the potential of chemical tunability is enormous, most of the research on MXenes is based on the $\text{Ti}_3\text{C}_2\text{T}_x$ composition, as demonstrated by the outermost pie chart in Figure 2.14. As the Nb_2CT_x phase has even demonstrated superconductivity,¹⁵⁵ and with the prediction of even higher conductivities for nitride-based MXenes,¹⁷⁶ we are likely far away from discovering all the possibilities that MXenes might offer.

2.2.3 MXenes for energy storage

Figure 2.14 demonstrates how energy storage has been the most studied application area for MXenes. The high electronic conductivity and the 2D nature of MXenes has made them interesting candidates for electrochemical capacitor electrodes due their high surface area, as well as for intercalation-based electrodes in supercapacitors and rechargeable batteries.¹⁷⁷⁻¹⁷⁹ In aqueous solutions MXenes show primarily a double-layer capacitive behaviour.¹⁷⁸ However, with the intercalation of protons in acidic solutions it becomes pseudocapacitive,¹⁸⁰ leading to ultrahigh capacitance values of 400 F/g and 1500 F/cm³ at 10 ms charge/discharge cycles for $\text{Ti}_3\text{C}_2\text{T}_x$ MXene.¹⁸¹ This has made it one of the best supercapacitor materials to date, surpassing the currently used porous carbon electrodes exhibiting values at 150-200 F/g and 50-100 F/cm³.¹⁷⁸ However, with the limited electrochemical stability window of aqueous electrolytes, which may be fur-

ther compromised by the catalytic effect of MXenes for water splitting,^{182,183} the energy density that can be obtained from these supercapacitors is still limited.¹⁷⁸ Even though the voltage window has been improved with non-aqueous electrolytes, the energy density remained low.¹⁷⁸ This is assumed to originate from the lack of protons, which is found to be the main contributor to the pseudocapacitive charge transfer through faradaic reactions with the oxygen surface terminations:¹⁸⁰



where x is the surface H coverage on the MXene. In aqueous solutions, high capacitances ($\sim 70 \text{ F/cm}^3$) have also been achieved in non-acidic solutions of Na^+ , K^+ , Mg^{2+} and Al^{3+} ions, demonstrating the possibility to reversibly intercalate several cations of various charged states.¹⁸⁴

For high-energy applications, MXenes have also been extensively investigated as battery electrodes in non-aqueous electrolytes, where Naguib et al. first reported on the use of Ti_2CT_x in LiBs back in 2012.²² Since then, MXenes have been reported for a range of different battery chemistries based on the intercalation of Li^+ ,²³ Na^+ ,^{185?} K^+ ,^{25,186} Mg^{2+} ,³⁷⁻³⁹ Zn^{2+} ¹⁸⁷⁻¹⁸⁹ and Al^{3+} .²⁶ Similar to faradaic charge transfer in protic solutions, the intercalation of these cations has generally demonstrated a pseudocapacitive behaviour with sloped voltage profiles, as schematically illustrated in Figure 2.15.¹⁷⁹ This has led to generally low average voltages ($< 1.5 \text{ V}$), which usually has made them most applicable as anode materials in e.g. LiBs. Additionally, anion intercalation has also been investigated, but found unlikely due to the negatively charged surfaces of the MXene layers.¹⁹⁰ The performance of MXene electrodes for LiBs and RMBs will be discussed later in Section 2.2.3.

Due to the combination of high electronic conductivity and chemically active surface sites, MXenes have also been extensively applied in various electrode heterostructures.¹⁹² Due to the facile mixing of delaminated MXenes with other dispersions, various 3D architectures have been achieved using MXenes as a conductive and mechanically stable skeleton.¹⁹³ Most notable is probably the utilisation of MXenes in Li-S batteries, where the MXene is used to chemically adsorb polysulfides, and thereby improve the cycle life of Li-S batteries.¹⁹⁴ In recent years, a similar effect has also been demonstrated in Mg-S batteries.^{195,196} With respect to facilitating practical Li-S batteries, the high surface area of MXene films with lithiophilic nucleation sites have been reported to prevent the growth of Li-dendrites, which might enable practical use of the Li metal anode.^{197,198}

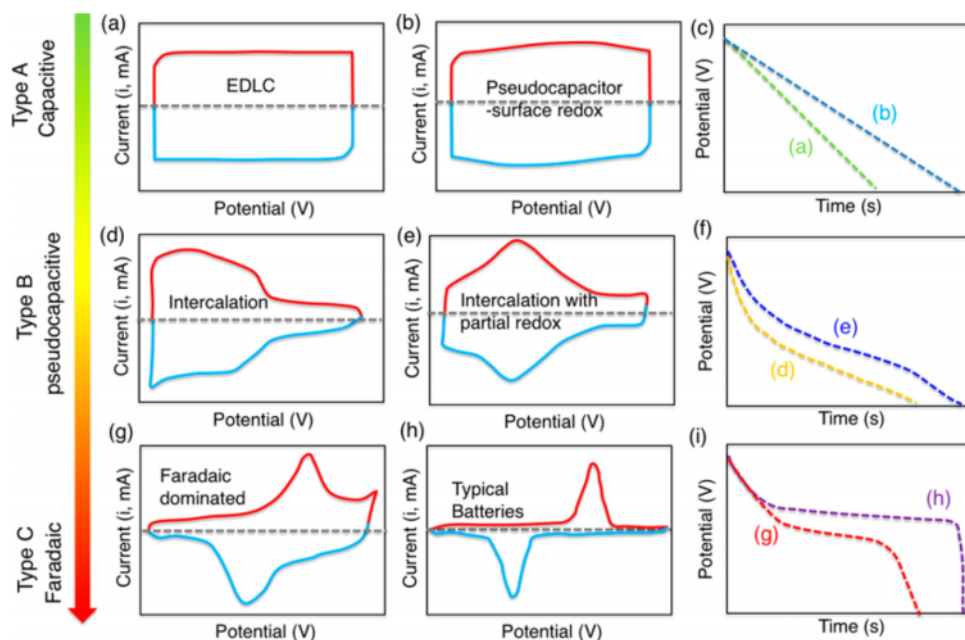


Figure 2.15: Schematic cyclic voltammograms (a, b, d, e, g, h) and galvanostatic discharge curves (c, f, i) of various kinds of energy-storage materials. (a, c) Show a purely capacitive contribution, whereas (b, d, e, f) represent various types of pseudocapacitive materials (incl. MXenes). (g, h, i) Display common faradaic behaviour which is usually observed in batteries. Reproduced with permission from Ref¹⁹¹. Copyright ©2018 American Chemical Society.

Multilayered particles vs. delaminated MXene films

Electrodes based on delaminated MXene films have displayed significantly higher gravimetric capacities compared to those based on multilayered particles, and even exceeds the theoretically predicted capacities calculated for one cation per formula unit.^{30,164} Nevertheless, these delaminated MXene electrodes face significant challenges with respect to achieving high areal capacities (mAh/cm^2), which currently leaves them uncompetitive as energy dense electrode materials. This is due to a high porosity of the delaminated films and/or a reduced accessibility of cation sites upon increasing the film thickness. Since the MXene layers commonly restack horizontally, as illustrated in Figure 2.16, this leads to a slow vertical ion transport in the MXene films, which causes a significant capacity loss upon increasing the film thickness beyond a few microns.¹⁴⁵ To overcome this problem, Xia et al. demonstrated a method to vertically align $\text{Ti}_3\text{C}_2\text{T}_x$ sheets and thereby allow for nearly thickness independent electrode performances in aqueous supercapacitors. By mechanical shearing of surfactant bonded MXene sheets mixed with carbon nanotubes, they were able to form $200\ \mu\text{m}$ thick films that could deliver an areal

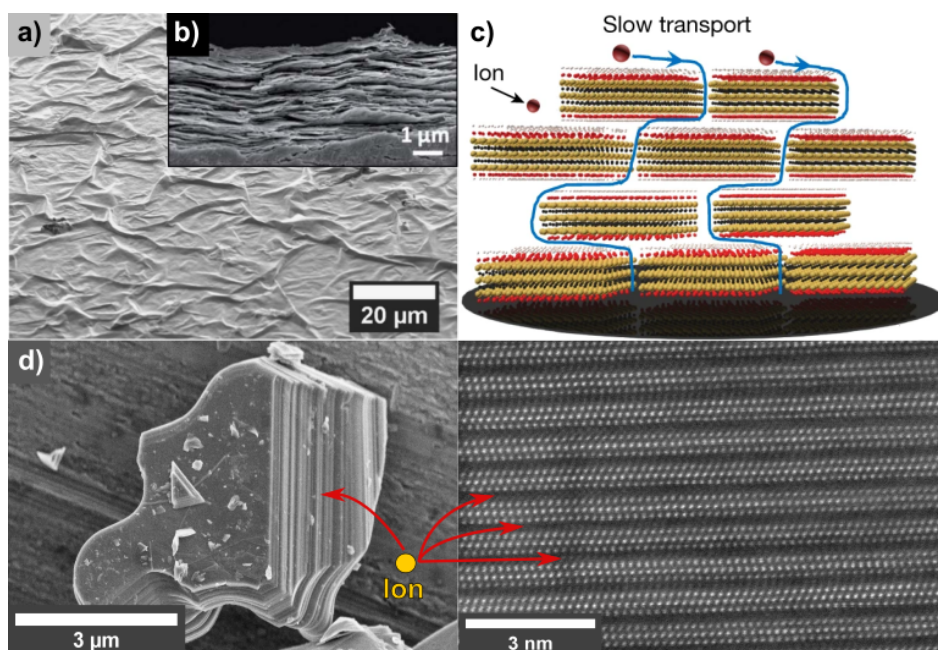


Figure 2.16: Comparison of multilayer particles and restacked films of delaminated $\text{Ti}_3\text{C}_2\text{T}_x$ MXene. (a) Shows a top view of a delaminated film. Reproduced from Ref¹⁹⁵ under the Creative Commons Licence [CC BY 4.0](https://creativecommons.org/licenses/by/4.0/). (b) Displays side-view of a delaminated film. Reproduced from Ref²⁰¹ with permission from the Royal Society of Chemistry. (c) Schematic of the ion transport in restacked MXene sheets. Adapted from Ref¹⁹⁹. Copyright ©2018 Springer Nature. (d) SEM and TEM image of a multilayered particle illustrating ion-intercalation. Adapted from Paper III, which is accepted at the Elsevier Journal FlatChem.

capacitance of 0.6 F/cm^2 while retaining a gravimetric capacitance of around 200 F/g (per mass of MXene).¹⁹⁹ However, due to the high porosity of these electrodes, the volumetric capacitance was only 30 F/cm^3 , which is less than half the capacitance of current carbon-based electrodes.¹⁷⁸ To fully optimise the energy density of MXene electrodes, intercalation into multilayered particles may therefore be necessary, as illustrated in Figure 2.16d. In addition to facilitating simple implementation in common electrode manufacturing procedures, multilayered particles would also limit the porosity of the electrodes and thereby allow for enhanced volumetric capacities. As an example, Prenger et al. recently demonstrated a 10-fold increase in areal capacitance (5.7 F/cm^2) of multilayered $\text{Ti}_3\text{C}_2\text{T}_x$ particles compared to the delaminated counterpart in their study of aqueous supercapacitors.²⁰⁰ This was achieved by cation pre-intercalation of the multilayered particles, which increased both the interlayer spacing between the MXene layers and the oxidation state of the Ti-atoms.

MXenes electrodes for Li and Mg batteries

Figure 2.17 illustrates the electrochemical performance of two MXene compositions for LiBs. First of all, it shows how Ti_2CT_x demonstrates a higher capacity than the $\text{Ti}_3\text{C}_2\text{T}_x$ phase with an extra set of MX elements per MXene sheet. Additionally, it demonstrates how the gravimetric capacities for delaminated MXene films are significantly higher than for the multilayered particles. To date, the highest capacity obtained for multilayered MXene particles have been demonstrated for attrition milled V_2CT_x , which showed a reversible capacity of ~ 280 mAh/g at 1C.²³ The pseudocapacitive-behaviour upon Li-insertion, as demonstrated by the semi-rectangular CV curves in Figure 2.17b, results in an average voltage of around 1 V. With such a high operating voltage, combined with a relatively low capacity, MXene particles are currently not competitive with modern graphite anodes with respect to energy density. However, one of the main advantages for MXene electrodes is their great rate performance, as illustrated in Figure 2.17a. As the multilayered Ti_2CT_x MXene is able to deliver around 50 % of the initial capacity at a high current density of 5 A/g (~ 20 C), this shows a significantly improved rate-performance compared to current graphite anodes.^{52,202} This feature may enable the use of MXene electrodes for high-power battery chemistries and has also made MXenes interesting electrode materials for Lithium-ion capacitors.²⁰³

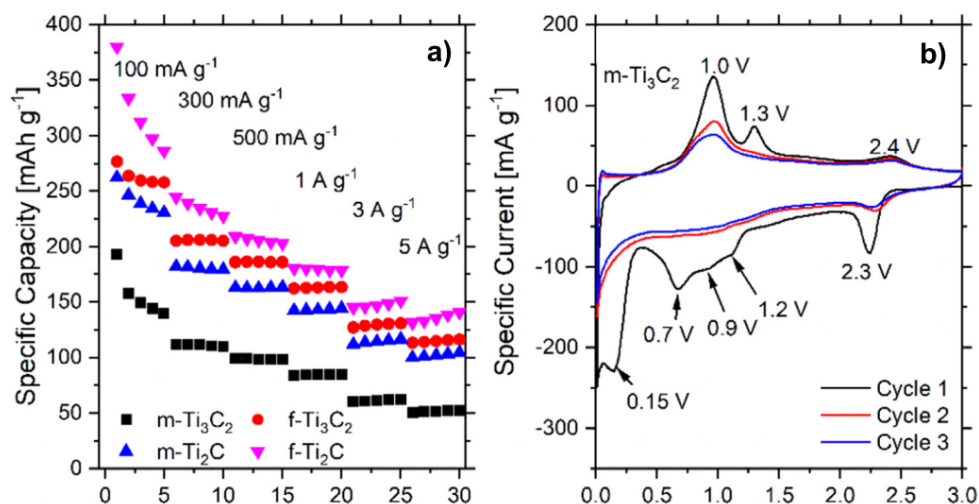


Figure 2.17: Electrochemical performance of two MXene compositions in LiBs, where (a) shows a comparison of the rate-capability of multilayered ("m-") and few-layered/delaminated ("f-") Ti_3C_2 and Ti_2C MXene, and (b) shows the three first CV cycles of multilayered Ti_3C_2 . Adapted from Ref¹⁶⁴. Copyright ©2021 American Chemical Society.

Furthermore, several DFT screenings have demonstrated a great potential for Mg-ion storage in MXenes, with theoretical capacities > 400 mAh/g and voltages ranging from -0.8 V to 1.2 V vs. Mg/Mg^{2+} .^{27,28} Due to the reasonably high average voltages and the desire to use a Mg metal anode, MXenes are most relevant as cathode material for RMBs. Despite the potential, there are only three articles to date that report experimental studies on MXenes as RMB electrodes.^{37–39} With the APC-THF electrolyte, they all demonstrated close to zero capacities with the pristine multilayered $\text{Ti}_3\text{C}_2\text{T}_x$ particles, as illustrated in Figure 2.18a. However, by various modifications of the MXene, they were able to demonstrate reversible capacities of > 50 mAh/g (Figure 2.18b and c). All three reports used the intercalation of large organic cations, such as cetyltrimethylammonium (CTA^+), which resulted in an interlayer spacing around 15 Å. This is approximately 50 % higher than what is commonly observed for non-intercalated $\text{Ti}_3\text{C}_2\text{T}_x$, demonstrating a signifi-

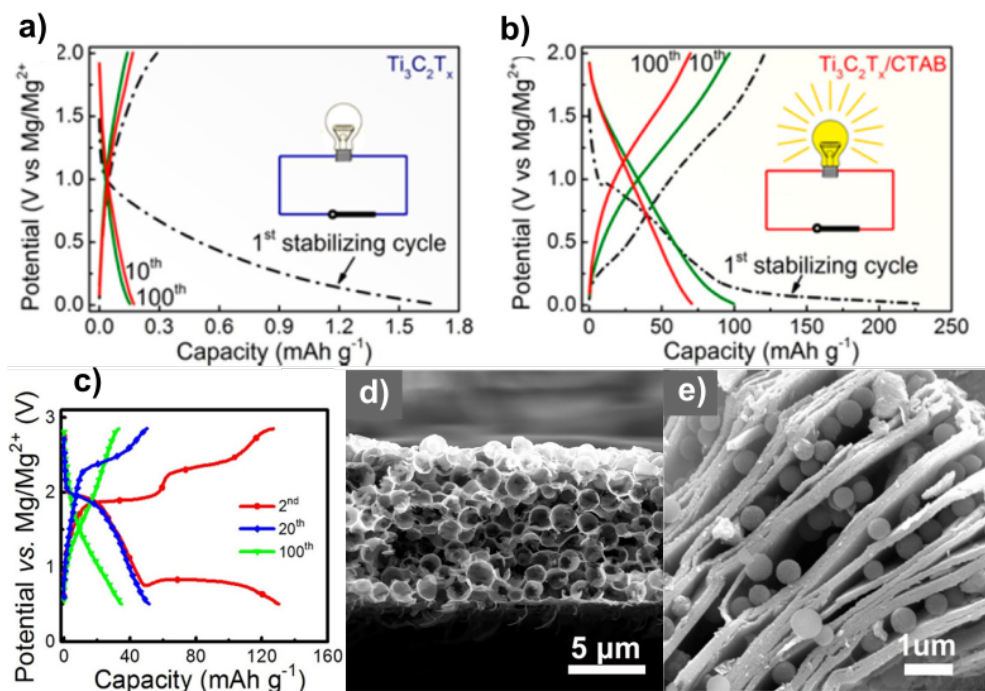


Figure 2.18: Overview of the MXene cathodes reported for RMBs. (a, b) Show voltage profiles for multilayered $\text{Ti}_3\text{C}_2\text{T}_x$ particles and delaminated $\text{Ti}_3\text{C}_2\text{T}_x$ films intercalated by cetyltrimethylammonium cations (CTA^+), respectively. Reproduced from Ref³⁸. Copyright ©2018 American Chemical Society. (c, d) Display voltage profile and cross section SEM image of macroporous electrodes. Adapted from Ref¹³¹. Copyright ©2019 American Chemical Society. (e) Shows a SEM image of the sandwich composite between $\text{Ti}_3\text{C}_2\text{T}_x$ and carbon nanospheres. Reproduced from Ref³⁹ with permission from the Royal Society of Chemistry.

cant expansion of the MXene structure.¹⁵⁰ One study reported on a sandwich-composite with carbon nanospheres (Figure 2.18e),³⁹ while the other investigations utilised delaminated MXenes with various degrees of porosity.^{37,38} Zhao et al. even demonstrated a ~90 % porosity of their electrodes after depositing the delaminated MXene around spherical polymer particles which were subsequently burned away at elevated temperatures (Figure 2.18d). Prior to cycling, these electrodes were also soaked in APC-THF electrolyte, leading to pre-intercalation of Mg and other electrolyte components. This resulted in significant charge/discharge plateaus (Figure 2.18c), in contrast to the sloped voltage curves observed in the other studies (Figure 2.18b). These plateaus were ascribed to the intercalation of entire salt molecules - RMgCl, where R = phenyl - based on EDS measurements of electrodes at different state of charge/discharge.

The best electrochemical performance of these electrodes was demonstrated by the sandwich composite of MXene and carbon nanospheres, as reported by Liu et al.³⁹ It was able to deliver a prolonged capacity of 150 mAh/g at a current density of 50 mA/g for 400 cycles, with an average voltage around 0.7 V. However, as these capacities were based only on the mass of the MXene material, and with low loadings around 2 mg/cm², the reproducibility of this work remains uncertain. Hence, verification would be required to fully establish the potential of this composite electrode. Apart from slightly lower specific capacities, the delaminated Ti₃C₂T_x electrodes reported by Xu et al. demonstrated comparable performance with similarly sloped voltage profiles (Figure 2.18b). However, the exact storage mechanism for both of these MXene electrodes is not clear and would need to be further elucidated. Although they report on lower migration barriers for Mg²⁺ ions in Ti₃C₂T_x pre-intercalated with cetyltrimethylammonium cations (CTA⁺),^{38,39} the large interlayer spacings could also facilitate the intercalation of singly charged MgCl⁺ ions or solvent molecules that shield the double charge of the Mg-ions. With high surface areas of 103.8 m²/g and 46.4 m²/g, the capacitive contribution is also shown to be > 50 % in both studies, indicating mostly surface reactions. The true nature of the changes in interlayer spacing observed upon charge/discharge of these electrodes, is therefore not trivial. As opposed to cations like Li⁺ and Na⁺,²⁰⁴⁻²⁰⁶ there has currently been no clear evidence for the intercalation of desolvated Mg²⁺ ions.

Additionally, there have also been some reports on combining a Mg metal anode with Li-insertion in MXene, which is usually denoted as Mg-Li hybrid batteries.^{36,207} However, as these hybrid batteries are based on Mg- and Li-ion storage in the electrolyte, their feasibility for practical batteries with lean electrolytes is very limited.

2.2.4 Termination control

Motivation

In order to optimise the intercalation properties of MXenes, it is essential to control the local environment in which the ions are moving. One option is by intercalation of specific cations to increase the interlayer spacing and change the possible migration pathways. This was illustrated by the reduced migration barriers for Mg-ions in CTA⁺ pre-intercalated Ti₃C₂T_x MXene, as discussed in the last part of Section 2.2.3. Another approach to adjust the local electrochemical environment is by controlling the termination groups that reside on the surface of the 2D MXene sheets, as these terminations are the contact point between the intercalating ion and the MXene. DFT calculations have shown that the termination groups greatly affect the intercalating voltage and the ion migration barriers, as well as the possible side reactions that can take place. Already in 2012, Tang et al. demonstrated high migration barriers and low capacities for Li-ions in F- and OH-terminated Ti₃C₂T_x and suggested the utilisation of unterminated Ti₃C₂ for optimised LiB properties.³³ Two years later, three more DFT screenings further demonstrated how F- and OH-terminations generally result in low or negative intercalation voltages and high migration barriers for a range of different cations, and that O- and unterminated MXenes would be preferable (Figure 2.19).^{27,28,32} As O-terminated MXenes were predicted to yield the highest intercalation voltages, they were also especially interesting for MXene cathodes in RMBs. Additionally, Xie et al. demonstrated the possibility for adsorption of several layers of Li- and Mg-ions on O-terminated MXenes,

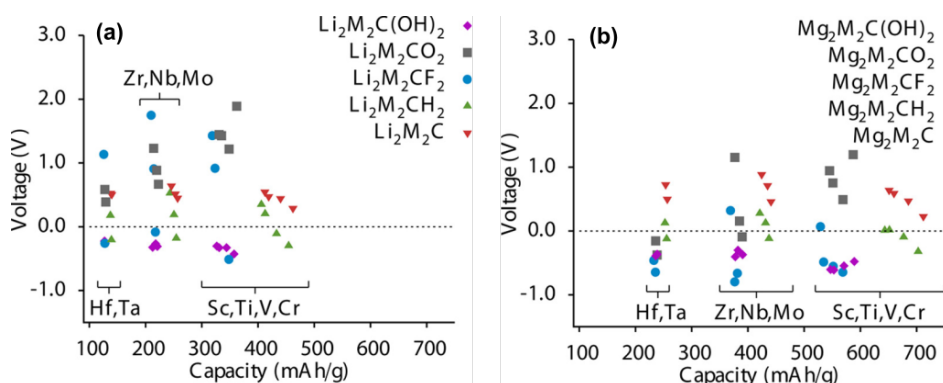


Figure 2.19: Theoretical cell voltages and gravimetric capacities for intercalation of two cations per formula unit into M₂CT_x MXene with various termination groups, shown for Li-ions (a) and Mg-ions (b). Adapted from Ref²⁸ under the Creative Commons Licence [CC BY 4.0](https://creativecommons.org/licenses/by/4.0/).

leading to theoretical capacities > 800 mAh/g for several of the MXene compositions with the minimum amount of transition metals per formula unit (M_2XT_x).^{27,32} They also demonstrated that reactions with multivalent cations (e.g. Mg^{2+}) could lead to the decomposition of the O-terminations, resulting in a conversion reaction to form MgO and unterminated MXene.²⁷ If the thermodynamics would allow for reversible conversion reactions, this decomposition could further add to the reversible capacities of the MXene electrodes. Hence, O-terminated MXenes have received special interest as electrode materials, both for the intercalation of alkali cations and for proton intercalation, due to the proposed storage mechanism presented in Equation 2.6.

However, formation of O-terminated MXene has proven to be a non-trivial task, as mixed terminations are found to be thermodynamically favourable.^{167,208} Although most DFT calculations are performed on homogeneously terminated surfaces, a more recent study demonstrated how weighted averages based on mixed terminations work well for properties such as lattice parameters, work functions and electronic density of states.²⁰⁹ Hence, although complete homogenisation of the termination groups may prove difficult, adjusting the termination mixture could greatly affect the properties of MXenes.

Due to the difficulty of distinguishing OH-terminations from intercalated water and O-terminations by methods such as X-ray photoelectron spectroscopy (XPS) and energy dispersive X-ray spectroscopy (EDS), the quantification of these terminations has proven difficult.¹⁴³ Some reports have even argued that OH-terminations do not form on MXenes,²¹⁰ which is in contrast to the general opinion on MXene terminations.^{141,143} To date, the best verification of OH-terminations on V_2CT_x and $Ti_3C_2T_x$ MXenes come from nuclear magnetic resonance (NMR) and neutron scattering data.^{211–213}

Termination control can be accomplished by different approaches. Whereas some MXene compositions (i.e. Mo_2CT_x) generally show minimal amounts of F-terminations regardless of HF concentration,¹⁶⁹ the more common compositions of e.g. V_2CT_x and $Ti_3C_2T_x$ form F-terminations as long as there is F present during etching.^{211,214} To control the terminations of these compositions, one solution is to modify the etching environment upon MXene synthesis, and thereby control the formation of the termination groups. Another possibility is to change the termination groups by a post-etching treatment. In the following sections, different methods to control the termination groups of common MXene compositions will be presented, with a focus on removing or substituting F-terminations.

F-free etching methods

As the etching environment determines what termination groups may be formed, this is one of the most efficient methods to control the termination groups. Generally, the amount of F-termination is related to the HF concentration, where the etching in low concentrated HF solutions, or in the fluoride salt solutions, is found to result in smaller amounts of F-terminations.^{150,211,214} However, as the presence of HF leads to the formation of F-terminations in most MXene compositions, other methods are required to synthesise F-free MXenes.

In 2018, Tengfei Li et al. reported on one of the first successful F-free etching methods, for the synthesis of $Ti_3C_2T_x$ MXene (Figure 2.20).⁴⁵ The method was inspired by

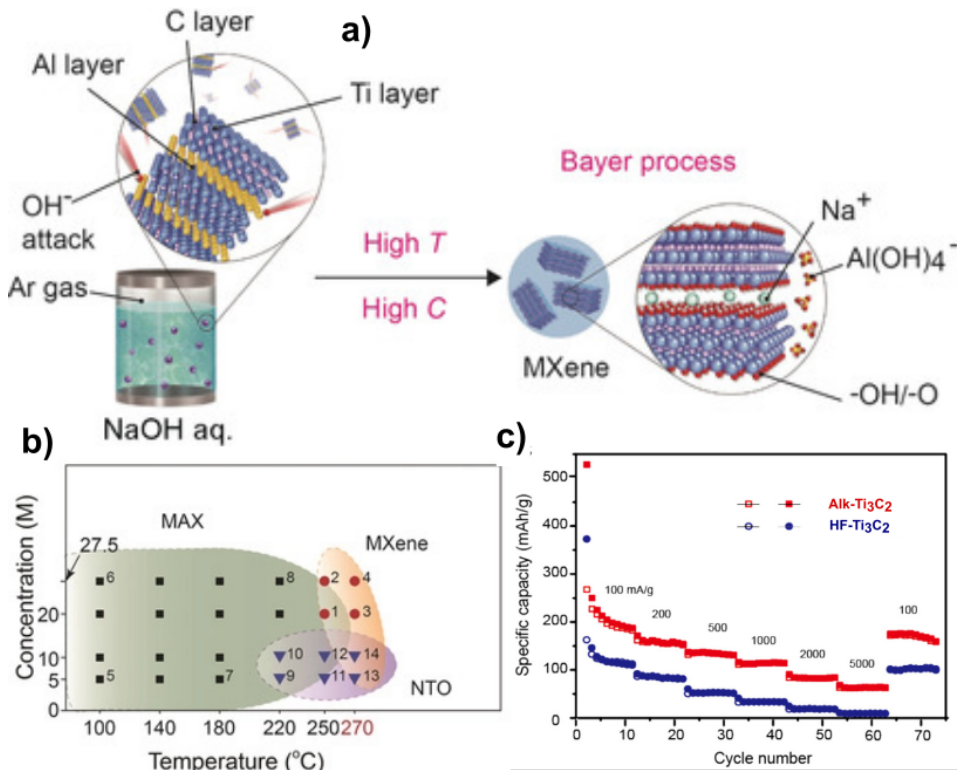


Figure 2.20: Overview of the hydrothermal etching of Ti_3AlC_2 in NaOH solutions, showing a schematic of the process in (a), and an overview of the products formed at various NaOH concentrations and temperatures in (b), where NTO indicates Na-Ti-O compounds. Reproduced from Ref⁴⁵ with permission from John Wiley and Sons. (c) Shows the LiB electrode performance of the alkali etched Ti_3C_2 MXene compared to the HF-etched MXene. Reproduced from Ref²¹⁵ under the Creative Commons Licence [CC BY-NC-ND 4.0](https://creativecommons.org/licenses/by-nc-nd/4.0/).

the Bayer process used for bauxite refining, and utilised high concentrations of NaOH and high temperatures to allow for the dissolution of Al oxides, and thereby a continued extraction of $\text{Al}(\text{OH})_4^-$, as illustrated in Figure 2.20a. Upon hydrothermal etching at 250 °C or higher, and with NaOH concentrations of 20 M or higher, the group was able to successfully remove Al, and form F-free $\text{Ti}_3\text{C}_2\text{T}_x$ MXene in an Ar filled steel autoclave (Figure 2.20b). At lower concentrations, various sodium titanates (denoted "NTO": $\text{Na}_2\text{Ti}_3\text{O}_7$ and $\text{Na}_2\text{Ti}_7\text{O}_{15}$) were formed, and at lower temperature the MAX phase remained intact. The same group also reported on the use of this F-free $\text{Ti}_3\text{C}_2\text{T}_x$ MXene as LiB electrodes, demonstrating improved performance compared to the HF-etched counterpart. However, as the performance reported for HF-etched $\text{Ti}_3\text{C}_2\text{T}_x$ electrodes was significantly poorer than previously reported (Figure 2.17a), these results should be further verified. In fact, no other groups seem to have reported on the utilisation of this method over the last four years, making it an unexplored method for MXene synthesis.

Another F-free etching method was demonstrated by Mian Li et al. in 2019, and is based on reactions between the MAX phase and molten salts exhibiting Lewis acid behaviour.¹⁵⁶ During the reaction Al was substituted by Zn from the molten ZnCl_2 and escaped through the formation of volatile Al-halides. At high ratios of ZnCl_2 :MAX phase, the A-element Zn again dissolves in the ZnCl_2 melt, leaving MXene sheets with mainly Cl-terminations after being washed in a HCl solution. Other Zn-based MAX phases were also demonstrated, such as Ti_2ZnN and V_2ZnC , but due to the stronger M-Zn bond strength in these MAX phases, the group was unable to exfoliate these compositions. The year after, Youbing Li et al. continued on this work and demonstrated a more general Lewis acidic etching route for MXene synthesis, demonstrating the possibility to exfoliate several different A-site MAX phase elements (Al, Zn, Si and Ga) by a range of chloride salts (AgCl , CuCl_2 , NiCl_2 , FeCl_2 , CoCl_2 and CdCl_2).²¹⁶ A few months later, Kamysbayev et al. presented an extensive report on molten salt etching in CdBr , causing the formation of bromide terminated MXenes, which further could be substituted to form homogeneously O-, S-, Se-, Te-, NH_2 and unterminated MXenes, as illustrated in Figure 2.21.¹⁵⁵ Interestingly, they showed that the substitution with divalent anions (S^{2-} , Se^{2-} and Te^{2-}) result in almost half the termination filling compared to the monovalent Br^- and Cl^- , and thus denotes these structures with only one terminating group (e.g. $\text{Ti}_3\text{C}_2\text{S}$). Similar to the chalcogenide electrodes presented in Section 2.1.3, S-terminated MXenes have been predicted to yield low migration barriers and lower intercalation voltages.²¹⁷⁻²²⁰ With theoretically high capacities stemming from the possibility of multilayer intercalation of Li- and Mg-ions, some S-terminated MXene compositions are expected to be very promising anode materials for LiBs and SiBs.^{217,220} Still, this potential remains to be experimentally verified.

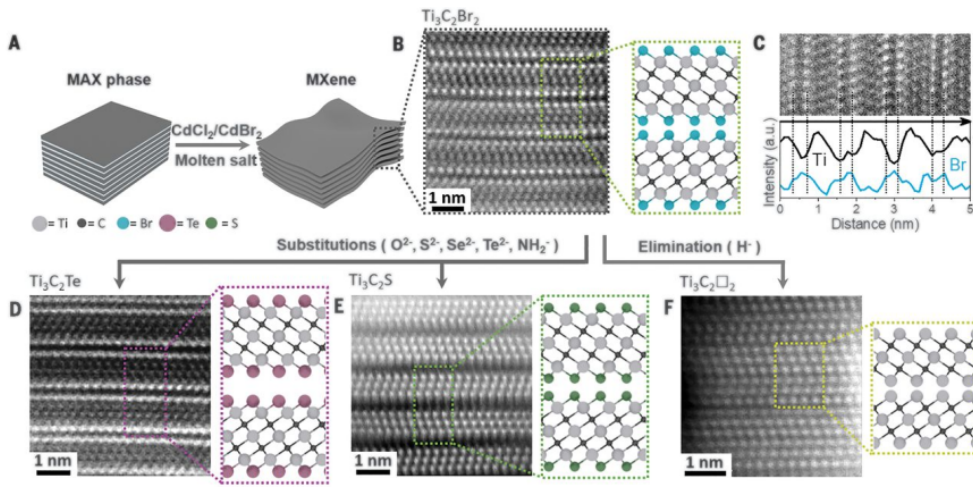


Figure 2.21: (A) Schematic of the molten salt etching in CdCl_2 and CdBr_2 . (B) Atomic-resolution high-angle annular dark-field (HAADF) image of $\text{Ti}_3\text{C}_2\text{Br}_2$ MXene obtained by etching Ti_3AlC_2 MAX phase in CdBr_2 . (C) EDS line scan of $\text{Ti}_3\text{C}_2\text{Br}_2$. HAADF images of (D) $\text{Ti}_3\text{C}_2\text{Te}$ and (E) $\text{Ti}_3\text{C}_2\text{S}$ MXenes by substitution of Br with Te and S termination groups. (F) HAADF image of underterminated Ti_3C_2 MXene obtained by reductive elimination of Br surface groups in LiH at 300°C . From Ref¹⁵⁵. Reprinted with permission from AAAS.

Although both etching methods presented above demonstrate successful synthesis of F-free MXene compositions, they both face challenges for commercial utilisation. As these methods are based on closed inert environments, they do not possess the same scalability potential as the solution-based HF etching methods. Even though Chen et al. demonstrated successful synthesis of 60 g batches by the Lewis acid etching in ambient conditions, this came at the expense of inhomogeneous terminations and/or partly oxidised samples.²²¹ For energy applications, where large amounts of material would be required, these etching methods therefore remain unsuitable. Until scalable etching methods to produce F-free MXene is demonstrated, post-etching treatments may be required for the scalable production of termination controlled MXene.

Post-etching treatments

Several post-etching treatments have been reported for the substitution of MXene terminations, including hydrothermal hydrolysis,^{224–226} dispersions in basic and acidic solutions,^{41,205,222,223,227,228} vacuum annealing,^{43,171,210,227,229,230} and annealing in inert, oxidising and reducing atmospheres.^{42,44,206,231} In 2017, Persson et al. demonstrated a complete removal of F-terminations by annealing at 750°C under ultrahigh vacuum.²¹⁰

In 2022, Hart et al. even showed how the O-terminations on the nearly F-free $\text{Mo}_2\text{TiC}_2\text{O}_x$ MXene could be reversibly removed and formed upon alternating vacuum and O_2 plasma annealing.²³² However, similar to the work of Persson, this was performed on thin films of $\text{Ti}_3\text{C}_2\text{T}_x$ MXene, and comparable termination control remains to be demonstrated for multilayered MXene particles. The reason for the lack of termination change in multilayered particles is not fully explained, but one possibility is that the MXene sheets in multilayered particles are too tightly bound to allow for termination substitution. At least, the annealing of multilayered V_2CT_x , $\text{Ti}_3\text{C}_2\text{T}_x$ and Ti_2CT_x particles did not demonstrate significant compositional changes upon exposure to various annealing atmospheres.^{42,44,206} Instead, the currently best F-removal that has been reported for multilayered MXene has been demonstrated in alkaline solutions, where the MXene phase is expanded by the intercalation of alkali cations, such as Li^+ , Na^+ and K^+ (Figure 2.22).^{222,223,227,228} By stirring of $\text{Ti}_3\text{C}_2\text{T}_x$ MXene in 1 M hydroxide solutions for 24 h, Luo et al. demonstrated almost 50 % reduction in F concentration, which is among the highest reported F reductions while showing insignificant impurities in the X-ray diffraction spectra.²²⁸

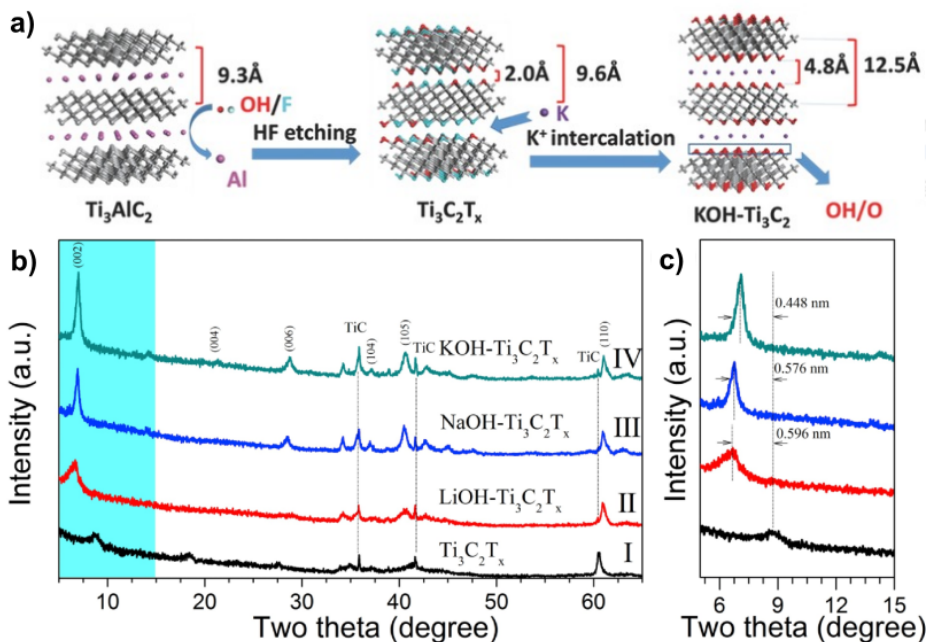


Figure 2.22: (a) Schematic of the MXene expansion and termination change by intercalation of K-ions into $\text{Ti}_3\text{C}_2\text{T}_x$ MXene in a KOH solution. Adapted from Ref²²² with permission from John Wiley and Sons. (b,c) X-ray diffractograms of $\text{Ti}_3\text{C}_2\text{T}_x$ MXene before and after intercalation of Li-, Na- and K-ions, where (c) zooms in on the cyan area in (b). Reproduced from Ref²²³ with permission from Elsevier.

One of the major challenges with changing the termination groups is to ensure a controlled oxidation of the MXene, while preventing decomposition into oxide phases. In general, the transformation from F- and OH- to O-terminations requires an oxidation of the M and X elements,^{35,233} unless the O-termination is bound to two transition metals. As several MXene phases are prone to oxidation,^{44,234–236} the controlled termination change becomes challenging. As an example, the $\text{Ti}_3\text{C}_2\text{T}_x$ phase is found to oxidise into a mixture of TiO_2 nanoparticles and amorphous carbon, as illustrated in Figure 2.23a. Similar oxidation is also shown for the V and Nb based MXenes in various atmospheres.^{44,237} As this oxidation starts at the surface of the particles,²³⁸ one should be careful to trust the termination quantifications obtained from surface sensitive techniques such as XPS.

Although Luo et al. showed the highest F-reduction for alkaline dispersions, they also demonstrated the formation of new particles at the particle surfaces, somewhat similar to those illustrated in Figure 2.23b.²²⁸ Utilising an elevated temperature of 80°C for only 1 h, Wei et al. demonstrated a lower F-reduction, albeit without significant surface

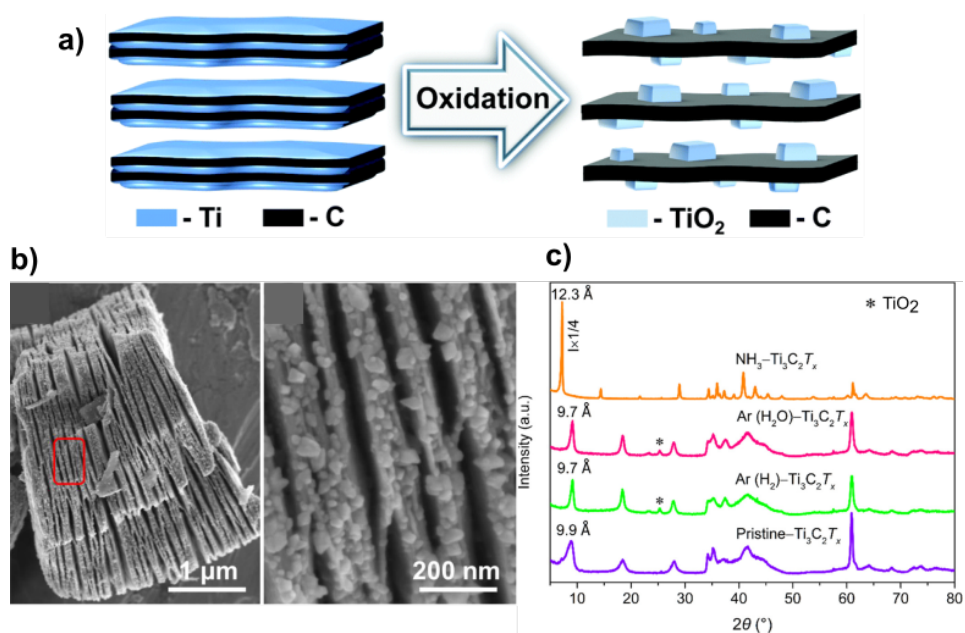
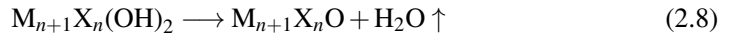
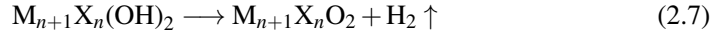


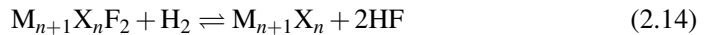
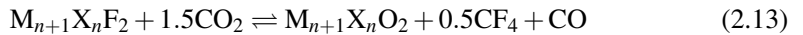
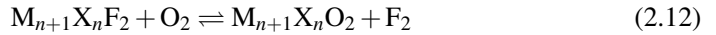
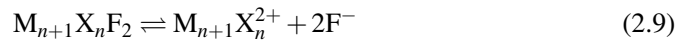
Figure 2.23: Oxidation of $\text{Ti}_3\text{C}_2\text{T}_x$ MXene. (a) Schematic of the oxidation process. Reproduced from Ref²²⁹ under the Creative Commons Licence CC BY 3.0. (b) SEM images of a partly oxidised $\text{Ti}_3\text{C}_2\text{T}_x$ MXene particle with TiO_2 nanoparticles on the surface. Reproduced from Ref²²⁵ with permission from Elsevier. (c) X-ray diffractograms of $\text{Ti}_3\text{C}_2\text{T}_x$ MXene before and after annealing in various atmospheres, demonstrating the formation of a TiO_2 reflection at 26° . Adapted from Ref²⁰⁶. Copyright ©2018 American Chemical Society.

oxidation.²²³ Oxidation of the $Ti_3C_2T_x$ phase has been observed during annealing, where Cheng et al. observed significant amounts of TiO_2 after annealing at $500^\circ C$ in humid and H_2 containing Ar atmospheres (Figure 2.23c).²⁰⁶

Another challenge with the currently proposed post-etching treatments is the understanding of what reactions cause the removal or substitution of termination groups. Hence, a short summary of possible reactions equations will be presented here followed by a short discussion related to their feasibilities. According to DFT calculations, the stability of the termination groups are found to be $Ti_3C_2O_2 > Ti_3C_2F_2 > Ti_3C_2(OH)_2$,^{239,240} where the OH-terminations are expected to decompose into H_2 or H_2O at elevated temperatures through the following reactions:²³⁹



However, due to the aforementioned challenge of characterising OH-terminations, the documentation of OH-termination decomposition through these reactions is uncertain, although Hart et al. claims to show this by electron energy loss spectroscopy (EELS).¹⁷¹ For the removal or substitution of F-terminations, there are several ways as to how this can occur, where some conceivable reactions are listed as follows:

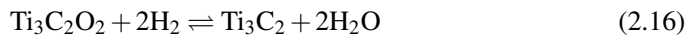


Although removal of single F atoms have been reported by thermogravimetric analysis (TGA),¹⁷¹ this would imply formation of a positive charge on the MXene as shown in Equation 2.9, making it an unlikely reaction for larger-scale termination change. Substituting OH- and F-terminations in aqueous solutions on the other hand (Equation 2.10),

would be more likely, and might explain some of the F-reduction that has been observed in alkaline solutions. Furthermore, due to the high reduction potential of $F_2(g)$ (2.89 V),²⁴¹ it is very unlikely that Equations 2.11 and 2.12 would be possible, although several studies seem to be based on them.^{43,210,231} Instead, the reduction of carbon in CO_2 to CO would be more feasible for F-substitution by forming CF_4 (Equation 2.13). Although CO_2 has been shown to oxidise $Ti_3C_2T_x$ and V_2CT_x particles above 300 °C,^{44,229,242} these studies have not investigated any potential F-reduction prior to oxidation. Moreover, the reduction through H_2 exposure could potentially result in unterminated MXenes through formation of HF (Equation 2.14), as H_2 annealing already has been demonstrated to reduce the F content in delaminated $Ti_3C_2T_x$ films.^{243,244}

Hydrolysis of MXenes to form HF is also a plausible reaction for removal of F-terminations through the formation of HF (Equation 2.15).²⁴⁵ However, due to the aforementioned problem of MXene oxidation in contact with water, the feasibility of these reactions have remained uncertain.^{234–236} Through hydrothermal treatments in DI water, it has been demonstrated that the $Ti_3C_2T_x$ and V_2CT_x MXene phases decompose into titanium and vanadium oxides at 200 °C, but none of the articles reported on any compositional changes at lower temperatures.^{225,226,229} Additionally, all these reports utilised air filled autoclaves, which would speed up the oxidation of the MXene phases. Gas hydrolysis has also been investigated by Cheng et al.,²⁰⁶ but apart from oxidation to TiO_2 at 500 °C, as illustrated in Figure 2.23c, they reported on minimal changes in F-concentrations.

Regarding the removal of O-terminations to form unterminated MXenes, Persson et al. have demonstrated how H_2 gas can be used to reduce O-terminated $Ti_3C_2O_2$ by the following reaction:²³⁰



Nonetheless, similar to their previous work, this has only been verified for thin films in ultrahigh vacuum. In order to selectively substitute or remove terminations on multi-layered MXene particles, further improvements on various post-etching treatments are therefore required.

3

Methods

3.1 Overview

This chapter provides an overview of the experimental work done as a part of this doctoral study. Most of the experiments are explained in detail in the corresponding papers, and the only non-published work presented in this thesis is the F-free alkaline etching of various MAX phases. A simplified outline of the work is illustrated in Figure 3.1.

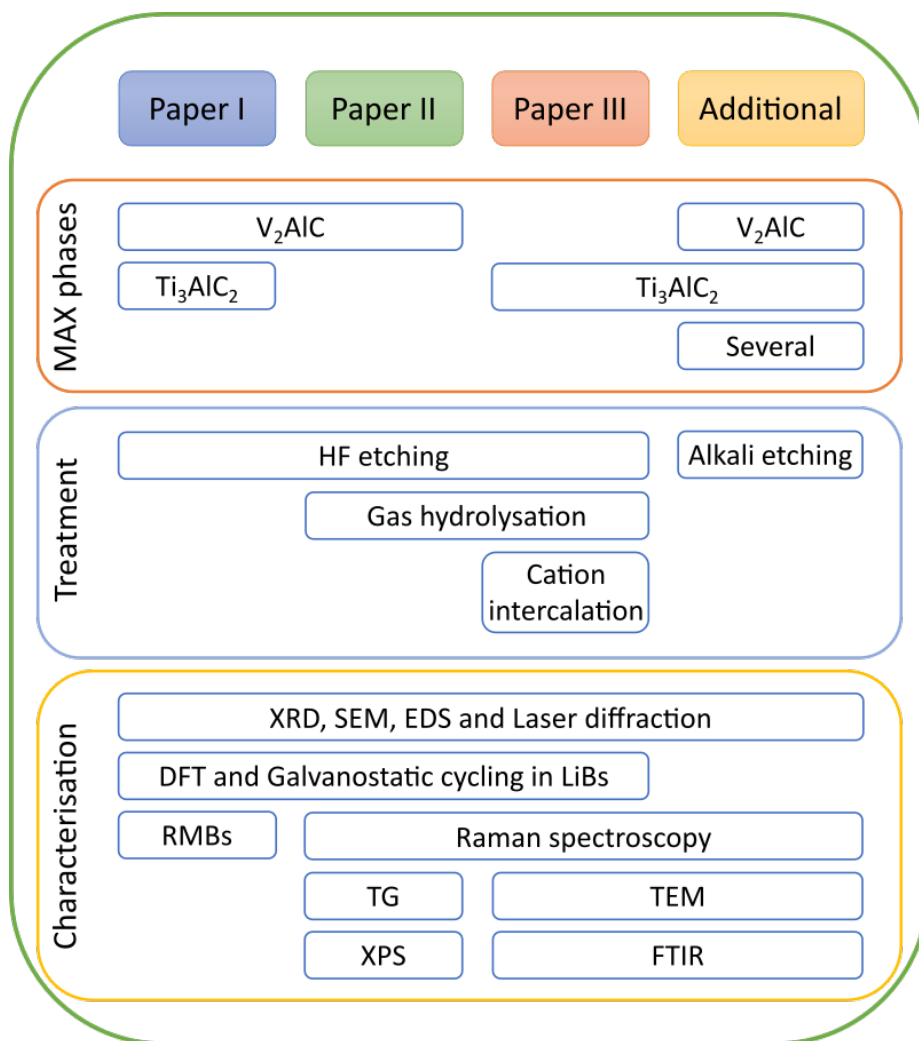


Figure 3.1: An outline of the experimental work presented in this chapter, organised by what papers each part is related to.

3.2 MXene synthesis

During this work, the synthesis of several different MXene compositions, with various degrees of phase purity, have been achieved, including $V_4C_3T_x$, Nb_2CT_x , $Nb_4C_3T_x$, Ti_2CT_x , V_2CT_x and $Ti_3C_2T_x$. The published work has, however, focused solely on the two latter phases due to the obtained phase purity and a general interest in these structures, where the V_2CT_x MXene was examined in Paper I and II and the $Ti_3C_2T_x$ MXene was utilised in Paper I and III. In this section, the synthesis of precursor MAX phases will be explained, followed by a description of the two etching methods that have been attempted as part of this work.

3.2.1 MAX phase synthesis

To obtain phase pure MXenes, it is essential to start with phase pure MAX phase precursors. Due to challenges with obtaining high enough purity by synthesis, several MAX phases were bought from Laizhou Kai Kai Ceramin Material Co., Ltd, as they delivered almost phase pure samples (> 97 %) of Ti_3AlC_2 , Ti_2AlC , Ti_2AlN , Ti_3AlCN , $TiMo_2AlC_2$ and V_4AlC_3 . For the V_2AlC phase, a single MAX phase with high phase purity was achieved by a solid state reaction with elemental powders of C (graphite, Timcal Timrex 99.5 %), Al (Alfa Aesar, 99.5 %, 325 mesh) and V (Sigma-Aldrich, 99.5 %, 325 mesh), based on previous reports.²³ This powder mixture was mixed by wet ball milling in isopropanol and pressed into 1 g pellets prior to heating at 1500 °C for 4 hours. The Nb_2AlC MAX phase was also attempted made with elemental powder of Nb (Sigma-Aldrich, 99.5 %, 325 mesh) based on the same report,²³ but unlike the V_2AlC phase it resulted in mixtures of the Nb_4AlC_3 and Nb_2AlC MAX phases. Before HF etching, the powders were wet planetary milled in isopropanol dispersions, in order to control the particle sizes. This was done in WC milling jars with WC milling balls to prevent impurity formation by the hard MAX phases. For the alkaline etching, particle sizes < 75 μm were used.

3.2.2 HF etching

The etching method used for the MXene synthesis in all three papers was by dispersing the MAX phases in pure HF solutions. This was done by slowly adding MAX phase powder to a polypropylene beaker containing the HF solution, in a ratio of 1 g MAX phase per 20 mL HF solution. Thereafter, the beaker was partly covered with parafilm and the dispersion was left stirring at room temperature for a certain amount of time.

For the etching of Ti_3AlC_2 , a 10 wt. % HF solution was used with a 24 h etching time, whereas the complete exfoliation of the V_2AlC MAX phase required a 48 wt. % HF solution and etching times of 96 and 72 h for Paper I and II, respectively. After the etching, the powder was washed by centrifugation, decantation and DI-water dilution until a $\text{pH} > 5$ was obtained. Lastly, the powders were vacuum filtered through $0.22\ \mu\text{m}$ pore sized polyvinylidene fluoride (PVDF) filter papers and further dried under vacuum at $120\ ^\circ\text{C}$ for 12 h to remove adsorbed water.

3.2.3 F-free alkaline etching

In addition to the reported results, the hydrothermal etching in alkaline solutions have been attempted for all the MAX phases available. This was based on the method reported by Li et al. and comprised the use of high concentration NaOH solutions to prevent the oxidation of the transition metal at high temperatures.⁴⁵ In this work, 50 mL of a 50 wt. %/19.1 M NaOH solution (Merck, 158793) was poured into a double neck round bottle, and bubbled with Ar gas (99.999 %) for > 1 h with a gas flow of 500 mL/min to remove O_2 gas from the solution. Then the solution was transferred to a 100 mL steel autoclave, followed by the addition of 0.2 g MAX phase powder. The autoclave was held in an Ar filled beaker, with continuous Ar blowing to prevent O_2 entering the autoclave before sealing it. Thereafter, the closed autoclave was put in a fume hood and heated with a constant power up to $270\ ^\circ\text{C}$ in approximately 1 h, before it was dwelled at that temperature for 12 h. After the autoclave had cooled down it was opened and the black suspension at the bottom of the autoclave was washed several times with DI water until reaching a $\text{pH} < 9$. In the end, the powder was vacuum filtered on $0.22\ \mu\text{m}$ pore sized PVDF filter papers and further dried under vacuum at $65\ ^\circ\text{C}$ for 3 h.

3.3 Post-etching treatments

After synthesising the V_2CT_x and $\text{Ti}_3\text{C}_2\text{T}_x$ MXene phases by HF etching, different post etching treatments were performed in Paper II and Paper III. They will be presented in the following section.

3.3.1 Cation intercalation

As reported in Paper III, the intercalation of various cations was performed to increase the interlayer spacing of the $\text{Ti}_3\text{C}_2\text{T}_x$ MXene structure. The method was based on previous

reports,^{157,246,247} and was done by dispersing 0.4 g of the $\text{Ti}_3\text{C}_2\text{T}_x$ powder in 50 mL salt solutions under constant agitation, before washing the powder several times with DI water through centrifugation. Lastly, the powders were vacuum filtered and vacuum dried at 40 °C for up to 1 h. The intercalation of TBA^+ ions was done by dispersing $\text{Ti}_3\text{C}_2\text{T}_x$ in a 1.2 M TBAOH solution over 12 h, while the intercalation of Li^+ , Na^+ and K^+ was accomplished in 2 M hydroxide solutions for 2 h. Mg-ion intercalation was realized by ion exchange of the Na-intercalated MXene. This was done by adding the Na- Ti_3C_2 powder to a 1 M solution of MgCl_2 for 3 h, before the powder was washed in DI water and left for another 20 h in a fresh MgCl_2 solution.

3.3.2 Gas hydrolysis

Gas hydrolysis was used as a method to remove F-terminations from the multilayered MXene particles and is reported for the V_2CT_x and $\text{Ti}_3\text{C}_2\text{T}_x$ MXene phases in Paper II and Paper III, respectively. It was performed by distributing 0.1 g of the MXene powder over a 1-2 cm^2 area in an alumina crucible before introducing it to a quartz tube furnace. After flushing the tube with Ar gas (99.999 %) for > 2 h at a flow rate of 200 mL/min, the furnace was heated to a given temperature at a rate of 300 °C/h and dwelled for 15 h with the same gas flow. To ensure H_2O vapour inside the quartz tube, the Ar gas was bubbled through a DI water bath prior to entering the tube. After the flushing step, this water bath was heated to a constant temperature of 80 °C, which results in a saturated water vapour pressure of 0.474 bar.²⁴⁸ To prevent air leakage into the furnace and to capture HF formed during the hydrolysis, the exhaust gas was bubbled through a 1 M $\text{Ca}(\text{NO}_3)_2$ solution. A schematic of the hydrolysis setup is displayed in Figure 3.2.

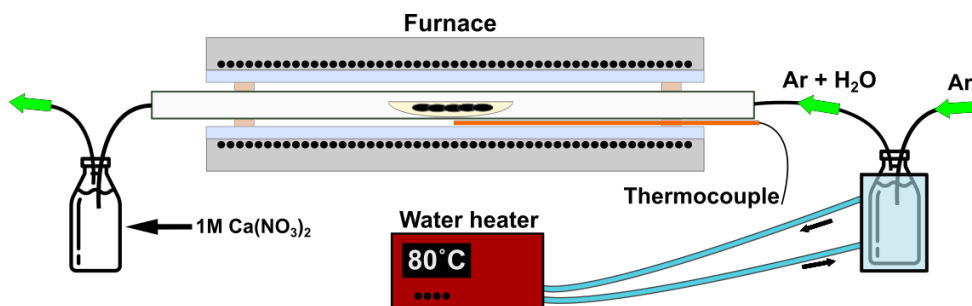


Figure 3.2: A schematic of the hydrolysis setup, showing how Ar gas is bubbled through a glass of DI water, heated to a controlled temperature. Reproduced from Ref.²⁴⁵ under the Creative Commons Licence [CC BY 4.0](https://creativecommons.org/licenses/by/4.0/).

3.4 Material characterisation

3.4.1 X-ray diffraction (XRD)

To investigate the crystallinity and phase purity of the samples, X-ray powder diffraction was performed using a Bruker D8 Focus Diffractometer with a 0.2 mm divergence slit and a Cu K α radiation source ($\lambda = 0.15406$ nm). Powder samples were prepared in Si cavity holders or dispersed on a Si wafer. Thin, solid samples were mounted on the Si wafer with a small amount of vacuum grease. The phase identification was done in the DIFFRAC.EVA software using the ICDD PDF-4+ database. In Paper III, the diffractograms were corrected for sample displacement based on structureless fittings to the P6₃/mmc space group in the TOPAS software, where some of the diffractograms also were analysed through Rietveld refinement.

3.4.2 Scanning electron microscopy (SEM)

To examine the morphology of the particles, SEM was carried out on either a Zeiss Ultra 55 field-emission SEM (FESEM) or a Zeiss SUPRA 55VP low-vacuum FESEM. The samples were prepared by sprinkling a small amount of MXene powder onto conductive carbon taped sample holders, and the measurements were performed under ultrahigh vacuum using an acceleration voltage of 5-10 kV, an aperture size of 30 μ m and a working distance of 8 mm.

3.4.3 Energy-dispersive X-ray spectroscopy (EDS)

Elemental composition was determined by EDS using an XFlash 4010 X-ray detector in the abovementioned SEM instruments. The measurements were done with an acceleration voltage of 10-15 kV, a working distance of 10 mm and an aperture size of 120 μ m. The mappings were acquired over 3 minutes and each point scan had an acquisition time of 30 seconds. The resulting spectra were then analysed in the Esprit 1.9 software and the average values of six or more point scans from each sample were calculated to obtain quantitative results. In Paper III, the standard deviations in the sets of point scans for all samples were also calculated.

3.4.4 Laser diffraction

The particle size distributions of the Ti_3AlC_2 and V_2AlC MAX phase powders prior to etching was obtained through laser diffraction measurements in a Horiba Partica LA-960 analyser. To avoid agglomeration, the MAX phase particles were dispersed in isopropanol and sonicated for a minimum of 2 minutes prior to measurements.

3.4.5 X-ray photoelectron spectroscopy (XPS)

XPS was used in Paper II to investigate the changes in oxidation states and surface chemical composition upon hydrolysis of the V_2CT_x MXene. The measurements were performed under ultrahigh vacuum using a SPECS XR-50 X-ray source with a Mg anode and a VG ESCA MKIV with a CLAM4 analyzer, and the XPS samples were prepared by gluing the MXene powder to a Si wafer substrate using silver glue. To compensate for static charges during the measurements, the Si_{2p} peak from the substrate was used as an internal reference. Additionally, satellite peaks stemming from the Mg $\text{K}\alpha_3$ and $\text{K}\alpha_4$ X-rays were removed prior to further analysis. The curve fitting was done using Shirley backgrounds in the Igor Pro 7 software and the quantification was calculated using established cross-section values.²⁴⁹

3.4.6 Raman spectroscopy

In Paper II and Paper III, the vibrational modes of the different samples were inspected by Raman spectroscopy with the use of a WITec Alpha 300r Confocal Raman Microscope. The samples were prepared by pressing small amounts of powder onto glass substrates, while the measurements were completed using 50x or 100x objectives, a 532 nm Ar laser, 5-10 second measuring times, 10 measurements per spectra, and a modest laser power of < 0.8 mW to prevent oxidation. At higher laser powers, the V_2CT_x and $\text{Ti}_3\text{C}_2\text{T}_x$ MXenes decomposed into V_2O_5 and TiO_2 phases respectively, in addition to amorphous C.

3.4.7 Transmission electron microscopy (TEM)

High resolution TEM micrographs and TEM EDS was used to obtain information on the atomic structure and local chemical composition of the $\text{Ti}_3\text{C}_2\text{T}_x$ phase in Paper III. The samples were prepared perpendicular to the (002) plane with focused ion beam (FIB, FEI FIB200) lamella preparation, using a Helios G4 UX dual beam. The lamellae were cut

out and thinned down to around 150 nm thick samples using Ga^+ ions. Initially with an acceleration voltage of 30 kV, before final thinning was done at 5 kV and 2 kV to minimise surface damage of the samples. The imaging was performed with a double Cs aberration corrected cold FEG Jeol ARM200FC, operated at 200 kV, and the TEM EDS maps were acquired in scanning TEM (STEM) mode with a 100 mm² Centurio X-ray detector, covering a solid angle of 0.98 steradian.

3.4.8 Fourier-transform infrared spectroscopy (FTIR)

FTIR was used in Paper III to obtain further information on the vibrational properties of the samples, and the measurements were conducted in a Bruker VERTEX 80v spectrometer. The results were obtained by diffuse reflectance measurements at 2 mBar, using a MXene:KBr powder mixture in a mass ratio of 1:39 to ensure reasonable absorption. Pure KBr powder was used as the reference.

3.4.9 Thermogravimetric analysis (TGA)

The thermal stability of the V_2CT_x MXene was measured using a NETZSCH STA 449 F3 Jupiter analyser and presented in Paper II. The measurements were done by distributing 15 mg of the powder in lid covered alumina containers, before heating it up to 300 °C, 600 °C and 800 °C and dwelling at these temperatures for 1 h. The utilised heating rate was 5 °C/min and during the whole experiments the flow of Ar gas was 30 mL/min.

3.5 Electrochemical characterisation

To assess the electrochemical performance of the different MXenes, 2016-type coin cells were assembled with the MXenes as the active material and cycled at constant currents (galvanostatic cycling). This section describes how the MXene electrodes were prepared and further assembled into coin cells, in addition to how the cells were tested after being assembled.

3.5.1 Electrode preparation

The electrodes were made by mixing 80 wt. % of the active material (MXene) in a slurry with 10 wt. % carbon black and 10 wt. % PVDF binder material, before drop casting

the slurry on precut current collectors and drying off the slurry solvent. The slurry was homogenised by first dry mixing a mixture of the active material and the carbon additive in a steel jar at 25 Hz for 10 minutes. Then a predissolved solution of PVDF in 1-ethyl-2-pyrrolidone (NEP) was added, followed by additional NEP to obtain a solid to liquid ratio of 1:6, before the mixture was further shaken for 30 min at 15 Hz together with a steel shaker ball. The resulting slurry was then drop cast onto 16 mm diameter precut current collectors using plastic pipettes. For Paper I, carbon paper (Spectracarb 2050A-0550) was used as the current collector, whereas Al foil and Cu foil were used for the electrodes in Paper II and Paper III, respectively. These circular electrodes were then dried on a 60 °C hotplate in a fume hood overnight, followed by further drying in a vacuum oven for a minimum of 3 hours, before the electrodes were introduced to an Ar filled glovebox ($\text{H}_2\text{O} < 0.1$ ppm, $\text{O}_2 < 0.1$ ppm). The vacuum drying temperature was 120 °C for Paper I, and reduced to 60 °C for Paper II and III to prevent unintentional H_2O deintercalation. In the end, these electrode preparations resulted in active mass loadings in the range of 1-4 mg/cm^2 .

3.5.2 Electrolyte preparation

Unlike Paper II and III, where a commercial LiB electrolyte (1 M LiPF_6 , EC:EMC 1:1, Sigma Aldrich) was utilised, several different electrolytes were mixed for the electrochemical testing of Mg-ion intercalation in Paper I. The most used electrolyte was the APC-THF electrolyte, with Mg_xCl_y^+ as the electroactive cation. This APC-THF electrolyte was also used to test the Li-ion intercalation properties of the MXene by adding a small amount of LiCl (0.4 M LiCl-APC-THF). In addition, three more electrolytes, with different solvents and electroactive cations, were used to test for Mg-intercalation, including $\text{Mg}(\text{TFSI})_2$ -2 MgCl_2 -DME, $\text{Mg}(\text{BH}_4)_2$ -THF and BMOC-DME. For the full description on the mixing of these electrolytes, the reader is referred to the Supplementary information of Paper I (see Appendix).

3.5.3 Coin cell assembly

The prepared electrodes were assembled as the working electrodes in coin cells with the different components illustrated in Figure 3.3. Polished Mg and Li chips were used as the counter electrode, together with an electrolyte amount of 55-75 μL both before and after insertion of the glass microfiber (Whatman GF/A) separator. Apart from the plastic gasket, the remaining parts were all stainless steel.

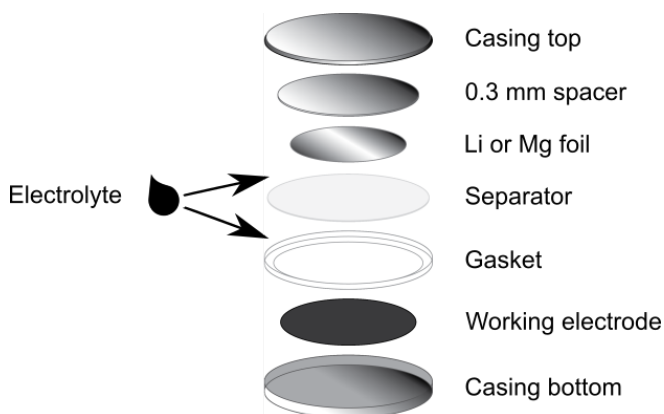


Figure 3.3: A schematic of the different components in the coin cell assembly.

3.5.4 Galvanostatic cycling

The coin cells were electrochemically characterised by galvanostatic charge/discharge cycles at a controlled temperature of 20 °C, 25 °C or 60 °C, using three different cyclers: BioLogic BCS-805, Maccor Model 4200 and Landt CT2001A. To assess the rate capability of the electrodes, current densities in the range of 10 mA/g to 400 mA/g were utilised.

3.6 Density functional theory (DFT) calculations

In Paper I, DFT was used to examine and understand the intercalation of Mg^{2+} ions in MXenes. Migration barriers and average voltages for Li^+ and Mg^{2+} ions were calculated for single-layer and multilayered V_2CT_x and $\text{Ti}_3\text{C}_2\text{T}_x$ MXenes with O, F and OH termination groups. Additionally, possible side reactions were identified.

In Paper II and III, DFT was used to calculate the Gibbs free energy of reactions related to the hydrolysis of V_2CT_x and $\text{Ti}_3\text{C}_2\text{T}_x$ MXenes, at various temperatures.

4

Summary of results

4.1 Foreword

This chapter summarises the main results from Paper I-III, presented in one section per paper, followed by unpublished work on the F-free etching of various MAX phases by hydrothermal processing in alkaline solutions. For the complete discussions and results related to the published work, the reader is referred to the appended papers at the end of this thesis.

4.2 Paper I: MXenes as cathode material in RMBs

4.2.1 Overview

In Paper I, the viability of MXenes as cathode material for RMBs was evaluated. To assess this, two MXene phases ($\text{Ti}_3\text{C}_2\text{T}_x$ and V_2CT_x) were synthesised from the corresponding MAX phases, and assembled into RMB coin cells for electrochemical cycling. To probe the possibility for Mg^{2+} ion desolvation and migration within the MXenes, several different electrolytes were tested at both 20 °C and 60 °C. In addition, DFT calculations were included to increase the understanding of the Mg-ion intercalation in these MXenes.

4.2.2 MXene synthesis

By ball milling and subsequent HF etching of the MAX phases, successful synthesis of $\text{Ti}_3\text{C}_2\text{T}_x$ and V_2CT_x MXenes with high purity and controlled particle size distribution was achieved. In Figure 4.1 this is demonstrated for the $\text{Ti}_3\text{C}_2\text{T}_x$ phase, showing the accordion-like morphology after etching, as well as a shift and broadening of the (002) reflection, which indicates an increased and less defined interlayer spacing compared to Ti_3AlC_2 . The complete exfoliation of the MAX phase was also supported by the accompanied removal of Al, as verified by EDS analysis. Similar results were obtained for the V_2CT_x MXene, although a small amount of Al_2O_3 impurities from the MAX phase remained after the etching.

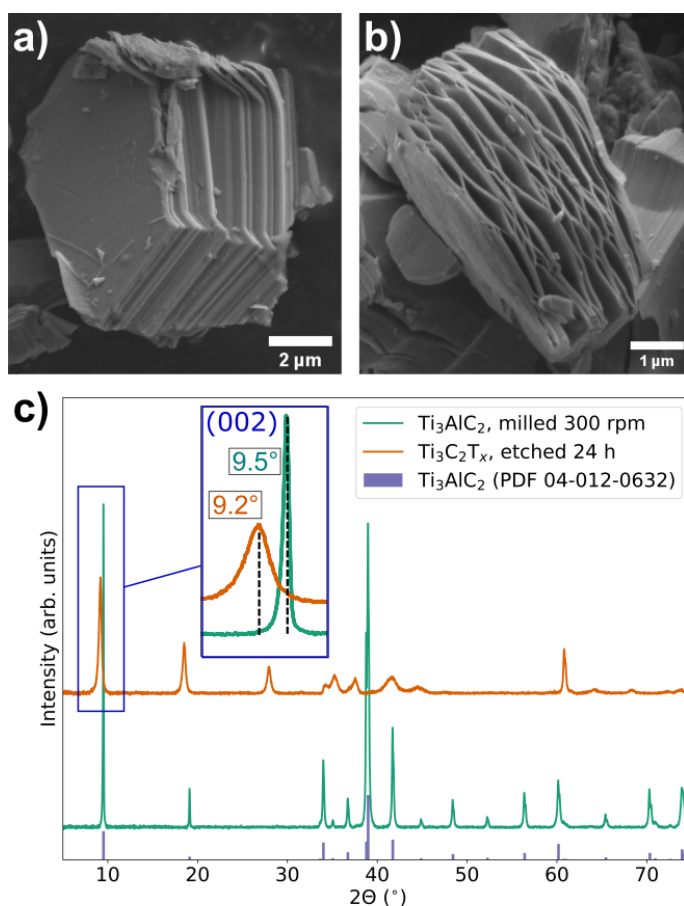


Figure 4.1: SEM micrographs of the Ti_3AlC_2 MAX phase before (a) and after (b) etching, and X-ray diffractograms of the same powders (c). Reproduced from Ref.³⁵ with permission from the Royal Society of Chemistry.

4.2.3 Electrochemical performance

When cycled with low current densities of 10 mA/g in the APC-THF electrolyte, both MXenes demonstrated marginal reversible capacities of 1-4 mAh/g, as shown in Figure 4.2a-b. Although a small capacity increase (from 1 mAh/g to 3 mAh/g) was achieved by increasing the cycling temperature to 60 $^\circ\text{C}$, no signs of Mg-intercalation were observed. Even after a 200 h potentiostatic hold step at 1 mV (Figure 4.2c), there were no indications of Mg-ions entering the Ti_3AlC_2 MXene, as the (002) reflection representing the interlayer spacing of the MXene remained unchanged (Figure 4.2d). Instead, the small reversible capacities measured were attributed to surface reactions at the MX-

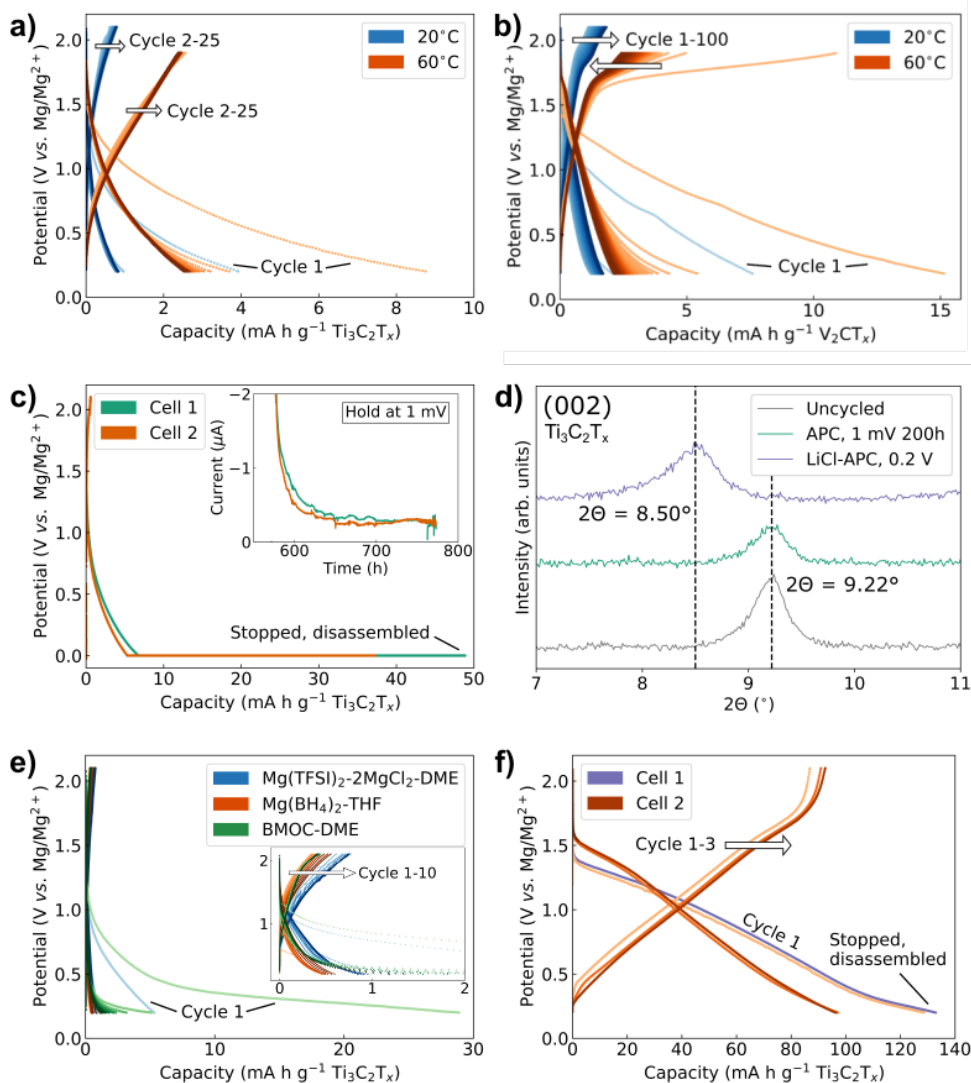


Figure 4.2: Electrochemical performance of $\text{Ti}_3\text{C}_2\text{T}_x$ (a, c-f) and V_2CT_x (b) electrodes cycled at a low current density of 10 mA/g in different electrolytes and temperatures. (a) and (b) show voltage profiles when cycled at 20 °C and 60 °C in APC-THF. (c) presents a 200 h potentiostatic hold step at 1 mV, where the inset shows the current upon holding the potential. (d) presents the (002) reflection of $\text{Ti}_3\text{C}_2\text{T}_x$ before and after complete discharge in electrolytes with and without Li ions. (e) presents cycling with three different electrolytes, and (f) shows voltage profiles with a Li-containing electrolyte. Adapted from Ref. ³⁵ with permission from the Royal Society of Chemistry.

ene/electrolyte interface, and the marginally higher capacity obtained from the V_2CT_x electrodes was therefore partly ascribed to a higher surface area than the $Ti_3C_2T_x$ particles.

Although different solvents and electroactive species may influence the electrochemical performance, the reversible capacities were not improved for any of the employed electrolytes (Figure 4.2e). The BMOC-DME electrolyte did result in a significantly higher first discharge of 30 mAh/g, which was also found to yield reversible charge and discharge plateaus when extending the lower cut-off voltage to 0.01 V. However, this capacity was not related to the intercalation of Mg^{2+} ions into the $Ti_3C_2T_x$ particles, as it was found to originate from a co-intercalation of Mg-ions and solvent molecules into the graphite current collector, similar to previous reports.^{250,251} As shown in Figure 4.2f, addition of LiCl to the APC-THF electrolyte resulted in reversible capacities of approximately 100 mAh/g and significant shifts in the (002) reflection (Figure 4.2d), attributed to the intercalation of Li-ions. This verified the functionality of the coin cell setup, including reversible Mg stripping from the anode and ion intercalation into MXene electrodes, and thereby emphasised the challenges related to intercalation of Mg^{2+} ions.

4.2.4 DFT calculations and conclusion

DFT calculations identified several important parameters influencing the ion intercalation properties of the MXenes, as shown in Figure 4.3. The termination groups were shown to greatly affect the intercalation voltage of both Li- and Mg-ions, where only O-terminations demonstrated positive average voltage for Mg-ion intercalation. Additionally, the OH- and F-terminations were found to react irreversibly with Mg-ions to form MgH_2 and MgF_2 . As no side reactions were found for O-terminations, they were shown to be the only viable termination for reversible intercalation of Mg-ions.

Furthermore, these calculations demonstrated comparable migration barriers inside multilayered particles and on single-layer MXene flakes. This is contrary to the reported experimental efforts that have focused mostly on increasing the surface area by delamination and intercalation of large organic molecules.³⁷⁻³⁹ As multilayered particles would result in the highest possible density and thereby an optimal energy density in MXene electrodes, delamination should ideally be avoided. Additionally, a low migration barrier for $MgCl^+$ on single-layer MXenes was calculated, which supports the claim that the above-mentioned reports only present reactions with $MgCl^+$ instead of Mg^{2+} .

By comparing the $Ti_3C_2O_2$ and V_2CO_2 phases, significant differences between various MXene compositions are evident. In addition to a slightly higher average voltage (1.5

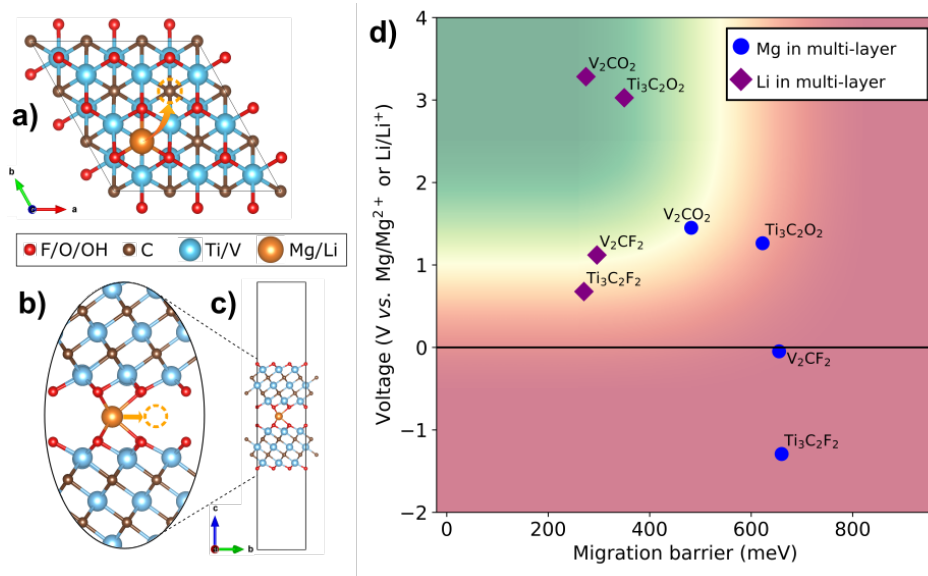


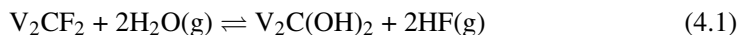
Figure 4.3: DFT calculations for Li- and Mg-ion intercalation in $\text{Ti}_3\text{C}_2\text{T}_x$ and V_2CT_x MXene with various surface terminations. (a) shows a top view of the migration paths for the cations, while (b) shows side views of the same migration paths from the unit cell (c). In (d) the intercalation voltage and migration barriers are plotted for Li- and Mg-ions in different MXene compositions, with colour coding illustrating combinations of feasible (green) and non-feasible (red) values for cathode materials. Adapted from Ref. ³⁵ with permission from the Royal Society of Chemistry.

V vs. 1.3 V vs. Mg/Mg^{2+}), the V_2CO_2 MXene possesses a considerably lower migration barrier for both Li- and Mg-intercalation (480 meV vs. 620 meV for Mg^{2+}). Although the migration barriers for Li-intercalation was found to be more than 200 meV lower for all compositions, a migration barrier of 480 meV in V_2CO_2 still could allow for measurable Mg^{2+} migration within reasonably sized MXene particles.¹⁰⁴ Hence, homogeneously terminated V_2CO_2 MXene was found to be the only composition to possess an acceptable combination of voltage and migration barrier for utilisation as an RMB cathode, as illustrated by the color coding in Figure 4.3d. The lack of Mg-ion intercalation observed experimentally for V_2CT_x was therefore ascribed to either 1) problems with the strongly coordinated Mg^{2+} ions entering the MXene structure or 2) irreversible reactions with the F- and OH-terminations. In conclusion, this work demonstrated how homogeneously terminated V_2CO_2 MXene may be a possible solution for Mg^{2+} intercalation, and prove to be a viable cathode material for RMB if successfully synthesised.

4.3 Paper II: Gas hydrolysis of V_2CT_x

4.3.1 Overview

In Paper II, gas hydrolysis was explored as a post-etching method to substitute F-terminations with O-based terminations in multilayered V_2CT_x MXene. To assess this, multilayered V_2CT_x MXene was hydrolysed at a set of temperatures between 100 °C and 500 °C, in a continuous flow of humidified Ar gas with a controlled partial pressure of water vapour corresponding to $p(H_2O) = 0.47$ bar. In addition to the experimental work, DFT calculations were conducted to assess the thermodynamic feasibility of the proposed hydrolysis reactions:



4.3.2 MXene synthesis

Similar to Paper I, complete exfoliation of the V_2AlC MAX phase was achieved by ball milling prior to the HF-etching step. This was verified by the total removal of Al and the lack of XRD reflections from the MAX phase after the etching step. Another similarity to the V_2CT_x obtained in Paper I was the presence of a small amount of Al_2O_3 after the HF-etching, which in this study was used as an XRD reference. However, one significant dissimilarity between the two phases, were the interlayer spacings. While the V_2CT_x MXene presented in Paper I displayed only one broad (002) reflection describing an interlayer spacing of approximately 9.6 Å, the phase presented in Paper II resulted in two (002) reflections representing interlayer spacings of 9.6 Å and 7.7 Å. This was ascribed to different amounts of intercalated water, where some particles in the V_2CT_x MXene presented in Paper II may have been partly dehydrated.

4.3.3 Gas hydrolysis

Upon hydrolysing the MXene at elevated temperatures, one of the main transformations before the MXene phase decomposed was related to shifts in the (002) reflection, as shown in Figure 4.4. At temperatures below 400 °C, the two (002) reflections shifted towards higher 2Θ values, indicating a reduction in the interlayer spacings. Additionally, the intensity of the two reflections shifted from the one at low 2Θ to the one at higher 2Θ , indicating an increased amount of particles with the lowest interlayer spacing. This densification of the MXene structure was attributed to the partial dehydration of the V_2CT_x particles at elevated temperatures. Above 300 °C, the MXene phase decomposed to a VC_xO_y phase, prior to complete oxidation to V_2O_5 after hydrolysis at 500 °C. This oxidation also resulted in formation of small nanoparticles on the edge surface of the MXene particles, while preserving the macroscopic morphology, which is similar to previous reports.⁴⁴

Importantly, the chemical composition of the V_2CT_x phase was found to change significantly before it decomposed at $T > 300$ °C, as shown in Figure 4.5. From the normalised EDS mapping spectra in Figure 4.5a, the F peak is significantly decreased after hydrolysis at 300 °C, followed by a complete removal after hydrolysis at 500 °C. A similar

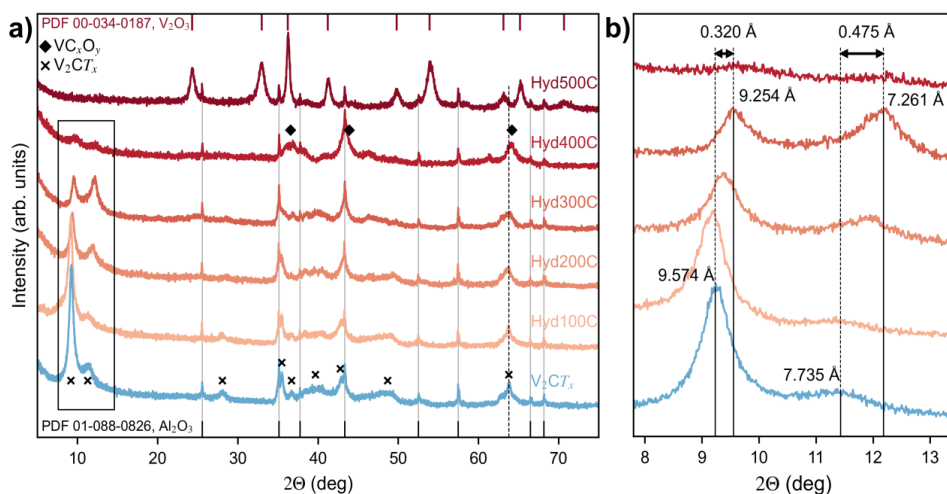


Figure 4.4: X-ray diffractograms of V_2CT_x before and after hydrolysis at various temperatures up to 500 °C, where (a) shows the full diffractograms and (b) presents the shifts in the (002) reflection marked with the corresponding interlayer spacings. The dashed line in (a) represents the position of the (110) MXene reflection at 63.8° . Reproduced from Ref.²⁴⁵ under the Creative Commons Licence [CC BY 4.0](https://creativecommons.org/licenses/by/4.0/).

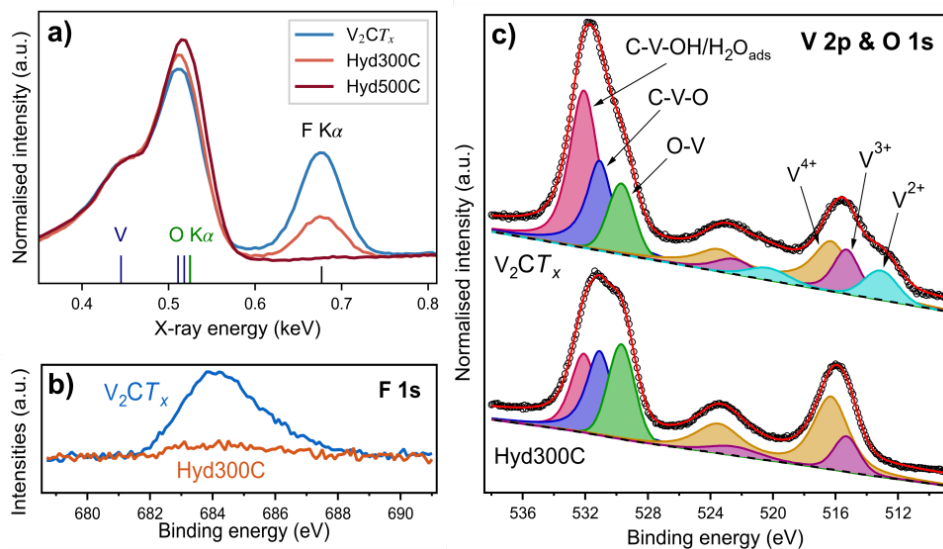


Figure 4.5: Chemical composition change of V_2CT_x upon hydrolysis, where (a) shows the lower energy region from EDS mapping spectra, (b) displays the F 1s XPS region and (c) presents the V 2p and O 1s XPS regions. Adapted from Ref. ²⁴⁵ under the Creative Commons Licence [CC BY 4.0](https://creativecommons.org/licenses/by/4.0/).

F reduction was found at the outer surface of the particles, where the hydrolysis at 300 °C caused the disappearance of the XPS F 1s peak, as presented in Figure 4.5b. Analysis of the V 2p and O 1s regions in the XPS spectra, presented in Figure 4.5c, demonstrated a partial oxidation from 2+ to 4+ states of the V atoms. It also revealed a reduced amount of OH-terminations and/or adsorbed H_2O , combined with an increased amount of O-V bonds, indicating formation of surface oxides upon hydrolysis. To quantify the bulk F reduction within the V_2CT_x particles, the average point scan values from several particles were calculated. These results demonstrated a clear trend in reducing the F concentration during hydrolysis, where the F content after hydrolysis at 300 °C was 69 % lower than for the pristine V_2CT_x . However, as the O $K\alpha$ EDS peak greatly overlapped with two of the V X-rays (Figure 4.5a), the quantification of the corresponding O content remained uncertain. Seeing that the hydrolysis resulted in a reduced interlayer spacing, the XPS O 1s spectra indicated no increase in the number of C-V-O bonds, combined with the DFT calculations predicting the formation of singly terminated V_2CO as the most thermodynamic favourable reaction, it was assumed that the hydrolysis resulted in a removal of F-terminations to form partly unterminated V_2CT_x .

To verify the importance of water vapour, the effect of hydrolysis was compared to annealing in dry Ar. This resulted in a similar trend with the gradual dehydra-

tion/decomposition of the MXene phase at elevated temperatures, but unlike hydrolysis, some MXene reflections remained even up to a temperature of 600 °C upon annealing in dry Ar. After Ar annealing at 800 °C, the MXene phase completely decomposed to various disordered VC_xO_y phases, as well as a highly crystalline VF_2 phase which demonstrated that Ar annealing was unable to remove all F. These results therefore proved the importance of water as a reactant to remove F-terminations from multilayered V_2CT_x , through the hydrolysis reactions initially presented.

4.3.4 Electrochemical performance in LiBs

Due to negligible obtained capacities for V_2CT_x cathodes in RMBs, the only electrochemical performance presented in this paper was related to LiBs. In Figure 4.6, the voltage plots of two cycles at different current densities were compared between V_2CT_x before and after hydrolysis at 300 °C. It displays almost identical profiles for the two electrodes at 10 mA/g, although the hydrolysed sample showed a 20 mAh/g increase below 1.5 V. However, by increasing the current density to 100 mA/g, the hydrolysed sample demonstrated an improved energy efficiency and 50 % higher capacity than the pristine V_2CT_x , which was attributed to the reduced migration barriers for Li-ions in both unterminated and O-terminated V_2CT_x .^{252–254} Additionally, a reduced irreversible plateau close to 1.6 V was observed in the first discharge of the hydrolysed MXene, which was attributed to the lower water content in between the MXene layers, as the formation of SEI occurs at even lower potentials for EC based electrolytes.^{255,256}

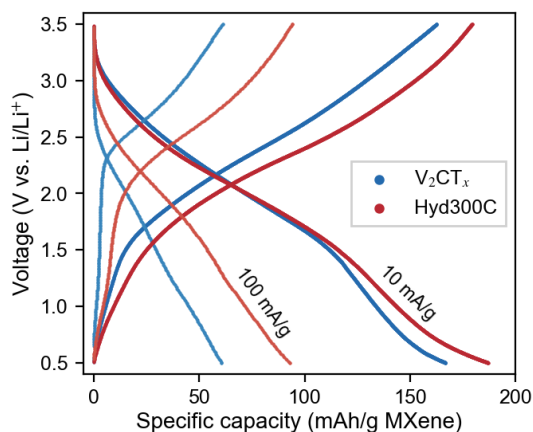


Figure 4.6: Voltage profiles of electrodes from V_2CT_x before and after hydrolysis at 300 °C cycled at two different current densities. Reproduced from Ref.²⁴⁵ under the Creative Commons Licence [CC BY 4.0](https://creativecommons.org/licenses/by/4.0/).

4.4 Paper III: Gas hydrolysis of $\text{Ti}_3\text{C}_2\text{T}_x$

4.4.1 Overview

In Paper III, gas hydrolysis was studied on the $\text{Ti}_3\text{C}_2\text{T}_x$ MXene to investigate if it would allow for similar F-termination substitution in this MXene phase. Initially, it was performed similar to Paper II, with gas hydrolysis of pristine HF-etched $\text{Ti}_3\text{C}_2\text{T}_x$ MXene. However, no reduction in F-terminations was observed, although DFT calculations indicated that hydrolysis should be thermodynamically feasible. Suspecting the absence of hydrolysis was due to lack of water insertion into the MXene, additional experiments were conducted after increasing the interlayer spacing of $\text{Ti}_3\text{C}_2\text{T}_x$ by pre-intercalating various cations.

4.4.2 MXene synthesis

Highly pure $\text{Ti}_3\text{C}_2\text{T}_x$ MXene with a controlled particle size distribution was synthesised by etching the commercial $\text{Ti}_3\text{C}_2\text{T}_x$ MAX phase in a HF solution after ball milling. The purity was confirmed by the complete removal of Al content, and the absence of Ti_3AlC_2 XRD-reflections, after the etching step. All X-ray diffractograms were adjusted for sample displacement through structureless Pawley fitting using the $P6_3/mmc$ space group.

4.4.3 Gas hydrolysis on pristine $\text{Ti}_3\text{C}_2\text{T}_x$

As shown in Figure 4.7, the hydrolysis of the pristine HF-etched $\text{Ti}_3\text{C}_2\text{T}_x$ MXene resulted in minimal changes to the MXene phase prior to oxidation at higher temperatures. After hydrolysis at 300 °C, insignificant changes in XRD, Raman, FTIR, SEM and EDS were observed, indicating virtual phase stability at these conditions. However, at temperatures above 300 °C, hydrolysis resulted in the decomposition of the MXene phase into a mixture of TiO_2 anatase nanoparticles and disordered graphitic carbon, initiating at the edge surface of the MXene particles. After hydrolysis at 500 °C, the MXene phase was completely oxidised into a mixture of C and several TiO_2 phases. With respect to the aim of the investigation, it was concluded that the gas hydrolysis of pristine HF-etched $\text{Ti}_3\text{C}_2\text{T}_x$ MXene did not result in any reduction of F-terminations.

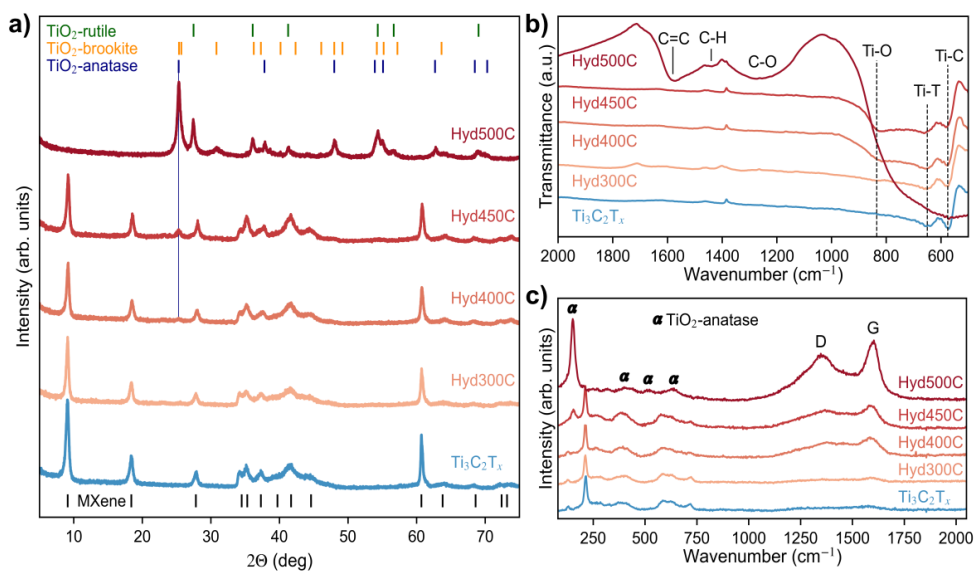


Figure 4.7: X-ray diffractograms (a), FTIR spectra (b) and Raman spectra (c) of $\text{Ti}_3\text{C}_2\text{T}_x$ MXene before and after hydrolysis at temperatures up to 500 °C. Reproduced from Paper III, which is accepted at the Elsevier journal FlatChem.

4.4.4 Gas hydrolysis on pre-intercalated $\text{Ti}_3\text{C}_2\text{T}_x$

As the interlayer spacing at 9.6 Å indicated a very dense packing of the MXene layers, cation intercalation prior to hydrolysis was attempted, to allow H_2O molecules to penetrate into the MXene structure and thereby react with the F-terminations. This was achieved by dispersing $\text{Ti}_3\text{C}_2\text{T}_x$ MXene powder in hydroxide solutions, which resulted in spontaneous intercalation of either K^+ , Na^+ , Li^+ , or TBA^+ . Mg^{2+} intercalation was achieved through subsequent ion substitution in a MgCl_2 solution. As shown in Figure 4.8, this resulted in significantly expanded interlayer spacings in the MXene, which was attributed to the joint intercalation of cations, hydroxide anions and one or two layers of water molecules. This expansion was denoted as a "pillaring" of the MXene structure. However, upon hydrolysing the pre-intercalated $\text{Ti}_3\text{C}_2\text{T}_x$ at 300 °C, some of the cations were either dehydrated and/or deintercalated, resulting in a collapse of the MXene pillaring. As shown in Figure 4.8b, the hydrolysis of these MXenes resulted in negligible F-reduction, which was ascribed to H_2O still being unable to enter the MXene structure. The K- and Na-intercalated $\text{Ti}_3\text{C}_2\text{T}_x$ MXene on the other hand remained stable during hydrolysis and demonstrated significant F reduction after the hydrolysis. Compared to the pristine $\text{Ti}_3\text{C}_2\text{T}_x$ the K- $\text{Ti}_3\text{C}_2\text{-Hyd}$ and Na- $\text{Ti}_3\text{C}_2\text{-Hyd}$ samples demonstrated 64

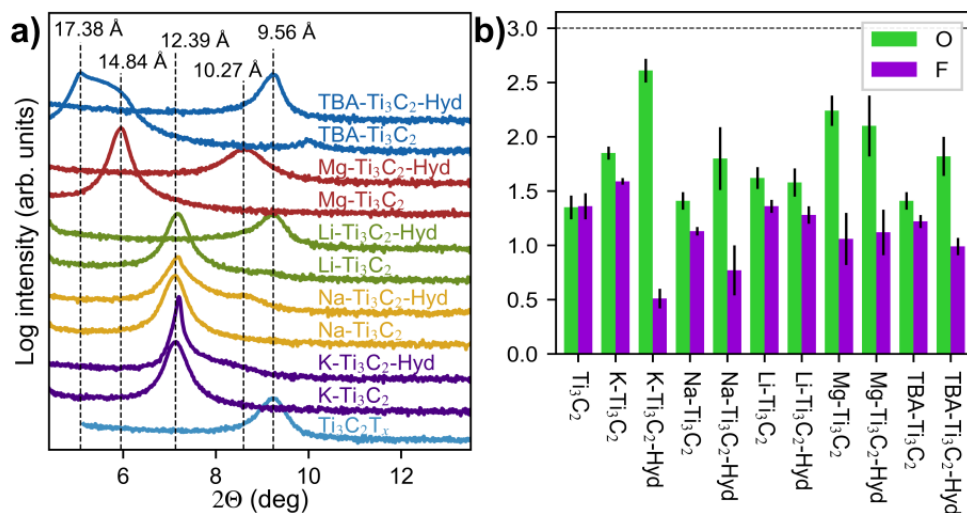


Figure 4.8: X-ray diffractograms (a) and EDS point scan averages (b) of $\text{Ti}_3\text{C}_2\text{T}_x$ before and after intercalation of various cations and the consecutive hydrolysis at $300\text{ }^\circ\text{C}$. The dashed line in (b) illustrates a Ti amount of 3 and the error bars represent the standard deviation from the set of point scans used for each sample. Adapted from Paper III, which is accepted at the Elsevier journal FlatChem.

% and 45 % less F content, respectively, with a comparable increase in O content. By increasing the hydrolysis time from 15 h to 50 h for the K- Ti_3C_2 sample a total F reduction of 78 % was achieved. Seeing that no signs of oxidation were observed in SEM, XRD, Raman or FTIR, these compositional changes were ascribed to changes in the termination groups. The substitution of termination groups was also shown to significantly shift the vibrational modes of the MXene in both Raman and FTIR spectra, matching well with expectations for less F-terminations.^{257–259} Additionally, the importance of water vapour was verified, as the annealing of K- Ti_3C_2 in dry Ar gas resulted in insignificant changes in the F content.

4.4.5 Electrochemical evaluation of K- Ti_3C_2 electrodes in LiBs

To investigate the change in electrochemical performance upon hydrolysing the MXene, electrodes from $\text{Ti}_3\text{C}_2\text{T}_x$, K- Ti_3C_2 and K- $\text{Ti}_3\text{C}_2\text{-Hyd}$ were charged and discharged at different current densities. The capacities shown in Figure 4.9a demonstrate how the intercalation of K- and OH-ions resulted in a significant capacity reduction from the pristine $\text{Ti}_3\text{C}_2\text{T}_x$, which is similar to what has been reported for K-intercalated $\text{Ti}_3\text{C}_2\text{T}_x$ in SiBs.²²⁸ However, the hydrolysis resulted in a slight capacity increase, which was

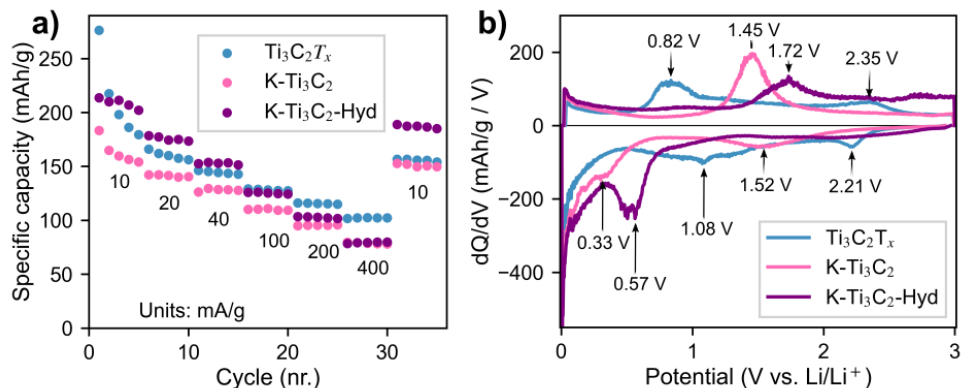


Figure 4.9: Electrochemical performance of $\text{Ti}_3\text{C}_2\text{T}_x$, $\text{K-Ti}_3\text{C}_2$ and $\text{K-Ti}_3\text{C}_2\text{-Hyd}$ electrodes, illustrated by delithiation capacities upon galvanostatic discharge and charge cycles at various current densities (a) and differential capacity plots from cycle number 3 (b). The negative values in the dQ/dV plot represent delithiation and positive values represent lithiation. Adapted from Paper III, which is accepted at the Elsevier journal FlatChem.

attributed to a lower amount of F- and OH-terminations that can irreversibly react with the intercalated Li-ions.^{32,33} Additionally, it was found that the $\text{K-Ti}_3\text{C}_2\text{-Hyd}$ electrodes resulted in the worst capacity retention upon increasing the current density. This was ascribed to changes in stacking upon hydrolysis, which is found to greatly influence the migration barriers for ion intercalation.³⁴ In Figure 4.9b, differential capacity plots from cycle 3 are presented for all electrodes, and they demonstrate how the lithiation and delithiation peaks shift significantly upon K-intercalation and the following hydrolysis. In general, it shows that the intercalation of K-ions results in a downward shift of the lithiation peaks and an upward shift of the delithiation peaks, leading to higher energy inefficiencies compared to the pristine $\text{Ti}_3\text{C}_2\text{T}_x$. This was also true for the $\text{K-Ti}_3\text{C}_2\text{-Hyd}$ sample, but after hydrolysis both peaks were shifted to higher voltages, which was as expected with a higher number of O-terminations (Section 2.2.4).

4.4.6 Thermal stability of $\text{Ti}_3\text{C}_2\text{T}_x$

Furthermore, the thermal stability of pristine HF-etched $\text{Ti}_3\text{C}_2\text{T}_x$ in various atmospheres was also investigated, and the hydrolysis was especially compared to the annealing in dry synthetic air, as shown in Figure 4.10. It was shown that the $\text{Ti}_3\text{C}_2\text{T}_x$ phase oxidises at lower temperatures in an O_2 containing atmosphere compared to in humid Ar gas, as a complete oxidation to TiO_2 phases occurred after air annealing at 400 °C, compared to 500 °C for hydrolysis. Additionally, air annealing was demonstrated to have an inferior

selectivity towards F removal compared with hydrolysis. Whereas hydrolysis resulted in an almost complete removal of F upon decomposition of the MXene phase, a TiOF_2 phase was formed during annealing in air, preserving more than 30 % of the F content. Similar results have also been reported for the annealing in pure O_2 atmospheres.²⁶⁰ However, regarding the oxidation of C, air annealing was much more efficient. While the hydrolysis preserved most of the C content even after complete decomposition of the MXene phase, annealing in air resulted in the removal of more than 70 % of the initial C content. As seen in Figure 4.10c and d, the morphology of the oxidised samples also dif-

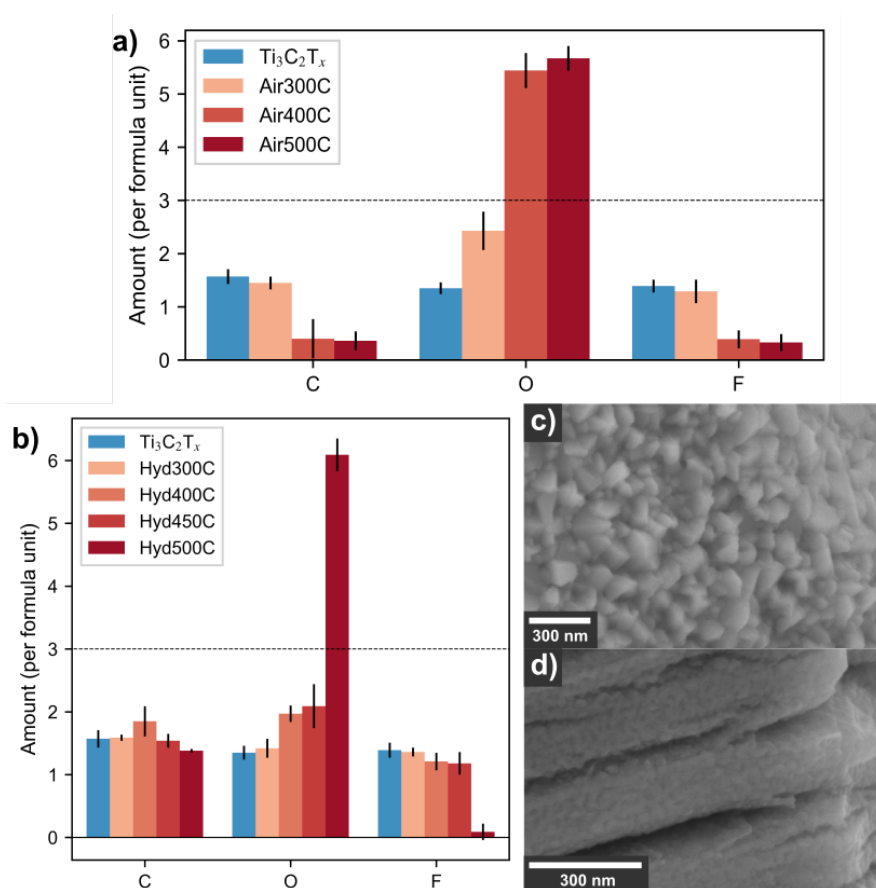


Figure 4.10: Comparison of annealing in dry synthetic air ("Air") and in humid Ar gas ("Hyd") at various temperatures, showing EDS average point scan values for Air (a) and Hyd (b) as well as high magnification SEM micrographs of Air (c) and Hyd (d) after annealing at 500 °C. The dashed lines in (a) and (b) illustrate a Ti amount of 3 and the error bars represent the standard deviation from the set of point scans used for each sample. Adapted from Paper III, which is accepted at the Elsevier journal FlatChem.

ferred significantly after annealing at 500 °C, where hydrolysis preserved the layered structure while air annealing resulted in a complete transformation into > 100 nm sized TiO₂ crystallites.

4.4.7 Cycling results of oxidised Ti₃C₂T_x MXene (not published)

Noteworthy, when cycled in LiB half cells, the oxidation of Ti₃C₂T_x MXene into a TiO₂/C composite upon hydrolysis resulted in significantly increased capacities compared to the pristine MXene (Figure 4.11). This is ascribed to Li-storage in the TiO₂ nanoparticles, based on the faradaic peaks at around 2 V in the differential capacity plots (Figure 4.11c),²⁶¹ in combination with a carbon conductive network to allow for

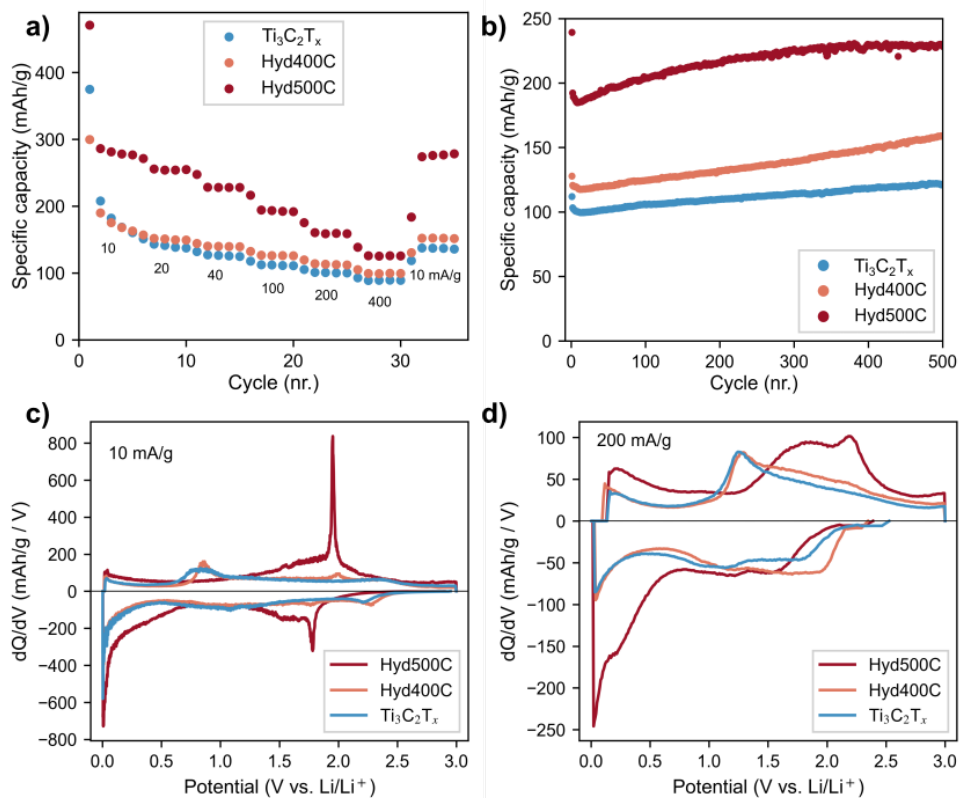


Figure 4.11: Rate performance (a), long term cycling (b) and differential capacity plots from cycles at low (c) and high (d) current densities of electrodes from pristine Ti₃C₂T_x MXene and Ti₃C₂T_x after hydrolysis at 400 °C and 500 °C. (c) and (d) are from cycle 3 and 23 in (a), respectively.

fast electron transport. Although similar composite electrodes are already well studied in LiBs, the results presented here demonstrate significantly higher capacities.^{229,262,263} With specific capacities as high as 270 mAh/g at low current densities (20 mA/g) and 210 mAh/g at a current density of 200 mA/g, the Hyd500C electrodes demonstrate more than 20 % higher capacities than the composites in the above-mentioned reports. The improved performance is ascribed to the hydrolysis being less selective towards C removal compared to other oxidation methods. With a more preserved carbon conductive network, more TiO₂ nanoparticles become accessible and give rise to an increased capacity of the composite electrode. The enhanced capacity may also be explained by Li being able to react with more C, which is demonstrated by the high capacities at voltages below 0.7 V vs. Li/Li⁺. Nonetheless, these composites will need to be improved significantly if they are to compete with state-of-the-art TiO₂ electrodes produced from simpler synthesis routes.²⁶⁴

4.5 F-free etching in alkaline solutions

4.5.1 Etching of the Ti_3AlC_2 MAX phase

Additional to the published work, it has been attempted to reproduce the F-free etching of the Ti_3AlC_2 MAX phase, reported by Li et al.,⁴⁵ in addition to investigating the methods' compatibility with other MAX phases. By hydrothermal etching in 50 wt. % NaOH solutions at 270 °C, successful exfoliation of the Ti_3AlC_2 MAX phase was confirmed by the results presented in Figure 4.12. In Figure 4.12a, the commonly observed shift of the (002) reflection is presented, in addition to the (hkl) marking of all MXene related reflections obtained from the structureless Pawley fitting to the $P6_3/mmc$ space group. From the SEM images in Figure 4.12b and c, it is shown that the layered morphology of the particles remain relatively intact, although the surface is rougher than what is commonly observed after HF etching. Nonetheless, as the TEM images in Figure 4.12d display the layered nanostructure of the $\text{Ti}_3\text{C}_2\text{T}_x$ sheets, successful MXene formation is verified. As shown in Figure 4.12e, the etching resulted in an average interlayer spacing of 12.04 Å, which matches well with what was observed after the intercalation of Na-ions in HF-etched $\text{Ti}_3\text{C}_2\text{T}_x$ (Figure 4.8). The significantly broader (002) reflection of the alkaline etched $\text{Ti}_3\text{C}_2\text{T}_x$ does however indicate a less defined/ordered interlayer spacing, as the FWHM of the peak covers interlayer spacings between 11.1 Å to 13.2 Å. This variation is attributed to various amounts of water molecules being intercalated in different parts of the particles. Indeed, after vacuum annealing for 12 h at 400 °C, the (002) reflection shifted to an average interlayer spacing of 10.4 Å, which also match well with the dehydration observed for the Na-intercalated $\text{Ti}_3\text{C}_2\text{T}_x$ upon hydrolysis at 300 °C (Figure 4.8). In total, these results demonstrate successful synthesis of Na-intercalated $\text{Ti}_3\text{C}_2\text{T}_x$ MXene through hydrothermal etching in a 50 wt. % NaOH solution.

However, it should also be pointed out that the alkaline etching also results in MXene impurities and formation of secondary phases, as illustrated by the results presented in Figure 4.13. First of all, a comparison of the FTIR spectra for HF- Ti_3C_2 and Alk- Ti_3C_2 demonstrates significant differences between the two phases. For the alkaline etched MXene it shows a significant absorption band below 1000 cm^{-1} , which can be ascribed to titanium oxide vibrations and resemble what was observed for the completely oxidised $\text{Ti}_3\text{C}_2\text{T}_x$ after gas hydrolysis or air annealing at 500 °C (Figure 4.7b). The Alk- Ti_3C_2 phase also resulted in a broad absorption band at $\sim 3300 \text{ cm}^{-1}$ and $\sim 1700 \text{ cm}^{-1}$, which is ascribed to O-H stretching and bending modes and originates from OH-terminations and intercalated water between the MXene layers. Furthermore, the SEM micrographs

in Figure 4.13b and c demonstrate how the alkaline etching resulted in the formation of several new particle morphologies, such as flower-like and cracked octahedrons. As the X-ray diffractogram in Figure 4.12a did not show any signs of impurities, it is assumed that the crystallite sizes of these impurities are too small to be detected by XRD. Sim-

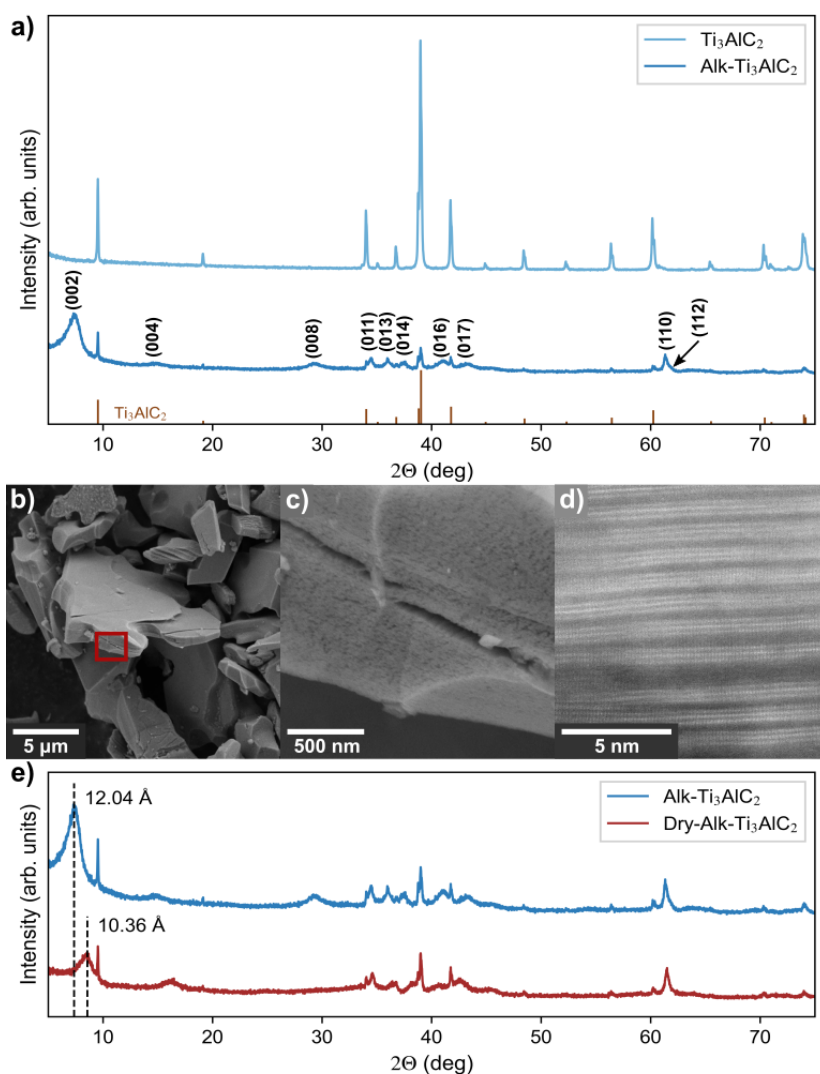


Figure 4.12: Proof of MXene formation after the hydrothermal alkaline etching of the Ti_3AlC_2 MAX phase, showing X-ray diffractograms before and after etching (a), SEM and TEM micrographs at various magnifications (b-d) and X-ray diffractograms of $\text{Alk-Ti}_3\text{AlC}_2$ before and after drying at 400°C for 12 h under vacuum. Figure (c) displays a magnified version of the red area in figure (b), and the PDF number for the Ti_3AlC_2 phase is 04-012-0632.

ilar morphologies have been reported for various controlled oxidations of the MXene phase, and thus support the partial oxidation of the MXene phase upon etching under these conditions.^{265,266} Comparable to previous reports, the EDS point scan averages presented in Figure 4.13d indicate that these particles are composed of sodium titanate ($\sim\text{Na}_2\text{Ti}_6\text{O}_{13}$).^{265,266} Additionally, the Raman spectra of these new particles differ significantly from the HF-MXene particles, as indicated by Figure 4.13e. In the optical microscope, these flower-like particles were also found to be white, compared to the black MXene particles, suggesting a tetravalent oxidation state of the titanium atoms.²⁶⁷ Furthermore, the TEM EDS mapping presented in Figure 4.13f shows that the alkaline etching results in a number of voids in the bulk of the particles, as well as regions with incomplete Al exfoliation. The incomplete Al exfoliation is also demonstrated by the remaining Ti_3AlC_2 reflections in the XRD spectra after etching. As an increased etching time did not result in notably enhanced etching yield, the method seems to be unable to completely etch all regions of the MAX phase. Hence, these results demonstrate an inferior control of the Al-removal by this alkaline etching method compared to HF etching.

Another challenge with this hydrothermal etching method is to prevent oxidation of the autoclave in the harsh etching environments that are used. In this work, significant Ni impurities (> 0.1 at. %) were measured by EDS and some Ni nanoparticles were even observed in the TEM EDS mapping after etching. This is assumed to come from oxidation of the steel autoclave that was used, as the alloy probably consisted of Ni. To prevent such impurities, utilisation of stable autoclaves would therefore be required.

Nonetheless, most of the results presented in Figure 4.13 also demonstrate successful MXene formation with interesting changes compared to the HF etched $\text{Ti}_3\text{C}_2\text{T}_x$. For the MXene related FTIR peaks in Figure 4.13a, the Alk- Ti_3C_2 phase shows significant shifts of the Ti-T and Ti-C peaks to 698 cm^{-1} and 615 cm^{-1} , respectively. These shifts are ascribed to changes in termination groups,²⁵⁸ and match well with what was observed after hydrolysis of K-intercalated $\text{Ti}_3\text{C}_2\text{T}_x$ in Paper III. Additionally, it should be noted that although significant amounts of impurity particles were observed, the majority of the particles showed a layered particle morphology with an EDS spectra indicating almost complete Al exfoliation and a MXene free of F-terminations, in addition to a similar amount of Na as the Na- Ti_3C_2 presented in Paper III. Furthermore, the Raman spectra from a layered Alk- Ti_3C_2 particle in Figure 4.13e demonstrates significant peak shifts compared with the HF etched counterpart. These shifts also resemble the shifts observed after hydrolysis of K-intercalated $\text{Ti}_3\text{C}_2\text{T}_x$ in Paper III, and are attributed to the lack of F-terminations and the increased number of O-terminations.^{257,259}

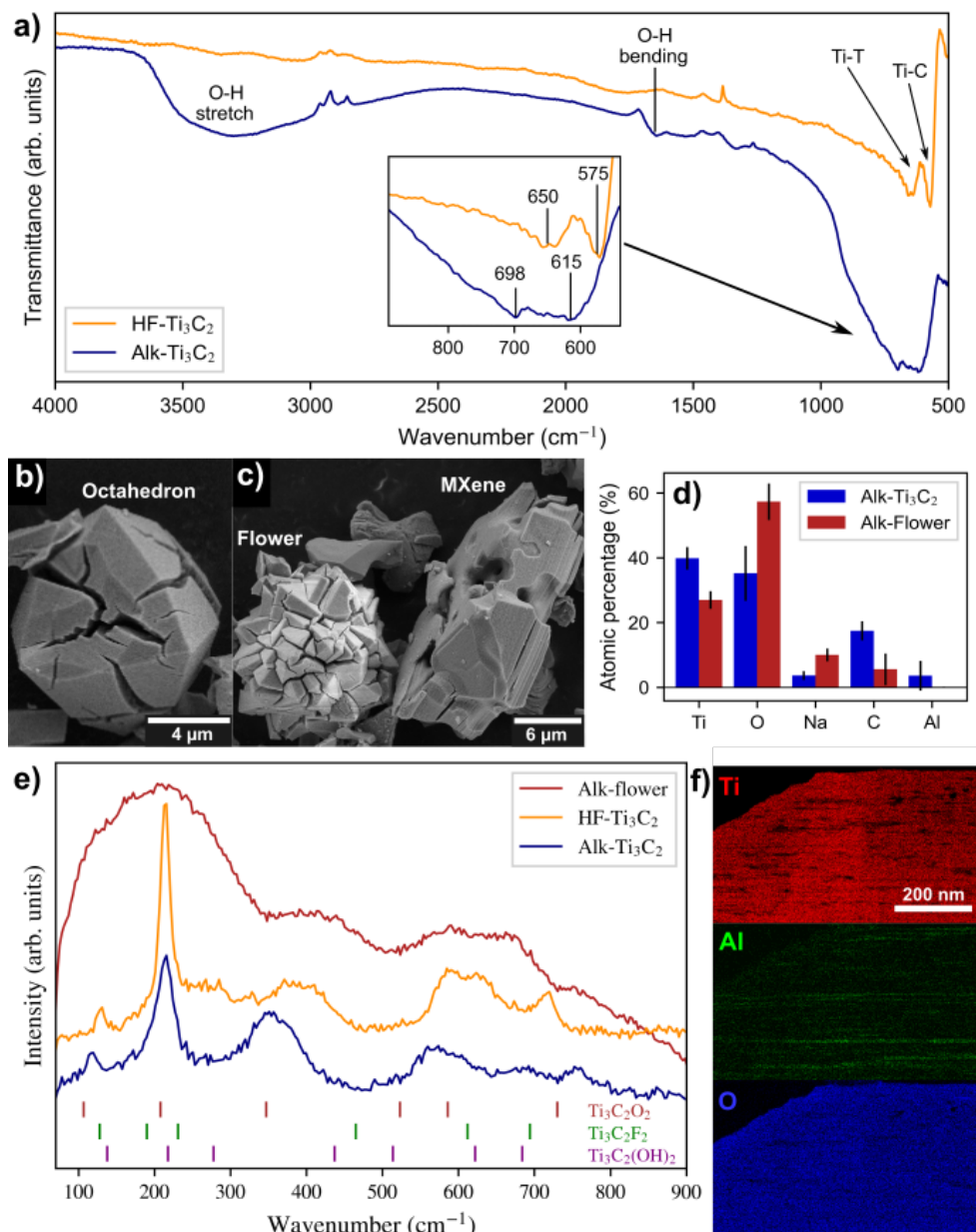


Figure 4.13: Additional characterisation of the Alk- Ti_3C_2 MXene compared to HF-etched $\text{Ti}_3\text{C}_2\text{T}_x$ MXene, showing FTIR spectra (a), SEM micrographs of different particle morphologies (b,c), EDS point scan averages of the different particle types with standard deviations (d), Raman spectra (e) and TEM EDS mapping of Ti, Al and O (f).

4.5.2 Alkaline etching of other MAX phases

As the hydrothermal alkaline etching method resulted in successful MXene formation for the Ti_3AlC_2 MAX phase, the method was also applied on the following MAX phases: Ti_2AlC , Ti_2AlN , Ti_3AlCN , $\text{TiMo}_2\text{AlC}_2$, Nb_4AlC_3 , Nb_2AlC , V_2AlC and V_4AlC_3 . This was done using the same etching conditions as for the Ti_3AlC_2 phase, in order to evaluate how these MAX phases responded to similar etching conditions. In Figure 4.14, X-ray diffractograms of the MAX phases with Ti-Al bonds (Ti_2AlC , Ti_2AlN and Ti_3AlCN) both before and after the alkaline etching are presented. Common to all compounds was a significant reduction of the MAX phase reflections upon etching, accompanied by the formation of a few new reflections. As the analysis software was unable to match these reflections with any plausible impurity phases, and due to the similarity of the broad (002) reflection to the Alk- Ti_3C_2 sample, these reflections might be related to the formation of MXenes. However, due to the low intensity of these reflections, it seems unlikely that MXenes of high purity/order are obtained from these etching conditions.

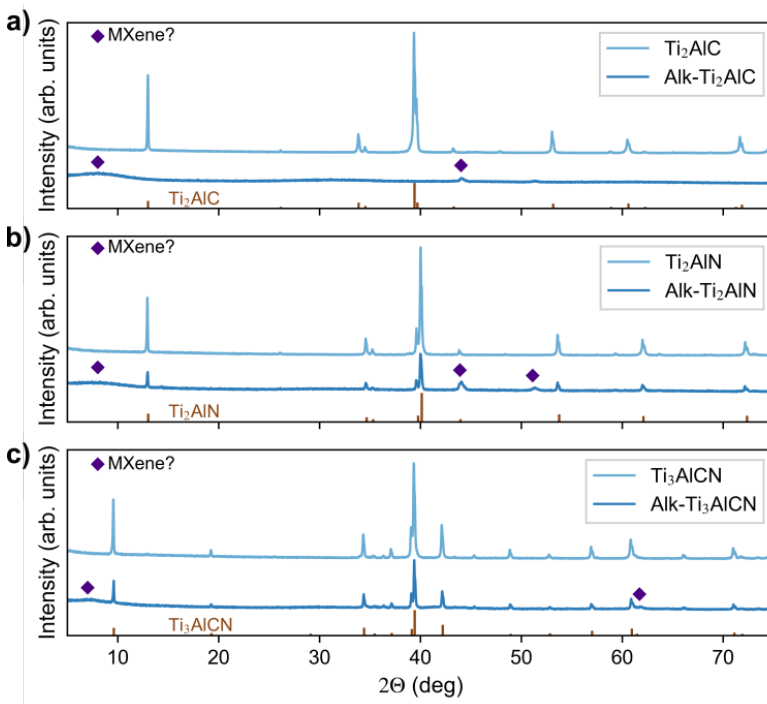


Figure 4.14: X-ray diffractograms of the Ti_2AlC (a), Ti_2AlN (b) and Ti_3AlCN (c) MAX phases before and after alkaline etching, where the purple diamonds indicate possible MXene-related reflections. The PDF numbers for the different phases are: 04-001-6044 for Ti_2AlC , 00-055-0434 for Ti_2AlN and 04-023-0983 for Ti_3AlCN .

From SEM micrographs of the Alk-Ti₂AlC powder (Figure 4.15), it was found that the alkaline etching resulted in the formation of similar particle morphologies to the impurities found for Alk-Ti₃AlC₂. In addition to the flower and octahedron morphologies, the Alk-Ti₂AlC powder also displayed particles with a bubble-cluster like morphology as well as other geometric shapes. In total, the amount of layered particles after etching was much less than after the etching of Ti₃AlC₂, which indicate an increased oxidation of the Ti₂AlC MAX phase under similar etching conditions. Interestingly, the EDS point scan measurements did not show any significant differences between the various particle morphologies, and demonstrated an almost complete removal of the C content in all of the measured particles. These results therefore oppose the possible formation of Ti₂C MXene from these etching conditions, and indicate that most of the MAX phase has been completely oxidised during the alkaline etching. Based on the EDS measurements, the stoichiometry of these oxidation products match reasonably well with the secondary phases formed for Alk-Ti₃AlC₂.

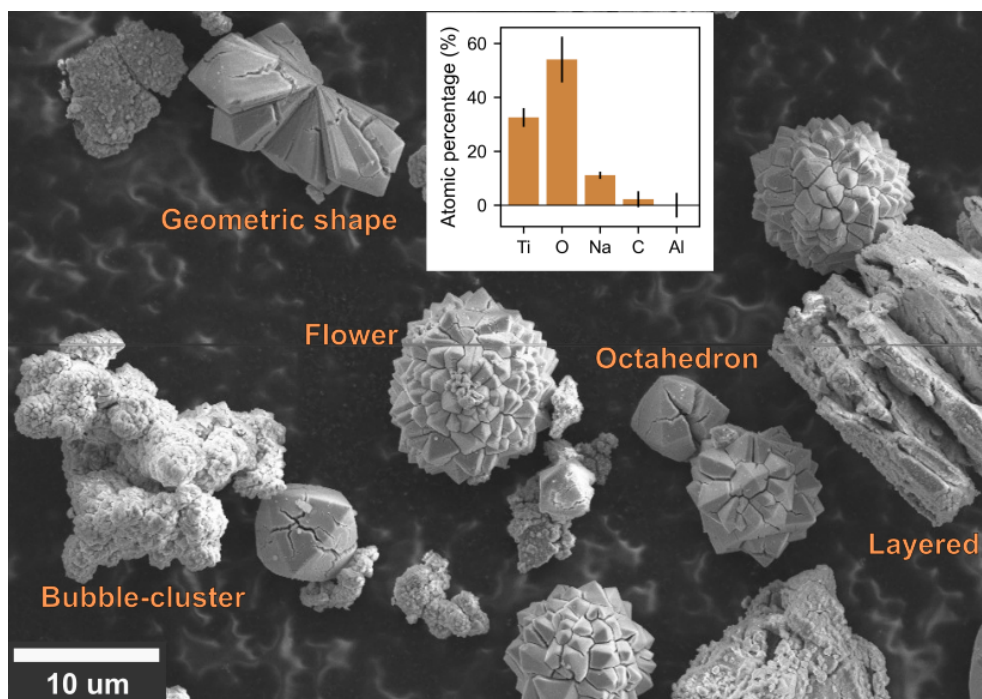


Figure 4.15: SEM micrograph of the Ti₂AlC MAX phase after alkaline etching showing various particle morphologies. The inset shows the average EDS point scan values obtained from different particles.

Furthermore, X-ray diffractograms of the $\text{TiMo}_2\text{AlC}_2$, V_2AlC and V_4AlC_3 MAX phases before and after alkaline etching are presented in Figure 4.16. It shows that all of the phases remain virtually unchanged after the alkaline etching, although the $\text{TiMo}_2\text{AlC}_2$ and V_4AlC_3 phases show an increased amount of TiC and VC, respectively. Considering that the etching of both of these phases resulted in a yield of 32 wt. %, the increased carbide amount after etching can be ascribed to a reduction of the MAX phases. For the V_2AlC MAX phase, the particles were completely dissolved in the NaOH solution upon etching, which based on its yellow colour indicates V in a pentavalent state.²⁶⁸ Figure 4.16c therefore displays the diffractogram measured after etching the phase at a reduced temperature of 200 °C. Similar to the above-mentioned MAX phases, it shows no significant changes after etching. It was also attempted to reduce the NaOH concentration to 5 M (at 270 °C), but this also resulted in the complete dissolution of the MAX phase.

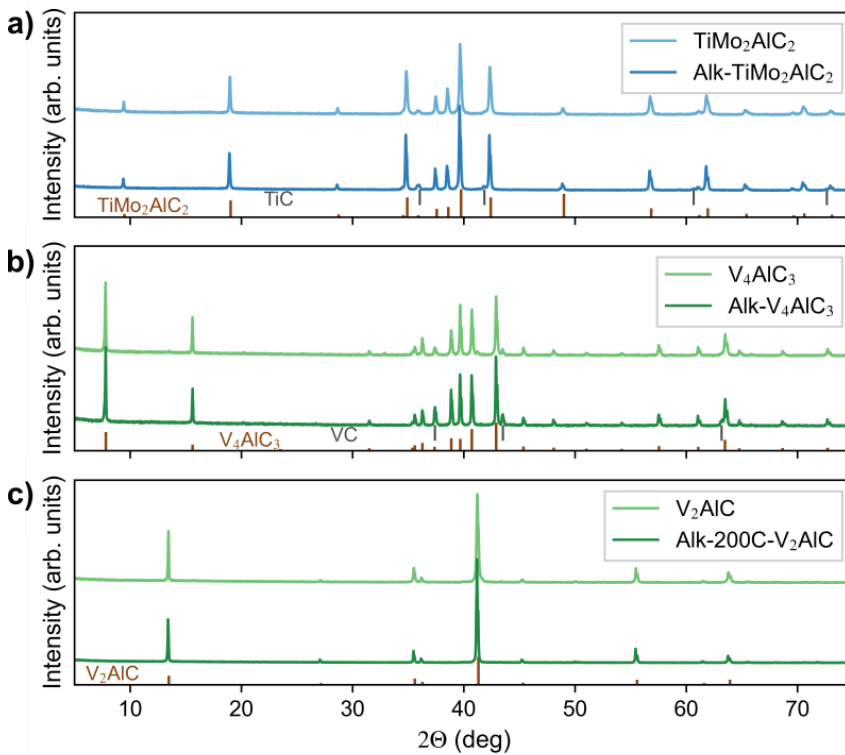


Figure 4.16: X-ray diffractograms of the $\text{TiMo}_2\text{AlC}_2$ (a) V_4AlC_3 (b) and V_2AlC (c) MAX phases before and after alkaline etching, where the V_2AlC was etched at a reduced temperature of 200 °C. The PDF numbers for the different phases are: 04-022-3612 for $\text{TiMo}_2\text{AlC}_2$, 01-089-3828 for TiC, 04-016-1947 for V_4AlC_3 , 04-004-6859 for VC and 04-005-0048 for V_2AlC .

In general, none of these phases displayed any signs of (002) MXene reflections at lower 2θ values, and these results thus indicate that the alkaline etching conditions tested here were unable to form MXenes from the $\text{TiMo}_2\text{AlC}_2$, V_2AlC and V_4AlC_3 MAX phases.

Unlike the above-mentioned MAX phases, the Nb_4AlC_3 , Nb_2AlC MAX phases showed complete transformations after the alkaline etching, as presented by the X-ray diffractograms in Figure 4.17. They display a complete oxidation of the MAX phases upon etching, to form a NaNbO_3 phase with high crystallinity. With this phase transition, the powder also changed colour from black to grey. These etching conditions thus seems to be too oxidising for a controlled Al-exfoliation of the Nb-based MAX phases.

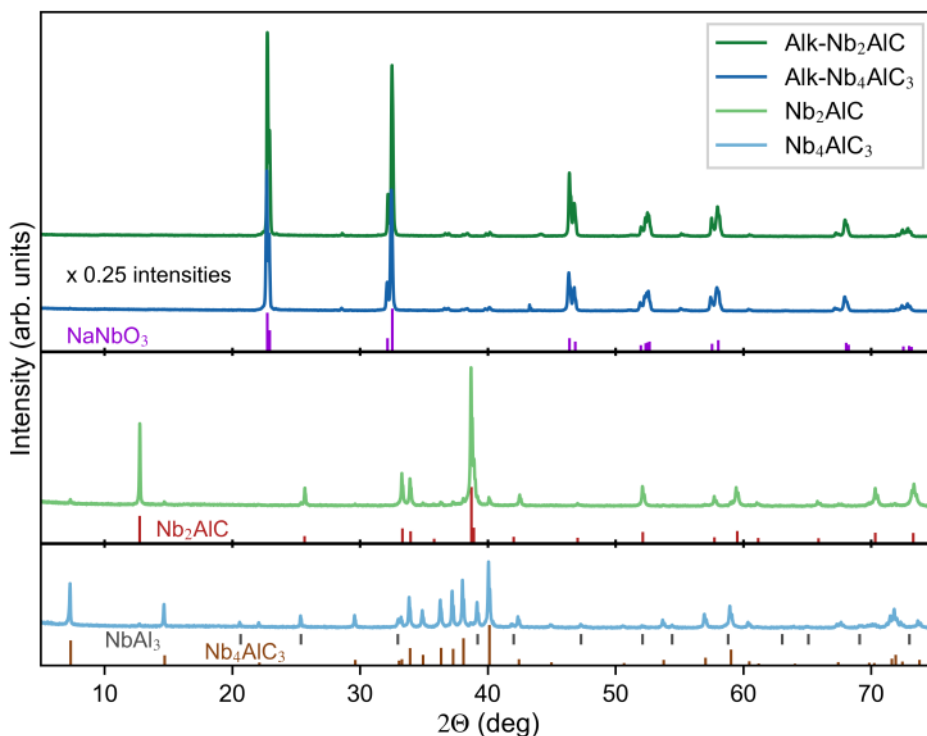


Figure 4.17: X-ray diffractograms of the Nb_4AlC_3 and Nb_2AlC MAX phases before and after alkaline etching. The PDF numbers for the different phases are: 00-033-1270 for NaNbO_3 , 04-001-6045 for Nb_2AlC , 04-015-4176 for Nb_4AlC_3 and 04-001-3168 for NbAl_3 .

4.5.3 Summary of alkaline etching results

The results from the alkaline etching on the different MAX phases is summarised in Table 4.1. This table also includes the etching yields obtained by measuring the mass of the dry powder before and after the etching, and shows that there are significant variations between the different MAX phases. In total, Ti_3AlC_2 was the only MAX phase that demonstrated formation of significant MXene by the alkaline etching conditions tested here. However, although these results give an indication to the feasibility of this method for the etching of various MAX phases, a limited set of etching conditions have been investigated. By adjusting the NaOH concentration, the temperature, the pressure and/or the etching time, it is possible that improved results can be achieved for other MAX phases as well. Nevertheless, the poor compatibility with most MAX phases demonstrated in this work might also explain why this etching method was reported by one group only, since first reported four years ago (Section 2.2.4). Considering that this group only has published work on alkaline etched Ti_3AlC_2 , the feasibility to use this method for other MAX phases remains to be proven. To the author's knowledge, this is the first report on the utilisation of hydrothermal alkaline etching on other MAX phases than Ti_3AlC_2 .

Table 4.1: Summary of the results from hydrothermal alkaline etching of the different MAX phases, using 50 wt. % NaOH and an etching temperature of 270 °C.

| MAX phase | Mass yield (%) | MXene? | Comment |
|-----------------------------|----------------|--------|--|
| Ti_3AlC_2 | 91 | Yes | Very disordered MXene |
| Ti_3AlCN | 85 | Maybe | Few layered particles remained |
| $\text{TiMo}_2\text{AlC}_2$ | 32 | No | Only relative increase in TiC amount |
| Ti_2AlC | 101 | Maybe | Almost all C content removed |
| Ti_2AlN | 93 | Maybe | Only XRD |
| Nb_2AlC | 100 | No | Complete oxidation into NaNbO_3 |
| Nb_4AlC_3 | 86 | No | Complete oxidation into NaNbO_3 |
| V_4AlC_3 | 32 | No | Only relative increase in VC amount |
| V_2AlC | 0 | No | Complete dissolution |

5

Conclusions and outlook

Introduction

Parts of this work has been related to the synthesis of F-free, multilayered MXene compositions and the investigation on how the change in termination affects the ion-intercalating properties of the MXene. The overall aim was to evaluate the feasibility of MXene electrodes in rechargeable batteries, and especially for RMBs and LiBs. In this chapter, a short presentation of the conclusions from each part will be presented, followed by personal perspectives on future outlooks.

Termination control of MXenes

Based on the calculated potential of O-terminations for ideal electrode performance, the goal was to synthesise F-free and ideally homogeneously O-terminated multilayered MXene particles. To achieve this, gas hydrolysis was chosen based on its theoretical promise compared to other oxidation methods, and was tested on two different MXene compositions: V_2CT_x and $Ti_3C_2T_x$. In Paper II and III it was proven that gas hydrolysis is an efficient method to remove F content, and that it prior to complete oxidation is able to reduce F-terminations by $\sim 70\%$ without significant oxidation. Furthermore, it was demonstrated that water is unable to penetrate into non-intercalated $Ti_3C_2T_x$ MXene, and that an increased interlayer spacing, by cation pre-intercalation (e.g. K^+ and Na^+), is required for successful hydrolysis. As gas hydrolysis has worked on both of the two studied MXenes so far, utilisation on other MXene compositions should also be explored. Furthermore, gas hydrolysis should be investigated on MXenes etched in fluoride salts, which results in less F-terminations than the HF-etching reported here. This would show whether a similar F-reduction could be obtained for already F-poor termination mixtures.

Although significant F-removal was achieved by gas hydrolysis, the composition of the resulting termination mixture was rather uncertain. For the V_2CT_x phase, insignificant changes in O content was measured by EDS, partly due to the overlap of V and O peaks. However, as the analysis of XPS results also demonstrated minimal O increase, it was speculated about the formation of partly unterminated V_2C MXene. For the $Ti_3C_2T_x$ phase, the comparative increase in O-content suggested that the F-terminations were substituted by O-containing terminations. Still, as it is impossible to separate between O- and OH-terminations by EDS, the true composition of the termination mixture remained uncertain. Even though high temperature annealing is expected to remove OH-terminations (Section 2.2.4), further characterisation by e.g. NMR would be required to determine the

true composition of the termination mixture after gas hydrolysis.^{211,212} Moreover, although no signs of significant oxidation was observed after gas hydrolysis at 300 °C, MXenes eventually form oxides even at room temperature.⁴⁰ Hence, the extent of surface oxidation during gas hydrolysis should be thoroughly investigated by surface sensitive methods such as XPS.

Considering the challenge of inserting water molecules during hydrolysis of the $\text{Ti}_3\text{C}_2\text{T}_x$ phase, it is possible that an increased interlayer spacing is a general requirement for post-etching termination change in multilayered MXene particles. Hence, several of the reaction mechanisms presented in Section 2.2.4 could prove effective on multilayered MXenes with expanded interlayer spacings. Due to the possibility of higher temperatures and continuous removal of reaction products, gas hydrolysis may prove a more optimal method than hydrothermal hydrolysis. However, as no previous efforts have been made towards controlled F-removal through this method, the potential of hydrothermal hydrolysis in inert atmospheres should be further evaluated. Moreover, H_2 annealing to form unterminated MXenes should be investigated, since it already has been demonstrated to remove O-terminations and generally improve the oxidation stability of delaminated MXene thin films.^{230,244} With the oxidation of $\text{Ti}_3\text{C}_2\text{T}_x$ being slower in alkaline environments,^{45,235} OH substitution of F-terminations in concentrated alkaline solutions would be interesting, as demonstrated by Equation 2.10. As an example, the alkaline etching results in Section 4.5 show how the $\text{Ti}_3\text{C}_2\text{T}_x$ MXene remains relatively stable at 270 °C in a 50 wt. % NaOH solution, and by increasing the concentration, even less oxidation is to be expected.⁴⁵

Even though one of the main motivations for post-etching treatments was the possibility for scalable production of termination controlled MXenes, most of the methods presented here may not be scalable. As an example, this work has presented gas hydrolysis on < 0.3 g batches in a closed environment for 15 h, which clearly illustrates how the scalability must be validated for this method to be viable for large-scale production of F-free MXenes. Although the Lewis acid method described in Section 2.2.4 also remains unpractical for large-scale applications, it has demonstrated the possibility to form homogeneously terminated MXenes with several different terminations (e.g. bare, S, Br, Cl, O). This again makes it the best method to date for investigating the properties that can be obtained with controlled termination groups. So far, this method has also been demonstrated to produce several different MXene compositions, such as $\text{Ti}_3\text{C}_2\text{T}_x$, Ti_2CT_x , $\text{Ti}_4\text{C}_3\text{T}_x$, Ti_3CNT_x , Nb_2CT_x and Ta_2CT_x .^{155,156,216,221} Although it currently remains inapplicable for some MXene phases (e.g. V_2CT_x),¹⁵⁶ it will most likely be the most utilised method for termination control in the near future.

In comparison, the hydrothermal alkaline etching method presented in Section 4.5 was shown to successfully form F-free $\text{Ti}_3\text{C}_2\text{T}_x$. However, with a 12 h etching in 50 wt. % NaOH solution at 270 °C, it was not found to form significant amounts of MXenes from any of the Ti_2AlC , Ti_2AlN , Ti_3AlCN , $\text{TiMo}_2\text{AlC}_2$, Nb_4AlC_3 , Nb_2AlC , V_2AlC or V_4AlC_3 MAX phases. Hence, these results suggest a possible limitation to the compatibility of this etching method, as it currently only has been demonstrated for one MXene composition. As the hydrothermal etching also resulted in structurally disordered $\text{Ti}_3\text{C}_2\text{T}_x$ MXene particles with a large amount of impurities, in addition to a non-homogeneous mixture of O/OH-terminations, the quality of the obtained MXene was inferior to what has been reported for the Lewis acid etching method.

MXene electrodes for rechargeable batteries

The overall aim of this project was to investigate the feasibility of MXene electrodes for rechargeable batteries, and in particular as cathodes in RMBs. Based on the theoretically predicted importance of MXenes' termination groups, most of the focus in this work was directed towards controlling the termination groups, as already discussed above. In LiB electrodes, it was found that the substitution of F-terminations into partly O-, OH- and unterminated MXene resulted in some changes in intercalation voltage, capacity, rate-capability and energy efficiency. Nonetheless, the magnitude of these effects did not match the theoretical predictions, which may be a result of the many different parameters that are involved. As an example, it was recently shown by Hadler-Jacobsen et al. that the stacking of the MXene sheets may have a greater impact on the ion migration barriers in multilayered particles than the termination groups.^{34,208} As the thermodynamically favourable stackings also depend on the mixture of termination groups, this illustrates the challenge of controlling single parameters when experimentally testing the ion-intercalation properties of MXenes. Considering the lack of homogeneous termination groups, and the general challenge of quantifying the true mixture of terminations, the control of the termination group mixture would require further optimisation. Hence, no clear conclusion on the termination groups' effect on the intercalating properties of MXenes can be drawn.

Regarding the feasibility of MXene electrodes in general this work does not provide any clear conclusion. For RMBs, this work has shown that the reversible intercalation of Mg^{2+} ions in MXenes seems unlikely, as there will be a trade-off between low intercalation voltages, sluggish kinetics and/or irreversible reactions, similar to other RMB cathode materials (Section 2.1.3). In this work, reversible capacities < 5 mAh/g were

observed for all multilayered MXene compositions and electrolytes tested in RMBs, indicating minimal reversible intercalation of Mg-ions. While the reports discussed in Section 2.2.3 demonstrated reversible capacities > 50 mAh/g in RMB cells, this was based on high surface area electrodes and most likely co-intercalation of other electrolyte components. Even if they were demonstrating reversible Mg-ion intercalation, their low capacities and average voltages still leave them uncompetitive with respect to state-of-the-art cathode materials. Consequentially, there has been no further reports on Mg-intercalation in MXenes after that. Hence, the current results generally indicate that MXenes are not feasible as cathode materials for RMBs. However, with the vast chemical and structural possibilities that MXenes offer, and the continuous improvements on how to control them (e.g. Lewis acid etching), a general conclusion about the feasibility of MXene cathodes for RMBs cannot be drawn at this stage. As concluded in Paper I, the most viable MXene composition for RMB cathodes, of the V_2CT_x and $Ti_3C_2T_x$ MXenes investigated, is homogeneously terminated, multilayered V_2CO_2 . Until such a MXene composition is verified and tested, the theoretical potential of RMB MXene cathodes remains unanswered.

In contrast to the limited Mg-intercalation, MXenes have been proven to reversibly intercalate a range of other ions, making them more useful for other battery chemistries. As discussed in Section 2.2.3, the gravimetric capacities of delaminated MXene films generally outperform those of the multilayered particles. However, until high areal and volumetric capacities can be achieved from such films, multilayered MXene particles remain the most relevant electrode material for high energy batteries. While significant reversible capacities have been demonstrated for a range of battery chemistries (e.g. Li-ion, Na-ion and K-ion), the generally sloped voltage profiles results in average voltages too high for competitive anode materials and too low for competitive cathode materials. However, MXenes have also demonstrated extremely fast rate-capabilities, making them highly interesting for high-power chemistries, such as alkali-ion capacitors. With the new possibilities to control the surface chemistry, it is also possible that the capability of MXene electrodes may improve significantly over the years to come. As an example, I- and Br-terminated MXenes have recently demonstrated distinct voltage plateaus in aqueous Zn-ion batteries, unlike the generally sloped voltage profiles reported for Cl- and O/OH/F-terminated MXenes.¹⁸⁹ Similarly, multilayered Ti_2NT_x with O- and Cl- terminations have also demonstrated a high reversible capacity of 303 mAh/g at 100 mA/g in LiBs, and a 52% capacity retention at 5 A/g,²⁶⁹ which is higher than previous reports on F-, OH- and O-terminated MXenes. This illustrates how the newly discovered termination groups may result in improved electrochemical performance of MXenes, making them more competitive electrode materials than they are today. Moreover,

the intercalation in MXenes is generally found to be more feasible in aqueous solutions, even for Mg^{2+} ions, making them suitable for aqueous supercapacitors with high power density, albeit low energy density.

Whereas the full potential of MXene electrodes remains unexplored, the currently reported performances makes it unlikely that MXenes will succeed any of the commonly used electrode materials in high-energy battery chemistries. However, with the interesting properties and the facile processing of MXenes, it is not unlikely that future commercial battery chemistries may contain MXenes. Perhaps not as the electrode material, but instead as a chemically binding electrical network, which may improve the performance of certain battery chemistries.

Bibliography

- [1] V. Masson-Delmotte, P. Zhai, A. Pirani, S. Connors, C. Péan, S. Berger, N. Caud, Y. Chen, L. Goldfarb, M. Gomis, M. Huang, K. Leitzell, E. Lonnoy, J. Matthews, T. Maycock, T. Waterfield, O. Yelekçi, R. Yu, and B. Zhou, *Climate Change 2021: The Physical Science Basis. Contribution of Working Group I to the Sixth Assessment Report of the Intergovernmental Panel on Climate Change*. Cambridge University Press, 2021.
- [2] E. Commission, “REPowerEU: affordable, secure and sustainable energy for Europe,” 2022. URL: <https://ec.europa.eu/info/strategy/priorities-2019-2024/european-green-deal/repowereu-affordable-secure-and-sustainable-energy-europe>, accessed: 22.09.2022.
- [3] IEA, “Net Zero by 2050,” *International Energy Agency*, 2021.
- [4] Henbest, Seb and Kimmel, Matthias and Callens, Jef and Vasdev, Amar and Brandily, Tifenn and Berryman, Ian and Danial, Josh and Vickers, Ben, “New Energy Outlook 2021,” 2021. URL: <https://about.bnef.com/new-energy-outlook/>, accessed: 24.08.2022.
- [5] IEA, “Global EV Outlook 2022,” *International Energy Agency*, 2022.
- [6] Bloomberg, “Lithium-ion Battery Market Size Worth \$182.53 Billion By 2030: Grand View Research, Inc.,” 2022. URL: <https://www.bloomberg.com/press-releases/2022-06-07/lithium-ion-battery-market-size-worth-182-53-billion-by-2030-grand-view-research-inc>, accessed: 24.08.2022.
- [7] D. Li, “Electric Vehicles to Drive Massive Battery Demand: BNEF Chart,” 2021. URL: <https://news.bloomberglaw.com/environment-and-energy/electric-vehicles-to-drive-massive-battery-demand-bnef-chart>, accessed: 26.09.2022.
- [8] M. Winter, B. Barnett, and K. Xu, “Before Li Ion Batteries,” *Chemical Reviews*, vol. 118, no. 23, pp. 11433–11456, 2018.
- [9] R. Schmuch, R. Wagner, G. Hörpel, T. Placke, and M. Winter, “Performance and cost of materials for lithium-based rechargeable automotive batteries,” *Nature Energy*, vol. 3, no. 4, pp. 267–278, 2018.
- [10] Bloomberg, “Battery Price Declines Slow Down in Latest Pricing Survey,” 2021. URL: <https://www.bloomberg.com/news/articles/2021-11-30/battery-price-declines-slow-down-in-latest-pricing-survey>, accessed: 25.08.2022.
- [11] M. S. Ziegler, J. Song, and J. E. Trancik, “Determinants of lithium-ion battery technology cost decline,” *Energy Environmental Science*, vol. 14, pp. 6074–6098, 2021.

- [12] BloombergNEF, "Battery Pack Prices Fall to an Average of \$132/kWh, But Rising Commodity Prices Start to Bite," 2021. URL: <https://about.bnef.com/blog/battery-pack-prices-fall-to-an-average-of-132-kwh-but-rising-commodity-prices-start-to-bite>, accessed: 25.08.2022.
- [13] Amnesty International, "Democratic Republic of Congo: "This is what we die for": Human rights abuses in the Democratic Republic of the Congo power the global trade in cobalt," 2016. URL: <https://www.amnesty.org/en/documents/afr62/3183/2016/en/>, accessed 26.09.2022.
- [14] Y.-K. Sun, "A Rising Tide of Co-Free Chemistries for Li-Ion Batteries," *ACS Energy Letters*, vol. 7, no. 5, pp. 1774–1775, 2022.
- [15] S. Dühnen, J. Betz, M. Kolek, R. Schmuch, M. Winter, and T. Placke, "Toward Green Battery Cells: Perspective on Materials and Technologies," *Small Methods*, vol. 4, no. 7, p. 2000039, 2020.
- [16] A. El Kharbachi, O. Zavorotynska, M. Latroche, F. Cuevas, V. Yartys, and M. Fichtner, "Exploits, advances and challenges benefiting beyond Li-ion battery technologies," *Journal of Alloys and Compounds*, vol. 817, p. 153261, 2020.
- [17] P. C. K. Vesborg and T. F. Jaramillo, "Addressing the terawatt challenge: scalability in the supply of chemical elements for renewable energy," *RSC Advances*, vol. 2, pp. 7933–7947, 2012.
- [18] Y. Liang, H. Dong, D. Aurbach, and Y. Yao, "Current status and future directions of multivalent metal-ion batteries," *Nature Energy*, vol. 5, no. 9, pp. 646–656, 2020.
- [19] M. Naguib, M. Kurtoglu, V. Presser, J. Lu, J. Niu, M. Heon, L. Hultman, Y. Gogotsi, and M. W. Barsoum, "Two-Dimensional Nanocrystals Produced by Exfoliation of Ti_3AlC_2 ," *Advanced Materials*, vol. 23, no. 37, pp. 4248–4253, 2011.
- [20] B. Anasori, M. R. Lukatskaya, and Y. Gogotsi, "2D metal carbides and nitrides (MXenes) for energy storage," *Nature Reviews Materials*, vol. 2, no. 2, p. 16098, 2017.
- [21] M. Naguib, V. N. Mochalin, M. W. Barsoum, and Y. Gogotsi, "25th Anniversary Article: MXenes: A New Family of Two-Dimensional Materials," *Advanced Materials*, vol. 26, no. 7, pp. 992–1005, 2014.
- [22] M. Naguib, J. Come, B. Dyatkin, V. Presser, P.-L. Taberna, P. Simon, M. W. Barsoum, and Y. Gogotsi, "MXene: a promising transition metal carbide anode for lithium-ion batteries," *Electrochemistry Communications*, vol. 16, no. 1, pp. 61–64, 2012.
- [23] M. Naguib, J. Halim, J. Lu, K. M. Cook, L. Hultman, Y. Gogotsi, and M. W. Barsoum, "New Two-Dimensional Niobium and Vanadium Carbides as Promising Materials for Li-Ion Batteries," *Journal of the American Chemical Society*, vol. 135, no. 43, pp. 15966–15969, 2013.
- [24] S. Kajiyama, L. Szabova, K. Sodeyama, H. Iinuma, R. Morita, K. Gotoh, Y. Tateyama, M. Okubo, and A. Yamada, "Sodium-Ion Intercalation Mechanism in MXene Nanosheets," *ACS Nano*, vol. 10, no. 3, pp. 3334–3341, 2016.
- [25] M. Naguib, R. A. Adams, Y. Zhao, D. Zemlyanov, A. Varma, J. Nanda, and V. G. Pol, "Electrochemical performance of MXenes as K-ion battery anodes," *Chemical Communications*, vol. 53, pp. 6883–6886, 2017.

- [26] A. VahidMohammadi, A. Hadjikhani, S. Shahbazmohamadi, and M. Beidaghi, "Two-Dimensional Vanadium Carbide (MXene) as a High-Capacity Cathode Material for Rechargeable Aluminum Batteries," *ACS Nano*, vol. 11, no. 11, pp. 11135–11144, 2017.
- [27] Y. Xie, Y. Dall'Agnese, M. Naguib, Y. Gogotsi, M. W. Barsoum, H. L. Zhuang, and P. R. C. Kent, "Prediction and Characterization of MXene Nanosheet Anodes for Non-Lithium-Ion Batteries," *ACS Nano*, vol. 8, no. 9, pp. 9606–9615, 2014.
- [28] C. Eames and M. S. Islam, "Ion Intercalation into Two-Dimensional Transition-Metal Carbides: Global Screening for New High-Capacity Battery Materials," *Journal of the American Chemical Society*, vol. 136, no. 46, pp. 16270–16276, 2014.
- [29] D. Er, J. Li, M. Naguib, Y. Gogotsi, and V. B. Shenoy, "Ti₃C₂ MXene as a High Capacity Electrode Material for Metal (Li, Na, K, Ca) Ion Batteries," *ACS Applied Materials & Interfaces*, vol. 6, no. 14, pp. 11173–11179, 2014.
- [30] O. Mashtalir, M. Naguib, V. N. Mochalin, Y. Dall'Agnese, M. Heon, M. W. Barsoum, and Y. Gogotsi, "Intercalation and delamination of layered carbides and carbonitrides," *Nature Communications*, vol. 4, no. 1, p. 1716, 2013.
- [31] M.-Q. Zhao, X. Xie, C. E. Ren, T. Makaryan, B. Anasori, G. Wang, and Y. Gogotsi, "Hollow MXene Spheres and 3D Macroporous MXene Frameworks for Na-Ion Storage," *Advanced Materials*, vol. 29, no. 37, p. 1702410, 2017.
- [32] Y. Xie, M. Naguib, V. N. Mochalin, M. W. Barsoum, Y. Gogotsi, X. Yu, K.-W. Nam, X.-Q. Yang, A. I. Kolesnikov, and P. R. C. Kent, "Role of Surface Structure on Li-Ion Energy Storage Capacity of Two-Dimensional Transition-Metal Carbides," *Journal of the American Chemical Society*, vol. 136, no. 17, pp. 6385–6394, 2014.
- [33] Q. Tang, Z. Zhou, and P. Shen, "Are MXenes Promising Anode Materials for Li Ion Batteries? Computational Studies on Electronic Properties and Li Storage Capability of Ti₃C₂ and Ti₃C₂X₂ (X = F, OH) Monolayer," *Journal of the American Chemical Society*, vol. 134, no. 40, pp. 16909–16916, 2012.
- [34] J. Hadler-Jacobsen and S. K. Schnell, "The Importance of Stacking and Coordination for Li, Na, and Mg Diffusion and Intercalation in Ti₃C₂T₂ MXene," *Advanced Materials Interfaces*, vol. 9, no. 17, p. 2200014, 2022.
- [35] H. Kaland, J. Hadler-Jacobsen, F. H. Fagerli, N. P. Wagner, Z. Wang, S. M. Selbach, F. Vullum-Bruer, K. Wiik, and S. K. Schnell, "Are MXenes suitable as cathode materials for rechargeable Mg batteries?," *Sustainable Energy Fuels*, vol. 4, pp. 2956–2966, 2020.
- [36] A. Byeon, M.-Q. Zhao, C. E. Ren, J. Halim, S. Kota, P. Urbankowski, B. Anasori, M. W. Barsoum, and Y. Gogotsi, "Two-Dimensional Titanium Carbide MXene As a Cathode Material for Hybrid Magnesium/Lithium-Ion Batteries," *ACS Applied Materials & Interfaces*, vol. 9, no. 5, pp. 4296–4300, 2017.
- [37] M.-Q. Zhao, C. E. Ren, M. Alhabeib, B. Anasori, M. W. Barsoum, and Y. Gogotsi, "Magnesium-Ion Storage Capability of MXenes," *ACS Applied Energy Materials*, vol. 2, no. 2, pp. 1572–1578, 2019.
- [38] M. Xu, S. Lei, J. Qi, Q. Dou, L. Liu, Y. Lu, Q. Huang, S. Shi, and X. Yan, "Opening Magnesium

- Storage Capability of Two-Dimensional MXene by Intercalation of Cationic Surfactant,” *ACS Nano*, vol. 12, no. 4, pp. 3733–3740, 2018.
- [39] F. Liu, Y. Liu, X. Zhao, X. Liu, and L.-Z. Fan, “Pursuit of a high-capacity and long-life Mg-storage cathode by tailoring sandwich-structured MXene@carbon nanosphere composites,” *Journal of Materials Chemistry A*, vol. 7, pp. 16712–16719, 2019.
- [40] M. Cao, F. Wang, L. Wang, W. Wu, W. Lv, and J. Zhu, “Room Temperature Oxidation of Ti_3C_2 MXene for Supercapacitor Electrodes,” *Journal of The Electrochemical Society*, vol. 164, no. 14, pp. A3933–A3942, 2017.
- [41] Y. Zhang, Y. Jiang, Z. Duan, Q. Huang, Y. Wu, B. Liu, Q. Zhao, S. Wang, Z. Yuan, and H. Tai, “Highly sensitive and selective NO_2 sensor of alkalized V_2CT_x MXene driven by interlayer swelling,” *Sensors and Actuators B: Chemical*, vol. 344, p. 130150, 2021.
- [42] R. B. Rakhi, B. Ahmed, M. N. Hedhili, D. H. Anjum, and H. N. Alshareef, “Effect of Postetch Annealing Gas Composition on the Structural and Electrochemical Properties of Ti_2CT_x MXene Electrodes for Supercapacitor Applications,” *Chemistry of Materials*, vol. 27, no. 15, pp. 5314–5323, 2015.
- [43] H. Xu, R. Zheng, D. Du, L. Ren, R. Li, X. Wen, C. Zhao, and C. Shu, “ V_2C MXene enriched with -O termination as high-efficiency electrocatalyst for lithium-oxygen battery,” *Applied Materials Today*, vol. 27, p. 101464, 2022.
- [44] R. Thakur, A. VahidMohammadi, J. Moncada, W. R. Adams, M. Chi, B. Tatarchuk, M. Beidaghi, and C. A. Carrero, “Insights into the thermal and chemical stability of multilayered V_2CT_x MXene,” *Nanoscale*, vol. 11, pp. 10716–10726, 2019.
- [45] T. Li, L. Yao, Q. Liu, J. Gu, R. Luo, J. Li, X. Yan, W. Wang, P. Liu, B. Chen, W. Zhang, W. Abbas, R. Naz, and D. Zhang, “Fluorine-Free Synthesis of High-Purity $Ti_3C_2T_x$ ($T=OH, O$) via Alkali Treatment,” *Angewandte Chemie International Edition*, vol. 57, no. 21, pp. 6115–6119, 2018.
- [46] J. B. Goodenough and K.-S. Park, “The Li-Ion Rechargeable Battery: A Perspective,” *Journal of the American Chemical Society*, vol. 135, no. 4, pp. 1167–1176, 2013.
- [47] P. Peljo and H. H. Girault, “Electrochemical potential window of battery electrolytes: the HOMO-LUMO misconception,” *Energy & Environmental Science*, vol. 11, pp. 2306–2309, 2018.
- [48] E. Tretkoff, J. Ouellette, and A. Chodos, “1800: Volta describes the Electric Battery,” *American Physical Society NEWS*, vol. 15, no. 3, 2006.
- [49] B. Scrosati, “History of lithium batteries,” *Journal of Solid State Electrochemistry*, vol. 15, no. 7, pp. 1623–1630, 2011.
- [50] C. Pillot, “The rechargeable battery market and main trends 2018-2030,” in *36th Annual International Battery Seminar & Exhibit. Avicenne Energy* (A. Energy, ed.), 2019.
- [51] Epec, “Battery cell comparison.” URL: <https://www.epectec.com/batteries/cell-comparison.html>, accessed: 31.08.2022.
- [52] H. Zhang, Y. Yang, D. Ren, L. Wang, and X. He, “Graphite as anode materials: Fundamental mechanism, recent progress and advances,” *Energy Storage Materials*, vol. 36, pp. 147–170, 2021.

- [53] R. Fong, U. von Sacken, and J. R. Dahn, "Studies of Lithium Intercalation into Carbons Using Non-aqueous Electrochemical Cells," *Journal of The Electrochemical Society*, vol. 137, pp. 2009–2013, 1990.
- [54] Y. Zhang, T.-T. Zuo, J. Popovic, K. Lim, Y.-X. Yin, J. Maier, and Y.-G. Guo, "Towards better Li metal anodes: Challenges and strategies," *Materials Today*, vol. 33, pp. 56–74, 2020.
- [55] C. Jin, T. Liu, O. Sheng, M. Li, T. Liu, Y. Yuan, J. Nai, Z. Ju, W. Zhang, Y. Liu, Y. Wang, Z. Lin, J. Lu, and X. Tao, "Rejuvenating dead lithium supply in lithium metal anodes by iodine redox," *Nature Energy*, vol. 6, no. 4, pp. 378–387, 2021.
- [56] C. Fang, X. Wang, and Y. S. Meng, "Key Issues Hindering a Practical Lithium-Metal Anode," *Trends in Chemistry*, vol. 1, no. 2, pp. 152–158, 2019.
- [57] N. Nitta, F. Wu, J. T. Lee, and G. Yushin, "Li-ion battery materials: present and future," *Materials Today*, vol. 18, no. 5, pp. 252–264, 2015.
- [58] M. N. Obrovac and L. Christensen, "Structural Changes in Silicon Anodes during Lithium Insertion/Extraction," *Electrochemical and Solid-State Letters*, vol. 7, no. 5, p. A93, 2004.
- [59] K. Feng, M. Li, W. Liu, A. G. Kashkooli, X. Xiao, M. Cai, and Z. Chen, "Silicon-Based Anodes for Lithium-Ion Batteries: From Fundamentals to Practical Applications," *Small*, vol. 14, no. 8, p. 1702737, 2018.
- [60] Z. Chen, I. Belharouak, Y.-K. Sun, and K. Amine, "Titanium-Based Anode Materials for Safe Lithium-Ion Batteries," *Advanced Functional Materials*, vol. 23, no. 8, pp. 959–969, 2013.
- [61] M. N. Obrovac and V. L. Chevrier, "Alloy negative electrodes for li-ion batteries," *Chemical Reviews*, vol. 114, no. 23, pp. 11444–11502, 2014.
- [62] G. G. Eshetu, H. Zhang, X. Judez, H. Adenusi, M. Armand, S. Passerini, and E. Figgemeier, "Production of high-energy Li-ion batteries comprising silicon-containing anodes and insertion-type cathodes," *Nature Communications*, vol. 12, no. 1, p. 5459, 2021.
- [63] E. Pohjalainen, T. Rauhala, M. Valkeapää, J. Kallioinen, and T. Kallio, "Effect of $\text{Li}_4\text{Tl}_5\text{O}_{12}$ Particle Size on the Performance of Lithium Ion Battery Electrodes at High C-Rates and Low Temperatures," *The Journal of Physical Chemistry C*, vol. 119, no. 5, pp. 2277–2283, 2015.
- [64] A. Manthiram, "A reflection on lithium-ion battery cathode chemistry," *Nature Communications*, vol. 11, no. 1, p. 1550, 2020.
- [65] K. Mizushima, P. Jones, P. Wiseman, and J. Goodenough, " Li_xCoO_2 ($0 < x < 1$): A new cathode material for batteries of high energy density," *Materials Research Bulletin*, vol. 15, no. 6, pp. 783–789, 1980.
- [66] J. Li, C. Lin, M. Weng, Y. Qiu, P. Chen, K. Yang, W. Huang, Y. Hong, J. Li, M. Zhang, C. Dong, W. Zhao, Z. Xu, X. Wang, K. Xu, J. Sun, and F. Pan, "Structural origin of the high-voltage instability of lithium cobalt oxide," *Nature Nanotechnology*, vol. 16, no. 5, pp. 599–605, 2021.
- [67] A.-H. Marincas, F. Goga, S.-A. Dorneanu, and P. Ilea, "Review on synthesis methods to obtain LiMn_2O_4 -based cathode materials for Li-ion batteries," *Journal of Solid State Electrochemistry*, vol. 24, no. 3, pp. 473–497, 2020.

- [68] H.-J. Noh, S. Youn, C. S. Yoon, and Y.-K. Sun, "Comparison of the structural and electrochemical properties of layered $\text{Li}[\text{Ni}_x\text{Co}_y\text{Mn}_z]\text{O}_2$ ($x = 1/3, 0.5, 0.6, 0.7, 0.8$ and 0.85) cathode material for lithium-ion batteries," *Journal of Power Sources*, vol. 233, pp. 121–130, 2013.
- [69] L.-X. Yuan, Z.-H. Wang, W.-X. Zhang, X.-L. Hu, J.-T. Chen, Y.-H. Huang, and J. B. Goodenough, "Development and challenges of LiFePO_4 cathode material for lithium-ion batteries," *Energy Environmental Science*, vol. 4, pp. 269–284, 2011.
- [70] B. Aktekin, M. Valvo, R. I. Smith, M. H. Sørby, F. Lodi Marzano, W. Zipprich, D. Brandell, K. Edström, and W. R. Brant, "Cation Ordering and Oxygen Release in $\text{LiNi}_{0.5-x}\text{Mn}_{1.5+x}\text{O}_{4-y}$ (LNMO): In Situ Neutron Diffraction and Performance in Li Ion Full Cells," *ACS Applied Energy Materials*, vol. 2, no. 5, pp. 3323–3335, 2019.
- [71] M. Zhao, B.-Q. Li, X.-Q. Zhang, J.-Q. Huang, and Q. Zhang, "A perspective toward practical lithium-sulfur batteries," *ACS Central Science*, vol. 6, no. 7, pp. 1095–1104, 2020.
- [72] T. Ohzuku and Y. Makimura, "Layered Lithium Insertion Material of $\text{LiCo}_{1/3}\text{Ni}_{1/3}\text{Mn}_{1/3}\text{O}_2$ for Lithium-Ion Batteries," *Chemistry Letters*, vol. 30, no. 7, pp. 642–643, 2001.
- [73] J. Salminen, T. Kallio, N. Omar, P. Van den Bossche, J. Van Mierlo, and H. Gualous, "Chapter 14 - Transport Energy - Lithium Ion Batteries," in *Future Energy (Second Edition)* (T. M. Letcher, ed.), pp. 291–309, Boston: Elsevier, 2014.
- [74] A. Gomez-Martin, F. Reissig, L. Frankenstein, M. Heidbüchel, M. Winter, T. Placke, and R. Schmuch, "Magnesium Substitution in Ni-Rich NMC Layered Cathodes for High-Energy Lithium Ion Batteries," *Advanced Energy Materials*, vol. 12, no. 8, p. 2103045, 2022.
- [75] H. Li, M. Cormier, N. Zhang, J. Inglis, J. Li, and J. R. Dahn, "Is Cobalt Needed in Ni-Rich Positive Electrode Materials for Lithium Ion Batteries?," *Journal of The Electrochemical Society*, vol. 166, no. 4, pp. A429–A439, 2019.
- [76] Y. Chen, T. Wang, H. Tian, D. Su, Q. Zhang, and G. Wang, "Advances in Lithium-Sulfur Batteries: From Academic Research to Commercial Viability," *Advanced Materials*, vol. 33, no. 29, p. 2003666, 2021.
- [77] E. R. Østli, *Stabilizing strategies for the high-voltage cathode material $\text{LiNi}_{0.5-x}\text{Mn}_{1.5+x}\text{O}_4$ (LNMO)*. NTNU. ISBN: 978-82-326-5225-9, 2022.
- [78] Morrow, "Morrow and Haldor Topsoe sign binding supply agreement for pilot production of cobalt-free material." URL: <https://www.morrowbatteries.com/post/morrow-and-haldor-topsoe-sign-binding-supply-agreement-for-pilot-production-of-cobalt-free-material>, accessed: 09.09.2022.
- [79] Fred Lambert, "Tesla is already using cobalt-free LFP batteries in half of its new cars produced." URL: <https://electrek.co/2022/04/22/tesla-using-cobalt-free-lfp-batteries-in-half-new-cars-produced/>, accessed: 09.09.2022.
- [80] Ai Root, "The Same Battery That Pads Tesla's Profits Can Help Other Car Makers Catch Up." URL: <https://www.barrons.com/articles/tesla-electric-vehicle-battery-profits-51660832313>, accessed: 09.09.2022.
- [81] M. Marcinek, J. Syzdek, M. Marczewski, M. Piszcz, L. Niedzicki, M. Kalita, A. Plewa-Marczewska,

- A. Bitner, P. Wiczorek, T. Trzeciak, M. Kasprzyk, P. Łęzak, Z. Zukowska, A. Zalewska, and W. Wiczorek, "Electrolytes for Li-ion transport - Review," *Solid State Ionics*, vol. 276, pp. 107–126, 2015.
- [82] K. Xu, "Electrolytes and Interphases in Li-Ion Batteries and Beyond," *Chemical Reviews*, vol. 114, no. 23, pp. 11503–11618, 2014.
- [83] K. Xu, "Nonaqueous Liquid Electrolytes for Lithium-Based Rechargeable Batteries," *Chemical Reviews*, vol. 104, no. 10, pp. 4303–4418, 2004.
- [84] M. Forsyth, L. Porcarelli, X. Wang, N. Goujon, and D. Mecerreyes, "Innovative electrolytes based on ionic liquids and polymers for next-generation solid-state batteries," *Accounts of Chemical Research*, vol. 52, no. 3, pp. 686–694, 2019.
- [85] K. J. Kim, M. Balaish, M. Wadaguchi, L. Kong, and J. L. M. Rupp, "Solid-State Li-Metal Batteries: Challenges and Horizons of Oxide and Sulfide Solid Electrolytes and Their Interfaces," *Advanced Energy Materials*, vol. 11, no. 1, p. 2002689, 2021.
- [86] L. Porz, T. Swamy, B. W. Sheldon, D. Rettenwander, T. Frömling, H. L. Thaman, S. Berendts, R. Uecker, W. C. Carter, and Y.-M. Chiang, "Mechanism of lithium metal penetration through inorganic solid electrolytes," *Advanced Energy Materials*, vol. 7, no. 20, p. 1701003, 2017.
- [87] T. D. Gregory, R. J. Hoffman, and R. C. Winterton, "Nonaqueous Electrochemistry of Magnesium: Applications to Energy Storage," *Journal of The Electrochemical Society*, vol. 137, no. 3, pp. 775–780, 1990.
- [88] R. Davidson, A. Verma, D. Santos, F. Hao, C. D. Fincher, D. Zhao, V. Attari, P. Schofield, J. Van Buskirk, A. Fraticelli-Cartagena, T. E. G. Alivio, R. Arroyave, K. Xie, M. Pharr, P. P. Mukherjee, and S. Banerjee, "Mapping mechanisms and growth regimes of magnesium electrodeposition at high current densities," *Materials Horizons*, vol. 7, pp. 843–854, 2020.
- [89] M. S. Ding, T. Diemant, R. J. Behm, S. Passerini, and G. A. Giffin, "Dendrite Growth in Mg Metal Cells Containing Mg(TFSI)₂/Glyme Electrolytes," *Journal of The Electrochemical Society*, vol. 165, no. 10, pp. A1983–A1990, 2018.
- [90] M. Fichtner, "CHAPTER 1 Motivation for a Magnesium Battery," in *Magnesium Batteries: Research and Applications*, pp. 1–16, The Royal Society of Chemistry, 2020.
- [91] European Commission, "Critical Raw Materials Resilience: Charting a Path towards greater Security and Sustainability," 2020. URL: <https://eur-lex.europa.eu/legal-content/EN/TXT/?uri=CELEX:52020DC0474>, accessed 09.09.2022.
- [92] U. G. Survey, "Mineral commodity summaries 2022," tech. rep., Survey, U.S. Geological, Reston, VA, 2022.
- [93] Trading Economics, "Lithium," 2022. URL: <https://tradingeconomics.com/commodity/lithium>, accessed: 09.09.2022.
- [94] Trading Economics, "Magnesium," 2022. URL: <https://tradingeconomics.com/commodity/magnesium>, accessed: 09.09.2022.
- [95] C. You, X. Wu, X. Yuan, Y. Chen, L. Liu, Y. Zhu, L. Fu, Y. Wu, Y.-G. Guo, and T. van Ree, "Advances in rechargeable Mg batteries," *Journal of Materials Chemistry A*, vol. 8, pp. 25601–25625, 2020.

- [96] P. Bonnick and J. Muldoon, "A Trip to Oz and a Peak Behind the Curtain of Magnesium Batteries," *Advanced Functional Materials*, vol. 30, no. 21, p. 1910510, 2020.
- [97] D. Aurbach, Z. Lu, A. Schechter, Y. Gofer, H. Gizbar, R. Turgeman, Y. Cohen, M. Moshkovich, and E. Levi, "Prototype systems for rechargeable magnesium batteries," *Nature*, vol. 407, no. 6805, pp. 724–727, 2000.
- [98] O. Mizrahi, N. Amir, E. Pollak, O. Chusid, V. Marks, H. Gottlieb, L. Larush, E. Zinigrad, and D. Aurbach, "Electrolyte solutions with a wide electrochemical window for rechargeable magnesium batteries," *Journal of The Electrochemical Society*, vol. 155, no. 2, p. A103, 2008.
- [99] R. E. Doe, R. Han, J. Hwang, A. J. Gmitter, I. Shterenberg, H. D. Yoo, N. Pour, and D. Aurbach, "Novel, electrolyte solutions comprising fully inorganic salts with high anodic stability for rechargeable magnesium batteries," *Chemical Communications*, vol. 50, pp. 243–245, 2014.
- [100] R. Mohtadi, M. Matsui, T. S. Arthur, and S.-J. Hwang, "Magnesium Borohydride: From Hydrogen Storage to Magnesium Battery," *Angewandte Chemie International Edition*, vol. 51, no. 39, pp. 9780–9783, 2012.
- [101] H. Xu, Z. Zhang, Z. Cui, A. Du, C. Lu, S. Dong, J. Ma, X. Zhou, and G. Cui, "Strong anion receptor-assisted boron-based Mg electrolyte with wide electrochemical window and non-nucleophilic characteristic," *Electrochemistry Communications*, vol. 83, pp. 72–76, 2017.
- [102] Z.-K. Z and F. M, "Beyond Intercalation Chemistry for Rechargeable Mg Batteries: A Short Review and Perspective," *Frontiers Chemistry*, vol. 6, no. 656, 2019.
- [103] M. Mao, T. Gao, S. Hou, and C. Wang, "A critical review of cathodes for rechargeable Mg batteries," *Chemical Society Reviews*, vol. 47, pp. 8804–8841, 2018.
- [104] P. Canepa, G. Sai Gautam, D. C. Hannah, R. Malik, M. Liu, K. G. Gallagher, K. A. Persson, and G. Ceder, "Odyssey of Multivalent Cathode Materials: Open Questions and Future Challenges," *Chemical Reviews*, vol. 117, no. 5, pp. 4287–4341, 2017.
- [105] R. Dominko, J. Bitenc, R. Berthelot, M. Gauthier, G. Pagot, and V. Di Noto, "Magnesium batteries: Current picture and missing pieces of the puzzle," *Journal of Power Sources*, vol. 478, p. 229027, 2020.
- [106] L. F. Wan, B. R. Perdue, C. A. Appleby, and D. Prendergast, "Mg Desolvation and Intercalation Mechanism at the Mo₆S₈ Chevrel Phase Surface," *Chemistry of Materials*, vol. 27, no. 17, pp. 5932–5940, 2015.
- [107] J. Niu, Z. Zhang, and D. Aurbach, "Alloy Anode Materials for Rechargeable Mg Ion Batteries," *Advanced Energy Materials*, vol. 10, no. 23, p. 2000697, 2020.
- [108] M. Liu, A. Jain, Z. Rong, X. Qu, P. Canepa, R. Malik, G. Ceder, and K. A. Persson, "Evaluation of sulfur spinel compounds for multivalent battery cathode applications," *Energy Environmental Science*, vol. 9, pp. 3201–3209, 2016.
- [109] J. Richard, A. Benayad, J.-F. Colin, and S. Martinet, "Charge Transfer Mechanism into the Chevrel Phase Mo₆S₈ during Mg Intercalation," *The Journal of Physical Chemistry C*, vol. 121, no. 32, pp. 17096–17103, 2017.

- [110] F. Liu, T. Wang, X. Liu, and L.-Z. Fan, "Challenges and Recent Progress on Key Materials for Rechargeable Magnesium Batteries," *Advanced Energy Materials*, vol. 11, no. 2, p. 2000787, 2021.
- [111] H. S. Kim, T. S. Arthur, G. D. Allred, J. Zajicek, J. G. Newman, A. E. Rodnyansky, A. G. Oliver, W. C. Boggess, and J. Muldoon, "Structure and compatibility of a magnesium electrolyte with a sulphur cathode," *Nature Communications*, vol. 2, no. 1, p. 427, 2011.
- [112] A. Rudola, A. J. R. Rennie, R. Heap, S. S. Meysami, A. Lowbridge, F. Mazzali, R. Sayers, C. J. Wright, and J. Barker, "Commercialisation of high energy density sodium-ion batteries: Faradion's journey and outlook," *Journal of Materials Chemistry A*, vol. 9, pp. 8279–8302, 2021.
- [113] Z. Rong, R. Malik, P. Canepa, G. Sai Gautam, M. Liu, A. Jain, K. Persson, and G. Ceder, "Materials Design Rules for Multivalent Ion Mobility in Intercalation Structures," *Chemistry of Materials*, vol. 27, no. 17, pp. 6016–6021, 2015.
- [114] S. Rasul, S. Suzuki, S. Yamaguchi, and M. Miyayama, "High capacity positive electrodes for secondary Mg-ion batteries," *Electrochimica Acta*, vol. 82, pp. 243–249, 2012.
- [115] R. Xiao, J. Xie, T. Luo, L. Huang, Y. Zhou, D. Yu, C. Chen, and Y. Liu, "Phase Transformation and Diffusion Kinetics of V_2O_5 Electrode in Rechargeable Li and Mg Batteries: A First-Principle Study," *The Journal of Physical Chemistry C*, vol. 122, no. 3, pp. 1513–1521, 2018.
- [116] H. D. Yoo, Y. Liang, H. Dong, J. Lin, H. Wang, Y. Liu, L. Ma, T. Wu, Y. Li, Q. Ru, Y. Jing, Q. An, W. Zhou, J. Guo, J. Lu, S. T. Pantelides, X. Qian, and Y. Yao, "Fast kinetics of magnesium monochloride cations in interlayer-expanded titanium disulfide for magnesium rechargeable batteries," *Nature Communications*, vol. 8, no. 1, p. 339, 2017.
- [117] Z. Li, B. P. Vinayan, P. Jankowski, C. Njé, A. Roy, T. Vegge, J. Maibach, J. M. G. Lastra, M. Fichtner, and Z. Zhao-Karger, "Multi-Electron Reactions Enabled by Anion-Based Redox Chemistry for High-Energy Multivalent Rechargeable Batteries," *Angewandte Chemie International Edition*, vol. 59, no. 28, pp. 11483–11490, 2020.
- [118] Y. Wang, Z. Liu, C. Wang, X. Yi, R. Chen, L. Ma, Y. Hu, G. Zhu, T. Chen, Z. Tie, J. Ma, J. Liu, and Z. Jin, "Highly Branched VS_4 Nanodendrites with 1D Atomic-Chain Structure as a Promising Cathode Material for Long-Cycling Magnesium Batteries," *Advanced Materials*, vol. 30, no. 32, p. 1802563, 2018.
- [119] X. Sun, P. Bonnick, and L. F. Nazar, "Layered TiS_2 Positive Electrode for Mg Batteries," *ACS Energy Letters*, vol. 1, no. 1, pp. 297–301, 2016.
- [120] Y. Gu, Y. Katsura, T. Yoshino, H. Takagi, and K. Taniguchi, "Rechargeable magnesium-ion battery based on a $TiSe_2$ -cathode with d-p orbital hybridized electronic structure," *Scientific Reports*, vol. 5, no. 1, p. 12486, 2015.
- [121] Y. Liang, R. Feng, S. Yang, H. Ma, J. Liang, and J. Chen, "Rechargeable Mg Batteries with Graphene-like MoS_2 Cathode and Ultrasmall Mg Nanoparticle Anode," *Advanced Materials*, vol. 23, no. 5, pp. 640–643, 2011.
- [122] X. Sun, P. Bonnick, V. Duffort, M. Liu, Z. Rong, K. A. Persson, G. Ceder, and L. F. Nazar, "A high capacity thiospinel cathode for Mg batteries," *Energy Environmental Science*, vol. 9, pp. 2273–2277, 2016.

- [123] P. Wang and M. R. Buchmeiser, "Rechargeable Magnesium-Sulfur Battery Technology: State of the Art and Key Challenges," *Advanced Functional Materials*, vol. 29, no. 49, p. 1905248, 2019.
- [124] Z. Zhang, Z. Cui, L. Qiao, J. Guan, H. Xu, X. Wang, P. Hu, H. Du, S. Li, X. Zhou, S. Dong, Z. Liu, G. Cui, and L. Chen, "Novel Design Concepts of Efficient Mg-Ion Electrolytes toward High-Performance Magnesium-Selenium and Magnesium-Sulfur Batteries," *Advanced Energy Materials*, vol. 7, no. 11, p. 1602055, 2017.
- [125] Z. Chen, Q. Yang, D. Wang, A. Chen, X. Li, Z. Huang, G. Liang, Y. Wang, and C. Zhi, "Tellurium: A High-Performance Cathode for Magnesium Ion Batteries Based on a Conversion Mechanism," *ACS Nano*, vol. 16, no. 4, pp. 5349–5357, 2022.
- [126] H. Tian, T. Gao, X. Li, X. Wang, C. Luo, X. Fan, C. Yang, L. Suo, Z. Ma, W. Han, and C. Wang, "High power rechargeable magnesium/iodine battery chemistry," *Nature Communications*, vol. 8, no. 1, p. 14083, 2017.
- [127] Y. Xu, Y. Ye, S. Zhao, J. Feng, J. Li, H. Chen, A. Yang, F. Shi, L. Jia, Y. Wu, X. Yu, P.-A. Glans-Suzuki, Y. Cui, J. Guo, and Y. Zhang, "In Situ X-ray Absorption Spectroscopic Investigation of the Capacity Degradation Mechanism in Mg/S Batteries," *Nano Letters*, vol. 19, no. 5, pp. 2928–2934, 2019.
- [128] A. Du, Z. Zhang, H. Qu, Z. Cui, L. Qiao, L. Wang, J. Chai, T. Lu, S. Dong, T. Dong, H. Xu, X. Zhou, and G. Cui, "An efficient organic magnesium borate-based electrolyte with non-nucleophilic characteristics for magnesium-sulfur battery," *Energy Environmental Science*, vol. 10, pp. 2616–2625, 2017.
- [129] T. Li, X. Bai, U. Gulzar, Y.-J. Bai, C. Capiglia, W. Deng, X. Zhou, Z. Liu, Z. Feng, and R. Proietti Zaccaria, "A Comprehensive Understanding of Lithium-Sulfur Battery Technology," *Advanced Functional Materials*, vol. 29, no. 32, p. 1901730, 2019.
- [130] L. Kong, C. Yan, J.-Q. Huang, M.-Q. Zhao, M.-M. Titirici, R. Xiang, and Q. Zhang, "A Review of Advanced Energy Materials for Magnesium-Sulfur Batteries," *Energy & Environmental Materials*, vol. 1, no. 3, pp. 100–112, 2018.
- [131] Z. Zhao-Karger, X. Zhao, D. Wang, T. Diemant, R. J. Behm, and M. Fichtner, "Performance Improvement of Magnesium Sulfur Batteries with Modified Non-Nucleophilic Electrolytes," *Advanced Energy Materials*, vol. 5, no. 3, p. 1401155, 2015.
- [132] H. Kaland, J. Hadler-Jacobsen, F. H. Fagerli, N. P. Wagner, S. K. Schnell, and K. Wiik, "Dipentamethylene Thiuram Tetrasulfide-Based Cathodes for Rechargeable Magnesium Batteries," *ACS Applied Energy Materials*, vol. 3, no. 11, pp. 10600–10610, 2020.
- [133] B. T. McAllister, L. T. Kyne, T. B. Schon, and D. S. Seferos, "Potential for disruption with organic magnesium-ion batteries," *Joule*, vol. 3, no. 3, pp. 620–624, 2019.
- [134] J. Bitenc, K. Pirnat, T. Bančič, M. Gaberšček, B. Genorio, A. Randon-Vitanova, and R. Dominko, "Anthraquinone-Based Polymer as Cathode in Rechargeable Magnesium Batteries," *ChemSusChem*, vol. 8, no. 24, pp. 4128–4132, 2015.
- [135] B. Pan, J. Huang, Z. Feng, L. Zeng, M. He, L. Zhang, J. T. Vaughey, M. J. Bedzyk, P. Fenter, Z. Zhang, A. K. Burrell, and C. Liao, "Polyanthraquinone-Based Organic Cathode for High-

- Performance Rechargeable Magnesium-Ion Batteries,” *Advanced Energy Materials*, vol. 6, no. 14, p. 1600140, 2016.
- [136] A. Vizintin, J. Bitenc, A. Kopač Lautar, K. Pirnat, J. Grdadolnik, J. Stare, A. Randon-Vitanova, and R. Dominko, “Probing electrochemical reactions in organic cathode materials via in operando infrared spectroscopy,” *Nature Communications*, vol. 9, no. 1, p. 661, 2018.
- [137] B. Anasori and Y. Gogotsi, *2D Metal Carbides and Nitrides (MXenes): Structure, Properties and Applications*. Springer International Publishing. ISBN: 978-3-030-19026-2, 2019.
- [138] K. Maleski and M. Alhabeab, *Top-Down MXene Synthesis (Selective Etching)*, pp. 69–87. Springer International Publishing, 2019.
- [139] M. Naguib, O. Mashtalir, J. Carle, V. Presser, J. Lu, L. Hultman, Y. Gogotsi, and M. W. Barsoum, “Two-dimensional transition metal carbides,” *ACS Nano*, vol. 6, no. 2, pp. 1322–1331, 2012.
- [140] A.J. Drexel Nanomaterials Institute, “Anasori MXene ACS Nano 20150825,” 2015. URL: https://www.youtube.com/watch?v=N_4mnjYuuIs, accessed 29.09.2022.
- [141] A. VahidMohammadi, J. Rosen, and Y. Gogotsi, “The world of two-dimensional carbides and nitrides (MXenes),” *Science*, vol. 372, no. 6547, p. eabf1581, 2021.
- [142] N. C. Frey, J. Wang, G. I. Vega Bellido, B. Anasori, Y. Gogotsi, and V. B. Shenoy, “Prediction of Synthesis of 2D Metal Carbides and Nitrides (MXenes) and Their Precursors with Positive and Unlabeled Machine Learning,” *ACS Nano*, vol. 13, no. 3, pp. 3031–3041, 2019.
- [143] H. Chen, H. Ma, and C. Li, “Host-Guest Intercalation Chemistry in MXenes and Its Implications for Practical Applications,” *ACS Nano*, vol. 15, no. 10, pp. 15502–15537, 2021.
- [144] P. O. Å. Persson, *MXene Surface Chemistry*, pp. 125–136. Springer International Publishing, 2019.
- [145] B. Anasori and Y. Gogotsi, *Introduction to 2D Transition Metal Carbides and Nitrides (MXenes)*, pp. 3–12. Springer International Publishing, 2019.
- [146] V. Nicolosi, M. Chhowalla, M. G. Kanatzidis, M. S. Strano, and J. N. Coleman, “Liquid Exfoliation of Layered Materials,” *Science*, vol. 340, no. 6139, p. 1226419, 2013.
- [147] H. Zhang, “Ultrathin Two-Dimensional Nanomaterials,” *ACS Nano*, vol. 9, no. 10, pp. 9451–9469, 2015.
- [148] M. N. Abdelmalak, *MXenes: A New Family of Two-Dimensional Materials and its Application as Electrodes for Li-ion Batteries*. Drexel University. ISBN: 978-1-303-89007-9, 2014.
- [149] M. Naguib, M. W. Barsoum, and Y. Gogotsi, “Ten Years of Progress in the Synthesis and Development of MXenes,” *Advanced Materials*, vol. 33, no. 39, p. 2103393, 2021.
- [150] M. Alhabeab, K. Maleski, B. Anasori, P. Lelyukh, L. Clark, S. Sin, and Y. Gogotsi, “Guidelines for Synthesis and Processing of Two-Dimensional Titanium Carbide ($\text{Ti}_3\text{C}_2\text{T}_x$ MXene),” *Chemistry of Materials*, vol. 29, no. 18, pp. 7633–7644, 2017.
- [151] S. Yang, P. Zhang, F. Wang, A. G. Ricciardulli, M. R. Lohe, P. W. M. Blom, and X. Feng, “Fluoride-Free Synthesis of Two-Dimensional Titanium Carbide (MXene) Using A Binary Aqueous System,” *Angewandte Chemie International Edition*, vol. 57, no. 47, pp. 15491–15495, 2018.

- [152] W. Sun, S. A. Shah, Y. Chen, Z. Tan, H. Gao, T. Habib, M. Radovic, and M. J. Green, "Electrochemical etching of Ti_2AlC to Ti_2CT_x (MXene) in low-concentration hydrochloric acid solution," *Journal of Materials Chemistry A*, vol. 5, pp. 21663–21668, 2017.
- [153] A. Jawaid, A. Hassan, G. Neher, D. Nepal, R. Pachter, W. J. Kennedy, S. Ramakrishnan, and R. A. Vaia, "Halogen Etch of Ti_3AlC_2 MAX Phase for MXene Fabrication," *ACS Nano*, vol. 15, no. 2, pp. 2771–2777, 2021.
- [154] C. Wang, H. Shou, S. Chen, S. Wei, Y. Lin, P. Zhang, Z. Liu, K. Zhu, X. Guo, X. Wu, P. M. Ajayan, and L. Song, "HCl-Based Hydrothermal Etching Strategy toward Fluoride-Free MXenes," *Advanced Materials*, vol. 33, no. 27, p. 2101015, 2021.
- [155] V. Kamysbayev, A. S. Filatov, H. Hu, X. Rui, F. Lagunas, D. Wang, R. F. Klie, and D. V. Talapin, "Covalent surface modifications and superconductivity of two-dimensional metal carbide MXenes," *Science*, vol. 369, no. 6506, pp. 979–983, 2020.
- [156] M. Li, J. Lu, K. Luo, Y. Li, K. Chang, K. Chen, J. Zhou, J. Rosen, L. Hultman, P. Eklund, P. O. Å. Persson, S. Du, Z. Chai, Z. Huang, and Q. Huang, "Element Replacement Approach by Reaction with Lewis Acidic Molten Salts to Synthesize Nanolaminated MAX Phases and MXenes," *Journal of the American Chemical Society*, vol. 141, no. 11, pp. 4730–4737, 2019.
- [157] M. Ghidui, J. Halim, S. Kota, D. Bish, Y. Gogotsi, and M. W. Barsoum, "Ion-Exchange and Cation Solvation Reactions in Ti_3C_2 MXene," *Chemistry of Materials*, vol. 28, no. 10, pp. 3507–3514, 2016.
- [158] M. Ghidui, M. R. Lukatskaya, M.-Q. Zhao, Y. Gogotsi, and M. W. Barsoum, "Conductive two-dimensional titanium carbide 'clay' with high volumetric capacitance," *Nature*, vol. 516, no. 7529, pp. 78–81, 2014.
- [159] M. Naguib, R. R. Unocic, B. L. Armstrong, and J. Nanda, "Large-scale delamination of multi-layers transition metal carbides and carbonitrides "MXenes";" *Dalton Transactions*, vol. 44, pp. 9353–9358, 2015.
- [160] K. Maleski, V. N. Mochalin, and Y. Gogotsi, "Dispersions of Two-Dimensional Titanium Carbide MXene in Organic Solvents," *Chemistry of Materials*, vol. 29, no. 4, pp. 1632–1640, 2017.
- [161] X. Li, W. Cai, J. An, S. Kim, J. Nah, D. Yang, R. Piner, A. Velamakanni, I. Jung, E. Tutuc, S. K. Banerjee, L. Colombo, and R. S. Ruoff, "Large-area synthesis of high-quality and uniform graphene films on copper foils," *Science*, vol. 324, no. 5932, pp. 1312–1314, 2009.
- [162] Z. Lin, A. McCreary, N. Briggs, S. Subramanian, K. Zhang, Y. Sun, X. Li, N. J. Borys, H. Yuan, S. K. Fullerton-Shirey, A. Chernikov, H. Zhao, S. McDonnell, A. M. Lindenberg, K. Xiao, B. J. LeRoy, M. Drndić, J. C. M. Hwang, J. Park, M. Chhowalla, R. E. Schaak, A. Javey, M. C. Hersam, J. Robinson, and M. Terrones, "2D materials advances: from large scale synthesis and controlled heterostructures to improved characterization techniques, defects and applications," *2D Materials*, vol. 3, no. 4, p. 042001, 2016.
- [163] C. E. Shuck and Y. Gogotsi, "Taking MXenes from the lab to commercial products," *Chemical Engineering Journal*, vol. 401, p. 125786, 2020.
- [164] P. Bärmann, L. Haneke, J. M. Wrogemann, M. Winter, O. Guillon, T. Placke, and J. Gonzalez-Julian,

- “Scalable Synthesis of MAX Phase Precursors toward Titanium-Based MXenes for Lithium-Ion Batteries,” *ACS Applied Materials & Interfaces*, vol. 13, no. 22, pp. 26074–26083, 2021.
- [165] C. E. Shuck, A. Sarycheva, M. Anayee, A. Levitt, Y. Zhu, S. Uzun, V. Balitskiy, V. Zahorodna, O. Gogotsi, and Y. Gogotsi, “Scalable Synthesis of $Ti_3C_2T_x$ MXene,” *Advanced Engineering Materials*, vol. 22, no. 3, p. 1901241, 2020.
- [166] J. Zhang, N. Kong, S. Uzun, A. Levitt, S. Seyedin, P. A. Lynch, S. Qin, M. Han, W. Yang, J. Liu, X. Wang, Y. Gogotsi, and J. M. Razal, “Scalable Manufacturing of Free-Standing, Strong $Ti_3C_2T_x$ MXene Films with Outstanding Conductivity,” *Advanced Materials*, vol. 32, no. 23, p. 2001093, 2020.
- [167] R. Ibragimova, P. Erhart, P. Rinke, and H.-P. Komsa, “Surface Functionalization of 2D MXenes: Trends in Distribution, Composition, and Electronic Properties,” *The Journal of Physical Chemistry Letters*, vol. 12, no. 9, pp. 2377–2384, 2021.
- [168] B. Anasori, C. Shi, E. J. Moon, Y. Xie, C. A. Voigt, P. R. C. Kent, S. J. May, S. J. L. Billinge, M. W. Barsoum, and Y. Gogotsi, “Control of electronic properties of 2D carbides (MXenes) by manipulating their transition metal layers,” *Nanoscale Horizons*, vol. 1, pp. 227–234, 2016.
- [169] J. Halim, S. Kota, M. R. Lukatskaya, M. Naguib, M.-Q. Zhao, E. J. Moon, J. Pitock, J. Nanda, S. J. May, Y. Gogotsi, and M. W. Barsoum, “Synthesis and Characterization of 2D Molybdenum Carbide (MXene),” *Advanced Functional Materials*, vol. 26, no. 18, pp. 3118–3127, 2016.
- [170] M. Khazaei, A. Ranjbar, M. Arai, T. Sasaki, and S. Yunoki, “Electronic properties and applications of MXenes: a theoretical review,” *Journal of Materials Chemistry C*, vol. 5, pp. 2488–2503, 2017.
- [171] J. L. Hart, K. Hantanasirisakul, A. C. Lang, B. Anasori, D. Pinto, Y. Pivak, J. T. van Omme, S. J. May, Y. Gogotsi, and M. L. Taheri, “Control of MXenes’ electronic properties through termination and intercalation,” *Nature Communications*, vol. 10, no. 1, p. 522, 2019.
- [172] K. Hantanasirisakul and Y. Gogotsi, “Electronic and Optical Properties of 2D Transition Metal Carbides and Nitrides (MXenes),” *Advanced Materials*, vol. 30, no. 52, p. 1804779, 2018.
- [173] T. S. Mathis, K. Maleski, A. Goad, A. Sarycheva, M. Anayee, A. C. Foucher, K. Hantanasirisakul, C. E. Shuck, E. A. Stach, and Y. Gogotsi, “Modified MAX Phase Synthesis for Environmentally Stable and Highly Conductive Ti_3C_2 MXene,” *ACS Nano*, vol. 15, no. 4, pp. 6420–6429, 2021.
- [174] A. Sarycheva, A. Polemi, Y. Liu, K. Dandekar, B. Anasori, and Y. Gogotsi, “2D titanium carbide (MXene) for wireless communication,” *Science Advances*, vol. 4, no. 9, p. eaau0920, 2018.
- [175] A. Lipatov, H. Lu, M. Alhabeib, B. Anasori, A. Gruverman, Y. Gogotsi, and A. Sinitskii, “Elastic properties of 2D $Ti_3C_2T_x$ MXene monolayers and bilayers,” *Science Advances*, vol. 4, no. 6, p. eaat0491, 2018.
- [176] N. Zhang, Y. Hong, S. Yazdanparast, and M. A. Zaeem, “Superior structural, elastic and electronic properties of 2D titanium nitride MXenes over carbide MXenes: a comprehensive first principles study,” *2D Materials*, vol. 5, no. 4, p. 045004, 2018.
- [177] S. Sun, C. Liao, A. M. Hafez, H. Zhu, and S. Wu, “Two-dimensional MXenes for energy storage,” *Chemical Engineering Journal*, vol. 338, pp. 27–45, 2018.

- [178] Z. Lin and P. Simon, *MXenes for Supercapacitor Application*, pp. 349–365. Springer International Publishing, 2019.
- [179] M. Okubo and A. Yamada, *MXenes for Batteries*, pp. 367–379. Springer International Publishing, 2019.
- [180] C. Zhan, M. Naguib, M. Lukatskaya, P. R. C. Kent, Y. Gogotsi, and D.-e. Jiang, “Understanding the MXene Pseudocapacitance,” *The Journal of Physical Chemistry Letters*, vol. 9, no. 6, pp. 1223–1228, 2018.
- [181] M. R. Lukatskaya, S. Kota, Z. Lin, M.-Q. Zhao, N. Shpigel, M. D. Levi, J. Halim, P.-L. Taberna, M. W. Barsoum, P. Simon, and Y. Gogotsi, “Ultra-high-rate pseudocapacitive energy storage in two-dimensional transition metal carbides,” *Nature Energy*, vol. 2, no. 8, p. 17105, 2017.
- [182] Z. W. Seh, K. D. Fredrickson, B. Anasori, J. Kibsgaard, A. L. Strickler, M. R. Lukatskaya, Y. Gogotsi, T. F. Jaramillo, and A. Vojvodic, “Two-Dimensional Molybdenum Carbide (MXene) as an Efficient Electrocatalyst for Hydrogen Evolution,” *ACS Energy Letters*, vol. 1, no. 3, pp. 589–594, 2016.
- [183] S. G. Peera, C. Liu, A. K. Sahu, M. Selvaraj, M. C. Rao, T. G. Lee, R. Koutavarapu, J. Shim, and L. Singh, “Recent Advances on MXene-Based Electrocatalysts toward Oxygen Reduction Reaction: A Focused Review,” *Advanced Materials Interfaces*, vol. 8, no. 23, p. 2100975, 2021.
- [184] M. R. Lukatskaya, O. Mashtalir, C. E. Ren, Y. Dall’Agnese, P. Rozier, P. L. Taberna, M. Naguib, P. Simon, M. W. Barsoum, and Y. Gogotsi, “Cation Intercalation and High Volumetric Capacitance of Two-Dimensional Titanium Carbide,” *Science*, vol. 341, no. 6153, pp. 1502–1505, 2013.
- [185] Y. Dall’Agnese, P.-L. Taberna, Y. Gogotsi, and P. Simon, “Two-Dimensional Vanadium Carbide (MXene) as Positive Electrode for Sodium-Ion Capacitors,” *The Journal of Physical Chemistry Letters*, vol. 6, no. 12, pp. 2305–2309, 2015.
- [186] F. Ming, H. Liang, W. Zhang, J. Ming, Y. Lei, A.-H. Emwas, and H. N. Alshareef, “Porous MXenes enable high performance potassium ion capacitors,” *Nano Energy*, vol. 62, pp. 853–860, 2019.
- [187] X. Li, M. Li, Q. Yang, H. Li, H. Xu, Z. Chai, K. Chen, Z. Liu, Z. Tang, L. Ma, Z. Huang, B. Dong, X. Yin, Q. Huang, and C. Zhi, “Phase Transition Induced Unusual Electrochemical Performance of V_2CT_x MXene for Aqueous Zinc Hybrid-Ion Battery,” *ACS Nano*, vol. 14, no. 1, pp. 541–551, 2020.
- [188] P. A. Maughan, N. Tapia-Ruiz, and N. Bimbo, “In-situ pillared MXene as a viable zinc-ion hybrid capacitor,” *Electrochimica Acta*, vol. 341, p. 136061, 2020.
- [189] M. Li, X. Li, G. Qin, K. Luo, J. Lu, Y. Li, G. Liang, Z. Huang, J. Zhou, L. Hultman, P. Eklund, P. O. Å. Persson, S. Du, Z. Chai, C. Zhi, and Q. Huang, “Halogenated Ti_3C_2 MXenes with Electrochemically Active Terminals for High-Performance Zinc Ion Batteries,” *ACS Nano*, vol. 15, no. 1, pp. 1077–1085, 2021.
- [190] N. Shpigel, A. Chakraborty, F. Malchik, G. Bergman, A. Nimkar, B. Gavriel, M. Turgeman, C. N. Hong, M. R. Lukatskaya, M. D. Levi, Y. Gogotsi, D. T. Major, and D. Aurbach, “Can Anions Be Inserted into MXene?,” *Journal of the American Chemical Society*, vol. 143, no. 32, pp. 12552–12559, 2021.
- [191] Y. Gogotsi and R. M. Penner, “Energy Storage in Nanomaterials - Capacitive, Pseudocapacitive, or Battery-like?,” *ACS Nano*, vol. 12, no. 3, pp. 2081–2083, 2018.

- [192] J. Nan, X. Guo, J. Xiao, X. Li, W. Chen, W. Wu, H. Liu, Y. Wang, M. Wu, and G. Wang, "Nano-engineering of 2D MXene-Based Materials for Energy Storage Applications," *Small*, vol. 17, no. 9, p. 1902085, 2021.
- [193] C. Ferrara, A. Gentile, S. Marchionna, and R. Ruffo, "Ti₃C₂T_x MXene compounds for electrochemical energy storage," *Current Opinion in Electrochemistry*, vol. 29, p. 100764, 2021.
- [194] Q. Zhao, Q. Zhu, Y. Liu, and B. Xu, "Status and Prospects of MXene-Based Lithium-Sulfur Batteries," *Advanced Functional Materials*, vol. 31, no. 21, p. 2100457, 2021.
- [195] H. Kaland, F. H. Fagerli, J. Hadler-Jacobsen, Z. Zhao-Karger, M. Fichtner, K. Wiik, and N. P. Wagner, "Performance Study of MXene/Carbon Nanotube Composites for Current Collector- and Binder-Free Mg-S Batteries," *ChemSusChem*, vol. 14, no. 8, pp. 1864–1873, 2021.
- [196] H. Xu, D. Zhu, W. Zhu, F. Sun, J. Zou, R. M. Laine, and W. Ding, "Rational design of high concentration electrolytes and MXene-based sulfur host materials toward high-performance magnesium sulfur batteries," *Chemical Engineering Journal*, vol. 428, p. 131031, 2022.
- [197] B. Li, D. Zhang, Y. Liu, Y. Yu, S. Li, and S. Yang, "Flexible Ti₃C₂ MXene-lithium film with lamellar structure for ultrastable metallic lithium anodes," *Nano Energy*, vol. 39, pp. 654–661, 2017.
- [198] C.-Y. Wang, Z.-J. Zheng, Y.-Q. Feng, H. Ye, F.-F. Cao, and Z.-P. Guo, "Topological design of ultrastrong MXene paper hosted Li enables ultrathin and fully flexible lithium metal batteries," *Nano Energy*, vol. 74, p. 104817, 2020.
- [199] Y. Xia, T. S. Mathis, M.-Q. Zhao, B. Anasori, A. Dang, Z. Zhou, H. Cho, Y. Gogotsi, and S. Yang, "Thickness-independent capacitance of vertically aligned liquid-crystalline MXenes," *Nature*, vol. 557, no. 7705, pp. 409–412, 2018.
- [200] K. Prenger, Y. Sun, K. Ganeshan, A. Al-Temimy, K. Liang, C. Dun, J. J. Urban, J. Xiao, T. Petit, A. C. T. van Duin, D.-e. Jiang, and M. Naguib, "Metal Cation Pre-Intercalated Ti₃C₂T_x MXene as Ultra-High Areal Capacitance Electrodes for Aqueous Supercapacitors," *ACS Applied Energy Materials*, vol. 5, no. 8, pp. 9373–9382, 2022.
- [201] D. Pinto, B. Anasori, H. Avireddy, C. E. Shuck, K. Hantanasirisakul, G. Deysheer, J. R. Morante, W. Porzio, H. N. Alshareef, and Y. Gogotsi, "Synthesis and electrochemical properties of 2D molybdenum vanadium carbides - solid solution MXenes," *Journal of Materials Chemistry A*, vol. 8, pp. 8957–8968, 2020.
- [202] J. B. Habedank, L. Kraft, A. Rheinfeld, C. Krezdorn, A. Jossen, and M. F. Zaeh, "Increasing the Discharge Rate Capability of Lithium-Ion Cells with Laser-Structured Graphite Anodes: Modeling and Simulation," *Journal of The Electrochemical Society*, vol. 165, no. 7, pp. A1563–A1573, 2018.
- [203] X. Zhang, L. Wang, W. Liu, C. Li, K. Wang, and Y. Ma, "Recent Advances in MXenes for Lithium-Ion Capacitors," *ACS Omega*, vol. 5, no. 1, pp. 75–82, 2020.
- [204] X. Wang, X. Shen, Y. Gao, Z. Wang, R. Yu, and L. Chen, "Atomic-Scale Recognition of Surface Structure and Intercalation Mechanism of Ti₃C₂T_x," *Journal of the American Chemical Society*, vol. 137, no. 7, pp. 2715–2721, 2015.
- [205] P. Bärmann, R. Nölle, V. Siozios, M. Rutttert, O. Guillon, M. Winter, J. Gonzalez-Julian, and T. Placke,

- “Solvent Co-intercalation into Few-layered $\text{Ti}_3\text{C}_2\text{T}_x$ MXenes in Lithium Ion Batteries Induced by Acidic or Basic Post-treatment,” *ACS Nano*, vol. 15, no. 2, pp. 3295–3308, 2021.
- [206] R. Cheng, T. Hu, H. Zhang, C. Wang, M. Hu, J. Yang, C. Cui, T. Guang, C. Li, C. Shi, P. Hou, and X. Wang, “Understanding the Lithium Storage Mechanism of $\text{Ti}_3\text{C}_2\text{T}_x$ MXene,” *The Journal of Physical Chemistry C*, vol. 123, no. 2, pp. 1099–1109, 2019.
- [207] F. Liu, Y. Liu, X. Zhao, K. Liu, H. Yin, and L.-Z. Fan, “Prelithiated V_2C MXene: A High-Performance Electrode for Hybrid Magnesium/Lithium-Ion Batteries by Ion Cointercalation,” *Small*, vol. 16, no. 8, p. 1906076, 2020.
- [208] J. Hadler-Jacobsen, F. H. Fagerli, H. Kaland, and S. K. Schnell, “Stacking Sequence, Interlayer Bonding, Termination Group Stability and Li/Na/Mg Diffusion in MXenes,” *ACS Materials Letters*, vol. 3, no. 9, pp. 1369–1376, 2021.
- [209] N. M. Caffrey, “Effect of mixed surface terminations on the structural and electrochemical properties of two-dimensional $\text{Ti}_3\text{C}_2\text{T}_2$ and V_2CT_2 MXenes multilayers,” *Nanoscale*, vol. 10, pp. 13520–13530, 2018.
- [210] I. Persson, L.-Å. Näslund, J. Halim, M. W. Barsoum, V. Darakchieva, J. Palisaitis, J. Rosen, and P. O. Å. Persson, “On the organization and thermal behavior of functional groups on Ti_3C_2 MXene surfaces in vacuum,” *2D Materials*, vol. 5, no. 1, p. 015002, 2017.
- [211] M. A. Hope, A. C. Forse, K. J. Griffith, M. R. Lukatskaya, M. Ghidui, Y. Gogotsi, and C. P. Grey, “NMR reveals the surface functionalisation of Ti_3C_2 MXene,” *Physycal Chemistry Chemical Physics*, vol. 18, pp. 5099–5102, 2016.
- [212] K. J. Harris, M. Bugnet, M. Naguib, M. W. Barsoum, and G. R. Goward, “Direct Measurement of Surface Termination Groups and Their Connectivity in the 2D MXene V_2CT_x Using NMR Spectroscopy,” *The Journal of Physical Chemistry C*, vol. 119, no. 24, pp. 13713–13720, 2015.
- [213] H.-W. Wang, M. Naguib, K. Page, D. J. Wesolowski, and Y. Gogotsi, “Resolving the Structure of $\text{Ti}_3\text{C}_2\text{T}_x$ MXenes through Multilevel Structural Modeling of the Atomic Pair Distribution Function,” *Chemistry of Materials*, vol. 28, no. 1, pp. 349–359, 2016.
- [214] H. He, Q. Xia, B. Wang, L. Wang, Q. Hu, and A. Zhou, “Two-dimensional vanadium carbide (V_2CT_x) MXene as supercapacitor electrode in seawater electrolyte,” *Chinese Chemical Letters*, vol. 31, no. 4, pp. 984–987, 2020.
- [215] L. Huang, T. Li, Q. Liu, and J. Gu, “Fluorine-free $\text{Ti}_3\text{C}_2\text{T}_x$ as anode materials for Li-ion batteries,” *Electrochemistry Communications*, vol. 104, p. 106472, 2019.
- [216] Y. Li, H. Shao, Z. Lin, J. Lu, L. Liu, B. Duployer, P. O. Å. Persson, P. Eklund, L. Hultman, M. Li, K. Chen, X.-H. Zha, S. Du, P. Rozier, Z. Chai, E. Raymundo-Piñero, P.-L. Taberna, P. Simon, and Q. Huang, “A general Lewis acidic etching route for preparing MXenes with enhanced electrochemical performance in non-aqueous electrolyte,” *Nature Materials*, vol. 19, no. 8, pp. 894–899, 2020.
- [217] Z. Chen, S. Huang, X. Yuan, X. Gan, and N. Zhou, “A comparative study of M_2CS_2 and M_2CO_2 MXenes as anode materials for lithium ion batteries,” *Applied Surface Science*, vol. 544, p. 148861, 2021.

- [218] Q. Meng, J. Ma, Y. Zhang, Z. Li, C. Zhi, A. Hu, and J. Fan, "The S-functionalized Ti_3C_2 MXene as a high capacity electrode material for Na-ion batteries: a DFT study," *Nanoscale*, vol. 10, pp. 3385–3392, 2018.
- [219] G. Chaney, D. Çakir, F. M. Peeters, and C. Ataca, "Stability of adsorption of Mg and Na on sulfur-functionalized MXenes," *Physical Chemistry Chemical Physics*, vol. 23, pp. 25424–25433, 2021.
- [220] Y.-M. Li, Y.-L. Guo, and Z.-Y. Jiao, "The effect of S-functionalized and vacancies on V_2C MXenes as anode materials for Na-ion and Li-ion batteries," *Current Applied Physics*, vol. 20, no. 2, pp. 310–319, 2020.
- [221] J. Chen, Q. Jin, Y. Li, H. Shao, P. Liu, Y. Liu, P.-L. Taberna, Q. Huang, Z. Lin, and P. Simon, "Molten Salt-Shielded Synthesis (MS^3) of MXenes in Air," *Energy & Environmental Materials*, vol. n/a, no. n/a, 2021.
- [222] J. Li, X. Yuan, C. Lin, Y. Yang, L. Xu, X. Du, J. Xie, J. Lin, and J. Sun, "Achieving High Pseudocapacitance of 2D Titanium Carbide (MXene) by Cation Intercalation and Surface Modification," *Advanced Energy Materials*, vol. 7, no. 15, p. 1602725, 2017.
- [223] Z. Wei, Z. Peigen, T. Wubian, Q. Xia, Z. Yamei, and S. ZhengMing, "Alkali treated $\text{Ti}_3\text{C}_2\text{T}_x$ MXenes and their dye adsorption performance," *Materials Chemistry and Physics*, vol. 206, pp. 270–276, 2018.
- [224] Y. Xu, S. Wang, J. Yang, B. Han, R. Nie, J. Wang, J. Wang, and H. Jing, "In-situ grown nanocrystal TiO_2 on 2D Ti_3C_2 nanosheets for artificial photosynthesis of chemical fuels," *Nano Energy*, vol. 51, pp. 442–450, 2018.
- [225] C. Yang, Y. Liu, X. Sun, Y. Zhang, L. Hou, Q. Zhang, and C. Yuan, "In-situ construction of hierarchical accordion-like $\text{TiO}_2/\text{Ti}_3\text{C}_2$ nanohybrid as anode material for lithium and sodium ion batteries," *Electrochimica Acta*, vol. 271, pp. 165–172, 2018.
- [226] M. Narayanasamy, B. Kirubasankar, M. Shi, S. Velayutham, B. Wang, S. Angaiah, and C. Yan, "Morphology restrained growth of V_2O_5 by the oxidation of V-MXenes as a fast diffusion controlled cathode material for aqueous zinc ion batteries," *Chemical Communications*, vol. 56, pp. 6412–6415, 2020.
- [227] J. Halim, I. Persson, P. Eklund, P. O. Å. Persson, and J. Rosen, "Sodium hydroxide and vacuum annealing modifications of the surface terminations of a Ti_3C_2 (MXene) epitaxial thin film," *RSC Advances*, vol. 8, pp. 36785–36790, 2018.
- [228] J. Luo, C. Fang, C. Jin, H. Yuan, O. Sheng, R. Fang, W. Zhang, H. Huang, Y. Gan, Y. Xia, C. Liang, J. Zhang, W. Li, and X. Tao, "Tunable pseudocapacitance storage of MXene by cation pillaring for high performance sodium-ion capacitors," *Journal of Materials Chemistry A*, vol. 6, pp. 7794–7806, 2018.
- [229] M. Naguib, O. Mashtalir, M. R. Lukatskaya, B. Dyatkin, C. Zhang, V. Presser, Y. Gogotsi, and M. W. Barsoum, "One-step synthesis of nanocrystalline transition metal oxides on thin sheets of disordered graphitic carbon by oxidation of MXenes," *Chemical Communications*, vol. 50, pp. 7420–7423, 2014.
- [230] I. Persson, J. Halim, H. Lind, T. W. Hansen, J. B. Wagner, L.-Å. Näslund, V. Darakchieva, J. Pali-

- saitis, J. Rosen, and P. O. Å. Persson, "2D Transition Metal Carbides (MXenes) for Carbon Capture," *Advanced Materials*, vol. 31, no. 2, p. 1805472, 2019.
- [231] Y. Wang, C. Ma, W. Ma, W. Fan, Y. Sun, H. Yin, X. Shi, X. Liu, and Y. Ding, "Enhanced low-temperature Li-ion storage in MXene titanium carbide by surface oxygen termination," *2D Materials*, vol. 6, no. 4, p. 045025, 2019.
- [232] J. L. Hart, K. Hantanasirisakul, Y. Gogotsi, and M. L. Taheri, "Termination-Property Coupling via Reversible Oxygen Functionalization of MXenes," *ACS Nanoscience Au*, vol. n/a, no. n/a, p. n/a, 2022.
- [233] N. Xue, X. Li, L. Han, H. Zhu, X. Zhao, J. Zhuang, Z. Gao, and X. Tao, "Fluorine-free synthesis of ambient-stable delaminated Ti_2CT_x (MXene)," *Journal of Materials Chemistry A*, vol. 10, pp. 7960–7967, 2022.
- [234] S. Huang and V. N. Mochalin, "Hydrolysis of 2D Transition-Metal Carbides (MXenes) in Colloidal Solutions," *Inorganic Chemistry*, vol. 58, no. 3, pp. 1958–1966, 2019.
- [235] S. Doo, A. Chae, D. Kim, T. Oh, T. Y. Ko, S. J. Kim, D.-Y. Koh, and C. M. Koo, "Mechanism and Kinetics of Oxidation Reaction of Aqueous $Ti_3C_2T_x$ Suspensions at Different pHs and Temperatures," *ACS Applied Materials & Interfaces*, vol. 13, no. 19, pp. 22855–22865, 2021.
- [236] T. Wu, P. R. C. Kent, Y. Gogotsi, and D.-e. Jiang, "How Water Attacks MXene," *Chemistry of Materials*, vol. 34, no. 11, pp. 4975–4982, 2022.
- [237] C. J. Zhang, S. J. Kim, M. Ghidui, M.-Q. Zhao, M. W. Barsoum, V. Nicolosi, and Y. Gogotsi, "Layered Orthorhombic $Nb_2O_5@Nb_4C_3T_x$ and $TiO_2@Ti_3C_2T_x$ Hierarchical Composites for High Performance Li-ion Batteries," *Advanced Functional Materials*, vol. 26, no. 23, pp. 4143–4151, 2016.
- [238] C. J. Zhang, S. Pinilla, N. McEvoy, C. P. Cullen, B. Anasori, E. Long, S.-H. Park, A. Seral-Ascaso, A. Shmeliov, D. Krishnan, C. Morant, X. Liu, G. S. Duesberg, Y. Gogotsi, and V. Nicolosi, "Oxidation Stability of Colloidal Two-Dimensional Titanium Carbides (MXenes)," *Chemistry of Materials*, vol. 29, no. 11, pp. 4848–4856, 2017.
- [239] T. Hu, M. Hu, B. Gao, W. Li, and X. Wang, "Screening Surface Structure of MXenes by High-Throughput Computation and Vibrational Spectroscopic Confirmation," *The Journal of Physical Chemistry C*, vol. 122, no. 32, pp. 18501–18509, 2018.
- [240] T. Hu, Z. Li, M. Hu, J. Wang, Q. Hu, Q. Li, and X. Wang, "Chemical Origin of Termination-Functionalized MXenes: $Ti_3C_2T_2$ as a Case Study," *The Journal of Physical Chemistry C*, vol. 121, no. 35, pp. 19254–19261, 2017.
- [241] A. Blackman and L. Gahan, *Aylward and Findlay's SI Chemical Data*. Milton, QLD, Australia: Wiley, 7 ed., 2013.
- [242] Y. Tian, Y. An, C. Wei, Y. Tao, Y. Zhang, H. Jiang, L. Tan, J. Feng, and Y. Qian, "Stable and dendrite-free lithium metal anodes enabled by carbon paper incorporated with ultrafine lithiophilic TiO_2 derived from MXene and carbon dioxide," *Chemical Engineering Journal*, vol. 406, p. 126836, 2021.
- [243] M. Lu, H. Li, W. Han, J. Chen, W. Shi, J. Wang, X.-M. Meng, J. Qi, H. Li, B. Zhang, W. Zhang, and W. Zheng, "2D titanium carbide (MXene) electrodes with lower-F surface for high performance lithium-ion batteries," *Journal of Energy Chemistry*, vol. 31, pp. 148–153, 2019.

- [244] Y. Lee, S. J. Kim, Y.-J. Kim, Y. Lim, Y. Chae, B.-J. Lee, Y.-T. Kim, H. Han, Y. Gogotsi, and C. W. Ahn, "Oxidation-resistant titanium carbide MXene films," *Journal of Materials Chemistry A*, vol. 8, pp. 573–581, 2020.
- [245] F. H. Fagerli, Z. Wang, T. Grande, H. Kaland, S. M. Selbach, N. P. Wagner, and K. Wiik, "Removing Fluoride-Terminations from Multilayered V_2CT_x MXene by Gas Hydrolyzation," *ACS Omega*, vol. 7, no. 27, pp. 23790–23799, 2022.
- [246] N. C. Osti, M. Naguib, A. Ostadhossein, Y. Xie, P. R. C. Kent, B. Dyatkin, G. Rother, W. T. Heller, A. C. T. van Duin, Y. Gogotsi, and E. Mamontov, "Effect of Metal Ion Intercalation on the Structure of MXene and Water Dynamics on its Internal Surfaces," *ACS Applied Materials & Interfaces*, vol. 8, no. 14, pp. 8859–8863, 2016.
- [247] N. C. Osti, M. Naguib, K. Ganeshan, Y. K. Shin, A. Ostadhossein, A. C. T. van Duin, Y. Cheng, L. L. Daemen, Y. Gogotsi, E. Mamontov, and A. I. Kolesnikov, "Influence of metal ions intercalation on the vibrational dynamics of water confined between MXene layers," *Physical Review Materials*, vol. 1, p. 065406, 2017.
- [248] A. Wexler, "Vapor Pressure Formulation for Water in Range 0 to 100 °C. A Revision," *Journal of research of the National Bureau of Standards - A, Physics and chemistry*, vol. 80A, no. 5, pp. 775–785, 1976.
- [249] J. Yeh, *Atomic Calculation of Photoionization Cross-sections and Asymmetry Parameters*. Gordon & Breach Science, Publishers. ISBN: 9782881245855, 1993.
- [250] C. God, B. Bitschnau, K. Kapper, C. Lenardt, M. Schmuck, F. Mautner, and S. Koller, "Intercalation behaviour of magnesium into natural graphite using organic electrolyte systems," *RSC Advances*, vol. 7, pp. 14168–14175, 2017.
- [251] D.-M. Kim, S. C. Jung, S. Ha, Y. Kim, Y. Park, J. H. Ryu, Y.-K. Han, and K. T. Lee, "Cointercalation of Mg^{2+} Ions into Graphite for Magnesium-Ion Batteries," *Chemistry of Materials*, vol. 30, no. 10, pp. 3199–3203, 2018.
- [252] D. Sun, Q. Hu, J. Chen, X. Zhang, L. Wang, Q. Wu, and A. Zhou, "Structural Transformation of MXene (V_2C , Cr_2C , and Ta_2C) with O Groups during Lithiation: A First-Principles Investigation," *ACS Applied Materials & Interfaces*, vol. 8, no. 1, pp. 74–81, 2016.
- [253] J. Hu, B. Xu, C. Ouyang, S. A. Yang, and Y. Yao, "Investigations on V_2C and V_2CX_2 ($X = F, OH$) Monolayer as a Promising Anode Material for Li Ion Batteries from First-Principles Calculations," *The Journal of Physical Chemistry C*, vol. 118, no. 42, pp. 24274–24281, 2014.
- [254] B. Yan, C. Lu, P. Zhang, J. Chen, W. He, W. Tian, W. Zhang, and Z. Sun, "Oxygen/sulfur decorated 2D MXene V_2C for promising lithium ion battery anodes," *Materials Today Communications*, vol. 22, p. 100713, 2020.
- [255] A. O. Tezel, D. K. Streich, A. Guéguen, M. Hahlin, S. Sunde, K. Edström, P. Novák, and A. M. Svensson, "Solid Electrolyte Interphase (SEI) Formation on the Graphite Anode in Electrolytes Containing the Anion Receptor Tris(hexafluoroisopropyl)borate (THFIPB)," *Journal of The Electrochemical Society*, vol. 167, no. 13, p. 130504, 2020.
- [256] R. Bernhard, M. Metzger, and H. A. Gasteiger, "Gas Evolution at Graphite Anodes Depending on

- Electrolyte Water Content and SEI Quality Studied by On-Line Electrochemical Mass Spectrometry,” *Journal of The Electrochemical Society*, vol. 162, no. 10, pp. A1984–A1989, 2015.
- [257] H. Li, S. Chen, D. W. Boukhvalov, Z. Yu, M. G. Humphrey, Z. Huang, and C. Zhang, “Switching the Nonlinear Optical Absorption of Titanium Carbide MXene by Modulation of the Surface Terminations,” *ACS Nano*, vol. 16, no. 1, pp. 394–404, 2022.
- [258] T. Hu, J. Wang, H. Zhang, Z. Li, M. Hu, and X. Wang, “Vibrational properties of Ti_3C_2 and $\text{Ti}_3\text{C}_2\text{T}_2$ (T = O, F, OH) monosheets by first-principles calculations: a comparative study,” *Physical Chemistry Chemical Physics*, vol. 17, pp. 9997–10003, 2015.
- [259] A. Sarycheva and Y. Gogotsi, “Raman Spectroscopy Analysis of the Structure and Surface Chemistry of $\text{Ti}_3\text{C}_2\text{T}_x$ MXene,” *Chemistry of Materials*, vol. 32, no. 8, pp. 3480–3488, 2020.
- [260] Z. Li, L. Wang, D. Sun, Y. Zhang, B. Liu, Q. Hu, and A. Zhou, “Synthesis and thermal stability of two-dimensional carbide MXene Ti_3C_2 ,” *Materials Science and Engineering: B*, vol. 191, pp. 33–40, 2015.
- [261] J. Wang, J. Polleux, J. Lim, and B. Dunn, “Pseudocapacitive Contributions to Electrochemical Energy Storage in TiO_2 (Anatase) Nanoparticles,” *The Journal of Physical Chemistry C*, vol. 111, no. 40, pp. 14925–14931, 2007.
- [262] F. Kong, X. He, Q. Liu, X. Qi, Y. Zheng, R. Wang, and Y. Bai, “Improving the electrochemical properties of MXene Ti_3C_2 multilayer for Li-ion batteries by vacuum calcination,” *Electrochimica Acta*, vol. 265, pp. 140–150, 2018.
- [263] Z. Guan, X. Wang, T. Li, Q. Zhu, M. Jia, and B. Xu, “Facile synthesis of rutile TiO_2 /carbon nanosheet composite from MAX phase for lithium storage,” *Journal of Materials Science & Technology*, vol. 35, no. 9, pp. 1977–1981, 2019.
- [264] Y. Liu and Y. Yang, “Recent Progress of TiO_2 -Based Anodes for Li Ion Batteries,” *Journal of Nanomaterials*, vol. 2016, p. 8123652, 2016.
- [265] Y. Li, X. Deng, J. Tian, Z. Liang, and H. Cui, “ Ti_3C_2 MXene-derived $\text{Ti}_3\text{C}_2/\text{TiO}_2$ nanoflowers for noble-metal-free photocatalytic overall water splitting,” *Applied Materials Today*, vol. 13, pp. 217–227, 2018.
- [266] Y. Dong, Z.-S. Wu, S. Zheng, X. Wang, J. Qin, S. Wang, X. Shi, and X. Bao, “ Ti_3C_2 MXene-Derived Sodium/Potassium Titanate Nanoribbons for High-Performance Sodium/Potassium Ion Batteries with Enhanced Capacities,” *ACS Nano*, vol. 11, no. 5, pp. 4792–4800, 2017.
- [267] X. Chen, L. Liu, and F. Huang, “Black titanium dioxide (TiO_2) nanomaterials,” *Chemical Society Reviews*, vol. 44, pp. 1861–1885, 2015.
- [268] I. Michos, Z. Cao, Z. Xu, W. Jing, and J. Dong, “Investigations on a mesoporous glass membrane as ion separator for a redox flow battery,” *Batteries*, vol. 5, no. 1, 2019.
- [269] Y. Cao, S. Wei, Q. Zhou, P. Zhang, C. Wang, K. Zhu, W. Xu, X. Guo, X. Yang, Y. Wang, X. Wu, S. Chen, and L. Song, “Ti-Cl Bonds decorated Ti_2NT_x MXene towards high-performance lithium-ion batteries,” *2D Materials*, 2022.

Appended papers


Paper I

H. Kaland, J. Hadler-Jacobsen, F. H. Fagerli, N. P. Wagner, Z. Wang, S. M. Selbach, F. Vullum-Bruer, K. Wiik and S. K. Schnell

Are MXenes Suitable as Cathode Material for Rechargeable Mg Batteries?

Reprinted from Sustainable Energy & Fuels **4**, 6, 2956-2966 (2020).

DOI: [10.1039/D0SE00087F](https://doi.org/10.1039/D0SE00087F)





PAPER



Cite this: *Sustainable Energy Fuels*,
2020, 4, 2956

Are MXenes suitable as cathode materials for
rechargeable Mg batteries?^{†‡}

Henning Kaland,^{‡a} Jacob Hadler-Jacobsen,^{‡a} Frode Håskjold Fagerli,^{‡a}
Nils P. Wagner,^{ab} Zhaohui Wang,^{ac} Sverre M. Selbach,^a Fride Vullum-Bruer,^{ad}
Kjell Wiik^{*a} and Sondre Kvalvåg Schnell^{‡a}

MXenes, a type of two-dimensional transition metal carbide/nitride, have received significant attention for electrochemical storage applications. With substantial capacities predicted for Mg ions, MXenes have been considered a promising candidate for cathode materials for rechargeable Mg batteries (RMBs). While there have been reports demonstrating reversible capacities of 100–200 mA h g⁻¹ for MXene-based cathodes, the understanding of the reactions occurring is limited. Here, we investigate unsolvated Mg²⁺ intercalation into multi-layered, non-delaminated MXene particles by electrochemical characterization of two common MXenes (Ti₃C₂T_x and V₂CT_x) with various electrolytes and at elevated temperatures, complemented by DFT calculations. Our experimental results show poor reversible capacities (<5 mA h g⁻¹) both at room temperature and at 60 °C, indicating that no intercalation of Mg ions occurs during cycling. DFT simulations show that Ti₃C₂T₂ with fluorine and hydroxyl termination groups has a negative average voltage for Mg²⁺ and reveal high migration barriers for oxygen termination groups, supporting the experimental results. The DFT calculations also reveal that upon magnesium intercalation in multi-layered V₂CF₂ and V₂C(OH)₂, MgF₂ or MgH₂ is formed rather than the electrochemical intercalation of Mg²⁺. However, multi-layered V₂CO₂ is found to have both a relatively high theoretical average voltage (~1.5 V) and a comparatively low migration barrier of 480 meV, allowing for Mg²⁺ intercalation and RMBs with energy densities comparable to Li-ion batteries. The findings emphasize the need to fully control the MXene termination groups. The possible reasons for the unsatisfactory and deviant electrochemical performance reported in this work and in the literature are critically reviewed to assess the feasibility of MXene cathodes for energy-dense RMBs.

Received 16th January 2020
Accepted 17th March 2020

DOI: 10.1039/d0se00087f

rscl.li/sustainable-energy

1 Introduction

Lithium-ion batteries (LiBs) currently represent state-of-the-art rechargeable battery technology but are still limited by factors such as safety and insufficient availability of raw materials.¹ With the expected increase in demand for electric vehicles and grid energy,² these limitations may render LiBs inapplicable as the sole solution for rechargeable battery systems. None of the current alternatives are able to compete with the energy density, power density, cycle life and cost of LiBs. However, the theoretical properties and advantage of environmentally friendly

compositions of various alternative battery technologies still make them attractive candidates for further investigations.^{3,4} One of these interesting battery technologies is rechargeable magnesium batteries (RMBs), due to the abundance of Mg in the Earth's crust, its low cost and the fact that Mg metal is less prone to form dendrites upon cycling than Li metal.^{5–7} The latter may enable safe operation of Mg metal anodes, which greatly outperforms today's graphite anode in LiBs in terms of both gravimetric (2205 vs. 372 mA h g⁻¹) and volumetric capacity (3833 vs. 800 mA h cm⁻³).³ Together with the low reduction potential of Mg metal,⁸ this opens up the possibility to have energy-dense batteries based on RMB technology.

Despite the compelling electrode properties of the Mg metal anode, RMBs still face significant challenges in terms of finding compatible electrolytes and suitable cathode materials.^{3,9} Due to the formation of impermeable layers on the Mg anode using common electrolyte salts and solvents, the number of candidates that demonstrate reversible plating/stripping of Mg have generally been limited to ethereal solutions of Mg salts based on Grignard reagents or hydride anions.^{10–14} The voltage window of these electrolytes is typically limited to around 2–3 V vs. Mg/

^aDepartment of Materials Science and Engineering, NTNU Norwegian University of Science and Technology, NO-7491, Trondheim, Norway. E-mail: sondre.k.schnell@ntnu.no

^bSINTEF Industry, Sustainable Energy Technology, NO-7465, Trondheim, Norway

^cSINTEF Industry, Metal Production and Processing, NO-7465, Trondheim, Norway

^dSINTEF Energy Research, Thermal Energy, NO-7465, Trondheim, Norway

[†] Electronic supplementary information (ESI) available: A full description of the experimental and computational methods used in this work. Additional figures and tables are also included there. See DOI: 10.1039/d0se00087f

[‡] These authors contributed equally to this work.

Mg²⁺, which therefore leads to the need for high capacity cathode materials in order to have a competitive energy density compared to LiBs.

To date, only a limited number of cathode materials have shown reversible electrochemical reactions with Mg ions. After the pioneering work of Gregory *et al.*, demonstrating reversible operation in 1990,¹⁵ the first practical RMB prototype is often attributed to the work of Aurbach *et al.* in 2000,¹⁶ who reported excellent cyclability and fast kinetics for their Mo₆S₈ Chevrel phase cathode. Despite its relatively low capacity and operating voltage, it remains one of the best candidates for a secondary battery based on Mg. Since then, various chalcogenides and oxides have been investigated,^{17–20} but while chalcogenides generally suffer from too low operating potentials, the oxides only work at extremely low current densities due to high Mg²⁺ migration barriers.⁸ Moreover, cathode materials relying on conversion reactions, particularly sulfur, have gained interest.^{21–26} However, detrimental soluble Mg polysulfides inhibit the cycling performance and the practical application of Mg–S batteries.²⁷ Consequently, there is still an urgent need for Mg cathode materials with sufficient capacity, kinetics and cyclability to enable competitive RMBs.

One interesting group of materials for RMB cathodes is transition metal carbides, carbonitrides, and nitrides known as MXenes. Since their discovery in 2011,²⁸ numerous structures have been investigated as electrode materials for various battery chemistries due to their unique two-dimensional structure offering high electronic conductivity, hydrophilicity, tunability and good mechanical strength.^{29–33} MXenes have a general composition of M_{n+1}X_nT_x (*n* = 1,2,3), where M represents an early transition metal (*i.e.* Sc, Ti, V, Cr, Nb, and Mo), X represents carbon and/or nitrogen and T is the surface terminating ion (F, O, and/or OH).³⁴ Due to their versatile structural possibilities and tunable surface chemistry, MXenes have been proposed as candidates in a range of applications from sensors to catalysts, as conductive additives and as electrode materials in both supercapacitors and rechargeable batteries.^{29,32,35} Screening of the intercalation properties of MXenes has shown promising theoretical capacities for Mg-ion intercalation (>400 mA h g^{−1}),^{36,37} which therefore have attracted interest for RMB research.

The first report on using MXenes as cathode materials with Mg²⁺ containing etheral solvents was by Byeon *et al.*³⁸ With the conventional APC-THF electrolyte, negligible capacities were reported for their freestanding film of a delaminated Ti₃C₂T_x/carbon nanotube composite cathode. With the addition of 0.4 M LiCl to the electrolyte, significant capacities were observed, assigned solely to Li⁺ intercalation by energy-dispersive X-ray spectroscopy (EDX).³⁸ Recently, several studies have reported similar initial capacities for pristine Ti₃C₂T_x, all tested with the APC-THF electrolyte at room temperature.^{39–41} By pre-incorporation of large organic molecules (*e.g.* cationic surfactants,⁴⁰ and phenyl–MgCl from the electrolyte⁴¹) or even carbon nanospheres,³⁹ reversible capacities of 100–200 mA h g^{−1} have been reported. However, all the mentioned studies have utilized delaminated Ti₃C₂T_x, and combined it with the mentioned spacer molecules/structures to obtain

a highly porous structure with a large surface area. The reported voltage profiles differ substantially, and the proposed charge storage mechanisms deviate accordingly: Mg ion intercalation assisted by cetyltrimethylammonium (CTA⁺), phenyl–MgCl intercalation, or a combined intercalation and conversion reaction.^{39–41} This raises a critical question about the possibility of unsolvated Mg²⁺ intercalation in MXenes, *versus* predominantly surface reactions and/or intercalation of complex ions. In order to enable competitive energy-dense Mg batteries, intercalation of unsolvated and non-complexed Mg²⁺ ions is necessary. Highly porous structures should therefore be avoided, favouring multi-layered MXenes compared to their delaminated counterpart.

In this paper, a systematic investigation on the feasibility of Mg²⁺ intercalation in MXenes for practical rechargeable Mg batteries is presented, combining experiments and Density Functional Theory (DFT) calculations. First, the MXene structure and morphology is explained before the proposed charge storage mechanism of MXenes for Mg batteries from the literature is critically reviewed. Then, we investigate unsolvated Mg²⁺ intercalation in Ti₃C₂T_x, which is the most studied MXene, as well as in V₂C₂T_x. The effects of an elevated temperature and electrolytes with different electroactive species are reported. The influence of termination groups (F, O, and OH) on Mg²⁺ migration barriers and operating voltages is assessed for both Ti₃C₂T_x and V₂C₂T_x MXenes. Migration barriers for Li⁺ and MgCl⁺ are also reported to gain further insights into the ion intercalation properties of MXenes and to resolve some of the discrepancies in the reported charge storage mechanisms. The complex relations between the MXene transition metal, the termination groups, and single-layer (*i.e.* delaminated) *versus* multi-layer MXene, and their effect on Mg²⁺ migration barriers and average operating voltages are studied. The findings reveal inherent challenges with some MXene compositions, whereas others stand out as possibly viable cathode candidates. Our work thus provides directions for further efforts to enable MXene cathode materials for rechargeable Mg batteries.

2 Results and discussion

2.1 Structure, intercalation and surface reactions

The peculiar structure of MXenes and different electrolyte–MXene interactions can give rise to different charge storage mechanisms, and may explain some of the deviant electrochemical performance reported for MXene electrodes. Thus, a brief overview on the proposed charge storage mechanism for Li ions in MXenes is presented before the reported work on MXenes as RMB cathodes is critically reviewed.

A typical Ti₃C₂T_x MXene particle is illustrated in Fig. 1, synthesized by conventional HF etching of the respective Ti₃AlC₂ MAX phase^{28,42} (experimental details in the ESI†). The accordion-like morphology is a result of the H₂ evolution during etching,²⁸ which gives rise to an open structure. Noteworthy, these easily observed large spacings from partly delaminated stacks (ranging from 30–500 nm, referred to as the interstack distance, should not be interchanged with the interlayer distance between each individual MXene layer (0.9–1.6 nm,

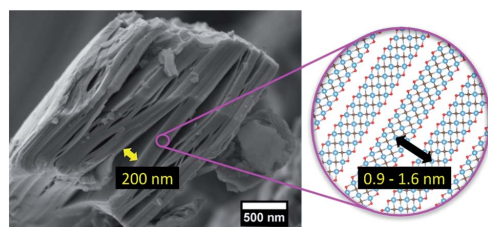


Fig. 1 Illustrating the difference between the interlayer distance between $\text{Ti}_3\text{C}_2\text{T}_x$ atomic layers (0.9–1.6 nm) and the spacing between stacks of multiple MXene atomic layers (30–500 nm), denoted by the interstack distance, which is visible via SEM.

shown in the inset in Fig. 1). True Mg^{2+} intercalation in MXenes should refer to Mg^{2+} insertion between the individual MXene layers, whereas the capacity obtained from electrochemical reactions between the stacks will be dominated by adsorption giving pseudocapacitive and/or electrical double-layer charge-storage.

Recently, Okubo *et al.* discussed the deviant voltage profiles reported for MXenes, with an emphasis on Li- and Na-ion intercalation.⁴³ For aqueous electrolytes, they state that solvated cations intercalate between the individual MXene layers, resulting in a large change in interlayer distance, as well as a change in the oxidation state of the metal atom in the MXene. In contrast, in nonaqueous electrolytes, solvated cations may initially intercalate, but the solvation shell quickly collapses and the desolvated cations continue to intercalate between the MXene layers. Okubo *et al.* named the charge storage mechanism of MXenes in nonaqueous electrolytes after the concept proposed by Augustyn *et al.*: intercalation pseudocapacitance.⁴⁴ This mechanism is reversible and occurs through ultrafast intercalation of cations with minor structural distortions, little to no diffusion limitations, and a change in the oxidation state of the intercalation host material. A similar charge storage mechanism may be postulated for Mg ions. However, the reported voltage profiles for non-aqueous Mg electrolytes deviate and the charge-storage mechanism is far from resolved,^{39–41} which will be discussed in the following sections.

Recently, substantial capacities were reported for $\text{Ti}_3\text{C}_2\text{T}_x$ MXene for RBMs, enabled by the pre-intercalation of organic molecules or carbon nanospheres.^{39,40} Xu *et al.* reported a cetyltrimethylammonium bromide (CTAB) pre-intercalated $\text{Ti}_3\text{C}_2\text{T}_x$ paper electrode with reversible capacities of $\sim 100 \text{ mA h g}^{-1}$ and a sloping voltage profile.⁴⁰ Through X-ray photoelectron spectroscopy (XPS) and DFT-simulations, it was proposed that the intercalated surfactant cation, CTA^+ , can induce charge transfer from CTA^+ to the MXene. This lowered the Mg diffusion barrier and enabled Mg-ion intercalation, either in the form of unsolvated Mg^{2+} or Mg^{2+} complexed with anions/solvent molecules. The *post mortem* XRD study at different states of charge supported a non-trivial reaction mechanism, where the *d*-spacing of the MXene changed substantially and the original crystallinity

was not recovered after charging. Liu *et al.* incorporated CTAB-grafted carbon nanospheres with $\text{Ti}_3\text{C}_2\text{T}_x$ and obtained capacities of around 200 mA h g^{-1} with a similar sloping voltage profile.³⁹ The increase in MXene *d*-spacing (0.19 nm) of the $\text{Ti}_3\text{C}_2\text{T}_x$ /carbon nanosphere composite was assigned to the intercalation of carbon nanospheres, and it was proposed that the expanded interlayers could provide additional diffusion paths and insertion sites for Mg^{2+} ions. However, it is not clear if the increased *d*-spacing and improved performance is better explained by the intercalation of CTAB, given the similar *d*-spacing increase (0.20 nm) and observed voltage profile by Xu *et al.*⁴⁰ This is further strengthened by the size of the carbon nanospheres, ranging from 100–700 nm in diameter. Still, the carbon nanospheres may seem to preserve the original crystallinity of $\text{Ti}_3\text{C}_2\text{T}_x$ during cycling, as evidenced by *post mortem* XRD. The capacity from non-diffusion processes dominated for both reported structures, ranging from 54–82% (ref. 40) to 55–92% (ref. 39) (depending on the scan rate), which indicates predominantly surface-controlled charge storage and limited Mg-ion intercalation. Besides, if the CTA^+ contributes nearly equally compared to the Mg ions to the charge storage,⁴⁰ the practically obtainable energy density will suffer, as the charge is stored in the electrolyte.

Another noteworthy attempt to enable MXene cathodes for RBMs was recently reported by Zhao *et al.*, demonstrating a 3D macroporous $\text{Ti}_3\text{C}_2\text{T}_x$ paper cathode with clear voltage plateaus and reversible capacities around 200 mA h g^{-1} .⁴¹ The paper cathode was fabricated through a sacrificial template method, obtaining a porosity of around 90%. The highly porous paper was soaked in APC-THF, which led to increased MXene *d*-spacing (from 1.36 to 1.55 nm) and substantial amounts of Mg, Al and Cl were observed by EDX. This was assigned to the pre-intercalation of whole salt molecules from the electrolyte such as (phenyl-MgCl)₂AlCl₃, which subsequently enabled the observed capacities. Through *post mortem* EDX, it was proposed that a reversible intercalation/deintercalation of phenyl-MgCl in the first set of discharge/charge plateaus at 2/2.4 V and a partly irreversible redox reaction between Mg-ions and $\text{Ti}_3\text{C}_2\text{T}_x$ in the second set at 0.8/1.9 V occurred. Thus, a reversible intercalation combined with a partly irreversible conversion mechanism was suggested. Still, the need for more evidence of the redox reactions between Mg ions and MXenes was correctly emphasized. For example, the theoretical capacity of $\text{Ti}_3\text{C}_2\text{T}_x$, with equal amounts of F, O, and OH terminations is 202 mA h g^{-1} , assuming one Mg ion per $\text{Ti}_3\text{C}_2\text{T}_x$. At full discharge, a modest Mg content of 0.38 per $\text{Ti}_3\text{C}_2\text{T}_x$ formula unit was reported, yet a capacity of $\sim 200 \text{ mA h g}^{-1}$ was achieved, indicative of a substantial amount of other electrochemical reactions. Still, the capacity from the first set of discharge/charge plateaus ($\sim 45 \text{ mA h g}^{-1}$) matches reasonably well with that of a one-electron reaction from a 0.38 content of the MgCl compound (40 mA h g^{-1}), justifying the proposed reversible phenyl-MgCl intercalation. For the remaining capacity, a careful *in situ* study may be needed to completely rule out contributions from residual H_2O /proton cycling, or side reactions due to the wide voltage window used.

In summary, the suitability of MXenes as a potential cathode for RBMs is yet to be determined. The above discussion raises a critical question about the feasibility of Mg^{2+} intercalation for practical RBMs, which will now be addressed.

2.2 Electrochemical performance and *post mortem* analysis

To assess the suitability of MXenes as intercalation cathodes for Mg batteries, non-delaminated $\text{Ti}_3\text{C}_2\text{T}_x$ powders were tested in coin cells with standard ethereal Mg electrolytes. $\text{Ti}_3\text{C}_2\text{T}_x$ MXene was synthesized by conventional HF etching of the respective Ti_3AlC_2 MAX phase based on previously established methods,^{28,42} and this is described in detail in the ESI.† Prior to the etching step, ball milling of the Ti_3AlC_2 MAX phase was carried out to ensure a narrow particle size distribution of 6 ± 2 μm , as shown in Fig. 2a and S1 (ESI†). The milled Ti_3AlC_2 was subsequently etched with 10 wt% HF for 24 h, yielding $\text{Ti}_3\text{C}_2\text{T}_x$ MXene with high phase purity, controlled size distribution and the characteristic accordion-like morphology (Fig. 2b). The left-shift of the (002) reflection from $2\theta_{\text{Ti}_3\text{AlC}_2} = 9.5^\circ$ to $2\theta_{\text{Ti}_3\text{C}_2\text{T}_x} = 9.2^\circ$ (Fig. 2c), corroborated by EDX measurements supporting the absence of aluminium (Table S1†), confirmed the complete conversion of the MAX phase to the MXene. $\text{Ti}_3\text{C}_2\text{T}_x$ cathodes were prepared by wet mixing the MXene powder (80 wt%) with carbon black (10 wt%) and polyvinylidene fluoride (PVDF) (10 wt%) in 1-ethyl-2-pyrrolidone (NEP), before drop casting the

slurry on graphite current collector discs. The dried cathodes were electrochemically characterized with a conventional APC-THF electrolyte at a low current density of 10 mA g^{-1} MXene in a voltage window of 0.2 to 2.1 V vs. Mg/Mg^{2+} . The resulting voltage profiles are depicted in Fig. 3a, demonstrating limited capacities, both at room temperature as well as at an elevated temperature of 60°C . The initial capacity is slightly higher, approaching 9 mA h g^{-1} at 60°C , but it stabilizes at 3 mA h g^{-1} from the second cycle, with an overall sloped voltage profile. Applying a potentiostatic hold step at 1 mV for 200 h, to allow sluggish Mg^{2+} diffusion to occur, resulted in increased capacities as seen in Fig. 3b. The inset shows how the cathodic current decreases exponentially before stabilizing at $\sim 0.3 \mu\text{A}$ during the 200 h hold step. However, *post mortem* analysis showed no change in the interlayer distance of $\text{Ti}_3\text{C}_2\text{T}_x$ (Fig. 3e), but rather a subtle change in the interlayer Bragg-reflection for graphite (Fig. S3†), and indication of electrolyte side reactions on the cell bottom casing (Fig. S6†). Also considering the similar voltage profile and obtained capacities for a carbon black reference electrode (90 wt% carbon black and 10 wt% PVDF on the same graphite paper current collector, shown in Fig. S4†), Mg^{2+} intercalation in $\text{Ti}_3\text{C}_2\text{T}_x$ MXene is precluded for APC-THF. This is consistent with the majority of earlier work on pristine $\text{Ti}_3\text{C}_2\text{T}_x$ without preintercalation of large molecules cycled in a similar voltage window.^{38–40} The discrepancy of the electrochemical performance with the work of Zhao *et al.*⁴¹ is not clear. An initial negligible capacity was reported, but the capacity increased to $>100 \text{ mA h g}^{-1}$ even with no preintercalation. It is speculated that the reported highly porous structure ($\sim 90\%$ porosity) and a large surface area are partly responsible for these capacities, in addition to the already discussed uncertainty in the reaction mechanism.

Given the complex and critical interaction between the cathode and the electrolyte, several other electrolytes were also prepared, verified (Fig. S2†) and tested (Fig. 3c). In the intercalation process, the Mg ions in the electrolyte must desolvate from the surrounding solvent molecules and/or anions before intercalating into the cathode structure. This critical process may be strongly influenced by the cathode material⁴⁵ and has not been addressed in the reported work on MXene cathodes so far.^{38–41} $\text{Mg}(\text{TFSI})_2\text{-}2\text{MgCl}_2\text{-DME}$ contains predominantly the same electroactive cations as APC-THF, namely MgCl^+ and/or Mg_2Cl_3^+ ,^{11,46} but is solvated by DME instead of THF. As shown by Wang *et al.*, DME displays substantially lower interaction energies with the Mg_2Cl_3^+ dimer compared to THF,⁴⁷ which can aid the desolvation process. However, $\text{Mg}(\text{TFSI})_2\text{-}2\text{MgCl}_2\text{-DME}$ displayed the same electrochemical behaviour as APC-THF (Fig. 3c). A thorough evaluation of the few Mg cathode materials verified to display unsolvated Mg^{2+} intercalation, emphasized the necessity of the cathode material's catalytic ability to break the strong ionic Mg-Cl bond prior to Mg^{2+} intercalation.⁴⁵ The Cl-free $\text{Mg}(\text{BH}_4)_2\text{-THF}$ electrolyte avoids this issue, having electroactive cations of solvated $[\text{Mg}\{(\mu\text{-H})_2\text{BH}_2\}]^+$ and Mg^{2+} .¹² Still, the obtained capacities with this electrolyte were even lower (Fig. 3c). Noteworthy, the BMOC-DME electrolyte enabled a relatively high first discharge capacity of nearly 30 mA h g^{-1} ,

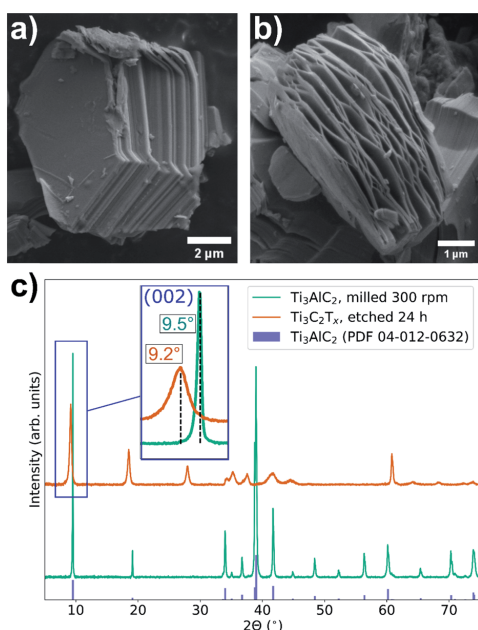


Fig. 2 SEM micrographs of (a) the Ti_3AlC_2 MAX phase after milling at 300 rpm for 2 h, (b) the $\text{Ti}_3\text{C}_2\text{T}_x$ MXene after etching with 10 wt% HF for 24 h showing the accordion-like morphology, and (c) X-ray diffractograms of both compounds confirming the shift of the (002) reflection to a larger d -spacing after etching (inset).

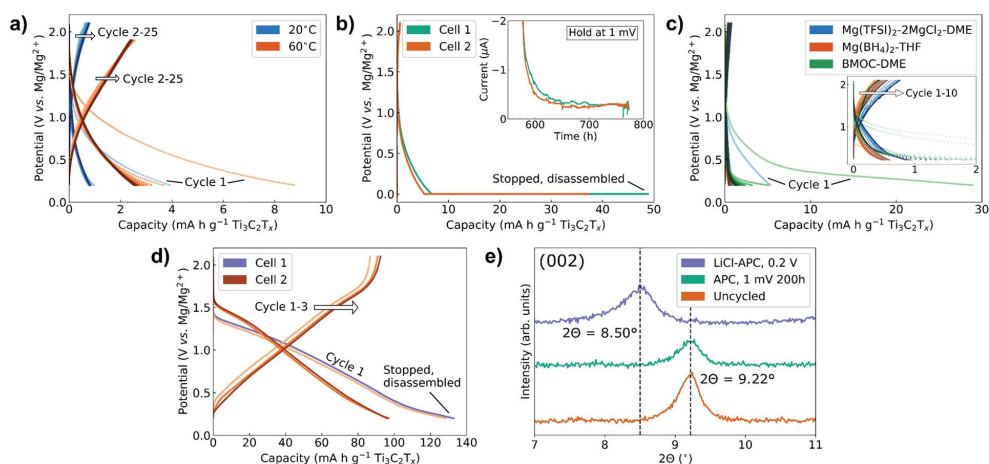


Fig. 3 Voltage profiles of $\text{Ti}_3\text{C}_2\text{T}_x$ with APC-THF electrolyte; (a) at 20 °C (blue colour gradient) and 60 °C (orange colour gradient) and (b) at 20 °C with a 200 h potentiostatic hold step on 1 mV (inset: cathodic current, thereby negative, as a function of time during the 200 h hold step). (c) Voltage profiles of the first ten cycles of $\text{Ti}_3\text{C}_2\text{T}_x$ with electrolytes of $\text{Mg}(\text{TFSI})_2\text{-}2\text{MgCl}_2\text{-DME}$ (blue colour gradient), $\text{Mg}(\text{BH}_4)_2\text{-THF}$ (orange colour gradient) and BMOc-DME (green colour gradient), where the inset magnifies the cycling $<2\text{ mA h g}^{-1}$. (d) APC-THF electrolyte with 0.4 M LiCl (showing two cells, where “Cell 1” was disassembled after the 1st discharge). (e) *Post mortem* XRD showing the (002) reflection of $\text{Ti}_3\text{C}_2\text{T}_x$ of an uncycled cell (orange), after the 200 h potentiostatic hold step on 1 mV with APC-THF (cyan, “Cell 1” in (b)), and after being discharged to 0.2 V with APC-THF with 0.4 M LiCl (purple, “Cell 1” in (d)). The colour gradients in (a), (c) and (d) represent increasing the cycle number.

together with a voltage plateau near the cut-off voltage of 0.2 V. The electroactive species of the BMOc-DME electrolyte has been proposed to be $[\text{Mg}(\text{DME})_n]^{2+}$ after a conditioning process.⁴⁸ This species circumvents the need of dissociating Mg^{2+} from Cl^- , in addition to benefiting the presumably lower desolvation energy with DME compared to THF. Lowering the cut-off voltage to 0.01 V vs. Mg/Mg^{2+} revealed the appearance of distinct voltage plateaus both on discharge and charge (Fig. S5a†). Interestingly, *post mortem* XRD proved the intercalation to be in the graphite current collector rather than the MXene (Fig. S5b†), where the voltage profile and graphite peak change resemble recent reports on co-intercalation of Mg^{2+} with DME/DMF in graphite.^{49,50} In summary, unsolvated Mg^{2+} intercalation in pristine $\text{Ti}_3\text{C}_2\text{T}_x$ MXene was not observed, independent of elevated temperatures and electrolytes.

For comparison, 0.4 M LiCl was added to the APC-THF electrolyte, based on a previous report.³⁸ With this electrolyte, reversible capacities approaching 100 mA h g^{-1} were obtained (Fig. 3d). A distinct left-shift of the (002) reflection (Fig. 3e) is assigned to Li^+ intercalation in $\text{Ti}_3\text{C}_2\text{T}_x$, as also shown by Byeon *et al.*³⁸ Substantially higher capacities were observed in this work, comparing the performances of pristine $\text{Ti}_3\text{C}_2\text{T}_x$ ($\sim 120\text{ mA h g}^{-1}$ vs. $\sim 35\text{ mA h g}^{-1}$ at 10 mA g^{-1}). Importantly, as the charge originates from the Li^+ in the electrolyte, the measured capacity is determined by the concentration of LiCl, the amount of electrolyte and the loading of $\text{Ti}_3\text{C}_2\text{T}_x$ per electrode. The electrolyte amount was not reported in the study by Byeon *et al.*, but a similar coin cell (CR2016) and separator (glass fibre) were used, which suggests a similar electrolyte amount. The LiCl concentration was identical, but the $\text{Ti}_3\text{C}_2\text{T}_x$

loading was 2–3 times higher in the study by Byeon *et al.*, offering a likely explanation for the higher capacities reported here. Noteworthy, considering the amount and concentration of LiCl in the electrolyte and the loading of $\text{Ti}_3\text{C}_2\text{T}_x$ in our work, a capacity of $\sim 560\text{ mA h g}^{-1}$ can be obtained solely by Li ions, assuming complete utilization of all Li ions in the electrolyte. This justifies the assignment of the capacity solely to Li ions. Besides, a carbon black reference electrode (90 wt% carbon black and 10 wt% PVDF on the same graphite paper current collector) demonstrates a significantly different voltage profile and much lower capacities with the same electrolyte (Fig. S4†), indicating negligible capacity contribution from Li^+ intercalation in the carbon black and/or graphite current collector within the 0.2–2.1 V vs. Mg/Mg^{2+} cycling window.

2.3 Migration barriers, average voltages and side reactions

The absence of Mg^{2+} intercalation in $\text{Ti}_3\text{C}_2\text{T}_x$ MXene was further examined by DFT calculations (see the ESI† for details). DFT is well suited to find a range of relevant battery material properties.⁵¹ Migration barriers, intercalation energies and average voltages were investigated for both Mg^{2+} and Li^+ in $\text{Ti}_3\text{C}_2\text{T}_2$ and V_2CT_2 with T = F, O and OH surface terminations. Geometrical relaxation was performed, which enabled the identification of side reactions. The utilized unit cells are shown in Fig. S9 in the ESI†, where the MXene layers are stacked as mirror images of each other with the Mg layers as the mirror plane (Fig. S13†). This corresponds to the stacking found experimentally for Na^+ intercalated in $\text{Ti}_3\text{C}_2\text{T}_x$.⁵² Phonon calculations^{53,54} were carried out to explore the dynamic stability of the MXene layers (Fig. S14†). To gain further understanding of the MXene

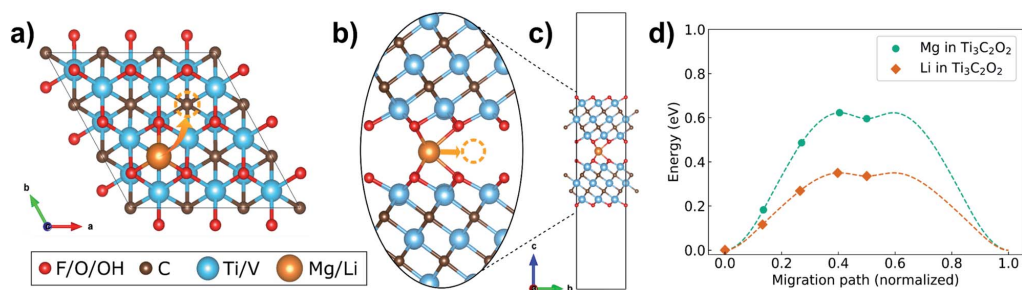


Fig. 4 (a) Top view of a single-layer/multi-layer MXene showing Mg/Li migration from one C-site to another C-site *via* the M-site. (b) Side view of the same in a multi-layer MXene ($\text{Ti}_3\text{C}_2\text{O}_2$ shown). (c) Unit cell used for simulations on a multi-layer MXene ($\text{Ti}_3\text{C}_2\text{O}_2$ shown). (d) Typical calculated cNEB profile of C-site to C-site migration, with the M-site located at the point halfway along the migration path (Mg^{2+} and Li^+ migration in multi-layer $\text{Ti}_3\text{C}_2\text{O}_2$ shown).

structure and its electrochemical behaviour, a single layer of the MXene (Fig. S9(b and d)†) was also studied to mimic adsorption and surface migration on a delaminated MXene and on free-standing MXene layers. Both for intercalation in the multi-layer MXene and adsorption on the single-layer MXene, the most stable site for Mg^{2+} and Li^+ was found to be above a carbon atom, referred to as the C-site (shown in Fig. 4a), while the site over the metal (Ti or V, referred to as the M-site) was found to be less favourable (Table S4†). The energy barriers for ion migration were calculated for one $\text{Mg}^{2+}/\text{Li}^+$ moving from a C-site to a neighbouring metastable M-site using the Climbing Image Nudge Elastic Band (cNEB) method.^{55–58} These results were mirrored to give migration energy barrier profiles between two adjacent C-sites. Tests were performed to confirm that the

minimum energy path from one C-site to the next C-site was *via* the M-site (see the ESI†). Fig. 4d shows a typical calculated cNEB profile, with the metastable M-site clearly visible halfway along the migration path. The migration energy barrier profile resembles the shape of Li and Na diffusion in graphite.⁵⁹ It is the energy maximum that is reported as the migration barrier. The calculated barriers for single-layer migration on $\text{Ti}_3\text{C}_2\text{O}_2$ MXene are in good agreement with earlier published results.^{37,40} The cNEB profiles for oxygen and fluorine terminated multi-layer $\text{Ti}_3\text{C}_2\text{T}_2$ and $\text{V}_2\text{C}_2\text{T}_2$ with Mg and Li can be found in the ESI (Fig. S10†). The DFT results are summarized in Fig. 5 and the implications for each MXene composition as a Mg cathode are summarized in Table 1.

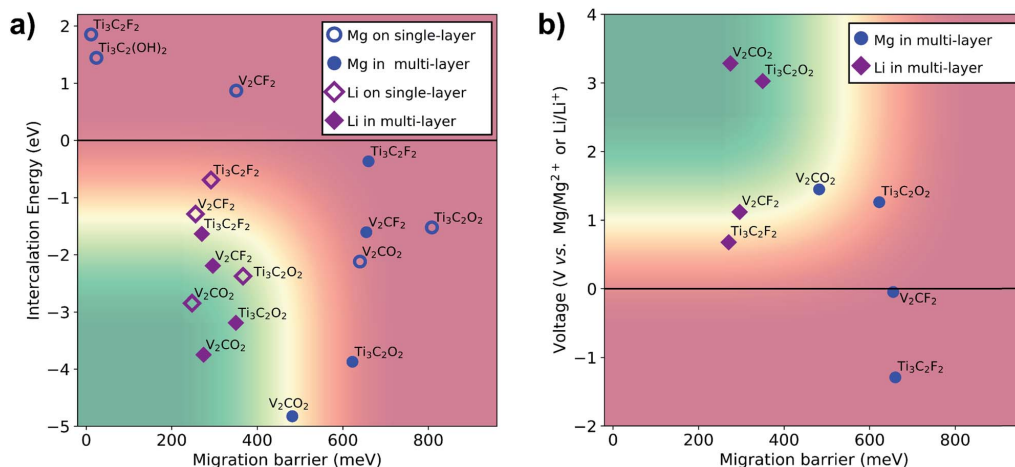


Fig. 5 (a) Intercalation energy and migration barriers for fluorine, oxygen and hydroxyl terminated $\text{Ti}_3\text{C}_2\text{T}_2$ and $\text{V}_2\text{C}_2\text{T}_2$ MXenes by DFT, for both Li^+ (purple diamonds) and Mg^{2+} (blue circles), for single-layer (empty symbols) and multi-layer (filled symbols) MXenes. (b) Average operation voltages and migration barriers for selected compositions from (a). The green regions represent combinations of sufficiently low migration barriers to allow for useful charging/discharging of $6\ \mu\text{m}$ sized particles at $25\ ^\circ\text{C}$ as well as suitable intercalation energies/voltages for practical RMB cathodes. See the ESI† for details, and Table S3† for the values presented in these plots.

Table 1 Implications of DFT simulations for multi-layered micron sized $\text{Ti}_3\text{C}_2\text{T}_x$ and V_2CT_x with different termination groups (T = F, O, and OH) as Mg cathode materials. The materials need to have spontaneous intercalation (negative intercalation energy), a migration barrier preferably below 530 meV, and Mg^{2+} intercalation must be more thermodynamically favourable than side reactions (e.g. reacting with the termination groups). Only V_2CO_2 passes all criteria

| | Spontaneous intercalation | Migration barrier < 530 meV | Side reactions |
|--------------------------------------|---------------------------|-----------------------------|------------------|
| $\text{Ti}_3\text{C}_2\text{F}_2$ | No | No | No |
| $\text{Ti}_3\text{C}_2(\text{OH})_2$ | No | N/A | No |
| $\text{Ti}_3\text{C}_2\text{O}_2$ | Yes | No | No |
| V_2CF_2 | No | No | Yes ^a |
| $\text{V}_2\text{C}(\text{OH})_2$ | No | N/A | Yes ^b |
| V_2CO_2 | Yes | Yes | No |

^a Formation of MgF_2 is more favourable than Mg^{2+} intercalation.

^b Formation of MgH_2 is more favourable than Mg^{2+} intercalation.

Our DFT calculations show that the termination groups strongly dictate the feasibility of MXene cathodes for RBMs. Fluorine and hydroxyl terminations in both multi-layer $\text{Ti}_3\text{C}_2\text{T}_x$ and V_2CT_x give a negative average voltage for Mg^{2+} intercalation and are thus thermodynamically unfavourable (Fig. 5b, Table S3†). This is in contrast to Li^+ intercalation, which is found to have a positive average voltage for all compositions studied in this work. However, the average voltage is found to be positive for Mg^{2+} into oxygen terminated multi-layer $\text{Ti}_3\text{C}_2\text{O}_2$ and V_2CO_2 , having decent values of 1.3 and 1.5 V, respectively. Still, these values assume homogeneous termination groups. Caffrey investigated the effect of mixed surface terminations, where it was found that certain properties, such as the work function, lattice parameters and electronic density of states, could be estimated by the weighted averages of the results from uniformly terminated MXenes.⁶⁰ From Table S1† we see that $\text{Ti}_3\text{C}_2\text{T}_x$ has an O/F ratio of 1.36, while V_2CT_x has an O/F ratio of 0.66. Considering that several recent reports claim that little or no OH terminations will be possible on the Ti_3C_2 surface,^{61,62} we can simplify the estimation by assuming all oxygen content to represent O-terminations. Using a weighted average, we therefore find the adjusted average voltages for the as-synthesized $\text{Ti}_3\text{C}_2\text{T}_x$ and V_2CT_x MXenes to be +0.19 and +0.55 V, respectively. These values indicate spontaneous intercalation of Mg^{2+} in both $\text{Ti}_3\text{C}_2\text{T}_x$ and V_2CT_x , suggesting that the intercalation energy is not a limiting factor for either of these two structures. Nonetheless, an average voltage of 0.19 or 0.55 V is too low for practical application, directing further work on oxygen terminated MXenes.

Even though oxygen terminated multi-layer $\text{Ti}_3\text{C}_2\text{O}_2$ showed a decent positive average voltage, Fig. 5 also reveals a high migration barrier of 620 meV for Mg^{2+} . According to Canepa *et al.*, a particle size of 6 μm requires a barrier as low as 470 meV at 25 °C or 530 meV at a temperature of 60 °C in order to reach theoretical capacity at a C-rate of C/10 (charging/discharging in 10 h).³ Thus, for Mg^{2+} in multi-layer $\text{Ti}_3\text{C}_2\text{O}_2$ with a migration

barrier of 620 meV, the attainable C-rate becomes approximately 1/3000 at room temperature and 1/500 at 60 °C, in order to be fully charged/discharged. In other words, the high migration barrier of 620 meV appears to strongly limit the performance of $\text{Ti}_3\text{C}_2\text{O}_2$ and may explain the experimental results showing no Mg^{2+} intercalation. However, the relation between migration barriers and attainable C-rates by Canepa *et al.* must be interpreted with great caution. One of the simplifications is that the time needed to fully charge/discharge a spherical particle is approximately the same as the necessary time an ion needs to reach the centre of the particle by random walk. Hence, the model approximates the necessary diffusion length to scale as \sqrt{Dt} , where D is the diffusion coefficient and t is the discharge/charge time. Another important assumption is that the model also assumes all kinetic factors other than solid state diffusion to not be rate limiting. Moreover, the presented migration barriers in this work are calculated on a barely discharged MXene cathode (1/9 filling of Mg atoms between two MXene layers in vacuum), and the migration barriers are expected to increase with a higher Mg content.¹⁸ Nonetheless, the model by Canepa *et al.*, combined with DFT, serves as a reasonable indication of which MXenes are the most promising RMB cathode materials and which most likely can be excluded.

Interestingly, the migration barrier for multi-layer V_2CO_2 was calculated to be only 480 meV for Mg^{2+} intercalation, which is below the presumed limit of 530 meV for 6 μm particles. Using the relation between the migration barrier and C-rate discussed above, the 480 meV migration barrier for Mg^{2+} corresponds to a C-rate of 1/15 at 25 °C,³ which should give substantial measurable capacity. To investigate this, V_2CT_x MXene was synthesized and tested as Mg cathodes (see the ESI† for details). However, it demonstrated the same poor performance as the $\text{Ti}_3\text{C}_2\text{T}_x$ MXene (Fig. S1, S7 and S8†). A plausible explanation is a detrimental influence of fluorine and/or hydroxyl terminations. Upon magnesiation, the DFT calculations show that Mg^{2+} reacts with the fluorine and hydroxyl terminations and forms MgF_2 and MgH_2 , respectively (Fig. S12†). Thus, even though the oxygen terminations may enable Mg^{2+} migration, the Mg^{2+} may be trapped irreversibly by the fluorine and/or hydroxyl terminations and block consecutive intercalation. This illustrates the critical need of controlling the termination groups.

Notably, Fig. 5a shows that there is no simple correlation between the intercalation energy and the migration energy barrier. The intercalation energy is calculated as the energy difference upon the insertion of one single Mg/Li into the MXene super cell (shown in Fig. 4a–c and S9a–d†) from a bulk Mg/Li-metal reservoir. Intuitively one could think that a larger amount of energy released upon the insertion of Mg/Li would reflect stronger bonds formed and thus also higher migration barriers. This does hold true when comparing e.g. Li and Mg in multi-layer V_2CO_2 . However, the opposite is seen when comparing V_2CT_2 with $\text{Ti}_3\text{C}_2\text{T}_2$ for the vast majority of the data points, i.e. V_2CT_2 has both lower migration barriers and higher energy released upon intercalation. As a result, V_2CT_2 appears to be a stronger cathode candidate than the most studied $\text{Ti}_3\text{C}_2\text{T}_2$,

as it is expected to demonstrate faster diffusion in addition to a higher average voltage.

As expected, Li^+ migration is exceedingly faster than Mg^{2+} migration for all structures, but the relative difference varies significantly (210–390 meV, Fig. S10†). Assuming that the ion migration can be approximately proportional to $\exp(-E_{\text{migration barrier}}/k_{\text{B}}T)$ as in transition state theory, every ~ 60 meV higher migration barrier translates to a ten factor slower migration, at 25 °C. Thus, while Li^+ has a 4.6×10^6 faster diffusion than Mg^{2+} in fluorine terminated $\text{Ti}_3\text{C}_2\text{F}_2$, the difference is reduced to a factor of 3600 in V_2CO_2 (Table S2†). The calculated Bader charge provide some insight into this,^{63–66} as they assigns the cumulative electronic charge density to atoms, where the atomic separation is defined by a minimum in the electronic charge density landscape. It can be seen from Fig. S11† that the oxygen is slightly more polarized in $\text{Ti}_3\text{C}_2\text{O}_2$ than in V_2CO_2 , which will lead to stronger Mg–O interactions and slower migration. Still, even though excellent rate capability has been reported for Li^+ in MXenes,⁶⁷ a 3600 times slower diffusion in V_2CO_2 will inevitably cause a considerably lower power density for Mg^{2+} , or a necessity of operating at an elevated temperature and/or downsizing the particles.

Noteworthy, the migration barriers decrease considerably when going from single layer to multi-layer for oxygen terminated $\text{Ti}_3\text{C}_2\text{O}_2$ and V_2CO_2 . For instance, the single-layer migration barrier for $\text{Ti}_3\text{C}_2\text{O}_2$ was calculated to be 810 meV and the multi-layer barrier to be 620 meV. Consequently, oxygen terminated multi-layer MXenes look much more promising than their delaminated fluorine-containing counterparts, where V_2CO_2 is the only composition that exhibits spontaneous Mg^{2+} intercalation with a feasible migration barrier and no observed side reactions from DFT calculations.

2.4 Mg^{2+} intercalation in MXenes

Ion intercalation in solids is complex and several critical criteria must be fulfilled. The average voltage must be positive, the ions must be able to enter the structure, and the ions must have sufficiently low migration barriers in order to achieve significant intercalation within the particles. The role of the M-element (Ti vs. V), the termination groups, and single layer vs. multi-layer and their influence on operating voltages and migration barriers have already been elaborated. High migration barriers and/or detrimental side reactions may explain the observed absence of Mg^{2+} intercalation in $\text{Ti}_3\text{C}_2\text{T}_x$ and V_2CT_x , but that is not the only challenge. The Bader charge analysis may explain the difference between Ti and V based MXenes (as discussed earlier), but it also provides direct insight into the complex charge transfer for MXenes. Strikingly, upon magnesian, the +1.7 charge from Mg is accompanied with a -1.7 charge distributed not only on the transition metal (Ti/V), but also to the oxygen termination group and even the carbon layer (Fig. S11†). In fact, the ratio of decrease in Bader charge between C : M : O is roughly 1 : 2 : 4, meaning that the largest charge decrease is in the oxygen termination group. This may support a recent X-ray absorption near edge structure (XANES) study that observed only a small change in the oxidation state

for Ti in parts of the lithiation process of the $\text{Ti}_3\text{C}_2\text{T}_x$ MXene.⁶⁸ More importantly, the initial low Bader charge of the transition metal (1.8–2.0 for Ti and 1.8 for V), together with the distributed charge transfer on the transition metal, termination group and carbon layer during discharge, gives a reasonable explanation of the calculated low operating voltages. The low voltages constrain the obtainable energy densities, which is addressed in Section 2.5.

Another crucial challenge is Mg^{2+} dissociation from the electrolyte, especially in the presence of chlorine ions. As mentioned earlier, the Mg–Cl bond in the MgCl^+ species is strong and reported to be over 3000 meV.⁶⁹ It has therefore been suggested that the success of the Mo_6S_8 Chevrel phase cathode for Mg batteries is partly due to molybdenum's ability to catalyse the breaking of the MgCl^+ bond.⁴⁵ Hence, an electrolyte with weakly solvated Mg^{2+} is necessary, or there needs to be some mechanism for Mg^{2+} to desolvate sufficiently easily for intercalation to occur. This last point is critical, as MgCl^+ was shown to have a significantly lower migration barrier of 350 meV (Table S3†) compared to the 810 meV for Mg^{2+} on single-layer $\text{Ti}_3\text{C}_2\text{O}_2$. Accordingly, if there is space for MgCl^+ to intercalate, as in the case of single layers or by preintercalation of large molecules, quick migration is to be expected, similar to that of monovalent ions such as Li^+ and Na^+ . It has been suggested that the capacity in interlayer expanded TiS_2 cathodes for Mg batteries in fact is due to MgCl^+ , and not Mg^{2+} .⁶⁹ Thus, it would also be important to rule out if the capacities measured with MXene based cathodes in the literature thus far are due to actual Mg^{2+} intercalation, or the much less desirable MgCl^+ intercalation. This is especially relevant for MXenes, where spacer molecules can be used to increase the interlayer distance such as in ref. 33 and 69. As discussed earlier, Zhao *et al.* assigned the first set of discharge/charge voltage plateaus for their $\text{Ti}_3\text{C}_2\text{T}_x$ cathode to reversible phenyl–MgCl intercalation. The low migration barrier reported for MgCl^+ here may support the proposed mechanism, or at least support the intercalation of a monovalent MgCl^+ compound. The reason MgCl^+ -intercalation is undesirable is that only the Mg constituent is stored densely in the Mg metal anode, while an excessive amount of electrolyte is needed to store the corresponding amount of chloride ions. The weight and volume added by the excessive amount of electrolyte will limit the energy density. This also highlights the need for reporting the amount of electrolyte, in addition to cathode loading.

Even if Mg^{2+} desolvation and anion dissociation is successful and the migration barriers inside the MXene are low, Mg^{2+} intercalation also depends on the local environment at the MXene edges. It is well established that the MXene surface is negatively charged, but a recent study also found the edges to be positively charged.⁷⁰ This will unavoidably lead to electrostatic repulsion between the MXene edge and the incoming Mg ions, and further complicate the cathode–electrolyte interface and desolvation process. Considering the stability of MgO and MgF_2 , $\text{Mg}(\text{OH})_2$ and MgH_2 as possible by-products, it is also likely that initial Mg^{2+} react irreversibly with the termination groups at the particle edge and block further Mg^{2+} intercalation.

This was found to happen spontaneously with V_2CF_2 and $V_2C(OH)_2$ in our DFT calculations (Fig. S12[†]), indicating that MgV_2CF_2 and $MgV_2C(OH)_2$ are very unstable.

2.5 MXenes as a rechargeable Mg battery cathode material

The MXene group of materials shows complex and flexible chemistries resulting in a large number of possible cathode designs, and this section aims to evaluate the potential of MXenes as RMB cathodes. Our DFT calculations show that both the elemental composition and the termination groups are imperative. Somewhat unexpected and in contrast to the experimental approach reported in the literature, multi-layer MXenes seem more promising than their single-layer counterparts, both in terms of lower migration barriers, higher average voltages and denser structure. The preintercalation of spacers does not appear to be a good approach, where the increased interlayer distance may give a single-layer type behaviour and solvated Mg-ion complexes may intercalate instead of Mg^{2+} . The relatively high average voltage and low migration barriers for oxygen terminated V_2CO_2 MXene suggests that Mg^{2+} intercalation may be possible. However, as fluorine and hydroxyl terminations give rise to unwanted side reactions, and since no reversible intercalation was observed experimentally for V_2CT_x with mixed terminations, controlling the termination group seems to be of critical importance.

Uniformly oxygen terminated V_2CO_2 stands out as a possible RMB cathode candidate. Given its calculated average voltage of 1.5 V and theoretical capacity of 367 mA h g^{-1} (based on 1 layer of Mg^{2+} intercalation, MgV_2CO_2 , and 2 electrons per Mg ion), this gives a material specific energy of 551 W h kg^{-1} . This is comparable to the specific energy of $LiMn_2O_4$ (vs. a graphite anode with a redox potential of 0.2 V vs. Li/Li^+) for Li-ion batteries.⁷¹ V_2CO_2 has a relatively high material density of 4.79 $g\ cm^{-3}$, yielding an impressive volumetric energy density of 2640 W h l^{-1} at the material level. However, this value is for dense multi-layered particles without the mentioned interstack distance. Still, if we consider a lower and more practically obtainable density of 1.5 $g\ cm^{-3}$, this will be compensated by the high volumetric capacity of the Mg anode. As a result, a full cell with a V_2CO_2 cathode and a Mg anode (with 0% Mg excess) has a high theoretical specific energy of 472 W h kg^{-1} and may reach a volumetric energy density of 723 W h l^{-1} , only considering the active materials and a V_2CO_2 density of 1.5 $g\ cm^{-3}$. In comparison, a $LiFePO_4$ -graphite full cell (1:1 capacity balanced) has a practical specific energy of 324 W h kg^{-1} and volumetric energy density of 724 W h l^{-1} , also considering the active materials only and a $LiFePO_4$ packing density of 2 $g\ cm^{-3}$.⁷²

Nevertheless, the viable energy densities of V_2CO_2 depend on uniformly terminated V_2CO_2 , which poses a crucial challenge. Recent work on fluorine-free synthesis of $Ti_3C_2T_x$ gives some promise,^{73–77} but a similar synthesis approach may not be feasible for V_2CO_2 given the much harsher etching conditions required for V_2CT_x , indicative of substantially stronger metal–aluminium bonds.⁷⁸ Furthermore, the prerequisite of having Mg^{2+} successfully desolvating from the electrolyte and entering

the interlayers still remains. These issues demand a critical assessment of the electrolyte–cathode interface and better fundamental understanding of the MXene surface chemistry, as well as our ability to fully control them. The above discussion leaves MXenes, with the right composition and structure, as a theoretically viable Mg cathode candidate, but with significant challenges for experimental realization. Further thorough screening of around 20 other MXenes²⁹ may also reveal other candidates for practical cathode materials for RMBs. Finally, the findings and critical aspects discussed herein are not only applicable to RMBs, and we believe the new insights can accelerate the research for MXene-based electrodes for other chemistries as well, such as Li-, Na-, K-, Ca- and Al-ion batteries.

3 Conclusions

In summary, we have assessed the promise and reality of MXenes as a potential cathode material for practical RMBs, combining experiments and atomistic computer simulations. Multi-layered $Ti_3C_2T_x$ and V_2CT_x MXenes were not observed to intercalate unsolvated Mg^{2+} at an elevated temperature of 60 °C and regardless of electrolytes. DFT calculations showed that the intercalation energies and migration barriers heavily depend on both the elemental composition and the termination groups of the MXenes. The most studied MXene, $Ti_3C_2T_x$, is precluded as a feasible Mg cathode candidate, where hydroxyl and fluorine terminations resulted in thermodynamically unfavourable average voltages and oxygen termination resulted in high migration barriers. However, oxygen terminated V_2CO_2 MXene is identified as a possibly viable cathode candidate, as it shows a combination of decent average operating potential (1.5 V) and feasible Mg^{2+} migration barriers. Still, side reactions of Mg^{2+} with the fluorine and/or hydroxyl terminations resulting in MgF_2/MgH_2 seem detrimental to Mg^{2+} intercalation in the as-synthesized V_2CT_x , in addition to the challenges related to the non-trivial desolvation of Mg^{2+} from the electrolyte. The current results indicate that the MXene 'M'-elements, termination groups and degree of delamination must all be carefully assessed to allow unsolvated Mg^{2+} intercalation. More research on the above-mentioned challenges, especially controlling the termination groups, is required to realize the theoretical potential of MXenes for energy dense RMB cathodes.

Conflicts of interest

There are no conflicts to declare.

Acknowledgements

This work was financially supported by the Research Council of Norway through a FRINATEK project, project number 275810, and through the Department of Materials Science and Engineering at NTNU Norwegian University of Science and Technology. We would also like to acknowledge Lars-Arne Bøge for performing the synthesis of the V_2CT_x MXene and preparing the V_2CT_x cathodes, Solveig Stubmo Aamlid and Benjamin Williamson for assistance with phonon calculations and Tor

Grande for valuable discussions. Sigma2 is acknowledged for CPU-time through project number NN9414K and NN9264K.

Notes and references

- 1 Y. Ding, Z. P. Cano, A. Yu, J. Lu and Z. Chen, *Electrochem. Energy Rev.*, 2019, **2**, 1–28.
- 2 G. Zubi, R. Dufo-López, M. Carvalho and G. Pasaoglu, *Renew. Sustain. Energy Rev.*, 2018, **89**, 292–308.
- 3 P. Canepa, G. Sai Gautam, D. C. Hannah, R. Malik, M. Liu, K. G. Gallagher, K. A. Persson and G. Ceder, *Chem. Rev.*, 2017, **117**, 4287–4341.
- 4 J. W. Choi and D. Aurbach, *Nat. Rev. Mater.*, 2016, **1**, 16013.
- 5 C. Ling, D. Banerjee and M. Matsui, *Electrochim. Acta*, 2012, **76**, 270–274.
- 6 M. Matsui, *J. Power Sources*, 2011, **196**, 7048–7055.
- 7 P. C. K. Vesborg and T. F. Jaramillo, *RSC Adv.*, 2012, **2**, 7933–7947.
- 8 M. Mao, T. Gao, S. Hou and C. Wang, *Chem. Soc. Rev.*, 2018, **47**, 8804–8841.
- 9 R. Mohtadi and F. Mizuno, *Beilstein J. Nanotechnol.*, 2014, **5**, 1291–1311.
- 10 N. Amir, Y. Vestfrid, O. Chusid, Y. Gofer and D. Aurbach, *J. Power Sources*, 2007, **174**, 1234–1240.
- 11 P. Canepa, S. Jayaraman, L. Cheng, N. N. Rajput, W. D. Richards, G. S. Gautam, L. A. Curtiss, K. A. Persson and G. Ceder, *Energy Environ. Sci.*, 2015, **8**, 3718–3730.
- 12 R. Mohtadi, M. Matsui, T. S. Arthur and S.-J. Hwang, *Angew. Chem., Int. Ed.*, 2012, **51**, 9780–9783.
- 13 I. Shterenberg, M. Salama, Y. Gofer and D. Aurbach, *Langmuir*, 2017, **33**, 9472–9478.
- 14 H. D. Yoo, I. Shterenberg, Y. Gofer, G. Gershinsky, N. Pour and D. Aurbach, *Energy Environ. Sci.*, 2013, **6**, 2265–2279.
- 15 T. D. Gregory, R. J. Hoffman and R. C. Winterton, *J. Electrochem. Soc.*, 1990, **137**, 775–780.
- 16 D. Aurbach, Z. Lu, A. Schechter, Y. Gofer, H. Gizbar, R. Turgeman, Y. Cohen, M. Moshkovich and E. Levi, *Nature*, 2000, **407**, 724–727.
- 17 G. Gershinsky, H. D. Yoo, Y. Gofer and D. Aurbach, *Langmuir*, 2013, **29**, 10964–10972.
- 18 X. Sun, P. Bonnick, V. Duffort, M. Liu, Z. Rong, K. A. Persson, G. Ceder and L. F. Nazar, *Energy Environ. Sci.*, 2016, **9**, 2273–2277.
- 19 X. Sun, P. Bonnick and L. F. Nazar, *ACS Energy Lett.*, 2016, **1**, 297–301.
- 20 L. Wang, K. Asheim, P. E. Vullum, A. M. Svensson and F. Vullum-Bruer, *Chem. Mater.*, 2016, **28**, 6459–6470.
- 21 A. Du, Z. Zhang, H. Qu, Z. Cui, L. Qiao, L. Wang, J. Chai, T. Lu, S. Dong, T. Dong, H. Xu, X. Zhou and G. Cui, *Energy Environ. Sci.*, 2017, **10**, 2616–2625.
- 22 H. O. Ford, L. C. Merrill, P. He, S. P. Upadhyay and J. L. Schaefer, *Macromolecules*, 2018, **51**, 8629–8636.
- 23 T. Gao, S. Hou, F. Wang, Z. Ma, X. Li, K. Xu and C. Wang, *Angew. Chem., Int. Ed.*, 2017, **56**, 13526–13530.
- 24 H. S. Kim, T. S. Arthur, G. D. Allred, J. Zajicek, J. G. Newman, A. E. Rodnyansky, A. G. Oliver, W. C. Boggess and J. Muldoon, *Nat. Commun.*, 2011, **2**, 427.
- 25 Z. Zhao-Karger, M. E. Gil Bardaji, O. Fuhr and M. Fichtner, *J. Mater. Chem. A*, 2017, **5**, 10815–10820.
- 26 Z. Zhao-Karger, X. Zhao, D. Wang, T. Diemant, R. J. Behm and M. Fichtner, *Adv. Energy Mater.*, 2015, **5**, 1401155.
- 27 M. Salama, R. Attias, B. Hirsch, R. Yemini, Y. Gofer, M. Noked and D. Aurbach, *ACS Appl. Mater. Interfaces*, 2018, **10**, 36910–36917.
- 28 M. Naguib, M. Kurtoglu, V. Presser, J. Lu, J. Niu, M. Heon, L. Hultman, Y. Gogotsi and M. W. Barsoum, *Adv. Mater.*, 2011, **23**, 4248–4253.
- 29 B. Anasori, M. R. Lukatskaya and Y. Gogotsi, *Nat. Rev. Mater.*, 2017, **2**, 16098.
- 30 D. Er, J. Li, M. Naguib, Y. Gogotsi and V. B. Shenoy, *ACS Appl. Mater. Interfaces*, 2014, **6**, 11173–11179.
- 31 F. Ming, H. Liang, W. Zhang, J. Ming, Y. Lei, A.-H. Emwas and H. N. Alshareef, *Nano Energy*, 2019, **62**, 853–860.
- 32 M. Naguib, J. Halim, J. Lu, K. M. Cook, L. Hultman, Y. Gogotsi and M. W. Barsoum, *J. Am. Chem. Soc.*, 2013, **135**, 15966–15969.
- 33 A. VahidMohammadi, A. Hadjikhani, S. Shahbazmohamadi and M. Beidaghi, *ACS Nano*, 2017, **11**, 11135–11144.
- 34 M. Naguib, V. N. Mochalin, M. W. Barsoum and Y. Gogotsi, *Adv. Mater.*, 2014, **26**, 992–1005.
- 35 M. R. Lukatskaya, S. Kota, Z. Lin, M.-Q. Zhao, N. Shpigel, M. D. Levi, J. Halim, P.-L. Taberna, M. W. Barsoum, P. Simon and Y. Gogotsi, *Nat. Energy*, 2017, **2**, 17105.
- 36 C. Eames and M. S. Islam, *J. Am. Chem. Soc.*, 2014, **136**, 16270–16276.
- 37 Y. Xie, Y. Dall'Agnese, M. Naguib, Y. Gogotsi, M. W. Barsoum, H. L. Zhuang and P. R. C. Kent, *ACS Nano*, 2014, **8**, 9606–9615.
- 38 A. Byeon, M.-Q. Zhao, C. E. Ren, J. Halim, S. Kota, P. Urbankowski, B. Anasori, M. W. Barsoum and Y. Gogotsi, *ACS Appl. Mater. Interfaces*, 2017, **9**, 4296–4300.
- 39 F. Liu, Y. Liu, X. Zhao, X. Liu and L.-Z. Fan, *J. Mater. Chem. A*, 2019, **7**, 16712–16719.
- 40 M. Xu, S. Lei, J. Qi, Q. Dou, L. Liu, Y. Lu, Q. Huang, S. Shi and X. Yan, *ACS Nano*, 2018, **12**, 3733–3740.
- 41 M.-Q. Zhao, C. E. Ren, M. Alhabeab, B. Anasori, M. W. Barsoum and Y. Gogotsi, *ACS Appl. Energy Mater.*, 2019, **2**, 1572–1578.
- 42 M. Alhabeab, K. Maleski, B. Anasori, P. Lelyukh, L. Clark, S. Sin and Y. Gogotsi, *Chem. Mater.*, 2017, **29**, 7633–7644.
- 43 M. Okubo, A. Sugahara, S. Kajiyama and A. Yamada, *Acc. Chem. Res.*, 2018, **51**, 591–599.
- 44 V. Augustyn, J. Come, M. A. Lowe, J. W. Kim, P.-L. Taberna, S. H. Tolbert, H. D. Abruña, P. Simon and B. Dunn, *Nat. Mater.*, 2013, **12**, 518.
- 45 L. F. Wan, B. R. Perdue, C. A. Appleby and D. Prendergast, *Chem. Mater.*, 2015, **27**, 5932–5940.
- 46 N. Pour, Y. Gofer, D. T. Major and D. Aurbach, *J. Am. Chem. Soc.*, 2011, **133**, 6270–6278.
- 47 L. Wang, B. Jiang, P. E. Vullum, A. M. Svensson, A. Erbe, S. M. Selbach, H. Xu and F. Vullum-Bruer, *ACS Nano*, 2018, **12**, 2998–3009.
- 48 H. Xu, Z. Zhang, Z. Cui, A. Du, C. Lu, S. Dong, J. Ma, X. Zhou and G. Cui, *Electrochem. Commun.*, 2017, **83**, 72–76.

- 49 C. God, B. Bitschnau, K. Kapper, C. Lenardt, M. Schmuck, F. Mautner and S. Koller, *RSC Adv.*, 2017, 7, 14168–14175.
- 50 D.-M. Kim, S. C. Jung, S. Ha, Y. Kim, Y. Park, J. H. Ryu, Y.-K. Han and K. T. Lee, *Chem. Mater.*, 2018, 30, 3199–3203.
- 51 S. Shi, J. Gao, Y. Liu, Y. Zhao, Q. Wu, W. Ju, C. Ouyang and R. Xiao, *Chin. Phys. B*, 2016, 25, 018212.
- 52 X. Wang, X. Shen, Y. Gao, Z. Wang, R. Yu and L. Chen, *J. Am. Chem. Soc.*, 2015, 137, 2715–2721.
- 53 A. Ganose, A. Jackson and D. Scanlon, *J. Open Source Softw.*, 2018, 3, 717.
- 54 A. Togo and I. Tanaka, *Scr. Mater.*, 2015, 108, 1–5.
- 55 G. Henkelman, G. Jóhannesson and H. Jónsson, in *Theoretical Methods in Condensed Phase Chemistry*, ed. S. D. Schwartz, Springer Netherlands, Dordrecht, 2002, pp. 269–302, DOI: 10.1007/0-306-46949-9_10.
- 56 G. Henkelman and H. Jónsson, *J. Chem. Phys.*, 2000, 113, 9978–9985.
- 57 G. Henkelman, B. P. Uberuaga and H. Jónsson, *J. Chem. Phys.*, 2000, 113, 9901–9904.
- 58 D. Sheppard, R. Terrell and G. Henkelman, *J. Chem. Phys.*, 2008, 128, 134106.
- 59 Z. Wang, A. P. Ratvik, T. Grande and S. M. Selbach, *RSC Adv.*, 2015, 5, 15985–15992.
- 60 N. M. Caffrey, *Nanoscale*, 2018, 10, 13520–13530.
- 61 M. A. Hope, A. C. Forse, K. J. Griffith, M. R. Lukatskaya, M. Ghidui, Y. Gogotsi and C. P. Grey, *Phys. Chem. Chem. Phys.*, 2016, 18, 5099–5102.
- 62 I. Persson, L.-Å. Näslund, J. Halim, M. W. Barsoum, V. Darakchieva, J. Palisaitis, J. Rosen and P. O. Å. Persson, *2D Materials*, 2017, 5, 015002.
- 63 G. Henkelman, A. Arnaldsson and H. Jónsson, *Comput. Mater. Sci.*, 2006, 36, 354–360.
- 64 E. Sanville, S. D. Kenny, R. Smith and G. Henkelman, *J. Comput. Chem.*, 2007, 28, 899–908.
- 65 W. Tang, E. Sanville and G. Henkelman, *J. Phys.: Condens. Matter*, 2009, 21, 084204.
- 66 M. Yu and D. R. Trinkle, *J. Chem. Phys.*, 2011, 134, 064111.
- 67 D. Sun, M. Wang, Z. Li, G. Fan, L.-Z. Fan and A. Zhou, *Electrochem. Commun.*, 2014, 47, 80–83.
- 68 Y. Xie, M. Naguib, V. N. Mochalin, M. W. Barsoum, Y. Gogotsi, X. Yu, K.-W. Nam, X.-Q. Yang, A. I. Kolesnikov and P. R. C. Kent, *J. Am. Chem. Soc.*, 2014, 136, 6385–6394.
- 69 H. D. Yoo, Y. Liang, H. Dong, J. Lin, H. Wang, Y. Liu, L. Ma, T. Wu, Y. Li, Q. Ru, Y. Jing, Q. An, W. Zhou, J. Guo, J. Lu, S. T. Pantelides, X. Qian and Y. Yao, *Nat. Commun.*, 2017, 8, 339.
- 70 V. Nattu, M. Sokol, L. Verger and M. W. Barsoum, *J. Phys. Chem. C*, 2018, 122, 27745–27753.
- 71 R. Schmuck, R. Wagner, G. Hörpel, T. Placke and M. Winter, *Nat. Energy*, 2018, 3, 267–278.
- 72 P. Meister, H. Jia, J. Li, R. Kloepsch, M. Winter and T. Placke, *Chem. Mater.*, 2016, 28, 7203–7217.
- 73 M. Li, J. Lu, K. Luo, Y. Li, K. Chang, K. Chen, J. Zhou, J. Rosen, L. Hultman, P. Eklund, P. O. Å. Persson, S. Du, Z. Chai, Z. Huang and Q. Huang, *J. Am. Chem. Soc.*, 2019, 141, 4730–4737.
- 74 T. Li, L. Yao, Q. Liu, J. Gu, R. Luo, J. Li, X. Yan, W. Wang, P. Liu, B. Chen, W. Zhang, W. Abbas, R. Naz and D. Zhang, *Angew. Chem., Int. Ed.*, 2018, 57, 6115–6119.
- 75 J. Lu, I. Persson, H. Lind, J. Palisaitis, M. Li, Y. Li, K. Chen, J. Zhou, S. Du, Z. Chai, Z. Huang, L. Hultman, P. Eklund, J. Rosen, Q. Huang and P. O. Å. Persson, *Nanoscale Adv.*, 2019, 1, 3680–3685.
- 76 S. Yang, P. Zhang, F. Wang, A. G. Ricciardulli, M. R. Lohe, P. W. M. Blom and X. Feng, *Angew. Chem., Int. Ed.*, 2018, 57, 15491–15495.
- 77 B. Zhang, J. Zhu, P. Shi, W. Wu and F. Wang, *Ceram. Int.*, 2019, 45, 8395–8405.
- 78 V. M. Hong Ng, H. Huang, K. Zhou, P. S. Lee, W. Que, J. Z. Xu and L. B. Kong, *J. Mater. Chem. A*, 2017, 5, 3039–3068.



Supplementary information

Are MXenes Suitable as Cathode Materials for Rechargeable Mg Batteries?

Henning Kaland,^{‡a} Jacob Hadler-Jacobsen,^{‡a} Frode Håskjold Fagerli,^{‡a} Nils P. Wagner,^{ab} Zhaohui Wang,^{ac} Sverre M. Selbach,^a Fride Vullum-Bruer,^{a,d} Kjell Wiik^{*a} and Sondre Kvalvåg Schnell^{*a}

^a Department of Materials Science and Engineering, NTNU Norwegian University of Science and Technology, NO-7491 Trondheim, Norway.

^b SINTEF Industry, Sustainable Energy Technology, NO-7465 Trondheim, Norway.

^c SINTEF Industry, Metal Production and Processing, NO-7465 Trondheim, Norway.

^d SINTEF Energy Research, Thermal Energy, NO-7465 Trondheim, Norway.

E-mail: kjell.wiik@ntnu.no, sondre.k.schnell@ntnu.no

[‡] These authors contributed equally to this work.

Experimental section

MAX phase preparation (Ti₃AlC₂ and V₂AlC)

Commercial Ti₃AlC₂ MAX phase was bought from Laizhou Kai Kai Ceramic Material Co., Ltd, while the V₂AlC MAX phase was synthesized through a solid state reaction of elemental precursor powders¹; vanadium (99.5%, 325 mesh, Sigma-Aldrich), aluminium (99.5%, 325 mesh, Alfa Aesar) and graphite (99.5%, 400 mesh, TIMCAL TIMREX). The powders were mixed in a molar ratio V:Al:C of 2:1.3:1 and mixed by wet ball milling for 18 h in an isopropanol dispersion. After evaporation of the isopropanol with the aid of a rotavapor (Büchi R210), the powder mixture was pressed into cylindrical 1 g pellets, put in an alumina crucible, inserted into a sealed tube furnace (Entech ETF 17) and heat treated at 1500 °C in an argon atmosphere. The heating program was initiated with a 1 h flushing step to remove oxygen from the tube, before the chamber was heated with a heating rate of 5 °C/min, held at the final temperature for 4 h, and then cooled to room temperature at the same rate. After the heat treatment, the pellets were ground down to powders using a steel mortar. To further reduce the particle size and narrow the particle size distribution, both MAX phase powders (Ti₃AlC₂ and V₂AlC) were planetary milled (Retsch PM 100) using a 125 ml tungsten carbide (WC) milling jar, 11 WC milling balls with a diameter of 7 mm and an amount of isopropanol to just cover the milling balls. Both MAX phases were milled at 300 rpm. 10 g of the Ti₃AlC₂ MAX phase was milled for 135 min, while 3 g of the V₂AlC was milled for 6 hours to achieve the desired particle size and size distribution of the two powders (Figure S1).

MAX phase etching (Ti₃C₂T_x and V₂CT_x)

The two MXenes were synthesized by exfoliation of the precursor MAX phases in aqueous HF solutions, based on previous work.^{1,2} After the milling process, 2.5 g of the Ti₃AlC₂ and V₂AlC powders were immersed in plastic beakers containing 50 ml of 10 wt% and 48 wt% HF solutions, respectively. In order to prevent excess heating and H₂ gas formation at the beginning of the etching, the powders were added slowly over a minimum of 15 minutes. After all the MAX phase powder was added, the plastic beakers were covered with parafilm to limit the evaporation during the etching process. However, in order to prevent build-up of H₂ gas inside the beaker, small holes were made in the parafilm. Then, the dispersions containing the Ti₃AlC₂ and V₂AlC powders were stirred using Teflon coated magnets at room temperature for 24 and 96 hours, respectively, in order to completely remove the aluminium from the parent MAX phases. After the etching process, the

powders were washed with deionized water in 125 ml plastic bottles, through several steps of centrifugation, decantation and dilution, to remove HF and other etching side products. This was continued until the dispersions had a pH > 5 (usually 5 times). The centrifugation was done using a VWR Mega Star 600 using an rpm of 4350 for 7 minutes, including a slow acceleration and deceleration time. Finally, to remove residual water, the powders were vacuum filtered using 0.22 μm pore sized hydrophilic Durapore membrane filters and dried under vacuum at 120 °C for 24 hours in a vacuum oven (Binder VD 23). After drying, the powders were scraped off the filter paper, and stored in glass sample bottles.

Materials characterization

The crystal structure of the synthesized materials was characterized by powder diffraction, conducted on a Bruker D8 Focus Diffractometer, utilizing a Cu K α radiation source ($\lambda = 1.5406 \text{ \AA}$), a 0.2 mm divergence slit, a step size of 0.0143 and a dwelling time of 0.68 s between 2 θ -values of 5° and 75°. The XRD measurements performed on the cathodes before and after cycling were done using inert sample holders, where the cathodes were held in place on a Si wafer with the aid of a small amount of vacuum grease. To characterize the particle sizes of the MAX phase powders, laser diffraction was conducted on a Horiba Partica LA-960, using isopropanol as the liquid medium and 2 minutes of sonication to break up agglomerates prior to the measurement. The particle morphology, microstructure and elemental composition was investigated by field emission scanning electron microscopy (LVFSEM, Zeiss SUPRA 55VP) equipped with energy dispersive X-ray spectroscopy (EDX). The morphology and microstructure were investigated with an acceleration voltage of 5 kV, whereas the EDX measurements were conducted at 15 kV. The reported EDX results are the average values of point scans on ten different particles.

Cathode preparation

Cathodes were prepared by mixing 80 wt% active material (120 mg), 10 wt% polyvinylidene fluoride binder (PVDF) (15 mg) and 10 wt% carbon black (15 mg) in 1 ml of 1-Ethyl-2-pyrrolidone (NEP) solvent, using a 5 ml steel shaker jar. A prepared solution of 5 wt% PVDF in NEP was used, in order to ensure a homogeneous solution of the binder before mixing. First, the dry powders were mixed using a shaker mill (Retsch MM 400) at 15 Hz for 20 minutes, before PVDF and NEP was added to the mixture. The final slurry was then mixed with a 7 mm steel ball an additional 40 minutes at 15 Hz, before the slurry was drop casted onto pre-cut carbon paper current collectors (Spectracarb 2050A-0550) with a diameter of 16 mm. Before being introduced into the glovebox, the cathodes were dried under vacuum at 120 °C for >3 h. The mass loadings of the active material varied between 1-2 mg/cm³. For preparation of the carbon black reference electrodes, the same procedure was performed, but with 90 wt% carbon black (45 mg), 10 wt% PVDF (5 mg) and 2 ml of NEP. The mass loadings of these were 0.5-1 mg/cm³.

Electrolyte mixing

The APC-THF electrolyte was prepared according to the procedure described by Byeon *et al.*³ First, 4 ml THF (> 99.9%, inhibitor-free, Sigma Aldrich) was slowly added to 2.5 ml of 2 M phenyl magnesium chloride in THF (Sigma Aldrich) in a glass bottle while stirring. Secondly, 4 ml of 0.5 M AlCl₃ in THF (Sigma Aldrich) was carefully added to the solution, before the solution was left stirring overnight. The 0.4 M LiCl in APC-THF electrolyte was prepared by dissolving 0.0509 g LiCl (99.7%, VWR) in 3 ml of the prepared APC-THF. The mixture was left stirring for 24 h to completely dissolve the LiCl salt.

The preparation of 0.25 M Mg(TFSI)₂ 0.5M MgCl₂ in DME was based on earlier studies.⁴⁻⁶ Ultradry Mg(TFSI)₂ (Solvionic, 99.5%, H₂O < 250 ppm) was further dried under vacuum at 240 °C in a vacuum chamber connected to the glovebox. Anhydrous MgCl₂ (Sigma, 99.9%), together with the electrolyte glass bottle and magnet was similarly dried at 150 °C for 15 h under vacuum. DME was dried with molecular sieves (UOP Type 3A) for > 48h. Typically, 0.8769 g Mg(TFSI)₂ and 0.2856 g MgCl₂ was mixed in 6 ml of dried DME using a syringe filter (Whatman R Puradisc, 0.2 mm, PTFE) to filter the DME, where the first 1 ml was discarded to avoid impurities from the filter. The resulting mixture was finally stirred 24 h.

0.5 M Mg(BH₄)₂ in THF was prepared according to Mohtadi *et al.*⁷ In a typical procedure, 0.1080 g Mg(BH₄)₂ (Sigma, 95%) was dissolved in 4 ml THF (> 99.9%, inhibitor-free, Sigma Aldrich) in a glass bottle, by stirring overnight. The Mg(BH₄)₂ and THF was used as-received, and the glass bottle and Teflon magnet was dried at 150 °C for 15 h under vacuum.

The BMOC-DME preparation was based on the procedure described by Xu *et al.*⁸ First, 0.004 g of MgO (99.99%, Sigma-Aldrich) was added to a glass bottle. Then, 128 ml of the anion receptor tris(2H-hexafluoroisopropyl) borate (THFPB), corresponding to 0.2048 g, was added. The THFPB has a melting point of 31 °C and was therefore first heated at 40 °C for 5 minutes on a hot plate to remove crystallized particles. Lastly, 2 ml of DME (99.5%, inhibitor-free, Sigma Aldrich) was added, and the electrolyte was stirred overnight. Prior to electrolyte preparation, the DME was dried using molecular sieves (UOP Type 3A°) for > 48 h. The dried DME was filtered through a syringe filter (Whatman R Puradisc, 0.2 mm, PTFE), where the first 1 ml was discarded to avoid impurities from the filter. The MgO and THFPB were used as-received.

Electrochemical measurements

To characterize the electrochemical performance of the prepared cathodes, Hohsen CR2016 coin cells were assembled in an argon filled glovebox (O₂ and H₂O levels < 0.1 ppm), with MXene or carbon black composites as the positive electrode material, Mg foil (Solution Materials) as the negative electrode, glass fibre separator (Whatman GF/A), a 0.3 mm stainless steel spacer and a total of 120 µl of one of the above-mentioned electrolytes. The Mg foil was polished with SiC sandpaper, cleaned with absolute ethanol and dried at 50 °C under vacuum > 2 h before being introduced to the glovebox, in order to remove oxide layers. The room temperature galvanostatic and potentiostatic cycling of the various cells were conducted on a Bio-Logic BCS-805 cycler in a temperature-controlled room at 20 °C. To test the cycling properties at elevated temperatures, a temperature chamber with a MACCOR 4200 cycler was used. Due to observed instability of the APC-THF electrolyte at 60 °C, the upper cut-off voltage was reduced to 1.9 V, as compared to 2.1 V for the room temperature cycling.

DFT calculations

The simulations were performed with the plane wave code Vienna *Ab Initio* Simulation package (VASP),⁹⁻¹¹ using the GGA functional PBEsol,¹² described by the projector augmented wave method (PAW). All calculations were performed at 0 Kelvin. The D2 method of Grimme¹³ was used to correct for Van der Waals interactions, with a vdW radius of 15 Å and a global scaling factor of 0.75. 4x4x1 k-points were used to sample the Brillouin zone for the 3x3 super cells used for calculating the migration barriers, ref Figure S9 (a,b,c,d). 12x12x4 k-points were applied to the unit cells used for calculating voltages and Bader charges, ref Figure S9 (e,f). The k-points were generated with the Monkhorst Pack method. An energy of 650 eV was used for plane wave cut-off. The Methfessel-Paxton scheme was used to account for partial occupancies with a smearing width of 0.1 eV. The electronic ground state was converged to $1 \cdot 10^{-6}$ eV, while the conjugate gradient method was used to relax the structures to the forces were less than 0.01 eV \AA^{-1} , unless otherwise stated.

The Climbing Image Nudged Elastic Band method (cNEB)¹⁴⁻¹⁸ was used to find the migration energy barriers, relaxing the forces to less than 0.02 eV \AA^{-1} . The RMM-DIIS quasi-Newton method was used for relaxing the forces for all systems, except for Mg on a single-layer of V_2CO_2 where the force based conjugate gradient method was used in addition due to convergence difficulties. 4 images were used for barriers on single-layers, and 3 images were used for barriers in multi-layer MXenes. The barriers were calculated for ions moving from a stable C-site to a metastable M-site, (Figure 4 and S9). These results were mirrored to give migration energy barrier profiles between two adjacent C-sites. Calculating the migration energy barriers directly between two C-sites was also tested for the multilayer system, showing for all cases that the minimum energy path went through the metastable M-site. However, some of the images did not relax to 0.02 eV \AA^{-1} , and the C-site to M-site approach was chosen instead.

Phonons for single-layer MXenes were calculated with VASP, using phonopy¹⁹ for setting up and performing the calculations, and Sumo²⁰ to facilitate plotting. The ground states were relaxed to forces less than $1 \cdot 10^{-4} \text{ eV \AA}^{-1}$ per atom with a quasi-Newton algorithm, and a 4x4x1 supercell (similar to Figure S9 b and d, but 4/3 times larger in the xy-plane and without Mg/Li) with 3x3x1 k-points. The electronic ground state was relaxed to $1 \cdot 10^{-8}$ eV. A 3x3x1 supercell for the phonon calculations was also attempted, but it proved infeasible as there were problems with an unstable phonon/negative frequency for V_2CO_2 in the M-point. Attempts at freezing in the phonon (performing geometric relaxation of V_2CO_2 with the unstable phonon given a certain amplitude), were not successful as the structure always relaxed back to the original ground state. However, V_2CO_2 's unstable phonon disappeared when the supercell size was increased to 4x4x1. This unstable phonon was therefore attributed to size effects.

Bader charges were calculated with scripts from the Henkelmann group.²¹⁻²⁴ The charges were converged with respect to the fine FFT-grid, and 168x168x1008 grid points were used for $\text{Ti}_3\text{C}_2\text{T}_2$, while 192x192x1008 grid points for V_2CT_2 . The super cells used for cNEB calculations (Figure S9 a, b, c and d) were relaxed with unit cell shape and ionic positions as free variables, but fixed volume, using a vacuum spacing of ~ 25 Å. Afterwards, Li/Mg/MgCl were relaxed onto the MXenes using a fixed volume and unit cell shape, but all other parameters free. For the cells used for calculating average voltages and Bader charges (Figure S9 e and f) all variables were free when relaxing. The

pseudopotentials supplied with the VASP package were used according to the recommendations of the Materials Project,²⁵ where Li had 3 valence electrons, Mg 8, C 4, O 6, F 7, Cl 7, Ti 10 and V 13 valence electrons. The initial geometries were based on data from^{26, 27}.

The voltages presented in Figure 5b were calculated according to the formula:

$$V = - \frac{E_{\text{intercalated MXene}} - E_{\text{Mg/Li}} - E_{\text{unintercalated MXene}}}{n_{\text{Mg/Li}}},$$

where $E_{\text{intercalated MXene}}$ is the energy for 100% intercalation (Figure S9 e and f), *i.e.* for $\text{MgTi}_3\text{C}_2\text{T}_2$, MgV_2CT_2 , $\text{LiTi}_3\text{C}_2\text{T}_2$, LiV_2CT_2 , $E_{\text{unintercalated MXene}}$ is the (fully relaxed) energy for $\text{Ti}_3\text{C}_2\text{T}_2/\text{V}_2\text{CT}_2$ (Figure S9 e and f without any Li or Mg), $E_{\text{Mg/Li}}$ is the energy for Li/Mg in bulk metal state, and where $n_{\text{valency intercalation metal}}$ was 2 for Mg and 1 for Li. Mg and Li metal was computed and relaxed with the same settings as the MXenes, except that $10 \times 10 \times 10$ k-points were used for a 2 atom unit cell with body centred cubic packing for Li, and $12 \times 8 \times 8$ k-points were used for a 4 atom orthogonal unit cell with hexagonal close packed Mg.

The intercalation energy in Figure 5a was calculated for the setup used for calculating the energy barriers, *i.e.* $1/9^{\text{th}}$ of the single-layer surface covered with Mg/Li, and $1/9^{\text{th}}$ of interlayer-layer space intercalated with Mg/Li, as shown in Figure S9 a, b, c, and d. The following formula was used:

$$E_{\text{intercalation}} = E_{\text{intercalated MXene}} - E_{\text{Mg/Li}} - E_{\text{unintercalated MXene}}$$

The figures showing the simulation setups were made with VESTA.²⁸

Supplementary figures and tables

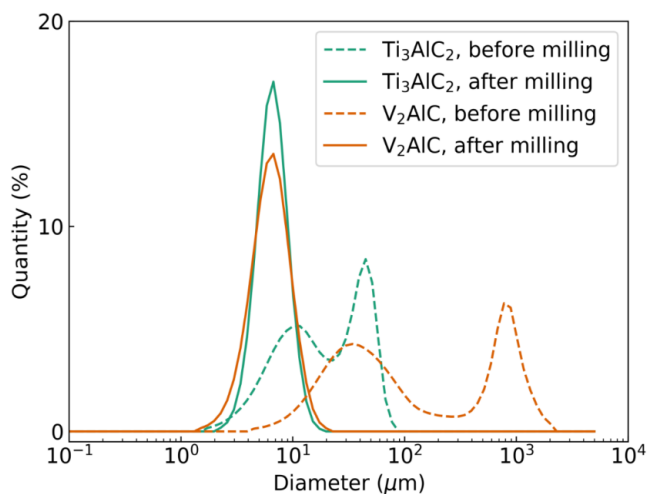


Figure S1 Particle size distribution from laser diffraction measurements of Ti_3AlC_2 and V_2AlC , before and after planetary milling at 300 rpm for 2 h and 4 h, respectively.

Table S1 EDX measurements from the two MAX phases before and after the etching. For simplicity, the elemental content is given relative to a unit cell value of 3 and 2 for the Ti_3AlC_2 and V_2AlC phases, respectively.

| MXene | Ti/V | Al | O | F |
|-----------------------------------|------|------|------|------|
| Ti_3AlC_2 | 3 | 1.15 | - | - |
| $\text{Ti}_3\text{C}_2\text{T}_x$ | 3 | 0.01 | 3.15 | 2.32 |
| V_2AlC | 2 | 1.22 | - | - |
| V_2CT_x | 2 | 0.10 | 0.63 | 0.95 |

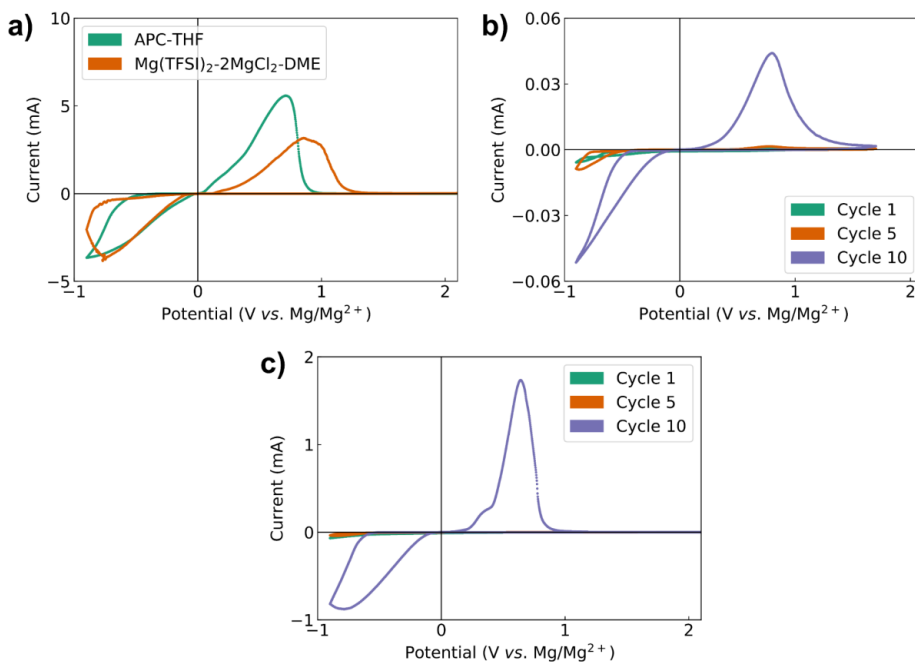


Figure S2 Cyclic voltammetry of all-phenyl complex in tetrahydrofuran (APC-THF) and Mg(TFSI)₂-2MgCl₂ in DME vs. a graphite disc electrode (a), Mg(BH₄)₂ in THF (b) and borate magnesium oxide complex in DME (BMOC-DME) (c). All demonstrates reversible Mg deposition and stripping. While (a) shows high current densities in the first cycle, (b) and (c) show decent current densities only after initial cycles. Due to the low cycling currents used throughout this work, 3-electrode cells showed that the electrolytes did not limit the cathode performance (data not shown).

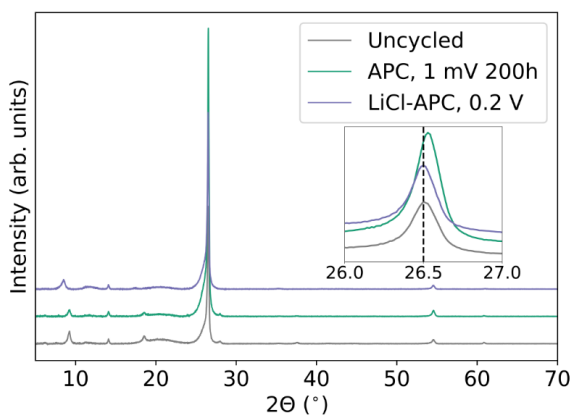


Figure S3 XRD of Ti₃C₂T_x electrode before cycling (grey), after the potentiostatic hold step at 1 mV for 200 h with APC-THF electrolyte (cyan), and after being discharged to 0.2 V with APC-THF with 0.4 M LiCl (purple). The peak at 2θ = 26.5° is assigned to the graphite current collector, shown in the inset.

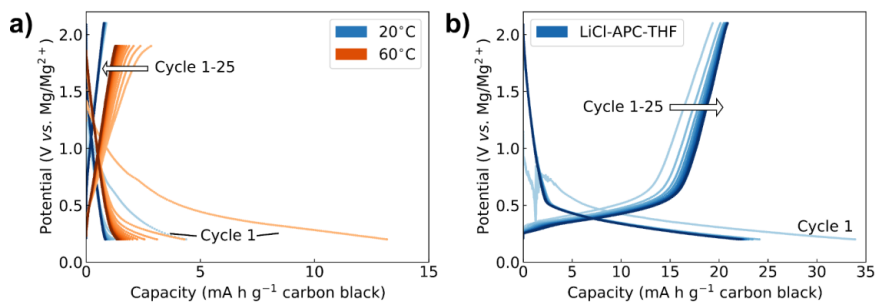


Figure S4 Voltage profiles of carbon black reference electrodes (90 wt% carbon black, 10 wt% PVDF) cycled with APC-THF at 20 °C and 60 °C (a), and APC-THF with 0.4 M LiCl (b).

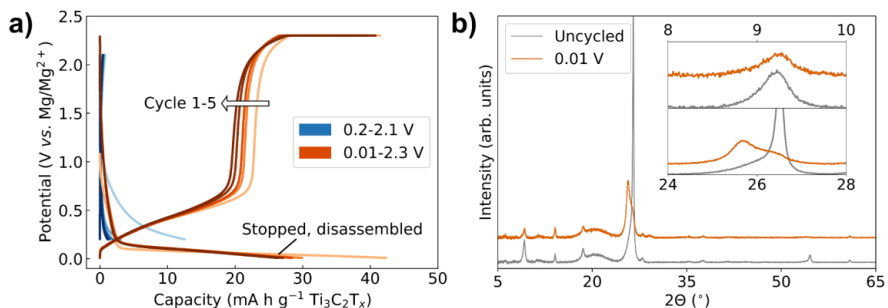


Figure S5 Voltage profiles of Ti₃C₂T_x with BMOC-DME electrolyte, cycled at 0.2-2.1 V, and 0.01-2.3 V (a), before being stopped at 0.01 V for post mortem XRD (b), demonstrating a shift in the graphite peak (bottom plot in inset).



Figure S6 Signs of side reactions on the bottom steel casing after performing the 200 h hold step at 1 mV vs. Mg/Mg²⁺ with the APC-THF electrolyte, after being rinsed in THF.

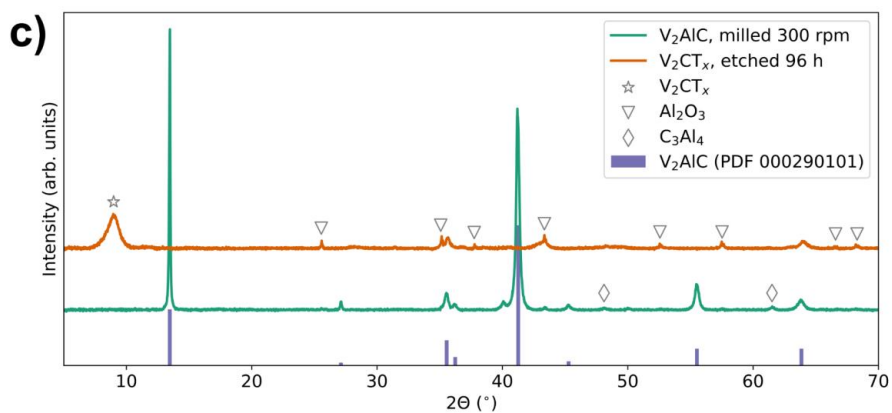
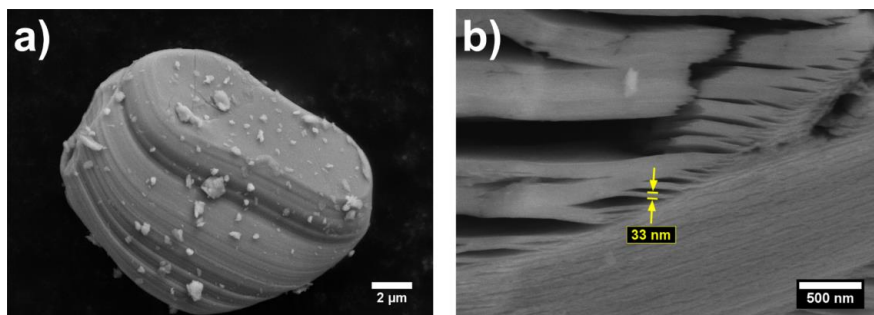


Figure S7 (a) V₂AlC MAX phase particle after milling at 300 rpm for 4 h. (b) V₂CT_x MXene, after etching for 96 h in 48 wt% HF. (c) XRD of both V₂AlC MAX phase and V₂CT_x MXene.

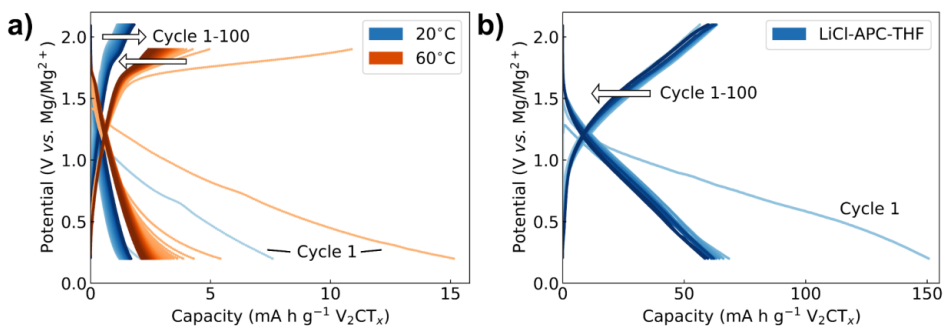


Figure S8 Voltage profiles of V₂CT_x with APC-THF electrolyte at 20 °C and 60 °C (a) and with APC-THF with 0.4 M LiCl (b).

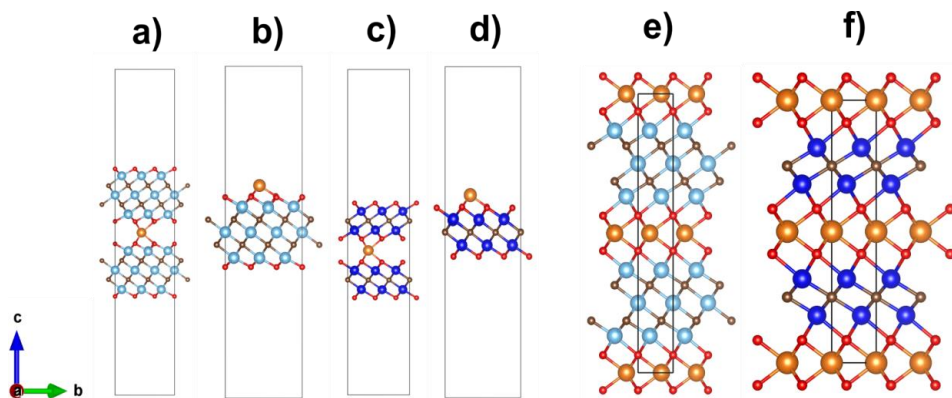


Figure S9 Side view of the different example unit cells used for DFT calculations. (e-f) was used for calculating the average voltage and Bader charges for multi-layer (ML) MXenes completely filled with Mg/Li. (a) and (c) were used for calculating the migration barrier in the fully charged limit for ML MXenes. Vacuum was added to avoid Mg^{2+} - Mg^{2+} interactions across the unit cells along the c-axis. (b) and (d) were used to calculate migration barriers in the fully charged limit for single-layer MXenes. Figure 4a shows top view of the migration barrier calculations.

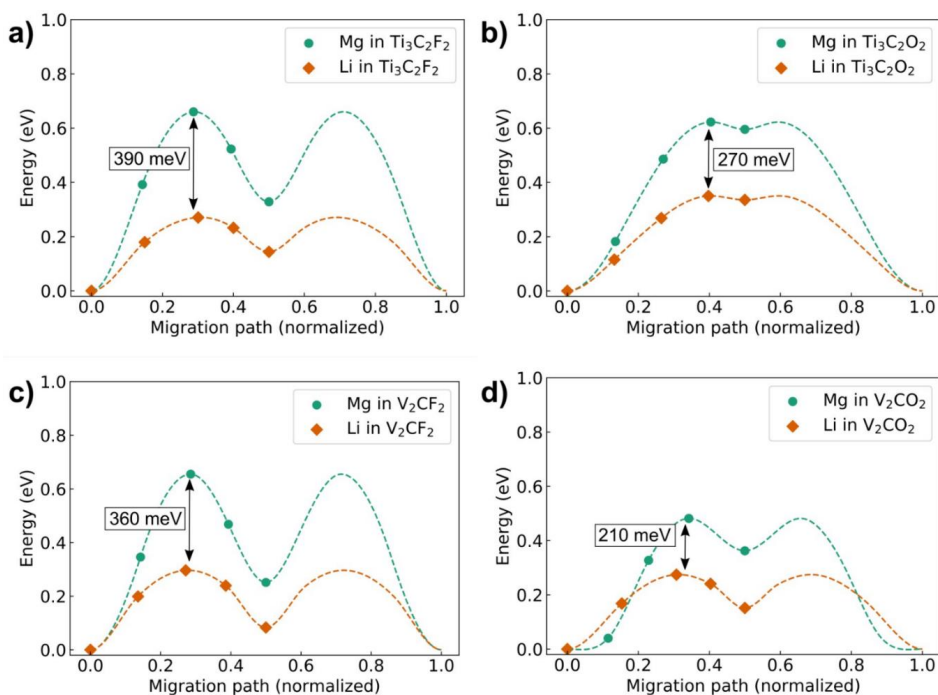


Figure S10 Climbing Image Nudge Elastic Band (cNEB) profiles of multi-layer $\text{Ti}_3\text{C}_2\text{F}_2$ (a), $\text{Ti}_3\text{C}_2\text{O}_2$ (b), V_2CF_2 (c) and V_2CO_2 (d) for the migration of Mg (circles) and Li (diamonds) from C-site to C-site. The stable C-site is with Li/Mg between to carbon atoms (Figure S9 and 4a). The metastable M-site

halfway along the migration path is with Li/Mg between two Ti/V atoms. The cNEB calculations were performed with three images between the C and M-site, to save computational cost and facilitate convergence. The migration path is normalized to ease the comparison, as the Mg migrates a longer path (more curved) than Li. The migration barrier difference between Mg and Li is noted in each panel.

Table S2 A comparison of the migration barriers of Mg-ions and Li-ions in various MXene structures, together with the relative differences in diffusion. Diffusion is proportional to the hopping probability, which again is proportional to $\exp(-E_a/k_bT)$, where E_a is the migration barrier, k_b is the Boltzmann constant and T is the temperature. The relative differences in diffusion (D_{Li}/D_{Mg}) is therefore calculated from the relative differences in $\exp(-E_a/k_bT)$ for Li and Mg at $T = 22$ °C.

| MXene | E_a^{Li} | $\exp(-E_a^{Li}/k_bT)$ | E_a^{Mg} | $\exp(-E_a^{Mg}/k_bT)$ | D_{Li}/D_{Mg} |
|---|------------|------------------------|------------|------------------------|-----------------|
| Ti ₃ C ₂ F ₂ | 270 | $2.44 * 10^{-5}$ | 660 | $5.30 * 10^{-12}$ | $4.60 * 10^6$ |
| Ti ₃ C ₂ O ₂ | 350 | $1.05 * 10^{-6}$ | 622 | $2.36 * 10^{-11}$ | $4.45 * 10^4$ |
| V ₂ CF ₂ | 296 | $8.77 * 10^{-6}$ | 655 | $6.45 * 10^{-12}$ | $1.36 * 10^6$ |
| V ₂ CO ₂ | 274 | $2.08 * 10^{-5}$ | 482 | $5.82 * 10^{-9}$ | $3.57 * 10^3$ |

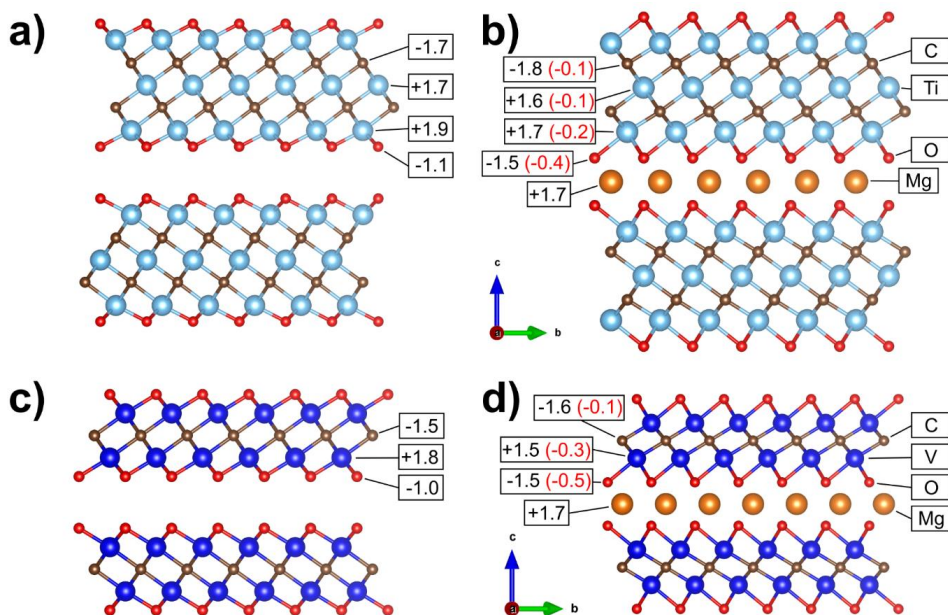


Figure S11 Bader charge analysis²¹ of Ti₃C₂O₂ (a, b) and V₂CO₂ (c, d) MXene before Mg intercalation (a, c) and after (b, d). Bader charge analysis assigns the cumulative electronic charge density to atoms, where the atom separation is defined by a minimum in the electronic charge density landscape. The charge change after Mg intercalation is noted in parenthesis. The unit cell used for the Bader charge calculation is shown in Figure S9 e-f.

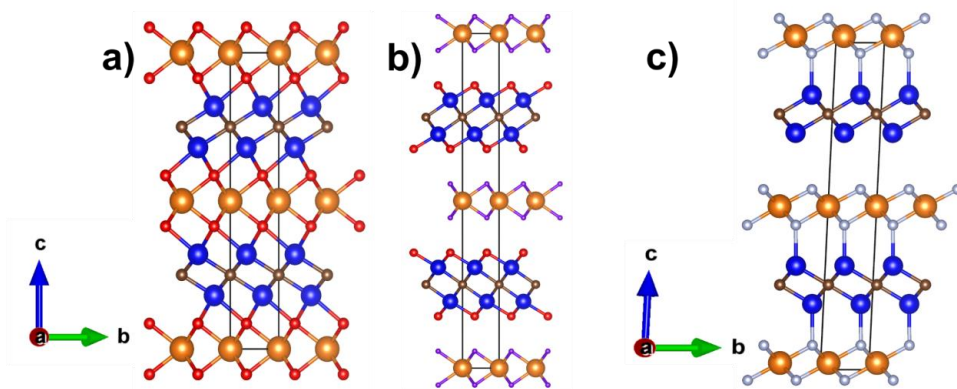


Figure S12 Visualization of the differences between introducing Mg (orange) into the V₂CT₂ MXene with the three different termination groups: V₂CO₂ (a), V₂C(OH)₂ (b) and V₂CF₂ (c). The different atoms are shown as blue (V), brown (C), red (O), grey (F) and purple (H) balls. Notably, the geometrically relaxed structures suggest that the Mg²⁺ reacts with the hydroxyl and fluorine termination groups, forming MgH₂ (b) and MgF₂ (c), respectively.

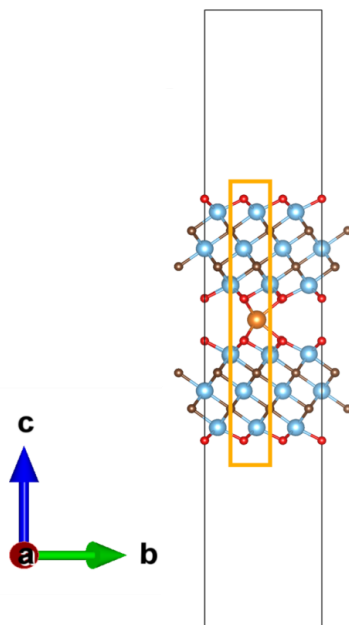


Figure S13 Close up of Figure S9 (a), with a rectangle to emphasize the stacking used for all the calculations.

Table S3 A summary of the intercalation energies, voltages and cNEB migration barriers calculated for Li and Mg intercalation into $Ti_3C_2T_2$ and V_2CT_2 MXenes with various termination groups (T). The unit cells used for these calculations are shown in Figure S9.

| Structure | Intercalation Energy (eV) | | Voltage (V vs. Mg/Mg ²⁺ or Li/Li ⁺) | cNEB migration barriers (meV) | |
|---------------------|---------------------------|--------------|--|-------------------------------|--------------|
| | Multi-layer | Single-layer | | Multi-layer | Single-layer |
| $Ti_3C_2F_2$ -Li | -1.63 | -0.69 | 0.68 | 270 | 292 |
| $Ti_3C_2F_2$ -Mg | -0.37 | 1.85 | -1.29 | 660 | 11 |
| $Ti_3C_2(OH)_2$ -Mg | - | 1.44 | -0.05 | - | 24 |
| $Ti_3C_2O_2$ -Li | -3.19 | -2.38 | 3.03 | 350 | 367 |
| $Ti_3C_2O_2$ -Mg | -3.87 | -1.52 | 1.26 | 622 | 808 |
| $Ti_3C_2O_2$ -MgCl | - | - | - | - | 351 |
| V_2CF_2 -Li | -2.19 | -1.29 | 1.12 | 296 | 256 |
| V_2CF_2 -Mg | -1.60 | 0.87 | -0.05 | 655 | 351 |
| $V_2C(OH)_2$ -Mg | - | 0.92 | -0.47 | - | - |
| V_2CO_2 -Li | -3.75 | -2.85 | 3.28 | 274 | 248 |
| V_2CO_2 -Mg | -4.83 | -2.12 | 1.45 | 482 | 640 |
| V_2CO_2 -MgCl | - | - | - | - | 269 |

Table S4 Summary of the total energies taken directly from the VASP output for the structures shown in Figure S9, with various degrees of Mg filling. The Mg site between two carbon atoms is referred to as the C-site, whereas the Mg site between two metal atoms (Ti/V) is referred to as the M-site. The bulk structure refers to the unit cells shown in Figure S9 e-f, whereas multi-layer refers to the ones in Figure S9 a and c. The total energies for Li and Mg metal are given for one bulk atom.

| Structure | Bulk (S9 e,f) (eV) | | Multi-layer (S9, a, c) (eV) | | | Single-layer (eV) (S9, b, d) | | |
|---------------------|--------------------|-------------------|-----------------------------|------------------|------------------|------------------------------|------------------|------------------|
| | 0% Mg | 100% Mg on C-site | 0% Mg | 1/9 Mg on C-site | 1/9 Mg on M-site | 0% Mg | 1/9 Mg on C-site | 1/9 Mg on M-site |
| $Ti_3C_2F_2$ -Li | -125.78 | -131.33 | -1131.11 | -1134.84 | -1134.70 | -565.15 | -567.94 | -567.76 |
| $Ti_3C_2F_2$ -Mg | -125.78 | -128.85 | -1131.11 | -1133.54 | -1133.21 | -565.15 | -565.36 | -565.35 |
| $Ti_3C_2(OH)_2$ -Mg | -150.26 | -154.16 | - | - | - | -674.82 | -675.42 | -675.43 |
| $Ti_3C_2O_2$ -Li | -136.91 | -147.16 | -1231.22 | -1236.51 | -1236.18 | -615.12 | -619.59 | -619.25 |
| $Ti_3C_2O_2$ -Mg | -136.91 | -146.08 | -1231.22 | -1237.16 | -1236.56 | -615.12 | -618.70 | -618.20 |
| $Ti_3C_2O_2$ -MgCl | - | - | - | - | - | -615.12 | -622.80 | -622.47 |
| V_2CF_2 -Li | -86.75 | -93.18 | -761.81 | -766.10 | -766.01 | -380.46 | -383.85 | -383.72 |
| V_2CF_2 -Mg | -86.75 | -90.68 | -761.81 | -765.47 | -765.22 | -380.46 | -381.65 | -381.49 |
| $V_2C(OH)_2$ -Mg | -109.79 | -112.03 | - | - | - | -492.45 | -493.58 | -493.58 |
| V_2CO_2 -Li | -95.96 | -106.72 | -862.63 | -868.47 | -868.32 | -430.77 | -435.72 | -435.53 |
| V_2CO_2 -Mg | -95.96 | -105.88 | -862.63 | -869.51 | -869.15 | -430.77 | -434.95 | -434.60 |
| V_2CO_2 -MgCl | - | - | - | - | - | -430.77 | -438.92 | -438.72 |
| Li metal | -2.10 | | | | | | | |
| Mg metal | -2.06 | | | | | | | |

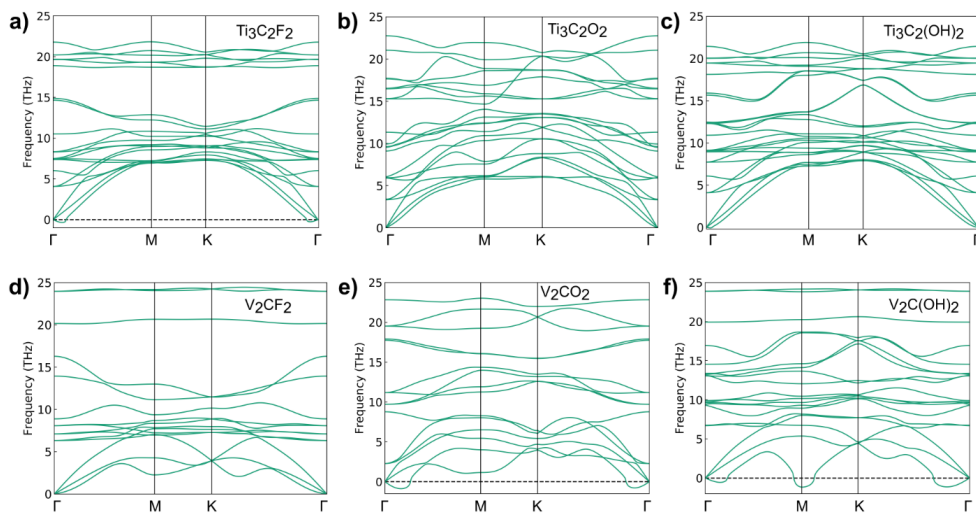


Figure S14 Calculated phonon dispersion diagrams for $\text{Ti}_3\text{C}_2\text{F}_2$ (a), $\text{Ti}_3\text{C}_2\text{O}_2$ (b), $\text{Ti}_3\text{C}_2(\text{OH})_2$ (c), V_2CF_2 (d), V_2CO_2 (e) and $\text{V}_2\text{C}(\text{OH})_2$ (f) using a $4\times 4\times 1$ single-layer supercell. All of the MXenes depicted stable phonons in the Γ , M and K points, except for $\text{V}_2\text{C}(\text{OH})_2$ which showed dynamic instability in the M point. This agrees well with previous reports for Ti_3CT_2 .²⁹ It should be noted that $\text{V}_2\text{C}(\text{OH})_2$ was stable in the M point when a $3\times 3\times 1$ supercell was used. The apparent dependency of the stability of the M point on the supercell size may explain the discrepancy to a recent study, where they reported that $\text{V}_2\text{C}(\text{OH})_2$ is dynamically stable and V_2CO_2 is unstable.³⁰

References:

1. M. Naguib, J. Halim, J. Lu, K. M. Cook, L. Hultman, Y. Gogotsi and M. W. Barsoum, *Journal of the American Chemical Society*, 2013, **135**, 15966-15969.
2. M. Matsui, *Journal of Power Sources*, 2011, **196**, 7048-7055.
3. A. Byeon, M.-Q. Zhao, C. E. Ren, J. Halim, S. Kota, P. Urbankowski, B. Anasori, M. W. Barsoum and Y. Gogotsi, *ACS Applied Materials & Interfaces*, 2017, **9**, 4296-4300.
4. *United States Pat.*, US20130252112A1, 2013.
5. T. Gao, S. Hou, F. Wang, Z. Ma, X. Li, K. Xu and C. Wang, *Angewandte Chemie International Edition*, 2017, **56**, 13526-13530.
6. I. Shterenberg, M. Salama, H. D. Yoo, Y. Gofer, J.-B. Park, Y.-K. Sun and D. Aurbach, *Journal of The Electrochemical Society*, 2015, **162**, A7118-A7128.
7. R. Mohtadi, M. Matsui, T. S. Arthur and S.-J. Hwang, *Angewandte Chemie International Edition*, 2012, **51**, 9780-9783.
8. H. Xu, Z. Zhang, Z. Cui, A. Du, C. Lu, S. Dong, J. Ma, X. Zhou and G. Cui, *Electrochemistry Communications*, 2017, **83**, 72-76.
9. G. Kresse and J. Furthmüller, *Computational Materials Science*, 1996, **6**, 15-50.
10. G. Kresse and J. Furthmüller, *Physical Review B*, 1996, **54**, 11169-11186.
11. G. Kresse and J. Hafner, *Physical Review B*, 1994, **49**, 14251-14269.
12. G. I. Csonka, J. P. Perdew, A. Ruzsinszky, P. H. T. Philipsen, S. Lebègue, J. Paier, O. A. Vydrov and J. G. Ángyán, *Physical Review B*, 2009, **79**, 155107.

13. S. Grimme, *Journal of Computational Chemistry*, 2006, **27**, 1787-1799.
14. G. Henkelman, G. Jóhannesson and H. Jónsson, in *Theoretical Methods in Condensed Phase Chemistry*, ed. S. D. Schwartz, Springer Netherlands, Dordrecht, 2002, DOI: 10.1007/0-306-46949-9_10, pp. 269-302.
15. G. Henkelman and H. Jónsson, *The Journal of Chemical Physics*, 2000, **113**, 9978-9985.
16. G. Henkelman, B. P. Uberuaga and H. Jónsson, *The Journal of Chemical Physics*, 2000, **113**, 9901-9904.
17. H. Jónsson and G. J. W. Mills, Karsten, in *Classical and Quantum Dynamics in Condensed Phase Simulations*, 2000, DOI: 10.1142/9789812839664_0016, pp. 385-404.
18. D. Sheppard, R. Terrell and G. Henkelman, *The Journal of Chemical Physics*, 2008, **128**, 134106.
19. A. Togo and I. Tanaka, *Scripta Materialia*, 2015, **108**, 1-5.
20. A. Ganose, A. Jackson and D. Scanlon, *Journal of Open Source Software*, 2018, **3**, 717.
21. G. Henkelman, A. Arnaldsson and H. Jónsson, *Computational Materials Science*, 2006, **36**, 354-360.
22. E. Sanville, S. D. Kenny, R. Smith and G. Henkelman, *Journal of Computational Chemistry*, 2007, **28**, 899-908.
23. W. Tang, E. Sanville and G. Henkelman, *Journal of Physics: Condensed Matter*, 2009, **21**, 084204.
24. M. Yu and D. R. Trinkle, *The Journal of Chemical Physics*, 2011, **134**, 064111.
25. A. Jain, S. P. Ong, G. Hautier, W. Chen, W. D. Richards, S. Dacek, S. Cholia, D. Gunter, D. Skinner, G. Ceder and K. A. Persson, *APL Materials*, 2013, **1**, 011002.
26. M. Khazaei, M. Arai, T. Sasaki, M. Estili and Y. Sakka, *Physical Chemistry Chemical Physics*, 2014, **16**, 7841-7849.
27. H. D. Yoo, Y. Liang, H. Dong, J. Lin, H. Wang, Y. Liu, L. Ma, T. Wu, Y. Li, Q. Ru, Y. Jing, Q. An, W. Zhou, J. Guo, J. Lu, S. T. Pantelides, X. Qian and Y. Yao, *Nature Communications*, 2017, **8**, 339.
28. K. Momma and F. Izumi, *Journal of Applied Crystallography*, 2011, **44**, 1272-1276.
29. T. Hu, J. Wang, H. Zhang, Z. Li, M. Hu and X. Wang, *Physical Chemistry Chemical Physics*, 2015, **17**, 9997-10003.
30. A. Champagne, L. Shi, T. Ouisse, B. Hackens and J.-C. Charlier, *Physical Review B*, 2018, **97**, 115439.

Paper II

F. H. Fagerli, Z. Wang, T. Grande, H. Kaland, S. M. Selbach, N. P. Wagner and K. Wiik

Removing Fluoride-terminations from Multilayered V_2CT_x MXene by Gas Hydrolyzation

Reprinted from ACS Omega **7**, 27, 23790-23799 (2022).

DOI: [10.1021/acsomega.2c02441](https://doi.org/10.1021/acsomega.2c02441)





Removing Fluoride-Terminations from Multilayered V_2CT_x MXene by Gas Hydrolyzation

Frode Håskjold Fagerli, Zhaohui Wang, Tor Grande, Henning Kaland, Sverre M. Selbach, Nils Peter Wagner, and Kjell Wiik*



Cite This: <https://doi.org/10.1021/acsomega.2c02441>



Read Online

ACCESS |



Metrics & More

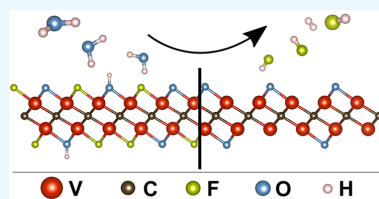


Article Recommendations



Supporting Information

ABSTRACT: Two-dimensional MXenes have shown great promise for many different applications, but in order to fully utilize their potential, control of their termination groups is essential. Here we demonstrate hydrolyzation with a continuous gas flow as a method to remove F-terminations from multilayered V_2CT_x particles, in order to prepare nearly F-free and partly bare vanadium carbide MXene. Density functional theory calculations demonstrate that the substitution of F-terminations is thermodynamically feasible and presents partly nonterminated V_2CO as the dominating hydrolyzation product. Hydrolyzation at elevated temperatures reduced the F content but only subtly changed the O content, as inferred from spectroscopic data. The ideal hydrolyzation temperature was found to be 300 °C, as a degradation of the V_2CT_x phase and a transition to vanadium oxycarbides and V_2O_3 were observed at higher temperature. When tested as electrodes in Li-ion batteries, the hydrolyzed MXene demonstrated a reduced polarization compared with the pristine MXene, but no change in intercalation voltage was observed. Annealing in dry Ar did not result in the same F reduction, and the importance of water vapor was concluded, demonstrating hydrolyzation as a new and efficient method to control the surface terminations of multilayered V_2CT_x post etching. These results also provide new insights on the thermal stability of V_2CT_x MXene in hydrated atmospheres.



INTRODUCTION

Since the first report of MXenes 11 years ago,¹ the research interest for this family of two-dimensional materials has grown exponentially. MXenes are transition metal carbides, nitrides and carbonitrides, where the transition metal “M” and the carbon or nitrogen “X” atoms are stacked in odd numbered layers (e.g., Ti_3C_2 , V_2C , and Nb_2C).² Because of their unique combination of tunable properties, such as metallic conduction, hydrophilic surfaces, adjustable interlayer spacings and rich surface chemistries, MXenes have been reported for a range of applications, from water purification and biomedicine to hydrogen evolution and energy storage.^{2–6} Not only can the combination of M and X elements, or the number of layers, change the properties of the MXene, but with the formation of surface terminal groups upon synthesis, such as -O, -OH, -F, and -Cl, the tuning possibilities of these materials are significant. However, although there have been reported dozens of different MX compositions, there are few methods to fully control the surface terminations on a limited number of MXenes.^{6,7} As the surface terminations determine the local environment in between the MXene layers, and properties such as electronic conduction and ion-intercalation, controlling them is of critical importance for full utilization of MXenes’ potential.^{8–11}

Using the most common etching methods for MXene consisting of HF solutions or a solution of HCl and F-salts, a

mixture of the above-mentioned termination groups are formed.^{12–14} Although there have been reports on vacuum annealing, oxygen annealing, and treatment in alkalic solutions, where the aim was to change the termination groups post etching, they usually only report on partly termination substitution and often in nonscalable methods such as on thin films.^{9,11,15–18} To prove useful for practical applications such as battery electrodes, the termination groups within the bulk of multilayered MXene particles must be reliably controlled. To the authors’ knowledge, it remains to be demonstrated a method to homogeneously control terminations in MXenes after the etching in F-containing solutions.

An example of a MXene where surface control is important is the V_2CT_x phase, which is one of the best compositions for electrode materials in supercapacitors and batteries because of its predicted potential.^{19–21} Even though V_2CT_x already has demonstrated some of the highest capacities of MXenes in Li-ion batteries (LiBs) and supercapacitors,^{22,23} there is still predicted higher capacity, higher voltage, and lower migration

Received: April 19, 2022

Accepted: June 10, 2022

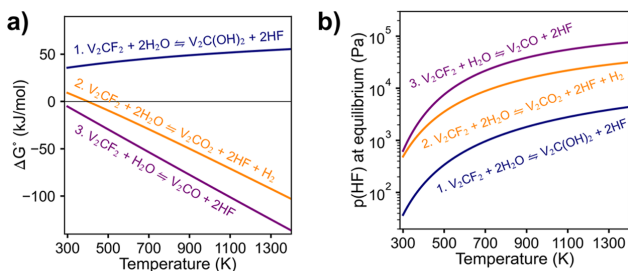


Figure 1. Thermodynamic properties from DFT calculations of three reactions for removal of F-termination from V_2CT_x . (a) shows ΔG° as a function of temperature, while (b) shows the equilibrium partial pressure of HF gas for the three reactions, considering a saturated water vapor pressure of 4.738×10^4 Pa.

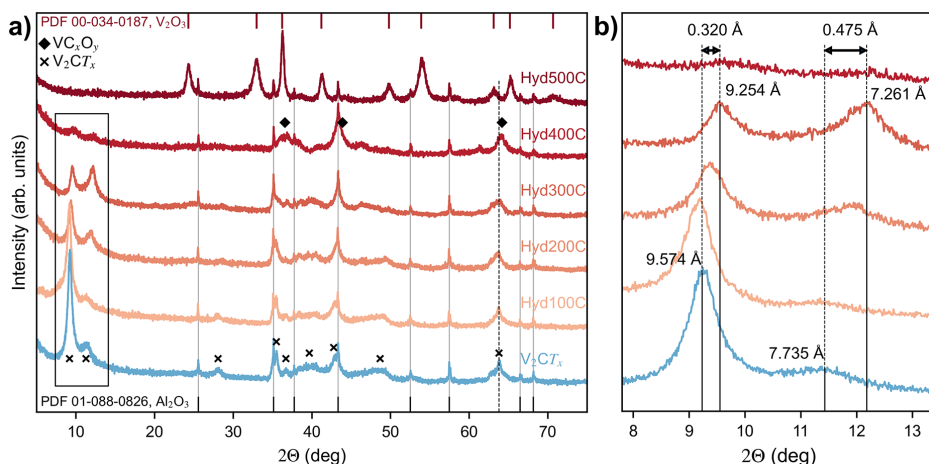


Figure 2. X-ray diffractograms of V_2CT_x hydrolyzed at different temperatures (a), where (b) shows a close-up of the (002) V_2CT_x reflections located inside the black rectangle in (a). In (a), there is also a dashed line indicating the position of the (110) MXene reflection at 63.8° .

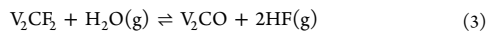
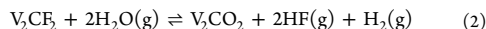
barriers in V_2CO_2 compared with OH- and F-terminated V_2CT_x .^{19,24–27} However, synthesizing V_2CO_2 without decomposing the MXene structure is challenging, because vanadium oxides can form at elevated temperatures by hydrothermal treatment,^{28,29} as well as by annealing in inert, reducing and oxidative atmospheres.^{30,31} Hence, changing the termination groups of V_2CT_x without formation of secondary phases remains a challenge.

In this work, we demonstrate the use of gas hydrolysis to change the surface terminations of V_2CT_x MXene. Three different hydrolyzation reactions are proposed, and density functional theory (DFT) calculations support that a shift from F termination to OH/O termination is thermodynamically feasible, given a continuous flow of humidified Ar gas. Therefore, V_2CT_x particles synthesized by regular HF-etching of V_2AlC were exposed to a controlled water vapor pressure at various temperatures. X-ray photoelectron spectroscopy (XPS) and energy dispersive X-ray spectroscopy (EDS) were used to verify the chemical change upon hydrolyzation at elevated temperature, indicating a significant reduction of F content upon hydrolyzation at elevated temperatures. X-ray diffraction (XRD), scanning electron microscopy (SEM), and Raman

spectroscopy were used to describe the structural changes, showing how the MXene phase remains stable up to 300 °C. These hydrolyzation results are also compared to annealing in dry Ar gas by thermogravimetric analysis (TGA), demonstrating that the water vapor is essential for the resulting change in termination. In the end, galvanostatic cycling of V_2CT_x electrodes in Li-ion batteries is presented to indicate the change in electrochemical properties of V_2CT_x upon modifying the MXene surface.

RESULTS AND DISCUSSION

Thermodynamics. With the intention of substituting F-terminations with O-containing terminations, the following three hydrolyzation reactions are suggested:



The variation in standard free energy with temperature for the three hydrolyzation reactions is given in Figure 1a. While reaction 1 remains positive for all temperatures, reaction 3 has

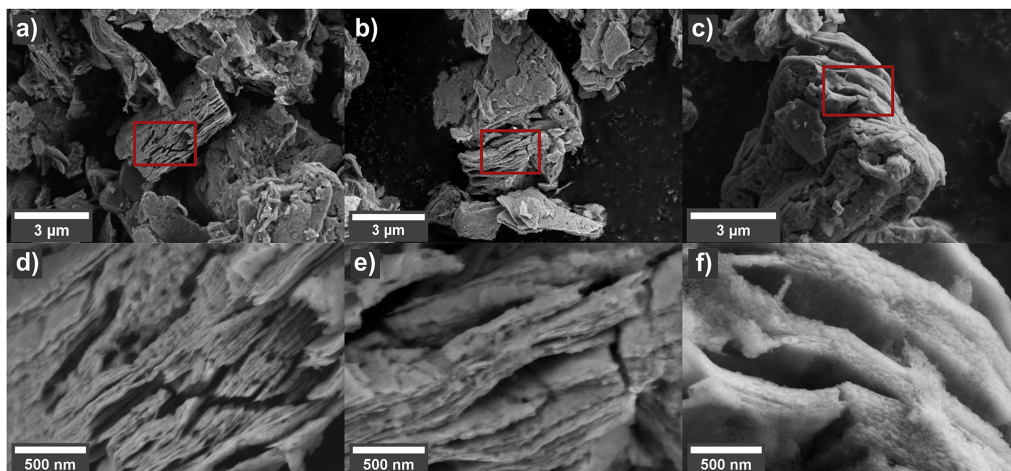
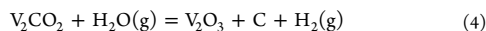


Figure 3. SEM images with low (a–c) and high (d–f) magnification: pristine V_2CT_x (a,d) and V_2CT_x hydrolyzed at 300 °C (b,e) and 500 °C (c,f). The high-magnification areas represent the red rectangle in the low-magnification images.

a negative ΔG° at $T > RT$ and **reaction 2** at $T > 400$ K, indicating spontaneous reactions at elevated temperatures. However, these results only illustrate the situation at standard conditions, and **Figure S11** demonstrates how the ΔG of **reaction 1** also becomes spontaneous with a sufficiently high ratio between the vapor pressure of H_2O and HF. In general, having a high vapor pressure of water and continuous removal of HF gas is beneficial for all the presented hydrolyzation reactions. With a given water vapor pressure of 4.738×10^4 Pa, originating from the saturated water gas at 80 °C,³² **Figure 1b** presents the calculated equilibrium partial pressures of HF gas for the three reactions and demonstrates that significant amounts of HF gas will be produced at elevated temperatures. It also shows that the dominating reaction would be substitution of two F terminations in favor of a single O-termination, leaving parts of the surface unterminated (V_2CO). In total, these results give a strong indication that the removal of F-terminations from V_2CT_x by hydrolyzation is possible, as all the proposed reactions show spontaneous reactions at achievable experimental conditions.

Structure and Morphology. The structural change of the V_2CT_x phase upon hydrolyzation is illustrated in **Figure 2**. It shows that the intensity of the MXene related reflections remain relatively stable up to a hydrolyzation temperature of 300 °C, before they are significantly reduced at 400 °C and virtually absent at 500 °C. The most likely explanation for the degradation at 400 °C can be described by the broad reflections emerging at around 36.6°, 43.5°, and 64.2° which most likely comes from a mixture of vanadium oxycarbides (denoted " VC_xO_y "), as both VC and VO crystallize in the same rock salt structure (space group $Fm\bar{3}m$)⁵³ and show XRD reflections in those three areas (PDF 01-074-1220 and PDF 04-004-9038). However, these reflections disappear upon increasing the temperature to 500 °C, where the only detectable reflections remaining are related to Al_2O_3 from the MAX phase synthesis and V_2O_3 . This indicates that the V_2CT_x first decomposes to VC_xO_y , followed by the formation of V_2O_3 at temperatures above 400 °C. The transition to V_2O_3

after hydrolyzation at 500 °C is also demonstrated by Raman measurements (**Figure S5**), where the MXene related vibration bands disappear in favor of V_2O_3 bands around 210 cm^{-1} , and the D and G bands are attributed to amorphous carbonaceous species that remain. For an oxygen terminated MXene phase (V_2CO_2), the degradation can be described by the following reaction:



However, apart from the degradation at 400 °C significant changes to the MXene phase after hydrolyzation at lower temperatures are observed. First, it should be noted that already in the pristine MXene, the (002) double reflection indicates that two different interlayer spacings are present in the MXene (9.574 and 7.735 Å, **Figure 2b**). This reflection splitting may be due to intercalation of water molecules in parts of the particles. Xie et al. calculated that the interlayer spacing of V_2CT_x lies around 7.5 Å with no intercalated water and around 9.5 Å with 2 layers of water molecules, in fair agreement with our experimental results.³⁴ Since previous articles often report on an interlayer spacing around 9.5 Å or higher, it is reasonable to assume that parts of our particles have been dried prior to the characterization.^{31,35,36} Interestingly, the split remains after hydrolyzation, although we see a shift in intensity toward the reflection at higher 2θ , indicating a reduction of interlayer spacing and less water between the layers. Additionally, we see an uneven shift of the two reflections toward larger 2θ upon increasing the hydrolyzation temperature. After hydrolyzation at 300 °C, the reduction of the interlayer spacing was 0.320 Å for the reflection at lower 2θ and 0.475 Å for the reflection at higher 2θ (**Figure 2b**). This change is ascribed to changes in the surface terminations of the MXene, as well as small changes in intercalated water.

Another interesting aspect with the XRD results is that no reflections related to the MAX phase remain after the etching, indicating complete Al removal from the MAX phase (**Figure S2**). This is usually not reported for HF-etched V_2AlC and demonstrates that reducing the particle size prior to etching

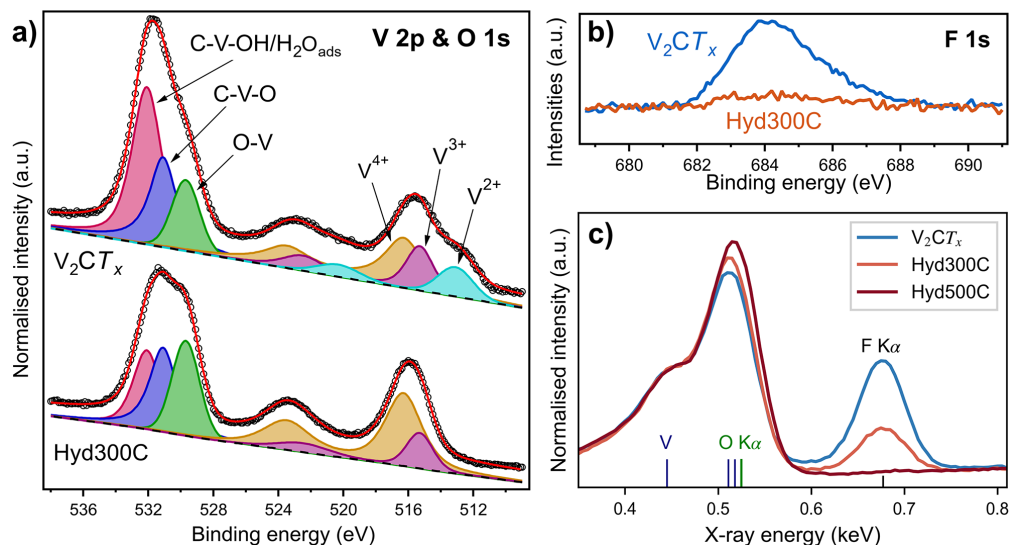


Figure 4. XPS spectra of the V 2p and O 1s region (a) and the F 1s region (b) for V_2CT_x and V_2CT_x hydrolyzed at 300 °C, where the intensity of (a) is normalized to the V peaks. (c) The lower energy region of EDS spectra obtained from mapping of V_2CT_x and V_2CT_x hydrolyzed at 300 °C and 500 °C, where the intensities are normalized to the V LL peak at 0.446 eV, to show the relative shift of the O and F content.

can help improve the etching yield of this phase.^{22,31} With an average size of 5.91 μm (Figure S3), it is shown that 72 h of etching in 48 wt % HF is enough for complete conversion to MXene at ~ 22 °C.

The change in morphology with hydrolysis and temperature is given in Figure 3. Although the macroscopic disc-like morphology remains similar even after the phase transition to V_2O_3 (a–c), the high-magnification images (d–f) reveal a formation of nanoparticles at the edges of the particles after hydrolyzation at 500 °C, which most likely represent V_2O_3 . A similar growth of oxide nanoparticles has been reported after hydrothermal treatment of V_2CT_x , although they report on higher oxidation states of V, corresponding to VO_2 and V_2O_5 .^{28,29} In Ti-based MXenes the formation of TiO_2 nanoparticles at the edges of $Ti_3C_2T_x$ and Ti_2CT_x is also commonly observed upon exposure to water and air at elevated temperatures.^{37–40} The average particle size of the MXenes is a few microns, indicating that the particle size is maintained upon etching, as it matches well with the V_2AlC MAX phase (Figures S3 and S4). Figure 3 also shows that the particles have a lot of cracks and uneven surfaces. This might originate from introduction of strain in the particles during milling of the MAX phase as it can also be seen in the MAX phase particles before etching (Figure S4).

Chemical Composition. The change in chemical environment upon hydrolyzation is described in Figure 4, where XPS is used to probe the outer surface of the MXene particles and EDS is used for bulk characterization. Figure 4a presents the deconvolution of the XPS regions of V 2p and O 1s from V_2CT_x before and after hydrolyzation at 300 °C. Based on the fitting parameters of previous work, the different V $2p_{3/2}$ peaks were assigned to V^{2+} (513.1 eV), V^{3+} (515.3 eV) and V^{4+} (516.3 eV).^{31,41,42} The paramagnetic splitting of V 2p is set to 7.2 eV with a split ratio of 0.5, which gives rise to the V $2p_{1/2}$

peaks at higher binding energies.⁴³ The distribution of oxidation states in the pristine V_2CT_x is in accordance with previous reports.^{31,44,45} Upon hydrolyzation, oxidation of the surface V atoms from 2+ to 4+ is evident, indicating possible oxide formation and/or change in the surface terminations. No contributions from V^{5+} (517.1 eV) in any of the spectra were detected, indicating that the hydrolyzation conditions are less oxidative than air.^{30,31} The deconvolution of the O 1s region is ascribed to vanadium oxides O–V (529.7 eV), O-terminated MXene as C–V–O (531.1 eV), and a combination of OH-terminated V_2CT_x and adsorbed water as C–V–OH/ H_2O_{ads} (532.1 eV).^{22,31,42,46,47} The changes upon hydrolyzation indicate partial increase of surface oxides, with a reduction in the amount of OH-terminations and adsorbed water. This corresponds well with the changes in the V 2p region, and the XRD results presented in Figure 2, as well as with previous reports on the effect of V_2CT_x annealing.³¹

In Table 1, the quantification of the chemical compositions of V_2AlC , V_2CT_x , and V_2CT_x after hydrolyzation at elevated temperatures is given. The EDS results are based on average values of several point scans and show a clear trend in reducing the concentration of F upon increasing the hydrolyzation temperature. The trend is supported by the EDS spectra from mapping presented in Figure 4c, demonstrating a significant reduction in the F $K\alpha$ peak at 0.68 keV upon increasing the hydrolyzation temperature. The EDS results indicate a F reduction of around 2/3 in the bulk of V_2CT_x particles hydrolyzed at 300 °C compared to pristine V_2CT_x . From Figure 4b, the reduction in F is even more significant at the outer surface of the particles as the F 1s peak is virtually absent after the hydrolyzation at 300 °C.

However, only minute changes in O-terminations are observed upon hydrolyzation. From Table 1, the EDS results indicate insignificant changes in the amount of O upon

Table 1. EDS Data Averaged from Several Point Scans of V_2AlC , Pristine V_2CT_x , and V_2CT_x Hydrolyzed at Different Temperatures^a

| sample | V | Al | O | F | O (XPS) | F (XPS) |
|-----------|---|------|------|------|---------|---------|
| V_2AlC | 2 | 0.93 | 0.07 | - | | |
| V_2CT_x | 2 | 0.03 | 0.27 | 1.00 | 1.31 | 0.54 |
| Hyd100C | 2 | 0.03 | 0.38 | 0.74 | | |
| Hyd200C | 2 | 0.05 | 0.28 | 0.49 | | |
| Hyd300C | 2 | 0.02 | 0.27 | 0.31 | 1.18 | 0.04 |
| Hyd400C | 2 | 0.09 | 0.35 | 0.15 | | |
| Hyd500C | 2 | 0.03 | 1.06 | 0.03 | | |

^aThe last two columns indicate the quantification obtained from the XPS fitting. All values are presented relative to one formula unit of V_2CT_x (or a V amount of 2).

increasing the hydrolyzation temperature, where the O content remains stable at around 0.3 per unit formula of V_2CT_x . It should be noted that the quantification of V and O content by EDS is uncertain due to overlapping peaks, which is shown in Figure 4c. Nonetheless, the XPS results of the O 1s region also demonstrate a similar trend, where no obvious increase in the O-content can be seen after the hydrolyzation at 300 °C. From these results, it is therefore difficult to conclude whether the hydrolyzation has resulted in an increase of O-terminations or if F-terminations are simply removed, resulting in the formation of nonterminated V_2C . Although formation of V_2C does not match well with the increased oxidation state of V, removal of terminations matches well with the 2θ shift in the XRD results (Figure 2b), as V_2C would have a smaller interlayer spacing than terminated V_2CT_x . Additionally, it should be noted that from the theoretically calculated $\Delta G^\circ(T)$ curves presented in Figure 1b, the formation of single terminated V_2CO is the most favorable reaction, indicating that formation of a partly nonterminated phase (V_2CO) is more favorable than forming two O-terminations (V_2CO_2). With that in mind, even though characterization of the surface terminations is challenging with respect to MXenes, a more thorough study would be needed to confirm the nature of the termination groups on hydrolyzation, and to better quantify the amount of O-terminations.

Thermal Stability. Figure 5 shows the TG curve of V_2CT_x in Ar atmosphere and the resulting X-ray diffractograms after various annealing temperatures. From the TG curve in Figure 5a, it is seen that the V_2CT_x shows a continuous mass loss but with three significant mass loss regions at ~ 80 – 280 °C,

~ 320 – 500 °C and above ~ 650 °C, matching well with previous reports.^{12,30} The initial mass loss is ascribed to desorption of physisorbed water, which is supported by the 2θ -shift of the (002) V_2CT_x reflections after annealing at 300 °C (Figure 5b). At higher temperatures (~ 320 – 480 °C), the removal of chemisorbed water due to OH-terminations is suggested.^{30,35} However, the XRD data show that this temperature also results in a degradation of the MXene structure, as the (002) reflections of V_2CT_x are significantly reduced after annealing up to 600 °C. Similar to hydrolyzation at 400 °C (Figure 2), the formation of broad reflections from oxycarbide (VC_xO_y) appear at this temperature. It is therefore suggested that the chemisorbed water may be required for the stability of the V_2CT_x phase. At the third mass loss region (>650 °C), the MXene phase is fully degraded. According to Wu et al. only V_2O_3 and V_8C_7 phases were left after annealing up to 1000 °C.³⁰ However, Figure 5b shows the presence of a VF_2 phase after 1 h at 800 °C, indicating that some of the F content remained at this temperature. There is a chance that the discrepancies between these results might come from the initial O:F ratio obtained after etching, where Wu et al. showed a much higher O content than what is presented here (0.98:0.30 vs 0.27:1.00). This might have led to V_2O_3 being formed instead of VF_2 . Since Matthews et al. showed a significant mass loss between 800 and 1000 °C, it might also be that F is removed above 800 °C, resulting in the formation of only oxides and carbides.³⁵

Comparing the results after annealing in pure Ar with the results from the hydrolyzation experiments (Figure 2), some differences with respect to the inclusion of water is observed. First, the remaining F phase after annealing at 800 °C in Ar (Figure 5b) indicates that the water vapor is essential for the removal of F during hydrolyzation, seeing that the F content was reduced to ~ 0 after hydrolyzation at 500 °C (Table 1). Additionally, the splitting of the (002) reflections remains even after annealing in dry Ar, indicating that the chemisorbed water reacts similarly in wet and dry Ar. Moreover, the decomposition of V_2CT_x starts at lower temperatures in the presence of water vapor, considering that the diffractogram after hydrolyzation at 400 °C resembles the one after annealing at 600 °C in Ar. However, even after annealing at 800 °C in dry Ar, the layered morphology of the particles remains (Figure S13), which is similar to what has been reported previously.^{30,31}

Electrochemical Properties. The cycling results of V_2CT_x electrodes in LiB half cells are presented in Figure 6. It shows

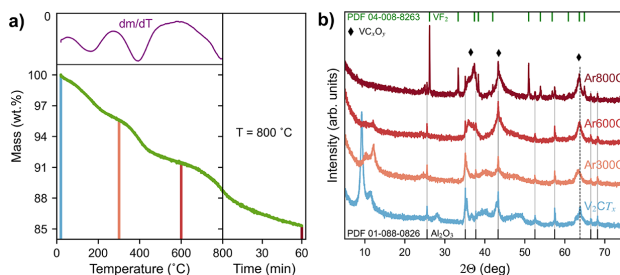


Figure 5. (a) TG curve of V_2CT_x heated in Ar atmosphere up to 800 °C followed by 60 min dwelling. The inset shows differential mass loss during the heating step. (b) The resulting X-ray diffractograms after heating up to 300 °C, 600 °C and 800 °C, shown in (a). The dwelling times at the different temperatures were 60 min, and the dashed line in (b) indicates the position of the (110) MXene reflection at 63.8°.

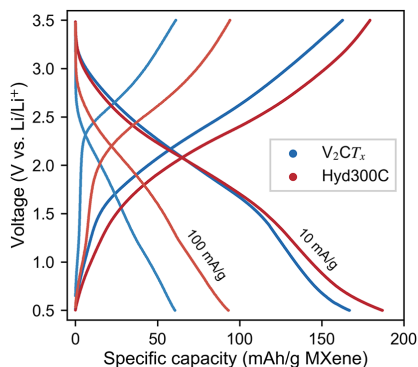


Figure 6. Voltage plots of two different cycles at two different current densities from V_2CT_x electrodes before and after hydrolyzation at 300 °C.

voltage profiles from two cycles at two different current densities (10 and 100 mA/g) and demonstrates similar profiles for the pristine V_2CT_x and the V_2CT_x hydrolyzed at 300 °C. Both materials display generally sloped curves indicative of the pseudocapacitive storage mechanism of MXenes.^{48,49} With sloped plateaus at around 1.5–3 V, these voltage profiles are also similar to previously reported profiles for V_2CT_x showing higher average voltages for V_2CT_x MXene compared with other MXene compositions.^{22,45,50} Another interesting similarity with previous reports is the irreversible plateau observed at ~1.6 V on the first discharge (Figure S16). As SEI formation is not expected to take place at such high voltages, it is possible that this plateau represents trapping of some Li-ions in V_2CT_x on the first cycle.⁵¹ Nevertheless, these cycling results verify the presence of V_2CT_x both before and after the hydrolyzation.

After comparing the electrochemical performance before and after hydrolyzation, only subtle differences are observed (Figure 6). This contrasts with some of the predicted changes from DFT calculations for changing termination groups. First, the average voltage was not increased after the removal of both F- and OH-terminations from hydrolyzation. This could be another indication of the hydrolyzation not resulting in any increase in the O-terminations, as the voltage then would have been expected to increase.^{19,52} Instead, this could also suggest the formation of nonterminated MXene. However, it might also be that the pseudocapacitive nature of the energy storage mechanism blurs out the effects of the intercalation voltages. Wang et al. presented similar voltages for V_2CT_x etched in milder F-conditions (HCl and F-salts), resulting in fewer F-terminations than what is obtained by HF-etching.⁴⁵ Although they demonstrated significantly higher capacities than by HF-etching, most of the capacity was obtained between 0.5 and 0.01 V. Above 0.5 V, their capacities were similar to the capacities obtained here.

The rate capability on the other hand was significantly improved after hydrolyzation of the MXene (Figure 6). Some of these changes can be related to the difference in loading (4.31 mg/cm² for V_2CT_x and 1.62 mg/cm² for Hyd300C), but they cannot explain all the changes. Upon increasing the current density from 10 mA/g to 100 mA/g, the overpotential of the pristine V_2CT_x increases more than for the hydrolyzed one. This change in polarization has previously been

demonstrated for F-free $Ti_3C_2T_x$ MXene⁵³ and matches better with calculated results, as both bare and O-terminated V_2CT_x have been shown to have lower migration barriers for Li-ions compared with OH- and F-terminated V_2CT_x .^{24–27} Notably, the reported F-free $Ti_3C_2T_x$ also did not result in any significant change in intercalation voltage.

Comparing the first cycles of both cells, the irreversible plateau at ~1.6 V is longer for the pristine V_2CT_x than for the V_2CT_x hydrolyzed at 300 °C (Figure S16). A possible explanation for this can be the reduction of the intercalated water between the MXene layers, where the pristine V_2CT_x has the highest amount of intercalated water. Similar water reduction has previously been reported at comparable voltages in $LiPF_6$ electrolytes with water impurities, where H_2O is reduced into OH^- and H_2 gas.^{54,55} However, if water reduction is the explanation of the irreversible plateau, it does not seem to have affected the long-term cycling performance of these electrodes significantly. Nonetheless, seeing that intercalated water remains in V_2CT_x even after annealing in dry Ar at 300 °C, further research should be directed toward understanding the effect of intercalated water in MXenes when cycling in nonaqueous electrolytes.

DISCUSSION

Among the possible post etch treatments of MXenes, the present investigation has demonstrated that hydrolyzation of V_2CT_x at elevated temperatures in a continuous flow of humidified Ar(g) can reduce the concentration of F-terminations. Although there have been several reports on hydrolysis of the $Ti_3C_2T_x$ MXene phase, most of them have been performed under closed conditions, building up significant partial pressures of the product gases resulting from the hydrolyzation reaction and thus limiting further reaction. To the authors' knowledge, there has only been reported one attempt on hydrolyzation of MXene in a continuous flow of humidified inert gas; however, this was performed on $Ti_3C_2T_x$ at moderate hydrolyzation conditions (1 h at 400 °C, with 25 °C water bath and 100 mL/min gas flow).⁴⁸ Based on the results presented here, the application of hydrolysis using a continuous flow of Ar(g) with a high partial pressure of $H_2O(g)$ opens up for new possibilities for post etching treatments of MXenes beyond only V_2CT_x .^{35,56}

Another way of circumventing F-terminations would be to synthesize the MXene in a F-free environment. For the $Ti_3C_2T_x$ phase, there has been reported several F-free etching methods, such as hydrothermal etching in NaOH solutions, in anhydrous halogen solutions and by molten salt reactions in both halogens and Lewis acids.^{7,53,57–59} Although the latter method was used to replace Al by Zn from V_2AlC in the formation of V_2ZnC , they were unable to further separate V_2Cl_2 sheets because of the high bond strength of V–Zn.⁵⁸ Homogeneously terminated MXenes can be prepared by the molten salt method, where successful formation of pure Br-, Cl-, I-, Te-, Se-, NH_2 -, S-, and O-terminations of both $Ti_3C_2T_x$ and Nb_2CT_x MXenes has been demonstrated.⁷ However, to the authors' knowledge, there has not yet been reported any successful etching of V_2CT_x using any of these methods. Until other etching methods are successfully implemented for V_2CT_x , post etching methods will still remain essential in order to control the surface chemistry of this MXene.

CONCLUSIONS

In summary, we have demonstrated gas hydrolyzation as a new and efficient method to significantly reduce the number of F-terminations from multilayered V_2CT_x MXene. DFT calculations demonstrated that several hydrolyzation reactions are possible and that a continuous gas flow during the hydrolyzation would be ideal in order to maintain a high enough ratio between water vapor and the gas products. The V_2CT_x was dehydrated upon annealing in both dry and wet Ar gas, leading to the removal of intercalated water and OH-terminations up to ~ 300 °C. Additionally, hydrolyzation at 300 °C resulted in a removal of F content by almost 70% from the bulk of V_2CT_x particles, thus demonstrating gas hydrolyzation as the most efficient post etching method for bulk F removal to date. However, at hydrolyzation temperatures above 300 °C, the MXene phase started to decompose, and a hydrolyzation temperature of 500 °C resulted in a complete transformation into V_2O_3 and C. In dry Ar, the decomposition started at slightly higher temperatures and only rock salt vanadium oxycarbides and VF_2 remained after annealing at 800 °C.

Although hydrolyzation resulted in a reduction of F-terminations, it did not result in any corresponding increase in O content of the MXene. Instead, formation of non-terminated V_2C is proposed, which is supported by the electrochemical performance of the hydrolyzed V_2CT_x . In LiB half cells, a reduced polarization was observed after hydrolyzation at 300 °C, matching well with the predicted lower migration barriers of bare and O-terminated V_2CT_x . All in all, our results present a new method for post etch removal of F-terminations from MXenes and introduces new insights on the thermal stability of V_2CT_x in a hydrated atmosphere.

METHODS

Synthesis of MAX Phase. The V_2AlC MAX phase was synthesized by a solid-state reaction of V (Sigma-Aldrich, 99.5%), Al (Alfa Aesar, 99.5%), and graphite (Timcal Timrex, 99.5%) powders in a molar ratio of 2:1.3:1. The powders were mixed by wet ball (YSZ) milling in isopropanol overnight, dried in a rotavapor (Büchi R210) and subsequently pressed into 1 g cylindrical pellets at 25 MPa. The pellets were annealed in flowing Ar atmosphere at 1500 °C with a heating rate of 5 °C/min and a dwelling time of 4 h in a tube furnace (Entech ETF 17). To prevent oxidation, the tube was flushed with Ar for 4 h before the heat treatment. The synthesized MAX phase powder was mortared manually in a steel mortar followed by planetary milling at 300 rpm for 10 h in isopropanol with WC milling balls and milling jar, to reduce the particle size and obtain a narrow particle size distribution prior to etching (Figure S3).

Synthesis of MXene. The multilayered V_2CT_x MXene particles were synthesized by slowly adding 2 g of the synthesized V_2AlC MAX phase powder in a polypropylene beaker with 40 mL of a 48 wt % HF solution over the time of 15 min. Thereafter, the beaker was partly covered with parafilm and etched at room temperature for 72 h under constant stirring. After the etching, the remaining powder dispersion was washed several times by centrifugation in DI-water dispersions, until reaching a pH > 5. In the end, the remaining dispersion was vacuum filtered through a 0.22 μ m pore sized PVDF filter paper, before the powder was vacuum-dried at 120 °C for 12 h.

Hydrolyzation. The hydrolyzation of V_2CT_x was performed by spreading out 0.1 g of the MXene powder over 1–2 cm² in an alumina crucible boat before introducing it to a quartz tube furnace (Figure S1). The furnace was sealed and after a 2 h flushing step with a flow rate of Ar gas (99.999%) at 200 mL/min, the furnace was heated to a given temperature at a rate of 200 °C/h and dwelled for 15 h with the same gas flow. To saturate the annealing atmosphere with H₂O after the flushing step, Ar gas was bubbled through a DI water container at 80 °C prior to entering the tube. With a saturated vapor pressure of 4.738×10^4 Pa,³² the water content in the Ar/H₂O mixture was 47%. The exhaust gas was bubbled through a solution of 1 M Ca(NO₃)₂ in order to prevent air leakage into the furnace and to capture HF formed during the hydrolyzation.

Characterization Techniques. The phase purity and crystalline structure of the products were characterized by X-ray powder diffraction (XRD, Bruker D8 Focus Diffractometer) using a Cu K α radiation source ($\lambda = 0.15418$ nm) and a 0.2 mm slit size. The XRD data were collected in a 2θ -range from 5 to 75° with a step size of 0.0143° and a 0.68 s step time. The Al₂O₃ residue obtained from the MAX phase synthesis was used as a reference for the measurements, adjusting and scaling the spectra relative to its (012) reflection located at 25.57°. Thermal stability (TGA) of the MXene was measured with a NETZSCH STA 449 F3 Jupiter analyzer by placing ~ 15 mg of the powder in α -Al₂O₃ containers with lid, heating it up under an Ar flow of 30 mL/min and a heating rate of 5 °C/min from RT to 300, 600, and 800 °C, with a dwelling time of 1 h. The particle size of the MAX phase was determined by laser diffraction (PSD, Horiba Partica LA-960) dispersing the powder in isopropanol to prevent agglomeration. The surface morphology and microstructure were investigated by a field-emission scanning electron microscope (FESEM, Carl Zeiss Ag – ULTRA 55) using an acceleration voltage of 5–10 kV. Energy dispersive X-ray spectroscopy (EDS) was used to assess chemical composition using an XFlash 4010 X-ray detector and an acceleration voltage of 10–15 kV. To obtain quantitative results, the average values from five or more point scans were chosen and analyzed using the Bruker Esprit 1.9 software (Figure S10). X-ray photoelectron spectroscopy (XPS) was used for further information on chemical composition of the powder. The XPS samples were made by gluing the MXene powder to a Si wafer substrate using silver glue, and the measurements were performed under ultrahigh vacuum using a SPECS XR-50 X-ray source with a Mg anode and a VG ESCA MKIV with a CLAM4 analyzer. The satellite peaks stemming from the Mg K α_3 and K α_4 were removed from the spectra before further data analysis were completed (Figure S14). To compensate for the static charge of the sample, the Si_{2p} peak from the substrate (99.3 eV) was used as an internal reference.⁴³ The fitting of the curves was completed in the Igor Pro 7 software, using a Shirley background, and the quantification was performed using known photoionization cross-section values.⁶⁰ The vibrational properties were investigated by a WITec Alpha 300r Confocal Raman Microscope, using a 100 \times objective, a 532 nm Ar laser and a laser power below 0.8 mW to prevent oxidation of the material (Figure S6).

Electrochemical Measurements. To assess the electrochemical performance of the materials, LiB half cells were prepared with the MXene as the working electrode. These electrodes were processed by mixing N-ethyl-2-pyrrolidone

(NEP)-slurries with 10 wt.% PVDF binder, 10 wt.% carbon black as conductive additive and 80 wt.% of the active material (V_2CT_x and V_2CT_x hydrolyzed at 300 °C). First, the carbon black and active material were mixed for 10 min at 25 Hz in a shaker mill. Next, a premade PVDF-NEP solution was added before the slurry was further diluted with additional NEP to obtain a solid to liquid ratio of 1:6. The slurries were then mixed by continuous shaking at 15 Hz for 30 min with a shaker ball and drop cast onto precut circular Al current collectors. The electrodes were dried at room temperature in a fume hood overnight before being dried in vacuum at 60 °C for at least 4 h. This resulted in active material loadings of 1.6–4.3 mg/cm². The electrodes were assembled into 2016-type coin cells in an argon-filled glovebox ($O_2 \leq 0.1$ ppm, $H_2O \leq 0.1$ ppm) using Li-foil as the counter electrode, glass microfiber (Whatman) as the separator, and 110 μ L 1 M LiPF₆ in ethylene carbonate and ethyl methyl carbonate with a volume ratio of 1:1 (EC/EMC 1:1) as the electrolyte. The assembled cells were galvanostatically cycled at various specific currents (10 mA/g–100 mA/g) in a voltage range of 0.5 to 3.5 V using a BioLogic BCS-805 cycler at a controlled temperature of 20 °C.

Theoretical Calculations. Density functional theory calculations were done with VASP^{61–64} using the PBEsol functional^{65–67} and a plane-wave energy cutoff of 650 eV. Gamma-centered k-point meshes with $\sim 0.2 \text{ \AA}^{-1}$ spacings were used for solid structures. Geometries were relaxed until the forces on the ions were below 10^{-4} eV/Å to obtain ground state energies ($E_0(T = 0 \text{ K})$). Vibrational properties of the solid were calculated with Phonopy,⁶⁸ and those for gaseous species were calculated by standard statistical mechanics.^{69,70} Corresponding zero-point energies (ZPE) were calculated for the solids and taken from the NIST-CCCBDB database for gaseous species.⁷¹ The thermodynamic properties of chemical reactions were evaluated following ref 72. Pseudopotentials, ΔG curves for more reactions, and a full description of the computational workflow are given in the [Supporting Information](#).

■ ASSOCIATED CONTENT

SI Supporting Information

(PDF) The Supporting Information is available free of charge at <https://pubs.acs.org/doi/10.1021/acsomega.2c02441>.

Detailed description of the DFT workflow with pseudopotentials and thermodynamic results for additional reactions, schematic of the hydrolyzation setup, additional experimental data including X-ray diffractogram of V_2AlC MAX phase before and after etching, PSD plots and SEM images from V_2AlC before and after wet milling, Raman spectra, EDS spectra, full XPS spectra and satellite removal of O 1s and V 2p regions, galvanostatic cycling plots of first cycles, and SEM images of V_2AlC and V_2CT_x after the TG annealing in Ar (PDF)

■ AUTHOR INFORMATION

Corresponding Author

Kjell Wiik – Department of Materials Science and Engineering, NTNU Norwegian University of Science and Technology, NO-7034 Trondheim, Norway; Email: kjell.wiik@ntnu.no

Authors

Frode Håskjold Fagerli – Department of Materials Science and Engineering, NTNU Norwegian University of Science and Technology, NO-7034 Trondheim, Norway; orcid.org/0000-0001-9764-1602

Zhaohui Wang – Department of Materials Science and Engineering, NTNU Norwegian University of Science and Technology, NO-7034 Trondheim, Norway; SINTEF Industry, NO-7034 Trondheim, Norway

Tor Grande – Department of Materials Science and Engineering, NTNU Norwegian University of Science and Technology, NO-7034 Trondheim, Norway

Henning Kaland – Department of Materials Science and Engineering, NTNU Norwegian University of Science and Technology, NO-7034 Trondheim, Norway; orcid.org/0000-0002-5886-9521

Sverre M. Selbach – Department of Materials Science and Engineering, NTNU Norwegian University of Science and Technology, NO-7034 Trondheim, Norway; orcid.org/0000-0001-5838-8632

Nils Peter Wagner – Department of Materials Science and Engineering, NTNU Norwegian University of Science and Technology, NO-7034 Trondheim, Norway; SINTEF Industry, NO-7034 Trondheim, Norway; orcid.org/0000-0002-8014-4324

Complete contact information is available at: <https://pubs.acs.org/doi/10.1021/acsomega.2c02441>

Author Contributions

T.G. conceived the main research plan with input from the rest of the authors. Z.W. performed the DFT calculations, while F.H.F. performed the experimental work and data analysis under supervision from N.W. and K.W. The manuscript was drafted by F.H.F. and finalized with input from all authors.

Notes

The authors declare no competing financial interest.

■ ACKNOWLEDGMENTS

The author would like to thank H. Røst and J. Wells at NTNU for help with XPS measurements and XPS data analysis as well as J. Hadler-Jacobsen (NTNU) and F. Vullum-Bruer (SINTEF Energi AS) for MXene related discussions. Funding comes from the Norwegian Research council through the project “High-capacity 2D layered materials for Mg-ion batteries” (project number 275810) and computational resources were provided by UNINETT Sigma2 through the project NN9264k.

■ REFERENCES

- (1) Naguib, M.; Kurtoglu, M.; Presser, V.; Lu, J.; Niu, J. J.; Heon, M.; Hultman, L.; Gogotsi, Y.; Barsoum, M. W. Two-Dimensional Nanocrystals Produced by Exfoliation of Ti_3AlC_2 . *Adv. Mater.* **2011**, *23*, 4248–4253.
- (2) Anasori, B.; Lukatskaya, M. R.; Gogotsi, Y. 2D metal carbides and nitrides (MXenes) for energy storage. *Nat. Rev. Mater.* **2017**, *2*, 16098.
- (3) Al-Hamadani, Y. A. J.; Jun, B. M.; Yoon, M.; Taheri-Qazvini, N.; Snyder, S. A.; Jang, M.; Heo, J.; Yoon, Y. Applications of MXene-based membranes in water purification: A review. *Chemosphere* **2020**, *254*, 126821.
- (4) Gao, G. P.; O'Mullane, A. P.; Du, A. J. 2D MXenes: A New Family of Promising Catalysts for the Hydrogen Evolution Reaction. *ACS Catal.* **2017**, *7*, 494–500.

- (5) Huang, K.; Li, Z. J.; Lin, J.; Han, G.; Huang, P. Two-dimensional transition metal carbides and nitrides (MXenes) for biomedical applications. *Chem. Soc. Rev.* **2018**, *47*, 5109–5124.
- (6) VahidMohammadi, A.; Rosen, J.; Gogotsi, Y. The world of two-dimensional carbides and nitrides (MXenes). *Science* **2021**, *372*, eabf1581.
- (7) Kamysbayev, V.; Filatov, A. S.; Hu, H.; Rui, X.; Lagunas, F.; Wang, D.; Klie, R. F.; Talapin, D. V. Covalent surface modifications and superconductivity of two-dimensional metal carbide MXenes. *Science* **2020**, *369*, 979–983.
- (8) Hajian, S.; Khakbaz, P.; Moshayedi, M.; Maddipatla, D.; Narakathu, B. B.; Turkani, V. S.; Bazuin, B. J.; Pourfath, M.; Atashbar, M. Z. Impact of Different Ratios of Fluorine, Oxygen, and Hydroxyl Surface Terminations on Ti₃C₂T_x MXene as Ammonia Sensor: A First-Principles Study. *IEEE Sens. J.* **2018**, *2018*, 1–4.
- (9) Schultz, T.; Frey, N. C.; Hantanasirisakul, K.; Park, S.; May, S. J.; Shenoy, V. B.; Gogotsi, Y.; Koch, N. Surface Termination Dependent Work Function and Electronic Properties of Ti₃C₂T_x MXene. *Chem. Mater.* **2019**, *31*, 6590–6597.
- (10) Xu, K.; Merlet, C.; Lin, Z.; Shao, H.; Taberna, P.-L.; Miao, L.; Jiang, J.; Zhu, J.; Simon, P. Effects of functional groups and anion size on the charging mechanisms in layered electrode materials. *Energy Storage Mater.* **2020**, *33*, 460–469.
- (11) Hart, J. L.; Hantanasirisakul, K.; Lang, A. C.; Anasori, B.; Pinto, D.; Pivak, Y.; van Omme, J. T.; May, S. J.; Gogotsi, Y.; Taheri, M. L. Control of MXenes' electronic properties through termination and intercalation. *Nat. Commun.* **2019**, *10*, 522.
- (12) Alhabeib, M.; Maleski, K.; Anasori, B.; Lelyukh, P.; Clark, L.; Sin, S.; Gogotsi, Y. Guidelines for Synthesis and Processing of Two-Dimensional Titanium Carbide (Ti₃C₂T_x MXene). *Chem. Mater.* **2017**, *29*, 7633–7644.
- (13) Wang, H.-W.; Naguib, M.; Page, K.; Wesolowski, D. J.; Gogotsi, Y. Resolving the Structure of Ti₃C₂T_x MXenes through Multilevel Structural Modeling of the Atomic Pair Distribution Function. *Chem. Mater.* **2016**, *28*, 349–359.
- (14) Hope, M. A.; Forse, A. C.; Griffith, K. J.; Lukatskaya, M. R.; Ghidui, M.; Gogotsi, Y.; Grey, C. P. NMR reveals the surface functionalisation of Ti₃C₂MXene. *Phys. Chem. Chem. Phys.* **2016**, *18*, 5099–5102.
- (15) Halim, J.; Persson, I.; Eklund, P.; Persson, P. O. A.; Rosen, J. Sodium hydroxide and vacuum annealing modifications of the surface terminations of a Ti₃C₂ (MXene) epitaxial thin film. *RSC Adv.* **2018**, *8*, 36785–36790.
- (16) Persson, I.; Näslund, L.-Å.; Halim, J.; Barsoum, M. W.; Darakchieva, V.; Palisaitis, J.; Rosen, J.; Persson, P. O. Å. On the organization and thermal behavior of functional groups on Ti₃C₂MXene surfaces in vacuum. *2D Mater.* **2018**, *5*, 015002.
- (17) Persson, I.; Halim, J.; Hansen, T. W.; Wagner, J. B.; Darakchieva, V.; Palisaitis, J.; Rosen, J.; Persson, P. O. Å. How Much Oxygen Can a MXene Surface Take Before It Breaks? *Adv. Funct. Mater.* **2020**, *30*, 1909005.
- (18) Liu, P.; Ding, W.; Liu, J.; Shen, L.; Jiang, F.; Liu, P.; Zhu, Z.; Zhang, G.; Liu, C.; Xu, J. Surface termination modification on high-conductivity MXene film for energy conversion. *J. Alloys Compd.* **2020**, *829*, 154634.
- (19) Eames, C.; Islam, M. S. Ion Intercalation into Two-Dimensional Transition-Metal Carbides: Global Screening for New High-Capacity Battery Materials. *J. Am. Chem. Soc.* **2014**, *136*, 16270–16276.
- (20) Xie, Y.; Dall'Agnese, Y.; Naguib, M.; Gogotsi, Y.; Barsoum, M. W.; Zhuang, H. L.; Kent, P. R. C. Prediction and Characterization of MXene Nanosheet Anodes for Non-Lithium-Ion Batteries. *ACS Nano* **2014**, *8*, 9606–9615.
- (21) Zhan, C.; Sun, W.; Kent, P. R. C.; Naguib, M.; Gogotsi, Y.; Jiang, D.-e. Computational Screening of MXene Electrodes for Pseudocapacitive Energy Storage. *J. Phys. Chem. C* **2019**, *123*, 315–321.
- (22) Naguib, M.; Halim, J.; Lu, J.; Cook, K. M.; Hultman, L.; Gogotsi, Y.; Barsoum, M. W. New Two-Dimensional Niobium and Vanadium Carbides as Promising Materials for Li-Ion Batteries. *J. Am. Chem. Soc.* **2013**, *135*, 15966–15969.
- (23) Shan, Q.; Mu, X.; Alhabeib, M.; Shuck, C. E.; Pang, D.; Zhao, X.; Chu, X.-F.; Wei, Y.; Du, F.; Chen, G.; Gogotsi, Y.; Gao, Y.; Dall'Agnese, Y. Two-dimensional vanadium carbide (V₂C) MXene as electrode for supercapacitors with aqueous electrolytes. *Electrochem. Commun.* **2018**, *96*, 103–107.
- (24) Tang, Q.; Zhou, Z.; Shen, P. Are MXenes Promising Anode Materials for Li Ion Batteries? Computational Studies on Electronic Properties and Li Storage Capability of Ti₃C₂ and Ti₃C₂ × 2 (X = F, OH) Monolayer. *J. Am. Chem. Soc.* **2012**, *134*, 16909–16916.
- (25) Hu, J.; Xu, B.; Ouyang, C.; Yang, S. A.; Yao, Y. Investigations on V₂C and V₂CX₂ (X = F, OH) Monolayer as a Promising Anode Material for Li Ion Batteries from First-Principles Calculations. *J. Phys. Chem. C* **2014**, *118*, 24274–24281.
- (26) Yan, B.; Lu, C.; Zhang, P.; Chen, J.; He, W.; Tian, W.; Zhang, W.; Sun, Z. Oxygen/sulfur decorated 2D MXene V₂C for promising lithium-ion battery anodes. *Mater. Today Commun.* **2020**, *22*, 100713.
- (27) Sun, D.; Hu, Q.; Chen, J.; Zhang, X.; Wang, L.; Wu, Q.; Zhou, A. Structural Transformation of MXene (V₂C, Cr₂C, and Ta₂C) with O Groups during Lithiation: A First-Principles Investigation. *ACS Appl. Mater. Interfaces* **2016**, *8*, 74–81.
- (28) Luo, W.; Liu, Y.; Li, F.; Huo, J.; Zhao, D.; Zhu, J.; Guo, S. H₂O assisted hydrothermal oxidation of partially etched vanadium carbides (MXene) and their electrochemical properties as anode for Li-ion batteries. *Appl. Surf. Sci.* **2020**, *523*, 146387.
- (29) Narayanasamy, M.; Kirubasankar, B.; Shi, M.; Velayutham, S.; Wang, B.; Angaiah, S.; Yan, C. Morphology restrained growth of V₂O₅ by the oxidation of V-MXenes as a fast diffusion controlled cathode material for aqueous zinc ion batteries. *Chem. Commun.* **2020**, *56*, 6412–6415.
- (30) Wu, M.; Wang, B.; Hu, Q.; Wang, L.; Zhou, A. The Synthesis Process and Thermal Stability of V₂C MXene. *Materials* **2018**, *11*, 2112.
- (31) Thakur, R.; VahidMohammadi, A.; Moncada, J.; Adams, W. R.; Chi, M.; Tatarchuk, B.; Beidaghi, M.; Carrero, C. A. Insights into the thermal and chemical stability of multilayered V₂C_tx MXene. *Nanoscale* **2019**, *11*, 10716–10726.
- (32) Wexler, A. Vapor pressure formulation for water in range 0 to 100 C. A revision. *J. Res. Natl. Bur. Stand. A Phys. Chem.* **1976**, *80*, 775.
- (33) Bauer, G.; Güther, V.; Hess, H.; Otto, A.; Roidl, O.; Roller, H.; Sattelberger, S.; Köther-Becker, S.; Beyer, T. Vanadium and Vanadium Compounds. In *Ullmann's Encyclopedia of Industrial Chemistry*; Wiley, 2017; pp 1–22.
- (34) Xie, Y.; Naguib, M.; Mochalin, V. N.; Barsoum, M. W.; Gogotsi, Y.; Yu, X.; Nam, K.-W.; Yang, X.-Q.; Kolesnikov, A. I.; Kent, P. R. C. Role of Surface Structure on Li-Ion Energy Storage Capacity of Two-Dimensional Transition-Metal Carbides. *J. Am. Chem. Soc.* **2014**, *136*, 6385–6394.
- (35) Matthews, K.; Zhang, T.; Shuck, C. E.; VahidMohammadi, A.; Gogotsi, Y. Guidelines for Synthesis and Processing of Chemically Stable Two-Dimensional V₂C_tx MXene. *Chem. Mater.* **2022**, *34*, 499–509.
- (36) He, H.; Xia, Q.; Wang, B.; Wang, L.; Hu, Q.; Zhou, A. Two-dimensional vanadium carbide (V₂C_tx) MXene as supercapacitor electrode in seawater electrolyte. *Chin. Chem. Lett.* **2020**, *31*, 984–987.
- (37) Xia, F.; Lao, J.; Yu, R.; Sang, X.; Luo, J.; Li, Y.; Wu, J. Ambient oxidation of Ti₃C₂MXene initialized by atomic defects. *Nanoscale* **2019**, *11*, 23330–23337.
- (38) Naguib, M.; Mashtalir, O.; Lukatskaya, M. R.; Dyatkin, B.; Zhang, C.; Presser, V.; Gogotsi, Y.; Barsoum, M. W. One-step synthesis of nanocrystalline transition metal oxides on thin sheets of disordered graphitic carbon by oxidation of MXenes. *Chem. Commun.* **2014**, *50*, 7420–7423.
- (39) Wang, K.; Zhou, Y.; Xu, W.; Huang, D.; Wang, Z.; Hong, M. Fabrication and thermal stability of two-dimensional carbide Ti₃C₂ nanosheets. *Ceram. Int.* **2016**, *42*, 8419–8424.

- (40) Rakhi, R. B.; Ahmed, B.; Hedhili, M. N.; Anjum, D. H.; Alshareef, H. N. Effect of Postetch Annealing Gas Composition on the Structural and Electrochemical Properties of Ti₂CTx MXene Electrodes for Supercapacitor Applications. *Chem. Mater.* **2015**, *27*, 5314–5323.
- (41) Biesinger, M. C.; Lau, L. W. M.; Gerson, A. R.; Smart, R. S. C. Resolving surface chemical states in XPS analysis of first row transition metals, oxides and hydroxides: Sc, Ti, V, Cu and Zn. *Appl. Surf. Sci.* **2010**, *257*, 887–898.
- (42) Choi, J.-G. The surface properties of vanadium compounds by X-ray photoelectron spectroscopy. *Appl. Surf. Sci.* **1999**, *148*, 64–72.
- (43) Chastain, J.; King, R. C., Jr *Handbook of X-ray photoelectron spectroscopy*; Perkin-Elmer: Waltham, MA, 1992, 261.
- (44) Zhang, W.; Peng, J.; Hua, W.; Liu, Y.; Wang, J.; Liang, Y.; Lai, W.; Jiang, Y.; Huang, Y.; Zhang, W.; Yang, H.; Yang, Y.; Li, L.; Liu, Z.; Wang, L.; Chou, S. Architecting Amorphous Vanadium Oxide/MXene Nanohybrid via Tunable Anodic Oxidation for High-Performance Sodium-Ion Batteries. *Adv. Energy Mater.* **2021**, *11*, 2100757.
- (45) Wang, L.; Liu, D.; Lian, W.; Hu, Q.; Liu, X.; Zhou, A. The preparation of V₂CTx by facile hydrothermal-assisted etching processing and its performance in lithium-ion battery. *J. Mater. Res. Technol.* **2020**, *9*, 984–993.
- (46) Halim, J.; Cook, K. M.; Naguib, M.; Eklund, P.; Gogotsi, Y.; Rosen, J.; Barsoum, M. W. X-ray photoelectron spectroscopy of select multi-layered transition metal carbides (MXenes). *Appl. Surf. Sci.* **2016**, *362*, 406–417.
- (47) Yamamoto, S.; Bluhm, H.; Andersson, K.; Ketteler, G.; Ogasawara, H.; Salmeron, M.; Nilsson, A. In situ x-ray photoelectron spectroscopy studies of water on metals and oxides at ambient conditions. *J. Condens. Matter Phys.* **2008**, *20*, 184025.
- (48) Cheng, R.; Hu, T.; Zhang, H.; Wang, C.; Hu, M.; Yang, J.; Cui, C.; Guang, T.; Li, C.; Shi, C.; Hou, P.; Wang, X. Understanding the Lithium Storage Mechanism of Ti₃C₂T_x MXene. *J. Phys. Chem. C* **2019**, *123*, 1099–1109.
- (49) Wang, X.; Mathis, T. S.; Li, K.; Lin, Z.; Vlcek, L.; Torita, T.; Osti, N. C.; Hatter, C.; Urbankowski, P.; Sarycheva, A.; Tyagi, M.; Mamontov, E.; Simon, P.; Gogotsi, Y. Influences from solvents on charge storage in titanium carbide MXenes. *Nat. Energy* **2019**, *4*, 241–248.
- (50) Naguib, M.; Come, J.; Dyatkin, B.; Presser, V.; Taberna, P.-L.; Simon, P.; Barsoum, M. W.; Gogotsi, Y. MXene: a promising transition metal carbide anode for lithium-ion batteries. *Electrochem. Commun.* **2012**, *16*, 61–64.
- (51) Xu, K. Nonaqueous Liquid Electrolytes for Lithium-Based Rechargeable Batteries. *Chem. Rev.* **2004**, *104*, 4303–4418.
- (52) Kaland, H.; Hadler-Jacobsen, J.; Fagerli, F. H.; Wagner, N. P.; Wang, Z.; Selbach, S. M.; Vullum-Bruer, F.; Wiik, K.; Schnell, S. K. Are MXenes suitable as cathode materials for rechargeable Mg batteries? *Sustain. Energy Fuels* **2020**, *4*, 2956–2966.
- (53) Huang, L.; Li, T.; Liu, Q.; Gu, J. Fluorine-free Ti₃C₂T_x as anode materials for Li-ion batteries. *Electrochem. Commun.* **2019**, *104*, 106472.
- (54) Bernhard, R.; Metzger, M.; Gasteiger, H. A. Gas Evolution at Graphite Anodes Depending on Electrolyte Water Content and SEI Quality Studied by On-Line Electrochemical Mass Spectrometry. *J. Electrochem. Soc.* **2015**, *162*, A1984–A1989.
- (55) Tezel, A. O.; Streich, D. K.; Guéguen, A.; Hahlin, M.; Sunde, S.; Edström, K.; Novák, P.; Svensson, A. M. Solid Electrolyte Interphase (SEI) Formation on the Graphite Anode in Electrolytes Containing the Anion Receptor Tris(hexafluoroisopropyl)borate (THFIPB). *J. Electrochem. Soc.* **2020**, *167*, 130504.
- (56) Huang, S.; Mochalin, V. N. Hydrolysis of 2D Transition-Metal Carbides (MXenes) in Colloidal Solutions. *Inorg. Chem.* **2019**, *58*, 1958–1966.
- (57) Jawaid, A.; Hassan, A.; Neher, G.; Nepal, D.; Pachter, R.; Kennedy, W. J.; Ramakrishnan, S.; Vaia, R. A. Halogen Etch of Ti₃AlC₂MAX Phase for MXene Fabrication. *ACS Nano* **2021**, *15*, 2771–2777.
- (58) Li, M.; Lu, J.; Luo, K.; Li, Y.; Chang, K.; Chen, K.; Zhou, J.; Rosen, J.; Hultman, L.; Eklund, P.; Persson, P. O. Å.; Du, S.; Chai, Z.; Huang, Z.; Huang, Q. Element Replacement Approach by Reaction with Lewis Acidic Molten Salts to Synthesize Nanolaminated MAX Phases and MXenes. *J. Am. Chem. Soc.* **2019**, *141*, 4730–4737.
- (59) Li, Y.; Shao, H.; Lin, Z.; Lu, J.; Liu, L.; Duployer, B.; Persson, P. O. Å.; Eklund, P.; Hultman, L.; Li, M.; Chen, K.; Zha, X.; Du, S.; Rozier, P.; Chai, Z.; Raymundo-Piñero, E.; Taberna, P.; Simon, P.; Huang, Q. A general Lewis acidic etching route for preparing MXenes with enhanced electrochemical performance in non-aqueous electrolyte. *Nat. Mater.* **2020**, *19*, 894–899.
- (60) Yeh, J. J. *Atomic Calculation of Photoionization Cross-sections and Asymmetry Parameters*; Gordon & Breach Science Publishers: Philadelphia, PA, 1993.
- (61) Kresse, G.; Furthmüller, J. Efficiency of ab-initio total energy calculations for metals and semiconductors using a plane-wave basis set. *Comput. Mater. Sci.* **1996**, *6*, 15–50.
- (62) Kresse, G.; Furthmüller, J. Efficient iterative schemes for ab initio total-energy calculations using a plane-wave basis set. *Phys. Rev. B* **1996**, *54*, 11169–11186.
- (63) Kresse, G.; Hafner, J. Ab initio molecular dynamics for liquid metals. *Phys. Rev. B* **1993**, *47*, 558.
- (64) Kresse, G.; Hafner, J. Ab initio molecular-dynamics simulation of the liquid-metal–amorphous-semiconductor transition in germanium. *Phys. Rev. B* **1994**, *49*, 14251.
- (65) Kresse, G.; Joubert, D. From ultrasoft pseudopotentials to the projector augmented-wave method. *Phys. Rev. B* **1999**, *59*, 1758.
- (66) Blöchl, P. E. Projector augmented-wave method. *Phys. Rev. B* **1994**, *50*, 17953.
- (67) Csonka, G. I.; Perdew, J. P.; Ruzsinszky, A.; Philippen, P. H. T.; Lebegue, S.; Paier, J.; Vydrov, O. A.; Ángyán, J. G. Assessing the performance of recent density functionals for bulk solids. *Phys. Rev. B* **2009**, *79*, 155107.
- (68) Togo, A.; Tanaka, I. First principles phonon calculations in materials science. *Scr. Mater.* **2015**, *108*, 1–5.
- (69) Atkins, P.; de Paula, J.; Keeler, J. *Atkins' Physical Chemistry*; Oxford University Press: Oxford, U.K., 2010.
- (70) Irikura, K. K. Appendix B Essential Statistical Thermodynamics. In *ACS Symposium Series*; Irikura, K. K., Frurip, D. J., Eds.; American Chemical Society: Washington, DC, 2001.
- (71) Johnson, R. D. NIST Computational Chemistry Comparison and Benchmark Database; <http://cccbdb.nist.gov/>, 2020.
- (72) Duan, Y.; Sorescu, D. C. Density functional theory studies of the structural, electronic, and phonon properties of Li₂O and Li₂CO₃: Application to CO₂ capture reaction. *Phys. Rev. B* **2009**, *79*, 014301.

Supplementary information:

Removing Fluoride-terminations from Multilayered V_2CT_x MXene by Gas Hydrolyzation

Frode Håskjold Fagerli,^a Zhaohui Wang,^{ab} Tor Grande,^a Henning Kaland,^a Sverre M. Selbach,^a Nils Peter Wagner^{ab} and Kjell Wiik^{*a}

a. Department of Materials Science and Engineering, NTNU Norwegian University of Science and Technology, Sem Sælands vei 12, NO-7034 Trondheim, Norway.

b. SINTEF Industry, Richard Birkelands vei 3, NO-7034 Trondheim, Norway.

Details of DFT calculations and workflow on the thermodynamic property evaluation of the proposed hydrolyzation reactions

Density functional theory (DFT) calculations were carried out using the projector augmented wave (PAW) method as implemented in the Vienna Ab initio Simulation Package (VASP),¹⁻⁴ using V_{sv} and standard C, O, H, F pseudopotentials, and PBEsol exchange-correlation functional.⁵⁻⁷ Plane wave basis sets were used with a kinetic energy cutoff of 650 eV. Gamma-centered k-point sampling was employed with a spacing close to 0.2 Å⁻¹ along the 3 axes of the reciprocal unit cells for all structures, except that for the isolated gas molecules which were placed in a 15x15x15 Å box and calculated by 1x1x1 gamma centered k-point. Spin-polarization were considered for all compounds.

The computational workflow on the evaluation of the thermodynamic properties of the proposed hydrolyzation reactions in this study included a *geometry relaxation* with a tight electronic convergence criterion of 1×10^{-8} eV and forces on the ions of less than -1×10^{-4} eV/Å. Ground state energies ($E_0(T=0\text{ K})$) were calculated for the optimized structures. *Thermal properties*, namely phonon free energy ($F(T)$), entropy ($S(T)$) and the phonon contribution on internal energy ($E(T)$), of all solids (V_2CF_2 , V_2CO_2 , V_2CO , $V_2C(OH)_2$, V_2O_3 , VF_2 , and VC) were calculated based on the optimized structures using frozen phonon method within the open-source package Phonopy.⁸ The corresponding entropy ($S(T)$) and enthalpy ($H(T)$) for gaseous species (F_2 , O_2 , H_2 , H_2O , HF , CO_2) were evaluated by standard statistical mechanics.^{9, 10} Zero-point energies (ZPE) were calculated by equation

$$ZPE = \frac{1}{2} \sum_{i=1}^n \nu_i \quad (1)$$

where ν_i is frequency. For solid compound, ZPE was $E(T)$ at $T \rightarrow 0$ obtained from phonon calculations. ν_i for gaseous species were taken from NIST- CCCBDB database.¹¹

Thermodynamic properties of reactions ($\Delta G(T)$, $\Delta H(T)$ and $\Delta S(T)$) were further evaluated according to an established method based on the ground state energy ($E_0(T=0\text{ K})$), ZPE, thermal energies ($F(T)$, $E(T)$, $S(T)$) of each individual compound.¹² Temperature dependent $H(T)$, at a given temperature was computed by a sum of the internal energy at zero Kelvin by DFT, plus ZPE and its contribution by phonon vibrations $E(T)$. Explicitly, enthalpy was approximated by the following equations:

For solids:

$$H(T) = E0 + E(T) \quad (2)$$

where ZPE is $E(T)$ at $T = 0$ K, and for gases:

$$H(T) = E0 + ZPE + aRT + \frac{5}{2}RT + \sum_{i=1}^n \frac{N_A h \nu_i}{e^{h\nu_i/kT} - 1} \quad (3)$$

where $a = 1$ and $3/2$ for linear and non-linear molecules respectively, N_A is Avogadro constant and k is Boltzmann constant. $S(T)$ for solid compounds was obtained by phonon calculations and for gases were taken from NIST-JANAF thermochemical table.¹³ As the thermal properties for each individual compound were obtained, the thermodynamic properties of the reactions could be evaluated by:

$$\Delta H(T) = H(T)_{products} - H(T)_{reactants} \quad (4)$$

$$\Delta S(T) = S(T)_{products} - S(T)_{reactants} \quad (5)$$

$$\Delta G(T) = \Delta H(T) - T\Delta S(T). \quad (6)$$

To calculate the partial pressure of HF gas at equilibrium, with a given water vapour pressure, the equation for Gibb's free energy was used with reaction coefficients given by the different hydrolysis reactions:

$$\Delta G^\circ = -RT \ln(K) = -RT \ln\left(\frac{p(\text{HF})^x}{p(\text{H}_2\text{O})^y}\right) \quad (7)$$

Table S1. Chosen DFT data for the reactions presented in Figure S11, being the change in ground state energy ($\Delta E0$), the change in Zero-point energy (ΔZPE), and the enthalpy change ($\Delta H(T)$) for the different reactions at three different temperatures: $T = 0$ K, 300 K and 600 K.

| Reaction | $\Delta E0$ (eV) | ΔZPE (eV) | $\Delta H(0K)$ (kJ/mol) | $\Delta H(300K)$ (kJ/mol) | $\Delta H(600K)$ (kJ/mol) |
|---|---------------------|----------------------|----------------------------|------------------------------|------------------------------|
| Termination change | | | | | |
| 1. $\text{V}_2\text{CF}_2 + 2\text{H}_2\text{O} (\text{g}) = \text{V}_2\text{C}(\text{OH})_2 + 2\text{HF} (\text{g})$ | 0.320 | -0.025 | 28.475 | 26.791 | 30.674 |
| 2. $\text{V}_2\text{CF}_2 + 2\text{H}_2\text{O} (\text{g}) = \text{V}_2\text{CO}_2 + 2\text{HF} (\text{g}) + \text{H}_2 (\text{g})$ | 0.621 | -0.296 | 31.352 | 35.757 | 40.386 |
| 3. $\text{V}_2\text{CF}_2 + \text{H}_2\text{O} (\text{g}) = \text{V}_2\text{CO} + 2\text{HF} (\text{g})$ | 0.368 | -0.065 | 29.165 | 31.137 | 30.646 |
| 4. $\text{V}_2\text{C}(\text{OH})_2 = \text{V}_2\text{CO}_2 + \text{H}_2 (\text{g})$ | 0.301 | -0.271 | 2.8765 | 8.967 | 9.713 |
| Decomposition of MXene | | | | | |
| 5. $\text{V}_2\text{C}(\text{OH})_2 + \text{H}_2\text{O} (\text{g}) = \text{V}_2\text{O}_3 + \text{C} + 2 \text{H}_2 (\text{g})$ | 0.616 | -0.427 | 18.273 | 27.071 | 30.895 |
| 6. $\text{V}_2\text{CF}_2 + 1.5 \text{H}_2\text{O} (\text{g}) = 0.5 \text{V}_2\text{O}_3 + \text{VC} + 2\text{HF} (\text{g}) + 0.5\text{H}_2 (\text{g})$ | 0.974 | -0.205 | 74.271 | 79.133 | 81.518 |
| 7. $\text{V}_2\text{CO} + 0.5 \text{H}_2\text{O} (\text{g}) = 0.5 \text{V}_2\text{O}_3 + \text{VC} + 0.5 \text{H}_2 (\text{g})$ | 0.607 | -0.139 | 45.105 | 47.997 | 50.872 |
| 8. $\text{V}_2\text{CF}_2 = \text{VC} + \text{VF}_2$ | 0.365 | -0.019 | 33.383 | 33.776 | 34.262 |
| 9. $\text{V}_2\text{C}(\text{OH})_2 + 3\text{H}_2\text{O} (\text{g}) = \text{V}_2\text{O}_3 + \text{CO}_2 (\text{g}) + 4\text{H}_2 (\text{g})$ | 2.107 | -0.855 | 120.730 | 135.410 | 144.930 |
| 10. $\text{V}_2\text{CO}_2 + 3\text{H}_2\text{O} (\text{g}) = \text{V}_2\text{O}_3 + \text{CO}_2 (\text{g}) + 3\text{H}_2 (\text{g})$ | 1.806 | -0.584 | 117.850 | 126.440 | 135.220 |
| 11. $\text{V}_2\text{CO} + 4\text{H}_2\text{O} (\text{g}) = \text{V}_2\text{O}_3 + \text{CO}_2 (\text{g}) + 4\text{H}_2 (\text{g})$ | 2.059 | -0.815 | 120.040 | 131.060 | 144.960 |
| 12. $\text{V}_2\text{CF}_2 + 5\text{H}_2\text{O} (\text{g}) = \text{V}_2\text{O}_3 + \text{CO}_2 (\text{g}) + 2\text{HF} (\text{g}) + 4\text{H}_2 (\text{g})$ | 2.427 | -0.880 | 149.200 | 162.200 | 175.610 |

Additional figures and tables

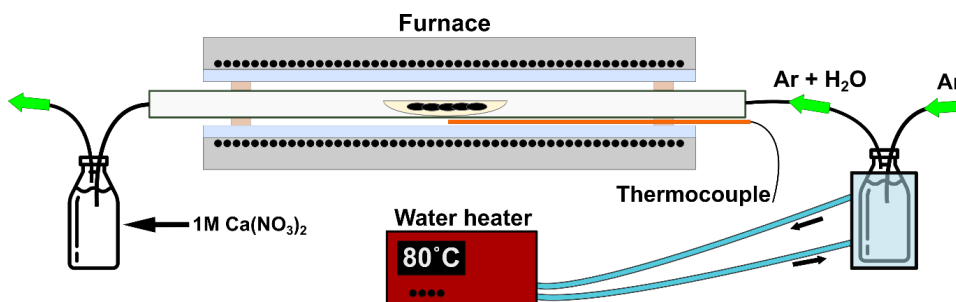


Figure S1. The setup of the hydrolysis furnace with a water heated gas bubble flask in front of the furnace to ensure high water vapour pressure inside the reaction tube. A solution of 1M $\text{Ca}(\text{NO}_3)_2$ was used at the end to bind potential HF gas from the hydrolysis reaction.

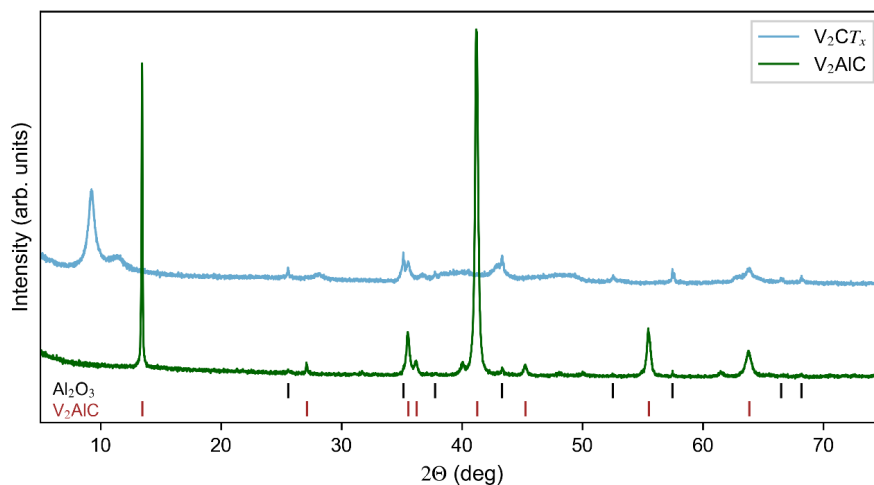


Figure S2. X-ray diffractogram of the V_2AlC MAX phase after milling and the resulting V_2CT_x after etching of the milled MAX phase in 48 wt. % HF for 72 h. The marked V_2AlC reflections come from PDF 00-029-0101 and the Al_2O_3 reflections from PDF 01-088-0826.

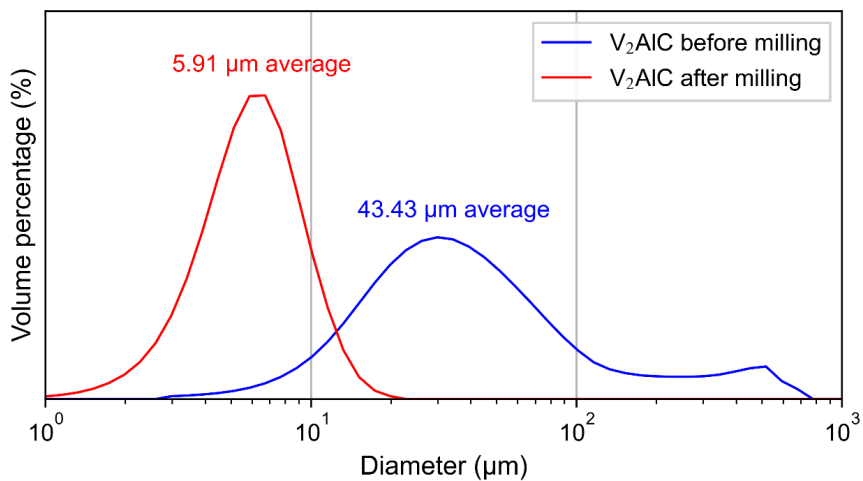


Figure S3. Particle size distribution, obtained by laser diffraction, of V₂AIC MAX phase before and after wet milling for 10 hours at 300 rpm.

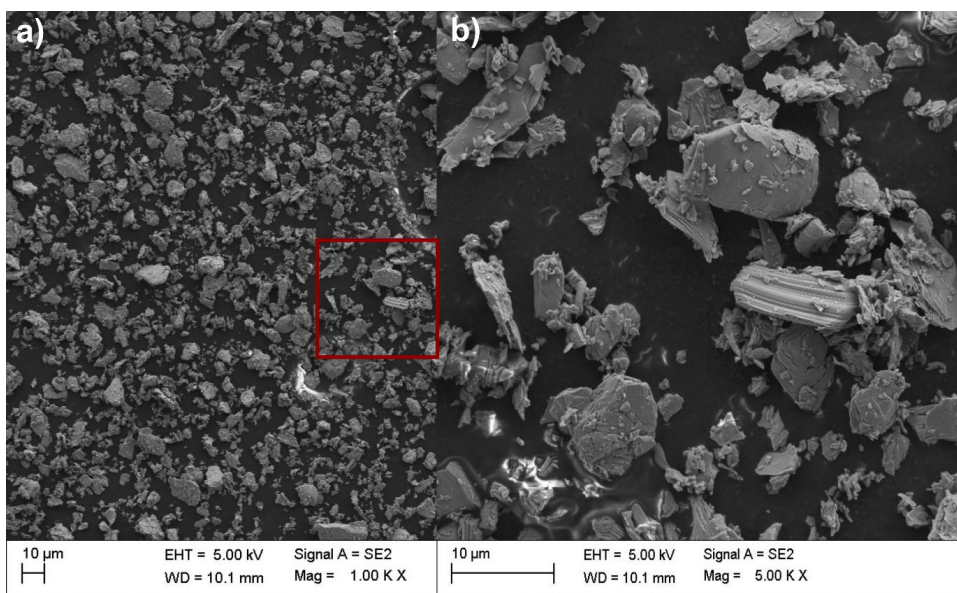


Figure S4. SEM images at 1k (a) and 5k (b) magnification of V₂AIC after wet milling showing the particle size distribution and the variation in morphology of the particles. The area of figure (b) is marked in red in figure (a).

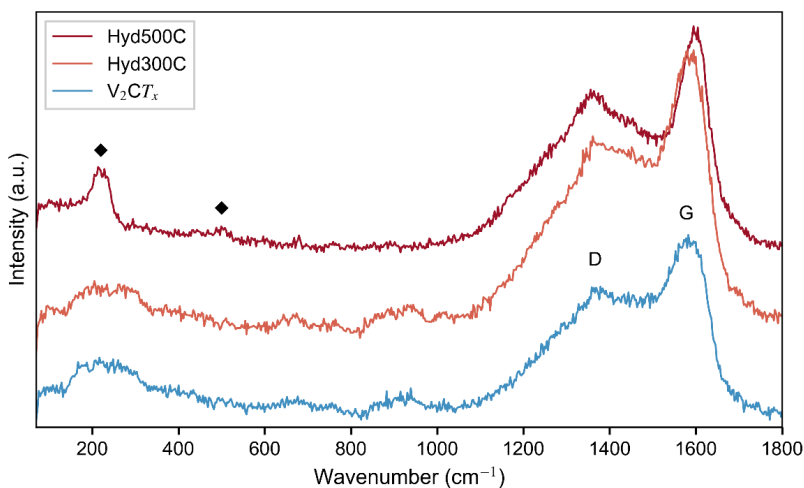


Figure S5. Raman spectra of V_2CT_x before and after hydrolysis at 300 °C and 500 °C indicating the formation of V_2O_3 , marked with diamonds, at the highest temperature.¹⁴ MXene bands at around 220 cm^{-1} , 650 cm^{-1} and 900 cm^{-1} remain stable up to 300 °C, and the spectra partly resemble those presented in previous reports.¹⁵⁻¹⁷ The presence of C D and G bands indicate that some amorphous C remain even after complete decomposition of the MXene phase. The presence of these carbon peaks, and a great variation of MXene peaks have previously been reported by Thakur et al.¹⁸

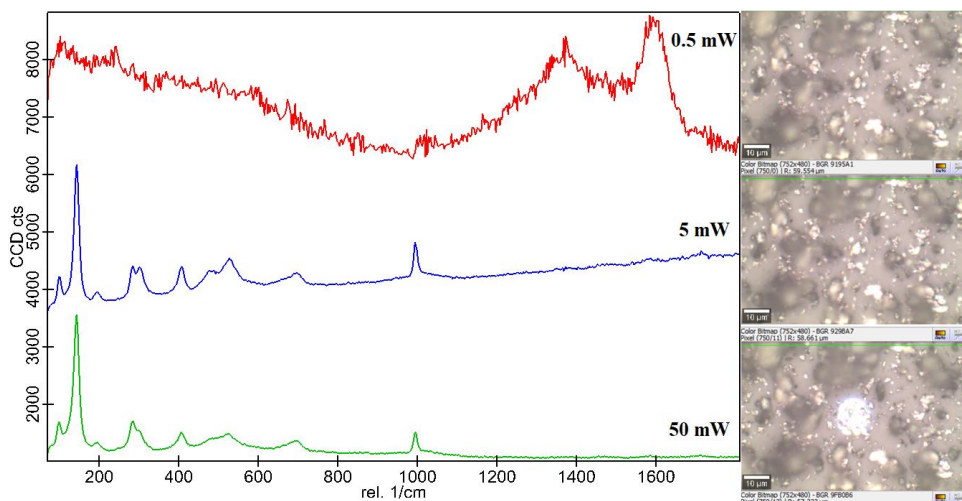


Figure S6. Raman spectra of V_2CT_x hydrolysed at 500 °C at different laser powers. Initially there is only visible peaks related to C at 1400 and 1600 cm^{-1} . The peaks that arise at higher laser powers match ok with $\alpha-V_2O_5$,¹⁹ showing how the phase oxidizes and forms large white particles under the influence of the Raman laser at higher laser powers.

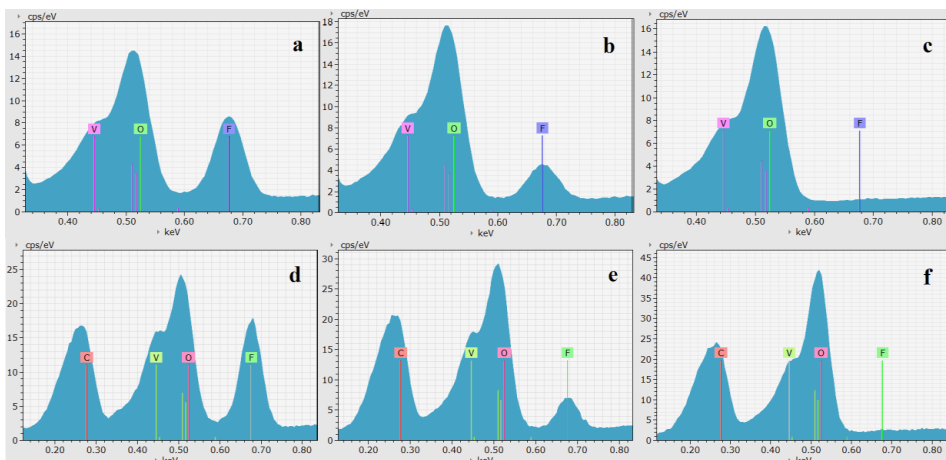


Figure S7. Showing the low energy region of EDS spectra obtained from mapping of pristine V_2CT_x (a), V_2CT_x hydrolysed at 300 °C (b) and 500 °C (c), and from a representative point scan measurement of pristine V_2CT_x (d), V_2CT_x hydrolysed at 300 °C (e) and 500 °C (f). The C peak is omitted from the mapping plots due to the high intensity coming from the carbon tape background. From these figures we see a clear trend in reduction of F from hydrolysis at increased temperature. Due to the overlap of the $La1$ (0.510 eV) and $L61$ (0.518 eV) peak from V with the only EDS peak of O ($K\alpha1$, 0.525 eV), it is difficult to get any useful quantification data of the O content. The remaining V peaks are LL (0.446 eV), LE (0.454 eV) and L63 (0.590 eV).

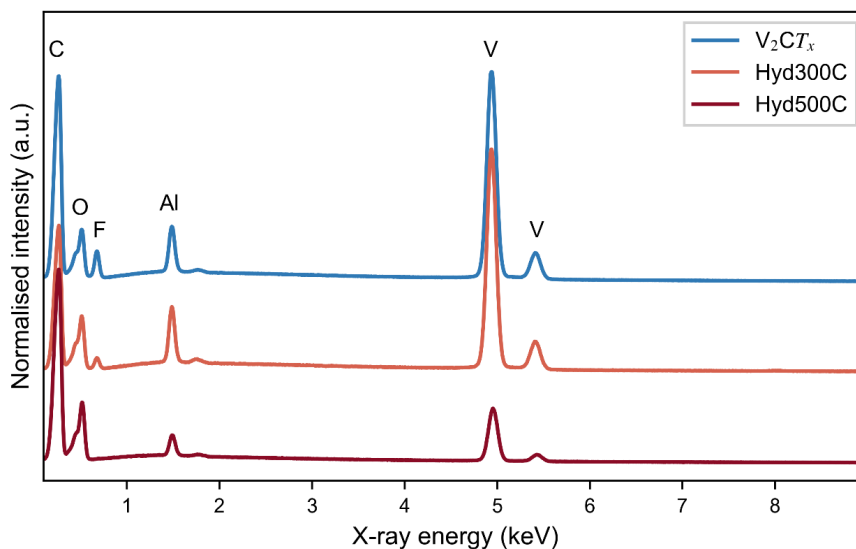


Figure S8. Full spectra of the EDS mapping of V_2CT_x presented in Figure 4. The intensity of the peaks at higher energy (Al and V) are lower for the powder hydrolysed at 500 °C due to a lower acceleration voltage (10 keV vs. 15 keV) of the electron beam used for the measurements. The peaks at lower energies (C, O and F) should not be influenced significantly by this change, as these X-rays do not live long enough to travel from deep within the particles. Al is present in these mapping spectra due to rests of Al_2O_3 particles from the MAX phase synthesis.

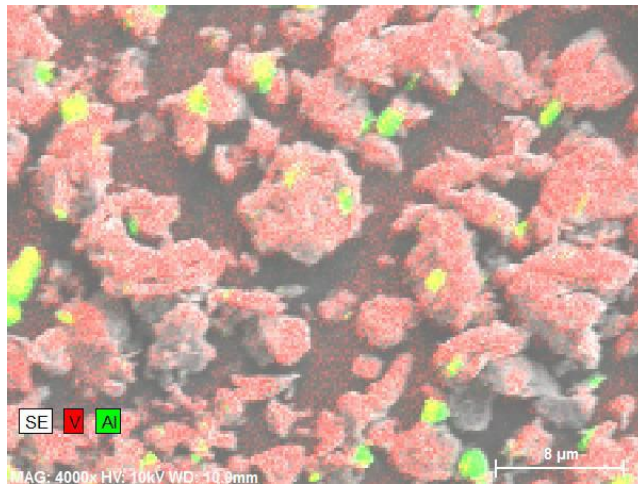


Figure S9. EDS mapping of the V_2CT_x that is used for the results in Figure 4c and Figure S8. The green dots indicate several Al rich particles that represent Al_2O_3 .

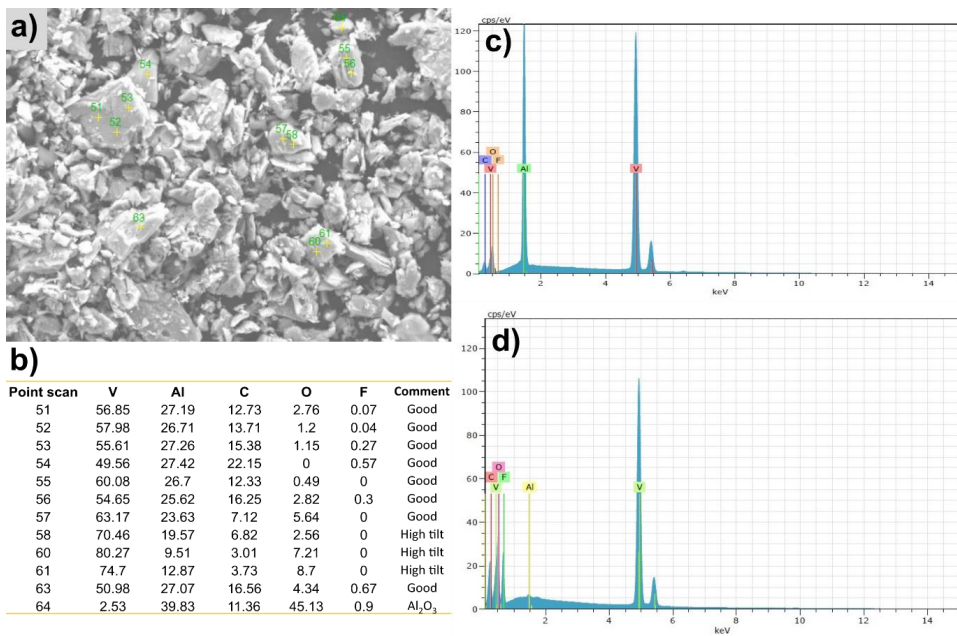


Figure 10 Demonstration of how the EDS average values were obtained, showing the points that were scanned from the V_2AlC MAX phase (a), and the resulting atomic percentages of different elements for each point scan after analysis (b). In (b) it is commented which spectra were used for the average value, as some of the spectra were from Al_2O_3 particles or had very high uncertainties due to high tilt of the particles. In (c) and (d), representative point scan spectra from before (c) and after etching (d) are shown to visually demonstrate the removal of Al upon etching as presented in Table 1.

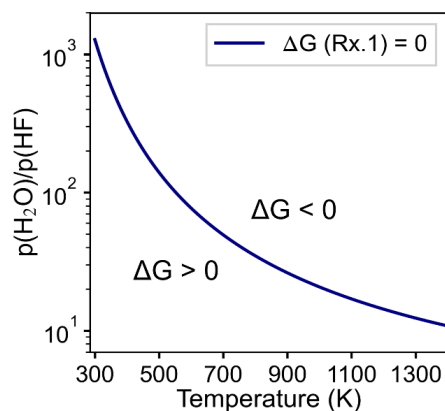


Figure S11. A curve indicating the partial pressure ratio between H₂O and HF required to make reaction 1 in Fig. 1 have $\Delta G = 0$. To the right of this line, this reaction would also be thermodynamically spontaneous.

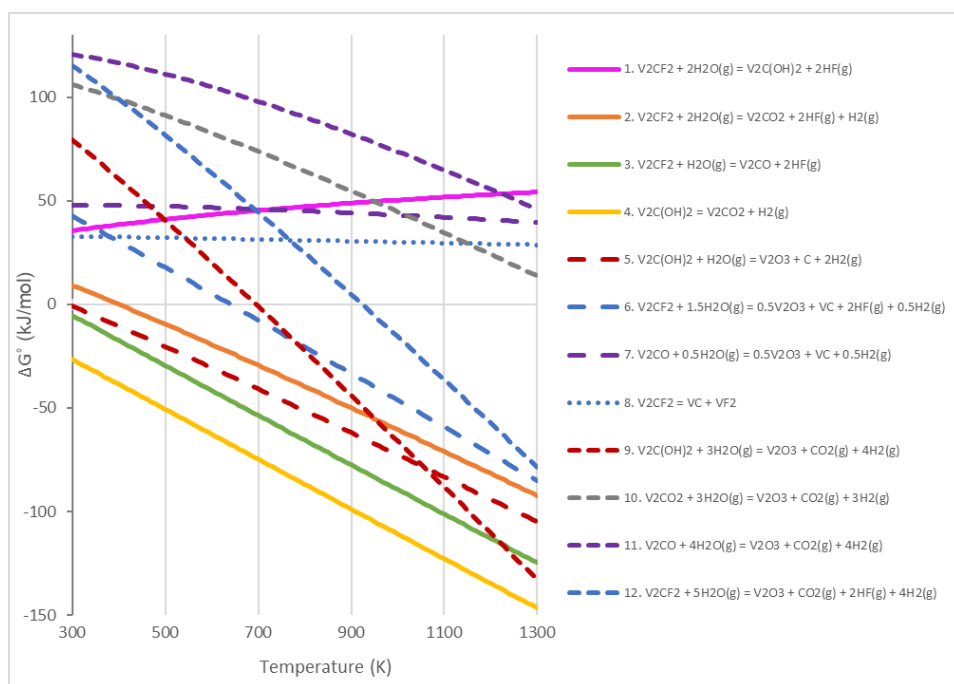


Figure S12. ΔG° as a function of temperature for several reactions of V_2CT_x , including four termination group alternating reactions shown in solid lines (1-4), as well as various decomposition reactions (5-12) in dashed lines. The decomposition reactions are coloured by the termination of the reactant V_2CT_x phase. Reactions 1-3 are already presented in Fig. 1a.

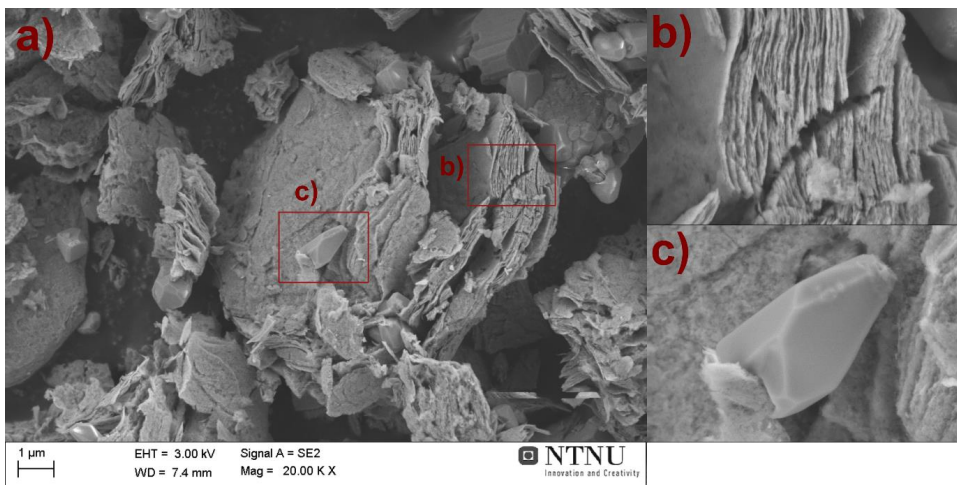


Figure S13. Overview SEM image of V_2CT_x after TG annealing in Ar to $800\text{ }^\circ\text{C}$ (a) where we see that the layered morphology of the particles remains (b) although we also see possible formation of crystalline VF_2 particles (c).

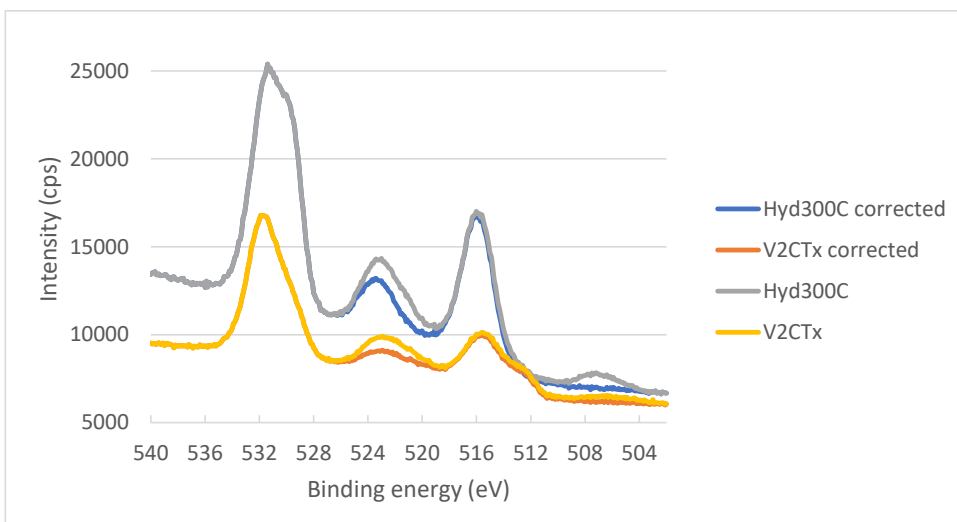


Figure S14. The XPS data of the V $2p$ and O $1s$ region before and after removing the Mg $K\alpha$ satellites for both pristine V_2CT_x and the MXene hydrolysed at $300\text{ }^\circ\text{C}$. The satellite free ("corrected") values were used in the XPS fitting of this region used in Figure 4.

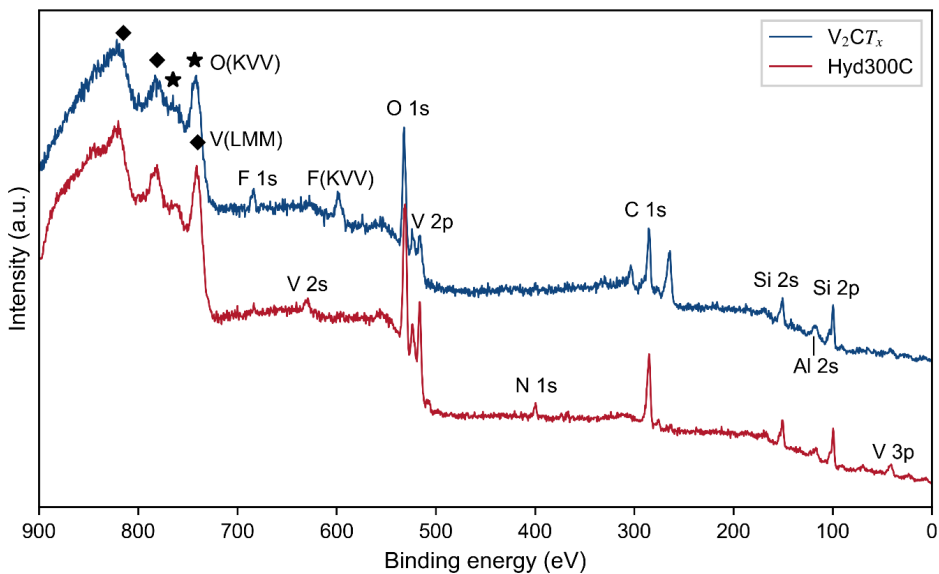


Figure S15. Full XPS spectra of V_2CT_x , before and after hydrolysis at $300\text{ }^\circ\text{C}$ without the removal of Mg $K\alpha$ satellites. The Si peaks come from the powder being dispersed on a Si wafer substrate and were used as internal reference. The peaks at around 265 eV and 305 eV in the pristine sample have not been assigned to any chemical component.

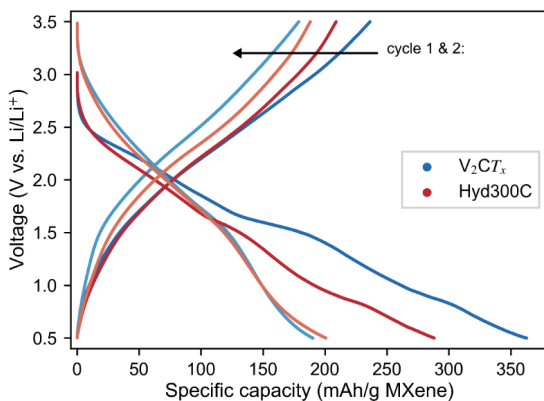


Figure S16. First two cycles from the galvanostatic cycling of LiBs with pristine V_2CT_x and V_2CT_x hydrolysed at $300\text{ }^\circ\text{C}$. On the first cycle, there are two irreversible discharge plateaus, where the one at $\sim 0.9\text{ V}$ can be assigned to SEI formation.²⁰ The plateau at 1.6 V might come from irreversible intercalation of Li-ions in between the MXene flakes.

References:

- (1) Kresse, G.; Furthmüller, J. Efficiency of ab-initio total energy calculations for metals and semiconductors using a plane-wave basis set. *Comput. Mater. Sci.* **1996**, *6*, 15-50.
- (2) Kresse, G.; Furthmüller, J. Efficient iterative schemes for ab initio total-energy calculations using a plane-wave basis set. *Phys. Rev. B* **1996**, *54*, 11169-11186.
- (3) Kresse, G.; Hafner, J. Ab initio molecular dynamics for liquid metals. *Phys. Rev. B* **1993**, *47*, 558.
- (4) Kresse, G.; Hafner, J. Ab initio molecular-dynamics simulation of the liquid-metal–amorphous-semiconductor transition in germanium. *Phys. Rev. B* **1994**, *49*, 14251.
- (5) Kresse, G.; Joubert, D. From ultrasoft pseudopotentials to the projector augmented-wave method. *Phys. Rev. B* **1999**, *59*, 1758.
- (6) Blöchl, P. E. Projector augmented-wave method. *Phys. Rev. B* **1994**, *50*, 17953.
- (7) Csonka, G. I.; Perdew, J. P.; Ruzsinszky, A.; Philipsen, P. H. T.; Lebègue, S.; Paier, J.; Vydrov, O. A.; Ángyán, J. G. Assessing the performance of recent density functionals for bulk solids. *Phys. Rev. B* **2009**, *79*, 155107.
- (8) Togo, A.; Tanaka, I. First principles phonon calculations in materials science. *Scr. Mater.* **2015**, *108*, 1-5.
- (9) Peter Atkins, P.; De Paula, J. *Phys. Chem.*; Oxford University Press, **2010**.
- (10) Irikura, K. K. Appendix B Essential Statistical Thermodynamics. In ACS Symposium Series, Washington DC; **2001**.
- (11) Johnson, R. D. NIST Computational Chemistry Comparison and Benchmark Database; <http://cccbdb.nist.gov/>, **2020**.
- (12) Duan, Y.; Sorescu, D. C. Density functional theory studies of the structural, electronic, and phonon properties of Li₂O and Li₂CO₃: Application to CO₂ capture reaction. *Phys. Rev. B* **2009**, *79*, 014301.
- (13) M. W. Chase and National Institute of Standards and Technology (U.S.), NIST-JANAF thermochemical tables, Am. Chem. Soc. & Am. Inst. Phys., 4th edn., 1998.
- (14) Tatsuyama, C.; Fan, H. Y. Raman scattering and phase transitions in V₂O₃ and (V_{1-x}Crx)₂O₃. *Phys. Rev. B* **1980**, *21*, 2977-2983.
- (15) Narayanasamy, M.; Kirubasankar, B.; Shi, M.; Velayutham, S.; Wang, B.; Angaiah, S.; Yan, C. Morphology restrained growth of V₂O₅ by the oxidation of V-MXenes as a fast diffusion controlled cathode material for aqueous zinc ion batteries. *Chem. Commun.* **2020**, *56*, 6412-6415.
- (16) Chen, J.; Chen, K.; Tong, D.; Huang, Y.; Zhang, J.; Xue, J.; Huang, Q.; Chen, T. CO₂ and temperature dual responsive "Smart" MXene phases. *Chem. Commun.* **2015**, *51*, 314-317.
- (17) Jastrzębska, A. M.; Scheibe, B.; Szuplewska, A.; Rozmysłowska-Wojciechowska, A.; Chudy, M.; Aparicio, C.; Scheibe, M.; Janica, I.; Ciesielski, A.; Otyepka, M.; Barsoum, M. W. On the rapid in situ oxidation of two-dimensional V₂CTz MXene in culture cell media and their cytotoxicity. *Mater. Sci. Eng. C* **2021**, *119*, 111431.
- (18) Thakur, R.; VahidMohammadi, A.; Moncada, J.; Adams, W. R.; Chi, M.; Tatarchuk, B.; Beidaghi, M.; Carrero, C. A. Insights into the thermal and chemical stability of multilayered V₂CTx MXene. *Nanoscale*, **2019**, *11*, 10716-10726.
- (19) Shvets, P.; Dikaya, O.; Maksimova, K.; Goikhman, A. A review of Raman spectroscopy of vanadium oxides. *J. Raman Spectrosc.* **2019**, *50*, 1226-1244.
- (20) Xu, K., Nonaqueous Liquid Electrolytes for Lithium-Based Rechargeable Batteries. *Chem. Rev.* **2004**, *104*, 4303-4418.

Paper III

F. H. Fagerli, P. E. Vullum, Z. Wang, T. Grande, S. M. Selbach, N. P. Wagner and K. Wiik

Bulk substitution of F-terminations from $Ti_3C_2T_x$ MXene by cation pillaring and gas hydrolysis

Accepted for publication in the Elsevier journal FlatChem.



Bulk substitution of F-terminations from $\text{Ti}_3\text{C}_2\text{T}_x$ MXene by cation pillaring and gas hydrolysis

Frode Håskjold Fagerli,^a Per Erik Vullum,^{bc} Tor Grande,^a Zhaohui Wang,^{ab} Sverre M. Selbach,^a Kjell Wiik^a and Nils Peter Wagner^{ab*}

a. Department of Materials Science and Engineering, Norwegian University of Science and Technology, NO-7034 Trondheim, Norway.

b. SINTEF Industry, NO-7034 Trondheim, Norway.

c. Department of Physics, Norwegian University of Science and Technology, NO-7034 Trondheim, Norway.

* nils.peter.wagner@sintef.no

Abstract

Applications of 2D MXenes are limited by the difficulty of controlling bulk termination groups after the initial HF etching step without forming surface oxides. Here, we report on gas hydrolysis using a continuous flow of Ar (g) with a controlled partial pressure of H₂O (g) as a new method to change the terminations of multilayered $\text{Ti}_3\text{C}_2\text{T}_x$ MXene particles (T = O, OH and F), and demonstrate pre-intercalation of cations as a necessity for successful hydrolysis as it enables water molecules to enter the $\text{Ti}_3\text{C}_2\text{T}_x$ MXene structure. Hydrolysis of pristine HF-etched $\text{Ti}_3\text{C}_2\text{T}_x$ shows no compositional change before oxidation into a TiO_2/C composite starts at $T > 300$ °C. However, by pre-intercalating various cations into the MXene structure prior to the hydrolysis, a pillaring of the structure is achieved, which for certain cations (K^+ and Na^+) remains even after hydrolysis at 300 °C. By hydrolysing K-intercalated $\text{Ti}_3\text{C}_2\text{T}_x$ at 300 °C, a significant bulk F reduction of 78 % was achieved, accompanied by a comparable increase in O content and insignificant surface oxidation of the particles. For other cations (Mg^{2+} , Li^+ and TBA⁺) the expanded interlayer spacing collapsed upon hydrolysis, resulting in no significant compositional changes. Moreover, hydrolysis is shown to give higher selectivity towards F removal compared to air annealing, which instead resulted in the oxidation of C to CO_2 and the formation of TiOF_2 . In Li-ion battery half cells, the intercalation of K-ions reduces both the capacity and energy efficiency compared to pristine $\text{Ti}_3\text{C}_2\text{T}_x$. Nevertheless, hydrolysis increases the capacity and intercalation voltage, and is thus a feasible method to control the electrochemical performance of $\text{Ti}_3\text{C}_2\text{T}_x$ MXene. In summary, gas hydrolysis is demonstrated as a selective and efficient method to substitute F terminations with O-related

terminations in multilayered MXene particles and pave the way for utilisation on other MXene compositions.

1. Introduction

MXenes are 2D materials with properties suitable for a wide range of applications, e.g. from electrochemical interference shielding and sensors to water desalination and biomedicine.[1–4] Consisting of transition metals ‘M’, and C and/or N as the ‘X’ element in a layered structure of $M_{y+1}X_y$ ($y = 1, 2, 3, 4$), these materials have demonstrated high electrical conductivity and intercalation capability for several cations, making them especially interesting as electrode materials in batteries and supercapacitors.[5–7] However, to optimise the intercalation properties of MXenes, control of their chemical composition is necessary. While the M and X elements can be controlled by choosing the correct MAX phase precursor, a mixture of surface terminations (T) are formed on the 2D sheets during synthesis, which is denoted by “ T_x ” (i.e., $Ti_3C_2T_x$).[8] So far, mainly -O, -OH and -F terminations stemming from etching in aqueous HF or HF forming solutions have been studied.[9,10] The combination of these termination groups is expected to greatly influence the intercalating properties, and DFT calculations predict higher capacities, lower migration barriers and higher open circuit voltages for O-terminated surfaces compared to F-terminated surfaces.[11–14] Control of termination groups is thus a key challenge for further development of MXenes in general, and especially for rechargeable batteries.[8]

Although the importance of termination control has been known for a decade, only limited progress has been made. In recent years, alternative etching methods based on anhydrous halogen solutions, molten salt reactions and hydrothermal etching in NaOH solutions have been developed, and have resulted in homogeneously terminated $Ti_3C_2T_x$ MXene (i.e. S-, Se-, Br-, Cl-, O-).[15–18] However, as HF etching remains the most scalable synthesis method, post-etching modification of the termination groups would accelerate the development of MXenes for batteries. Considering the most studied $Ti_3C_2T_x$ phase, one of the major challenges is related to its poor oxidative stability, as it oxidises into TiO_2 at elevated temperatures in both inert, reducing and oxidising atmospheres, as well as in aqueous dispersions.[19–22] However, changing the composition from $Ti_3C_2F_2$ to $Ti_3C_2O_2$ must be charge compensated by oxidation of the MXene. Therefore, controlling the selectivity of the chemical reactions upon post-etching treatments is essential to control the termination change while preventing oxidation into TiO_2 phases.

Previously reported methods to control the surface terminations include annealing in vacuum, CO₂, O₂, H₂ and inert atmospheres,[20,23–25] dispersion in alkalic and acidic solutions,[26,27] as well as hydrothermal treatment.[24] Most of these methods do not reduce the F-content without the surface oxidizing into TiO₂. The results from Halim et al. indicate stable MXene thin films upon annealing at 550 °C in ultrahigh vacuum, which also resulted in a removal of most of the initial F content.[23] However, to date this method has only been demonstrated for thin films of unspecified thickness and not for multilayered MXene particles. Considering the chemistry of the F-removal, it seems unlikely that F-terminations will leave the MXene as F-ions or F₂ gas, as it would either require an electrical instability in the remaining MXene or a strong oxidation of the F-terminations. We recently reported on gas hydrolysis as a new method to remove F-terminations from V₂CT_x MXene by the formation of HF gas,[28] and now we apply a similar approach to control the terminations in Ti₃C₂T_x - one of the most studied MXene phases.

In this article, we report the structural and compositional changes in multilayered Ti₃C₂T_x particles from gas hydrolysis and demonstrate the essential role of cation intercalation prior to the hydrolysis. First, density functional theory (DFT) calculations on possible hydrolysis reactions are presented, guiding the experimental hydrolysis of pristine HF-etched Ti₃C₂T_x MXene up to 500 °C. These results are then compared with annealing in various atmospheres to identify differences in thermal stability and selectivity towards F-removal. Thereafter, intercalation of Li-, Na-, K-, Mg- and tetrabutylammonium-ions (TBA) as pillars for the MXene layers are demonstrated together with the changes upon subsequent gas hydrolysis. Finally, electrochemical cycling results from intercalated and hydrolysed MXenes are presented. To verify the bulk compositional changes within the particles, comprehensive characterization by energy dispersive X-ray spectroscopy (EDS) is performed with an electron acceleration voltage of 10 kV to ensure a data acquisition depth of > 300 nm.[29]

2. Methods

2.1. Synthesis of Ti₃C₂T_x

Prior to the etching, commercial Ti₃AlC₂ MAX phase powder (Laizhou Kai Kai Ceramic Materials Co., Ltd.) was planetary milled at 300 rpm for 150 min in isopropanol with the use of WC milling jar and balls, to obtain a small and controlled particle size and particle size distribution (Figure S1). Then, 2.5 g of the milled powder was slowly added over 15 minutes to a polypropylene beaker with 50 mL of a 10 wt. % HF solution, before the beaker was partly covered with parafilm and left at room temperature for 24 h under constant stirring. After the etching, the remaining powder dispersion was washed several times by centrifugation and decantation in DI-water dispersions until a pH > 5

was reached. Thereafter, the remaining dispersion was vacuum filtered through 0.22 μm pore sized PVDF filter papers, before the powder was vacuum dried at 60 $^{\circ}\text{C}$ for 4 h and the pristine $\text{Ti}_3\text{C}_2\text{T}_x$ powder was obtained.

2.2. Cation intercalation

The different cations were intercalated by dispersing 0.4 g of the $\text{Ti}_3\text{C}_2\text{T}_x$ powder in 50 mL salt solutions under constant agitation before washing the powder several times with DI water by centrifugation. Lastly, the powders were vacuum filtered and dried under vacuum at 40 $^{\circ}\text{C}$ for up to 1 h. TBA- Ti_3C_2 was prepared by dispersing $\text{Ti}_3\text{C}_2\text{T}_x$ in a 1.2 M TBAOH solution over 12 h, while K- Ti_3C_2 , Na- Ti_3C_2 , and Li- Ti_3C_2 were made using 2 M hydroxide solutions for 2 h. Mg- Ti_3C_2 , was made by substituting the Na-ions from Na- Ti_3C_2 . This was done by adding the Na- Ti_3C_2 powder to a 1 M MgCl_2 solution for 3 h, before the powder was washed in DI water and left for another 20 h in a fresh MgCl_2 solution.

2.3. Hydrolysis and annealing

Gas hydrolysis was performed as previously described [28] by distributing 0.1 g powder over 1-2 cm^2 in an alumina crucible followed by 2 hrs with 200 mL/min Ar gas (99.999%) flushing in a quartz tube furnace. Heating rates were kept at 300 $^{\circ}\text{C}/\text{h}$ followed by 15 hrs dwell time with the same gas flow. The Hyd300C notation indicates which hydrolysis temperature was used, which in this case was 300 $^{\circ}\text{C}$. The Ar gas was bubbled through a DI water bath, which after the flushing step was heated to and kept at a temperature of 80 $^{\circ}\text{C}$. This results in a saturated vapor pressure of 0.474 bar.[30] To prevent air leakage into the furnace and to capture HF formed during the hydrolysis, the exhaust gas was bubbled through a solution of 1M $\text{Ca}(\text{NO}_3)_2$. For Air- Ti_3C_2 , Ar- Ti_3C_2 , Ar/ H_2 - Ti_3C_2 and Vac- Ti_3C_2 the annealing gases were dry synthetic air, pure Ar gas (99.999 %), a 5 % H_2 mixture in pure Ar gas and a pressure of < 1 mbar, respectively. Annealing was done with the same heating parameters as for the hydrolysis.

2.4. Characterization techniques

Crystal structure and phase purity were characterized by X-ray powder diffraction (XRD, Bruker D8 Focus Diffractometer) using a 0.2 mm slit size and a Cu $\text{K}\alpha$ radiation source ($\lambda = 0.15406 \text{ nm}$). The XRD data were collected with a step size of 0.0143 $^{\circ}$ and a 0.68 s step time in a 2 θ -range from 4 to 75 $^{\circ}$, and the resulting diffractograms were adjusted for sample displacement by structureless fitting in the TOPAS software using a $\text{P6}_3/\text{mmc}$ space group (Figure S3). The particle size distribution (PSD) of the MAX phase was measured by laser diffraction (Horiba Partica LA-960) in isopropanol dispersions. The microstructure and surface morphology of the particles were investigated by a field-

emission scanning electron microscope (FESEM, Carl Zeiss Ag – ULTRA 55) using an acceleration voltage of 5 kV. Energy dispersive X-ray spectroscopy (EDS) was used to assess chemical composition using an XFlash 4010 X-ray detector and an acceleration voltage of 10 kV, resulting in an electron penetration depth > 300 nm for $Ti_3C_2T_x$ with a density of around 4.2 g/cm.^[29] To obtain quantitative results, the point scans were analysed using the Bruker Esprit 1.9 software, and the average values from minimum six point scans with a tilt < 32° relative to the detector were used for each material (Figure S2 and Table S1). The vibrational properties were investigated by a WITec Alpha 300r Confocal Raman Microscope, using a 100x objective, a 532 nm Ar laser and a laser power below 0.8 mW to prevent oxidation of the material.^[31] Additionally, Fourier-transform Infrared spectroscopy (FTIR, Bruker VERTEX 80v) Drifts measurements were performed at 2 mBar using KBr powder both as reference and for the sample mixture in a MXene:KBr mass ratio of 1:39. Transmission electron microscopy (TEM) was performed with a double Cs aberration corrected cold FEG Jeol ARM200FC, operated at 200 kV. EDS maps were acquired in scanning TEM (STEM) mode with a 100 mm² Centurio detector, covering a solid angle of 0.98 sr. The TEM samples were prepared perpendicular to the (002) plane by focused ion beam (FIB) lamella preparation, using a Helios G4 UX. All coarse thinning of the lamellae were done with 30 kV acceleration voltage for the Ga⁺ ions. Final thinning was done at 5 kV and then at 2 kV on either side of the lamellae to minimize surface damage.

2.5. Electrochemical measurements

To assess the electrochemical performance of the hydrolysed $Ti_3C_2T_x$, Li-ion battery half cells were prepared with MXene particles as the working electrode. These electrodes were processed by mixing N-ethyl-2-pyrrolidone (NEP)-slurries with 10 wt.% carbon black as conductive additive, 10 wt.% PVDF binder and 80 wt.% of the active material (various compositions of $Ti_3C_2T_x$). First the carbon black and active material were mixed in a shaker mill for 10 min at 25 Hz. Then, a premade PVDF-NEP solution was added before the slurry was further diluted with additional NEP to obtain a solid to liquid ratio of 1:6. Next, the slurry was mixed by continued shaking for 30 min at 15 Hz with a shaker ball and drop cast onto pre-cut circular Cu current collectors with a 16 mm diameter. The electrodes were dried on a 60 °C hot plate in a fume hood overnight before being dried under vacuum at 60 °C for a minimum of 3 h. This resulted in active material loadings of 1.8-2.8 mg/cm². The electrodes were assembled into 2016-type coin cells in an argon-filled glovebox ($O_2 \leq 0.1$ ppm, $H_2O \leq 0.1$ ppm) using Li-foil as the counter electrode, glass microfiber (Whatman) separator soaked in 110 μ L 1 M LiPF₆ in ethylene carbonate and ethyl methyl carbonate (EC:EMC 1:1 v:v) electrolyte. The assembled cells were galvanostatically cycled in a voltage range of 0.001 to 3.0 V at various specific currents (10 mA/g-400 mA/g) using BioLogic BCS-805 and Landt CT2001A cyclers at a controlled temperature of 25 °C.

2.6. Theoretical calculations

Density functional theory calculations were carried out with VASP using the PBEsol functional.[32–34] The Ti_pv and standard C, O, H, F pseudopotentials supplied with VASP were used and the plane-wave energy cut-off was set to 650 eV. Geometries were relaxed until the forces on the ions were below 10^{-4} eV/Å to obtain ground state energies ($E_0(T = 0 \text{ K})$), and for solid structures gamma-centred k-point meshes with $\sim 0.2 \text{ \AA}^{-1}$ spacings were used. Vibrational properties for gases were calculated by standard statistical mechanics,[35] and for solids phases with Phonopy.[36] Corresponding zero-point energies (ZPE) were calculated for the solids and taken from the NIST-CCCBDB database for gaseous species.[37] More details about the computational methods can be found in our previous work.[28]

3. Results and Discussion

3.1 DFT calculations of hydrolysis reactions

To investigate if the substitution of F terminations by hydrolysis would be feasible from a thermodynamic point of view, the change in Gibbs free energy for two different hydrolysis reactions were calculated. The results are given in Figure 1 and show how the formation of O-terminations is favoured compared to the formation of $\text{Ti}_3\text{C}_2(\text{OH})_2$. While the formation of $\text{Ti}_3\text{C}_2(\text{OH})_2$ has a positive ΔG° for all temperatures, the O-termination reaction shows a negative ΔG° at $T > 400 \text{ K}$. However, under non-standard conditions, ΔG will be affected by the ratio between the vapour pressure of H_2O and HF, where an excess H_2O will help to shift both reactions towards the product side. In Figure 1b, the equilibrium partial pressure of HF gas is presented as a function of temperature, assuming a constant high water vapour pressure of 0.473 bar. It shows that a significant amount of HF gas ($> 40 \text{ Pa}$) would be formed for both reactions at a temperature of 300°C (573 K), where the $\text{Ti}_3\text{C}_2\text{O}_2$ forming reaction shows the highest vapour pressure of 4000 Pa (0.04 bar). These thermodynamic results resemble what was found for the hydrolysis of V_2CT_x MXene, where a significant reduction of F content also was achieved experimentally.[28] Similarly for the $\text{Ti}_3\text{C}_2\text{T}_x$ MXene phase, substitution of F- with O-terminations by hydrolysis should be possible from a thermodynamic point of view.

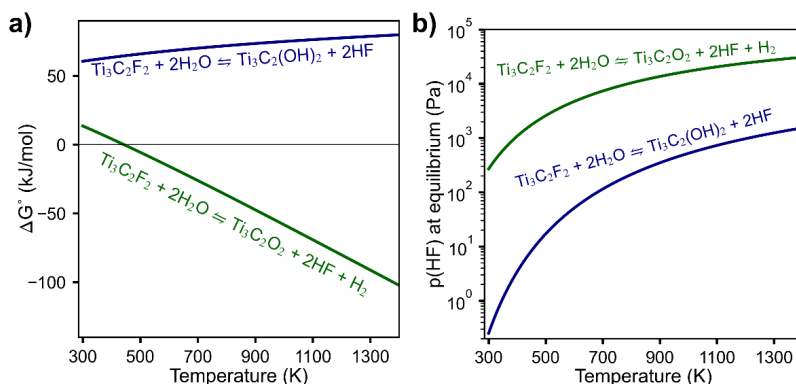


Figure 1. DFT results for two different F-removing hydrolysis reactions for $\text{Ti}_3\text{C}_2\text{T}_x$, where (a) shows ΔG° as a function of temperature and (b) shows the equilibrium partial pressure of HF gas as a function of temperature, using a high partial pressure of H_2O (0.474 bar).

3.2. Hydrolysis of pristine $\text{Ti}_3\text{C}_2\text{T}_x$

To assess if hydrolysis could alter the termination groups experimentally, HF-etched $\text{Ti}_3\text{C}_2\text{T}_x$ MXene (Figure S4) with mixed terminations was hydrolysed at various temperatures, using long hydrolysis times of 15 h to allow for complete reactions. In Figure 2, the structural and vibrational changes of the pristine $\text{Ti}_3\text{C}_2\text{T}_x$ MXene after hydrolysis at temperatures up to 500 °C are presented. The X-ray diffractograms in Figure 2a demonstrate how the $\text{Ti}_3\text{C}_2\text{T}_x$ phase remains stable up to 300 °C, while the (101) reflection of anatase at 25.3° appears at higher temperatures. After hydrolysis at 500 °C, the MXene phase is completely decomposed into three different TiO_2 phases (anatase, rutile and brookite) in roughly a 1:1:1 ratio (Figure S5a). The oxidation of $\text{Ti}_3\text{C}_2\text{T}_x$ is also confirmed by the vibrational spectra (Figure 2b and c), demonstrating an additional shoulder of Ti-O bonds above 300 °C in the FTIR spectra, and TiO_2 anatase peaks above 400 °C in the Raman spectra. These spectroscopic results also present the formation of disordered graphitic carbon, as the D and G Raman bands at 1345 cm^{-1} and 1595 cm^{-1} show a cumulative intensity ratio of $I_D/I_G > 1$ indicative of amorphous carbon,[38,39] and the various carbon-related vibrational modes in the FTIR spectra resembling graphene oxide.[40] This shows that the decomposition of $\text{Ti}_3\text{C}_2\text{T}_x$ MXene during hydrolysis results in a TiO_2/C composite that match well with previous reports on oxidation of $\text{Ti}_3\text{C}_2\text{T}_x$. [21,24,41] Apart from this oxidation, the MXene phase does not change much with the hydrolysis at lower temperatures. A slight shift in the (002) reflection upon increasing the hydrolysis can be seen in Figure S6a, which indicates a reduction in the interlayer spacing from 9.56 Å to 9.47 Å. Such changes in interlayer spacings are usually ascribed to deintercalation of H_2O from the MXene, but as the FTIR spectra do not give any indication of H_2O (Figure S7), and

considering that each layer of water molecules is predicted to increase the spacing by more than 2 Å,[11,42] dehydration is an unlikely explanation. Instead, the reduction in interlayer spacing upon hydrolysis might be ascribed to changes in the stacking of the MXene, as there are changes in intensity of the reflections between 33° and 45° upon hydrolysis, as well as a significant shift in the (110) reflection at 61° (Figure S6b).[43]

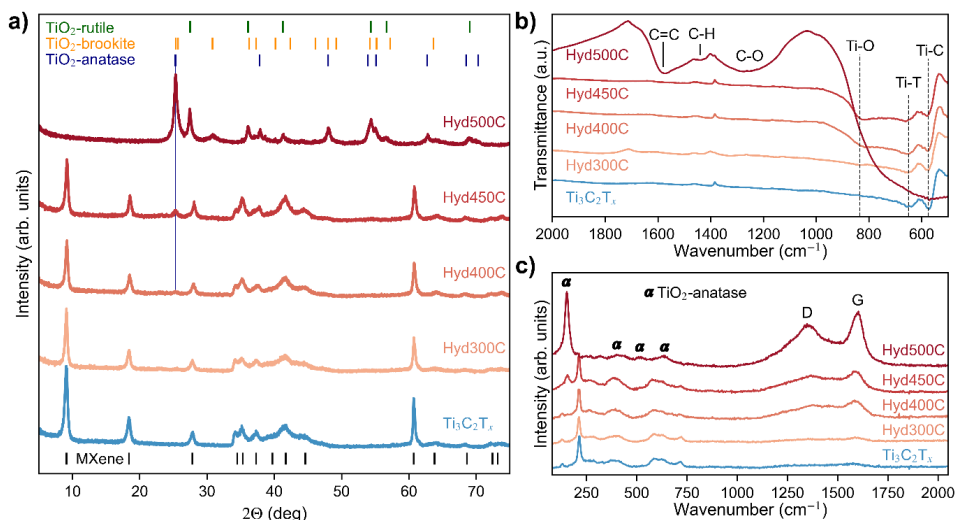


Figure 2. XRD diffractograms (a), Raman spectra (b) and FTIR spectra (c) of $Ti_3C_2T_x$ before and after hydrolysis at various temperatures. The peaks at around 1380 cm^{-1} in the FTIR spectra come from impurities in the measurement chamber, and the (hkl) MXene reflections are labelled in Figure S4.

In Figure 3a-d, the structural change of the MXene particles upon hydrolysis is presented through high-angle annular dark-field STEM (HAADF-STEM) micrographs. They show how the layered structure remains upon hydrolysis, although nanoparticles are formed after hydrolysis at 400 °C (Figure 3c and Figure S8). Based on the results presented in Figure 2, these nanoparticles are ascribed to TiO₂ (anatase). Although the macroscopic morphology of the particles remains even after hydrolysis at 500 °C (Figure S8), the layered microstructure is no longer observed after complete oxidation. For the powders hydrolysed at 300 °C on the other hand, TiO₂ nanoparticles are not observed, which further suggests insignificant oxidation by hydrolysis at this temperature. Additionally, an AB stacking of the pristine $Ti_3C_2T_x$ is demonstrated by the red lines in Figure 3b,[44] which is similar to previously reported HAADF micrographs.[15,20] As the micrographs of the Hyd400C sample were viewed along the [100] zone axis (Figure 3d), no more information about the MXene stacking could be obtained from these particles.

To measure the chemical compositional change in the bulk of the $\text{Ti}_3\text{C}_2\text{T}_x$ particles upon hydrolysis several SEM-EDS point scans from each sample were measured and the average results are presented in Figure 3e. These values are presented relative to one formula unit of $\text{Ti}_3\text{C}_2\text{T}_x$ (per 3 Ti) and display how the O content increases with the oxidation of the MXene and ends up at twice the amount of Ti after hydrolysis at 500 °C, which again matches the formation of TiO_2 . At the same time the C content remains roughly unchanged, demonstrating that H_2O is not sufficiently oxidising to form CO/CO_2 at these temperatures. When it comes to the removal of F terminations, hydrolysis seems to fail, as there are no significant changes in the F content after hydrolysis at 300 °C. The slight reduction at higher temperatures is likely related to the oxidation of the MXene phase, as the EDS results follow the same trends as the XRD, Raman and FTIR results presented in Figure 2. As TEM EDS mapping of the edge surfaces demonstrated insignificant changes in local O and F concentrations before and after hydrolysis at 400 °C (Figure S9), it is concluded that the gas hydrolysis of pristine HF-etched $\text{Ti}_3\text{C}_2\text{T}_x$ does not result in any substitution of F-terminations.

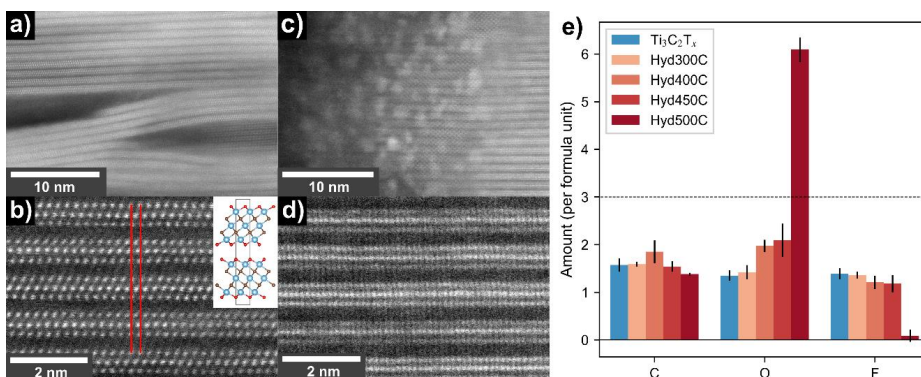


Figure 3. HAADF-STEM images at two different magnifications of pristine $\text{Ti}_3\text{C}_2\text{T}_x$ MXene viewed along the $[2\bar{1}0]$ zone axis (a,b) and of $\text{Ti}_3\text{C}_2\text{T}_x$ after hydrolysis at 400 °C viewed along the $[100]$ zone axis (c,d), where the inset in (b) illustrates the AB stacking marked by the red lines. (e) shows the SEM EDS average values from point scans performed on pristine $\text{Ti}_3\text{C}_2\text{T}_x$ and $\text{Ti}_3\text{C}_2\text{T}_x$ hydrolysed at different temperatures, where the dashed line illustrates a Ti amount of 3 and the error bars represent the standard deviation from the set of point scans used for each sample.

Nonetheless, based on the oxidation products formed at elevated temperatures, gas hydrolysis still shows a higher selectivity towards F removal compared to other annealing atmospheres, as discussed further in the Supplementary Information (Figure S10-S14). Although annealing in dry synthetic air resulted in similar oxidation as the hydrolysis, it started at a lower temperature (300 °C for air and 400 °C for hydrolysis) and ended up with other products (Figure S10). While the annealing in dry air resulted in an oxidation of C to CO/CO_2 and the formation of a TiOF_2 phase, hydrolysis removed all F content while preserving most of the carbon content. Annealing in inert

(Ar), reducing (H₂/Ar) and vacuum environments on the other hand, only resulted in minor oxidation to TiO₂ anatase (Figure S13 and S14) and insignificant compositional changes even after annealing at 500 °C (Table S1). These results are further in the Supplementary Information. Noteworthy, the EDS mapping results show similar trends as the point scan averages (Table S2). Hence, use of EDS mapping may prove to be sufficient for rough quantification of O and F content for MXenes, if the number of impurity particles in the mapped regions are consistent.

3.3. Hydrolysis of pre-intercalated Ti₃C₂T_x

Considering the small interlayer spacing of the HF-etched Ti₃C₂T_x, which may have impeded the intercalation of H₂O molecules and thus also the hydrolysis reactions, pre-intercalation of various cations was attempted (denoted cation pillaring) to expand the interlayer spacing in the Ti₃C₂T_x structure prior to hydrolysis. This cation pillaring was achieved by dispersing pristine Ti₃C₂T_x powders in various hydroxide solutions to form Ti₃C₂T_x intercalated with Li⁺, Na⁺, K⁺, Mg²⁺ and tetrabutylammonium/TBA⁺ (denoted “X-Ti₃C₂”, where “X” represents the cation). As presented in the X-ray diffractograms in Figure 4a, this pre-intercalation resulted in significant expansion of the interlayer spacings, from 9.56 Å in the pristine Ti₃C₂T_x, to around 12.4 Å for K-Ti₃C₂, Na-Ti₃C₂ and Li-Ti₃C₂, 14.8 Å for Mg-Ti₃C₂ and 17.4 Å for TBA-Ti₃C₂. Considering Mg-ion are shown to co-intercalate with two layers of water molecules at ambient conditions, whereas the alkali cations only co-intercalate with one layer, these results are in good agreement with previous reports.[45,46] However, after hydrolysing the pre-intercalated MXenes at 300 °C (X-Ti₃C₂-Hyd), the (002) reflections of the Li-Ti₃C₂, Mg-Ti₃C₂, and TBA-Ti₃C₂ samples are shifted back towards the pristine Ti₃C₂T_x, indicating a reduced interlayer spacing and hence a collapse of the pillared MXene structure. As the EDS results indicate insignificant changes in F content, it is assumed that the hydrolysis of these samples was unsuccessful due to the lack of H₂O intercalation. For the K-Ti₃C₂ and Na-Ti₃C₂ samples, however, the pillared MXene structures remained even after hydrolysis, which is demonstrated by the almost unchanged interlayer spacings (Fig. 6a). Unlike the non-pillared MXenes, the hydrolysis of these structures resulted in significant F reduction (45 % for Na-Ti₃C₂ and 64 % for K-Ti₃C₂ vs. pristine Ti₃C₂T_x), accompanied by a comparable increase in O content (Figure 4b). Seeing that these samples did not show any signs of oxidation (Figure S15-18), these changes are ascribed to alterations in the mixture of termination groups. By extending the hydrolysis time of K-Ti₃C₂ from 15 h to 50 h an additional reduction of F content was achieved (78 % vs. pristine Ti₃C₂T_x, Table S1), indicating an extensive removal of F terminations from the bulk of the Ti₃C₂T_x particles upon hydrolysis. Furthermore, to ensure that the compositional changes were not related to the mere dehydration of the MXene, the K-Ti₃C₂ MXene was also annealed at 300 °C in dry Ar gas. Seeing that

this resulted in insignificant changes in the F content (Table S1), the importance of water vapour to selectively remove F-terminations is demonstrated.

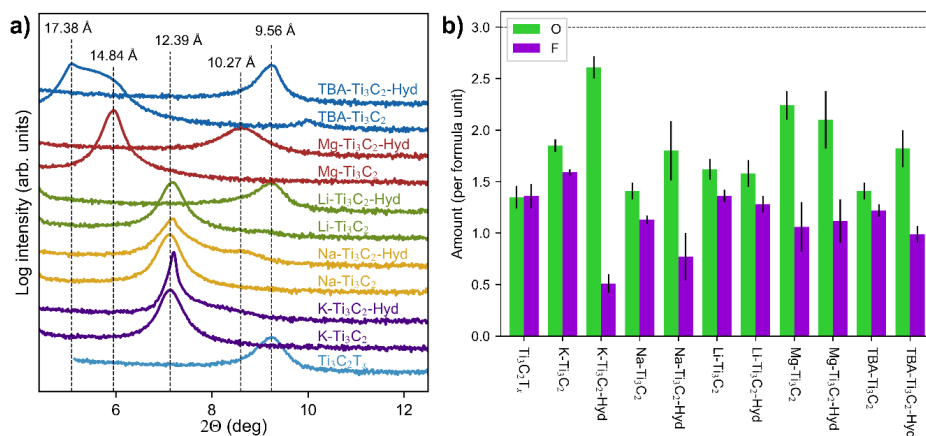


Figure 4. Logarithmic intensities of low angle X-ray diffractograms (a) and EDS quantification of O and F (b) from the intercalation of various cations in Ti₃C₂T_x followed by hydrolysatation at 300 °C. The dotted lines in (a) indicate the position of the (002) reflection for the different samples with the resulting interlayer spacings. The dashed line in (b) illustrates a Ti amount of 3 and the error bars represent the standard deviation from the set of point scans used for each sample.

To ensure charge neutrality upon cation intercalation, all cations must have been co-intercalated with anions. Since hydroxide salts were used, it is likely that a certain amount of OH⁻ ions remain within the structure and assist the pillaring of the MXene. In the EDS data (Figure 4b), this can be seen by the increase in the O content for all cation-intercalated samples compared to the pristine Ti₃C₂T_x. Strikingly, no Cl content was detected in the Mg-Ti₃C₂ samples after the cation substitution in MgCl₂ solutions (Table S1), implying that no anion substitution has taken place. The increase in O content can also be partly ascribed to the intercalation of H₂O, which seems to match well with the higher interlayer spacing of Mg-Ti₃C₂. However, as the EDS data are acquired under high vacuum, it is difficult to know how much of the intercalated water remains within the structure during the measurements. The relative changes between F and O content on the other hand, is ascribed to changes in termination groups, and shows how the K-Ti₃C₂ and Na-Ti₃C₂ samples show the highest termination substitutions upon hydrolysatation.

Apparent for all the pre-intercalated structures upon hydrolysatation is a shift in the (002) reflection towards higher 2θ value and thereby also a smaller interlayer spacing. For the TBA-Ti₃C₂ sample it is likely that the TBA molecules decompose, as it matches well with the reduction in the C content (Table S1) and with previous reports on decomposition of intercalated TBA molecules by Ar annealing.[47,48] Similarly to the TBA-Ti₃C₂-Hyd, the interlayer spacing of Li-Ti₃C₂-Hyd is

approximately the same as the pristine $\text{Ti}_3\text{C}_2\text{T}_x$. Surprisingly, this suggests a complete removal of the intercalated species upon hydrolysis, as intercalated Li-ions have been reported to result in up to a 20 % increase in interlayer spacing compared to the pristine MXene, both with and without the co-intercalation of solvents.[5,20,26] However, as the Li deintercalation is found to be very endothermic, it is possible that the slight increase in temperature is sufficient.[49] For the Mg-intercalated $\text{Ti}_3\text{C}_2\text{T}_x$ on the other hand, the reduction from 14.84 Å to around 10.3 Å upon hydrolysis is ascribed to the dehydration of water molecules, seeing that the Mg content remains unchanged (Table S1) and due to the removal of O-H vibrational modes in the FTIR spectra (Figure S15). As intercalated Mg-ions are calculated to have an ionic radius of 0.72 Å,[50] this correlates well with the difference in interlayer spacing from the pristine $\text{Ti}_3\text{C}_2\text{T}_x$. However, seeing that the cation intercalation must have been accompanied by intercalation of OH-ions for charge neutrality, there is also a possibility that the Mg-ions have bonded with residual OH-ions or with F-terminations to form insoluble $\text{Mg}(\text{OH})_2$ and/or MgF_2 (Table S3).[13] Furthermore, a similar dehydration can be observed for Na- $\text{Ti}_3\text{C}_2\text{-Hyd}$, where a shoulder to the (002) reflection arises at around the same location as for Mg- $\text{Ti}_3\text{C}_2\text{-Hyd}$. This partial dehydration is also causing a general broadening of the XRD reflections with $l \neq 0$ in the Miller indices (hkl) after hydrolysis (Figure S16), as the interlayer spacing becomes less ordered. Although a small shoulder to the (002) reflection also appears after the hydrolysis of K- Ti_3C_2 , the hydrolysis generally resulted in a sharpening of the reflections with $l \neq 0$ and thereby an increased ordering of the interlayer spacing. The minor shifts (0.12 Å) of the main (002) reflections in Na- Ti_3C_2 and K- Ti_3C_2 upon hydrolysis are almost identical, and may be ascribed to a small reduction in intercalated water.[42] However, as the reduction is less than 5 % of one water layer,[42,46] the FTIR spectra in Figure S15 show no indications of H_2O , and according to previous reports claiming hydrophobic nature of these cations in MXenes,[50,51] this change might also be ascribed to changes in termination groups and stacking.[44] In Figure S17, a significant shift in the stacking sensitive (110) reflection can be seen after the hydrolysis of the K-intercalated MXene. Nonetheless, as the K- Ti_3C_2 sample maintained the best pillaring upon hydrolysis and the highest reduction of F content, it is reasonable to assume an essential role of the cation pillaring in the successful F removal by gas hydrolysis.

As demonstrated by the Raman and FTIR spectra in Figure 5, the change in termination by hydrolysis also resulted in significant shifts in the vibrational modes of $\text{Ti}_3\text{C}_2\text{T}_x$. In the FTIR spectra, three vibrational modes are assigned to Ti-C and Ti-T modes (T = termination group) at 575 cm^{-1} and 650 cm^{-1} for the pristine $\text{Ti}_3\text{C}_2\text{T}_x$, respectively, as well as K-T modes at around 955 cm^{-1} . Upon intercalation of K-ions, the Ti-related modes do not shift significantly. However, upon hydrolysis of K- Ti_3C_2 , the Ti-T and Ti-C modes are shifted by 20-50 cm^{-1} to higher wavenumbers,

which is ascribed to a reduced amount of F-terminations.[52] Similarly, the K-T vibration is shifted slightly down, which also match with the change in terminations. Additionally, in the Raman spectra in Figure 5b, there are significant shifts in the out-of-plane A_{1g} (C) peak at 717 cm^{-1} upon both K-intercalation and hydrolysis, which correspond with an increased interlayer spacing as well as the reduction of F-terminations.[31] In addition, there are significant shifts in the in-plane E_g peaks at around 209 cm^{-1} , 380 cm^{-1} and 610 cm^{-1} , and small shifts in the A_{1g} peak at 209 cm^{-1} and the resonant peak at 121 cm^{-1} , which also match with the expected changes for increased amounts of O-terminations.[31,53]

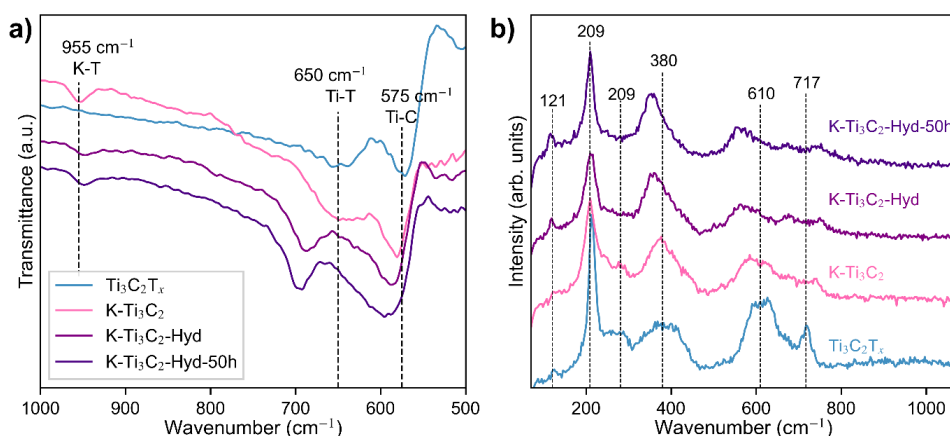


Figure 5. FTIR (a) and Raman (b) spectra of $\text{Ti}_3\text{C}_2\text{T}_x$ and $\text{K-Ti}_3\text{C}_2$ before and after hydrolysis at $300\text{ }^\circ\text{C}$ for 15 h and 50 h. The dotted lines in both spectra are used to indicate the location of the vibrational modes for the pristine $\text{Ti}_3\text{C}_2\text{T}_x$ and thus illustrate the shifts that occur upon intercalation of K-ions and after hydrolysis.

Furthermore, an interesting aspect with the hydrolysis of the cation pillared MXenes is the trend of which cations were able to hold the intercalated water upon hydrolysis. Based on the hydration enthalpies presented in Table S3, one would assume the opposite results, as Mg-ions have the highest hydration enthalpy of the four cations (Mg^{2+} , Li^+ , Na^+ and K^+), and therefore would be expected to hold the surrounding water molecules the strongest. Although previous reports suggest a clay-like behaviour of MXenes with 1-2 layers of water molecules following the intercalation of cations,[42,54–56] there are also reports suggesting that larger cations such as K would even extract water from the MXenes upon intercalation.[50] Based on the lack of H_2O vibrations in the FTIR spectra of $\text{K-Ti}_3\text{C}_2$, it is possible that the K-, Na- and Li-intercalated samples encompass zero layers of water molecules. However, due to the similarity of the interlayer spacings for all these cations and the calculated size of one layer of water molecules, the presence of intercalated water is very likely. Instead, the dehydration of the MXenes can most likely be attributed to the diffusion of intercalated

water, where the diffusion coefficient is larger for the smaller cations.[42,56] This implies that although K-ions have the lowest hydration enthalpy, they have the strongest ability to prevent water molecules from leaving the interlayers of the MXene upon increasing the temperature. In fact, by hydrolysis at 300 °C, the thermal energy may even be high enough to dehydrate all the different cations regardless of the hydration enthalpy. Additionally, it should be highlighted that the amount of co-intercalated water seems to strongly affect the stacking faults in the $Ti_3C_2T_x$ layers. While all the cation-intercalated structures with one water layer (K- Ti_3C_2 , Na- Ti_3C_2 and Li- Ti_3C_2) shows significantly more defined reflections in the 35-45° region compared to the pristine $Ti_3C_2T_x$, the Mg- Ti_3C_2 sample with two layers of water molecules does not.[43]

3.4. Electrochemical evaluation of hydrolysed K-intercalated $Ti_3C_2T_x$

As the hydrolysis of K- Ti_3C_2 resulted in the greatest F reduction, the electrochemical performance of $Ti_3C_2T_x$, K- Ti_3C_2 and K- Ti_3C_2 -Hyd electrodes was evaluated by galvanostatic charge and discharge cycling in LiB half cells. Capacity plots from tests at various current densities are presented in Figure 6a and b and they demonstrate how intercalation of K-ions resulted in a significant capacity reduction, both at low and high current densities. A similar capacity reduction upon K-intercalation has been reported for Na-ion batteries,[51] and may be ascribed to the K-ions blocking some of the possible intercalation sites for Li-ions upon cycling. With an approximated ~10 % K occupation of the intercalation sites inside the MXene (Table S1), and considering the possible blocking by the co-intercalated OH-ions, the reduction of around 20 % is to be expected. However, for the hydrolysed sample the capacity is increased, which can be ascribed to a reduced amount of F and OH-terminations that are assumed to either sterically hinder some Li-ion intercalation or end up with the formation of LiF or LiOH side products.[11,12] Seeing that the pristine $Ti_3C_2T_x$ and K- Ti_3C_2 electrodes show a significant capacity fade upon the first cycles, it is possible that the hydrolysed sample results in the formation of less side products during cycling, which again enables capacities closer to the theoretical limit of 268 mAh/g for $Ti_3C_2O_2Li_2$. [11,57] At lower current densities, the delithiation capacities obtained with K- Ti_3C_2 -Hyd electrodes are higher than the pristine $Ti_3C_2T_x$, with 187 mAh/g vs. 156 mAh/g at cycle 33 (Figure 6a), even though all of the intercalated K-ions remained after hydrolysis (Table S1). At higher current densities on the other hand, the capacity fades quickly and at current densities > 40 mA/g the capacity of the pristine $Ti_3C_2T_x$ is higher. This capacity reduction at higher current densities may partly be ascribed to K-ions blocking the Li-migration, as a similar trend is also observed for the K- Ti_3C_2 sample. However, as the capacity reduction in the hydrolysed sample is significantly bigger, it is also possible that the change in termination groups has an effect. Interestingly, DFT calculations predict lower migration barriers for Li-ions on O-terminated surfaces compared to F- and OH-terminated ones,[11,12] which should have

resulted in better rate performance. However, they also demonstrate how the stacking of the MXene sheets greatly influence the migration barriers.[58] As the K-Ti₃C₂-Hyd sample demonstrated a significant shift in the (001) reflection and thus a possible change in stacking (Figure S17), it is possible that the lesser rate capability of this material may be ascribed to stacking changes.

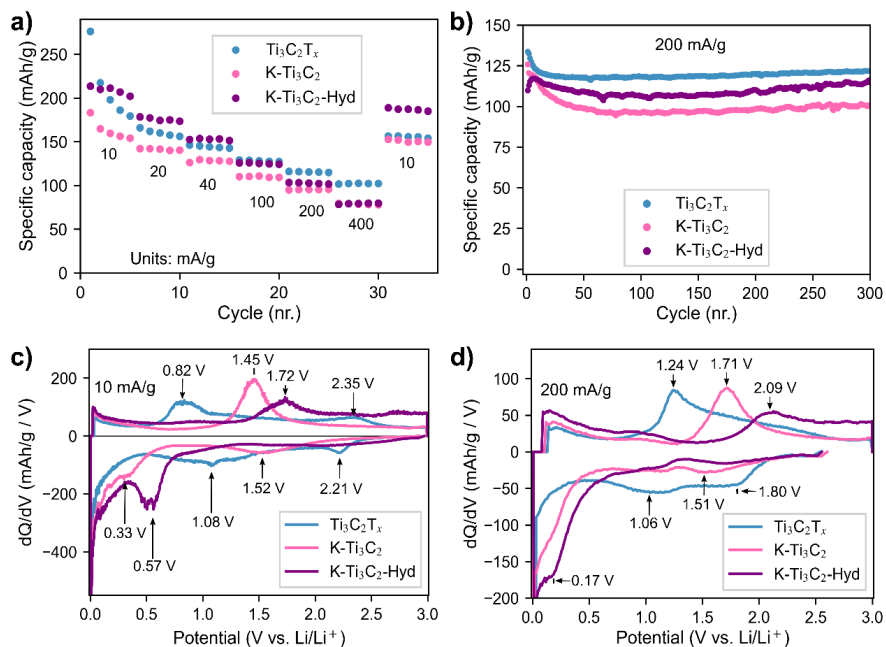


Figure 6. Electrochemical evaluation of Ti₃C₂T_x, K-Ti₃C₂ and K-Ti₃C₂-Hyd electrodes in LiB half cells, showing specific delithiation capacities per cycle during galvanostatic charge and discharge at various specific currents (a), and for long term cycling at 200 mA/g (b). Corresponding differential capacity profiles at 10 mA/g (c) and 200 mA/g (d) are from cycle 3 and 23 presented in (a), respectively.

The intercalation of K-ions and the following hydrolysis also affected the intercalation voltages during cycling, which is illustrated by the differential capacity plots in Figure 6c and d. From the low current density (10 mA/g) plot in Figure 6c, it is shown how the intercalation of K-ions lowered the voltage of the lithiation peaks from 2.21 V and 1.58 V in Ti₃C₂T_x to 1.52 V and 0.33 V, while the hydrolysis resulted in a shift of the biggest lithiation peak from 0.33 V to 0.57 V while flattening out the other peak. This shows that the intercalation of K-ions significantly lower the intercalation voltage of Li-ions, and that the removal of F-terminations by hydrolysis causes a slight increase in intercalation voltage matching well with more O-terminations being formed.[11–13] However, upon delithiation the peaks of the K-intercalated electrodes are moved to higher voltages, indicating a significant energy inefficiency compared to the pristine Ti₃C₂T_x. At higher current densities (Figure

6d), an even higher overpotential is observed for the K-intercalated electrodes, as the main lithiation peaks are shifted down to below 0.3 V, while the main delithiation peaks are shifted to 1.71 V and 2.09 V for K-Ti₃C₂ and K-Ti₃C₂-Hyd, respectively. The pristine Ti₃C₂T_x on the other hand, remains most of the lithiation and delithiation capacities between 1 V and 2 V, which is similar to what has been reported previously.[5,59]

Additionally, it should be noted that to the authors' knowledge, this is the first report on Li-intercalation in K pre-intercalated MXenes. Seeing that the K-ions may block some of the Li-intercalation sites, the K-intercalated Ti₃C₂T_x may be more suitable for other battery chemistries. In fact, for aqueous supercapacitors Prenger et al. recently demonstrated a 10-fold areal capacitance increase of multilayered Ti₃C₂T_x compared to delaminated films, by pre-intercalation of the same cations as presented here (Mg²⁺, Li⁺, Na⁺ and K⁺).[60] They also showed how the K-intercalated Ti₃C₂T_x phase resulted in the highest capacitance of all these cation-intercalated structures, which indicates how further investigation on this K-Ti₃C₂ phase also could be highly relevant for other applications.

4. Conclusion

Gas hydrolysis has been investigated as a method to substitute F-terminations with O- and OH- terminations on the 2D surfaces of Ti₃C₂T_x MXene, together with a comparison of the thermal stability of this phase in various atmospheres. Pristine HF-etched Ti₃C₂T_x MXene is found to remain stable up to a temperature of 300 °C, after which it starts to oxidise into TiO₂ nanoparticles and disordered graphitic carbon. Oxidation starts on the edge surfaces of the particles, but after hydrolysis at 500 °C the MXene phase is completely transformed to a TiO₂/C composite. The oxidation of Ti₃C₂T_x in humid inert atmosphere starts at a higher temperature (~400 °C) than in dry air (~300 °C). Compared to air annealing, hydrolysis also demonstrates a higher selectivity towards F removal. While the 500 °C annealing in dry air resulted in an oxidation of C to CO₂ and the formation of a TiOF₂ phase, hydrolysis at 500 °C removed almost all F content while preserving most of the carbon content. However, as the water molecules were unable to penetrate the pristine MXene structure, the hydrolysis resulted in no reduction of F-terminations prior to the decomposition.

We have shown that successful substitution of F-terminations from multilayered Ti₃C₂T_x particles requires a pillaring of the structure to allow for H₂O intercalation between the 2D layers. This was demonstrated by pre-intercalating Ti₃C₂T_x with various cations (Li⁺, Na⁺, K⁺, Mg²⁺, TBA⁺) together with

1-2 layers of H₂O molecules, which resulted in 2.8-7.8 Å increase in the interlayer spacing. Upon hydrolysis at 300 °C, three of the samples (Li-Ti₃C₂, Mg-Ti₃C₂ and TBA-Ti₃C₂) collapsed and ended up with an interlayer spacing matching the pristine HF-etched Ti₃C₂T_x (~9.7 Å), together with insignificant changes in F content. However, for the K-Ti₃C₂ and Na-Ti₃C₂ samples the pillaring structure remained after hydrolysis, which resulted in a significant reduction in F-terminations (45 % for Na-Ti₃C₂ and 64 % for K-Ti₃C₂ vs. pristine Ti₃C₂T_x) along with a similar increase in O content. By extending the hydrolysis time to 50 h, a total F reduction of 78 % was achieved, without any signs of surface oxidation. In addition, the fundamental role of H₂O vapour upon hydrolysis was proven by the insignificant F change upon annealing of the K-Ti₃C₂ sample in dry Ar gas. Cation intercalation followed by gas hydrolysis is thus proposed as a new method to substitute significant amounts of F-terminations from the bulk of Ti₃C₂T_x particles.

Moreover, the electrochemical performance of K-intercalated Ti₃C₂T_x before and after changing the termination groups by hydrolysis has been evaluated. Firstly, the K-intercalated electrodes demonstrated significantly worse energy efficiency compared to the pristine Ti₃C₂T_x, which was ascribed to steric hindrance. The intercalation of K-ions also reduced the specific capacity by blocking Li sites upon cycling. Hydrolysis of the MXene on the other hand, resulted in a slight increase in reversible capacity, which was ascribed to less irreversible reactions with F- and OH- terminations. Additionally, it resulted in increased (de)intercalation voltages and thereby demonstrate gas hydrolysis as a feasible method to control the electrochemical performance of Ti₃C₂T_x electrodes in LIBs.

Conflict of interest

The authors declare no competing financial interests.

Acknowledgements

This work was financially supported by the Research Council of Norway through the project “High-capacity 2D layered materials for Mg-ion batteries” (project number 275810). The computational resources were provided by UNINETT Sigma2 through the project NN9264K. The TEM work was carried out on NORTEM infrastructure, Grant 197405, TEM Gemini Centre, Norwegian University of Science and Technology (NTNU), Norway. The Research Council of Norway is acknowledged for the support to the Norwegian Micro- and Nano-Fabrication Facility, NorFab, project number 295864. Additionally, the authors would like to thank Prof. Andreas Erbe for his guidance in the

interpretation of the FTIR spectra, and Dr. Henning Kaland for useful discussions in the early stages of this work.

Author Contributions

Frode Håskjold Fagerli: Conceptualisation, Investigation, Formal analysis, Visualisation, Writing - Original draft. **Per Erik Vullum:** Investigation, Writing - Reviewing and Editing. **Tor Grande:** Conceptualization, Writing - Reviewing and Editing. **Zhaohui Wang:** Software, Writing - Reviewing and Editing. **Sverre M. Selbach:** Writing - Reviewing and Editing. **Kjell Wiik:** Supervision, Writing - Reviewing and Editing. **Nils Peter Wagner:** Supervision, Writing - Reviewing and Editing.

References

- [1] F. Shahzad, M. Alhabeab, C.B. Hatter, B. Anasori, S.M. Hong, C.M. Koo, Y. Gogotsi, Electromagnetic interference shielding with 2D transition metal carbides (MXenes), *Science* (80-.). 353 (2016) 1137–1140. <https://doi.org/10.1126/science.aag2421>.
- [2] Y. Cai, J. Shen, C.W. Yang, Y. Wan, H.L. Tang, A.A. Aljarb, C. Chen, J.H. Fu, X. Wei, K.W. Huang, Y. Han, S.J. Jonas, X. Dong, V. Tung, Mixed-dimensional MXene-hydrogel heterostructures for electronic skin sensors with ultrabroad working range, *Sci. Adv.* 6 (2020) 5367–5394. <https://doi.org/10.1126/sciadv.abb5367>.
- [3] Y.A.J. Al-Hamadani, B.M. Jun, M. Yoon, N. Taheri-Qazvini, S.A. Snyder, M. Jang, J. Heo, Y. Yoon, Applications of MXene-based membranes in water purification: A review, *Chemosphere.* 254 (2020) 126821. <https://doi.org/10.1016/J.CHEMOSPHERE.2020.126821>.
- [4] K. Huang, Z. Li, J. Lin, G. Han, P. Huang, Two-dimensional transition metal carbides and nitrides (MXenes) for biomedical applications, *Chem. Soc. Rev.* 47 (2018) 5109–5124. <https://doi.org/10.1039/c7cs00838d>.
- [5] M. Naguib, J. Come, B. Dyatkin, V. Presser, P.-L. Taberna, P. Simon, M.W. Barsoum, Y. Gogotsi, MXene: a promising transition metal carbide anode for lithium-ion batteries, *Electrochem. Commun.* 16 (2012) 61–64. <https://doi.org/10.1016/J.ELECOM.2012.01.002>.
- [6] R. Garg, A. Agarwal, M. Agarwal, A review on MXene for energy storage application: effect of interlayer distance, *Mater. Res. Express.* 7 (2020) 022001. <https://doi.org/10.1088/2053-1591/AB750D>.
- [7] M. Hu, H. Zhang, T. Hu, B. Fan, X. Wang, Z. Li, Emerging 2D MXenes for supercapacitors: status, challenges and prospects, *Chem. Soc. Rev.* 49 (2020) 6666–6693.

<https://doi.org/10.1039/DOCS00175A>.

- [8] A. VahidMohammadi, J. Rosen, Y. Gogotsi, The world of two-dimensional carbides and nitrides (MXenes), *Science*. 372 (2021). <https://doi.org/10.1126/SCIENCE.ABF1581>.
- [9] M.A. Hope, A.C. Forse, K.J. Griffith, M.R. Lukatskaya, M. Ghidui, Y. Gogotsi, C.P. Grey, NMR reveals the surface functionalisation of Ti₃C₂ MXene, *Phys. Chem. Chem. Phys.* 18 (2016) 5099–5102. <https://doi.org/10.1039/C6CP00330C>.
- [10] M. Naguib, V.N. Mochalin, M.W. Barsoum, Y. Gogotsi, 25th anniversary article: MXenes: A new family of two-dimensional materials, *Adv. Mater.* 26 (2014) 992–1005. <https://doi.org/10.1002/adma.201304138>.
- [11] Y. Xie, M. Naguib, V.N. Mochalin, M.W. Barsoum, Y. Gogotsi, X. Yu, K.-W. Nam, X.-Q. Yang, A.I. Kolesnikov, P.R.C. Kent, Role of Surface Structure on Li-Ion Energy Storage Capacity of Two-Dimensional Transition-Metal Carbides, *J. Am. Chem. Soc.* 136 (2014) 6385–6394. <https://doi.org/10.1021/ja501520b>.
- [12] Q. Tang, Z. Zhou, P. Shen, Are MXenes promising anode materials for Li ion batteries? Computational studies on electronic properties and Li storage capability of Ti₃C₂ and Ti₃C₂X₂ (X = F, OH) monolayer, *J. Am. Chem. Soc.* 134 (2012) 16909–16916. <https://doi.org/10.1021/JA308463R>.
- [13] H. Kaland, J. Hadler-Jacobsen, F.H. Fagerli, N.P. Wagner, Z. Wang, S.M. Selbach, F. Vullum-Bruer, K. Wiik, S.K. Schnell, Are MXenes suitable as cathode materials for rechargeable Mg batteries?, *Sustain. Energy Fuels*. 4 (2020) 2956–2966. <https://doi.org/10.1039/D0SE00087F>.
- [14] C. Eames, M.S. Islam, Ion intercalation into two-dimensional transition-metal carbides: Global screening for new high-capacity battery materials, *J. Am. Chem. Soc.* 136 (2014) 16270–16276. <https://doi.org/10.1021/ja508154e>.
- [15] V. Kamysbayev, A.S. Filatov, H. Hu, X. Rui, F. Lagunas, D. Wang, R.F. Klie, D. V. Talapin, Covalent surface modifications and superconductivity of two-dimensional metal carbide MXenes, *Science (80-.)*. 369 (2020) 979–983. <https://doi.org/10.1126/science.aba8311>.
- [16] L. Huang, T. Li, Q. Liu, J. Gu, Fluorine-free Ti₃C₂T_x as anode materials for Li-ion batteries, *Electrochem. Commun.* 104 (2019) 106472. <https://doi.org/10.1016/j.elecom.2019.05.021>.
- [17] Y. Li, H. Shao, Z. Lin, J. Lu, L. Liu, B. Duployer, P.O.Å. Persson, P. Eklund, L. Hultman, M. Li, K. Chen, X.H. Zha, S. Du, P. Rozier, Z. Chai, E. Raymundo-Piñero, P.L. Taberna, P. Simon, Q. Huang, A general Lewis acidic etching route for preparing MXenes with enhanced

- electrochemical performance in non-aqueous electrolyte, *Nat. Mater.* (2020) 1–6.
<https://doi.org/10.1038/s41563-020-0657-0>.
- [18] R.A. Vaia, A. Jawaid, A. Hassan, G. Neher, D. Nepal, R. Pachter, W. Joshua Kennedy, S. Ramakrishnan, Halogen etch of Ti₃AlC₂ MAX phase for mxene fabrication, *ACS Nano*. 15 (2021) 2771–2777. <https://doi.org/10.1021/ACSNANO.0C08630>.
- [19] Z. Li, L. Wang, D. Sun, Y. Zhang, B. Liu, Q. Hu, A. Zhou, Synthesis and thermal stability of two-dimensional carbide MXene Ti₃C₂, *Mater. Sci. Eng. B Solid-State Mater. Adv. Technol.* 191 (2015) 33–40. <https://doi.org/10.1016/j.mseb.2014.10.009>.
- [20] R. Cheng, T. Hu, H. Zhang, C. Wang, M. Hu, J. Yang, C. Cui, T. Guang, C. Li, C. Shi, P. Hou, X. Wang, Understanding the Lithium Storage Mechanism of Ti₃C₂T_x MXene, *J. Phys. Chem. C*. (2019) [acs.jpcc.8b10790](https://doi.org/10.1021/acs.jpcc.8b10790). <https://doi.org/10.1021/acs.jpcc.8b10790>.
- [21] S. Doo, A. Chae, D. Kim, T. Oh, T.Y. Ko, S.J. Kim, D.Y. Koh, C.M. Koo, Mechanism and Kinetics of Oxidation Reaction of Aqueous Ti₃C₂T_xSuspensions at Different pHs and Temperatures, *ACS Appl. Mater. Interfaces*. 13 (2021) 22855–22865.
<https://doi.org/10.1021/ACSAMI.1C04663>.
- [22] X. Zhang, Y. Liu, S. Dong, Z. Ye, Y. Guo, One-step hydrothermal synthesis of a TiO₂-Ti₃C₂T_x nanocomposite with small sized TiO₂ nanoparticles, *Ceram. Int.* 43 (2017) 11065–11070.
<https://doi.org/10.1016/J.CERAMINT.2017.05.151>.
- [23] J. Halim, I. Persson, P. Eklund, P.O.Å. Persson, J. Rosen, Sodium hydroxide and vacuum annealing modifications of the surface terminations of a Ti₃C₂ (MXene) epitaxial thin film, *RSC Adv.* 8 (2018) 36785–36790. <https://doi.org/10.1039/c8ra07270a>.
- [24] M. Naguib, O. Mashtalir, M.R. Lukatskaya, B. Dyatkin, C. Zhang, V. Presser, Y. Gogotsi, M.W. Barsoum, One-step synthesis of nanocrystalline transition metal oxides on thin sheets of disordered graphitic carbon by oxidation of MXenes, *Chem. Commun.* 50 (2014) 7420–7423.
<https://doi.org/10.1039/c4cc01646g>.
- [25] I. Persson, J. Halim, T.W. Hansen, J.B. Wagner, V. Darakchieva, J. Palisaitis, J. Rosen, P.O.Å. Persson, How Much Oxygen Can a MXene Surface Take Before It Breaks?, *Adv. Funct. Mater.* (2020) 1909005. <https://doi.org/10.1002/adfm.201909005>.
- [26] P. Bärmann, R. Nölle, V. Siozios, M. Rutttert, O. Guillon, M. Winter, J. Gonzalez-Julian, T. Placke, Solvent Co-intercalation into Few-layered Ti₃C₂T_x MXenes in Lithium Ion Batteries Induced by Acidic or Basic Post-treatment, *ACS Nano*. (2021).

<https://doi.org/10.1021/acsnano.0c10153>.

- [27] J. Li, X. Yuan, C. Lin, Y. Yang, L. Xu, X. Du, J. Xie, J. Lin, J. Sun, J. Li, X. Yuan, C. Lin, Y. Yang, L. Xu, X. Du, J. Xie, J. Lin, J. Sun, Achieving High Pseudocapacitance of 2D Titanium Carbide (MXene) by Cation Intercalation and Surface Modification, *Adv. Energy Mater.* 7 (2017) 1602725. <https://doi.org/10.1002/AENM.201602725>.
- [28] F.H. Fagerli, Z. Wang, T. Grande, H. Kaland, S.M. Selbach, N.P. Wagner, K. Wiik, Removing Fluoride-Terminations from Multilayered V2CTx MXene by Gas Hydrolyzation, *ACS Omega.* 7 (2022) 23790–23799. <https://doi.org/10.1021/acsomega.2c02441>.
- [29] F.A. Lukiyonov, E.I. Rau, R.A. Sennov, Depth range of primary electrons, electron beam broadening, and spatial resolution in electron-beam studies, *Bull. Russ. Acad. Sci. Phys.* 2009 734. 73 (2009) 441–449. <https://doi.org/10.3103/S1062873809040029>.
- [30] A. Wexler, Vapor pressure formulation for water in range 0 to 100 Degrees C. A revision, *J. Res. Natl. Bur. Stand. - A. Phys. Chem.* 80A (1976) 775–785. https://nvlpubs.nist.gov/nistpubs/jres/80A/jresv80An5-6p775_A1b.pdf (accessed July 2, 2022).
- [31] A. Sarycheva, Y. Gogotsi, Raman Spectroscopy Analysis of the Structure and Surface Chemistry of Ti₃C₂T_x MXene, *Chem. Mater.* 32 (2020) 3480–3488. <https://doi.org/10.1021/acs.chemmater.0c00359>.
- [32] G. Kresse, D. Joubert, From ultrasoft pseudopotentials to the projector augmented-wave method, *Phys. Rev. B.* 59 (1999) 1758. <https://doi.org/10.1103/PhysRevB.59.1758>.
- [33] P.E. Blöchl, Projector augmented-wave method, *Phys. Rev. B.* 50 (1994) 17953. <https://doi.org/10.1103/PhysRevB.50.17953>.
- [34] G. Kresse, J. Furthmüller, Efficient iterative schemes for *ab initio* total-energy calculations using a plane-wave basis set, *Phys. Rev. B.* 54 (1996) 11169. <https://doi.org/10.1103/PhysRevB.54.11169>.
- [35] K.J. Atkins, P. W., de Paula J., *Physical Chemistry*, 11th ed, Oxford Univ. Press. Oxford. (2017) 944.
- [36] A. Togo, I. Tanaka, First principles phonon calculations in materials science, *Scr. Mater.* 108 (2015) 1–5. <https://doi.org/10.1016/J.SCRIPTAMAT.2015.07.021>.
- [37] Russell D. Johnson, NIST Computational Chemistry Comparison and Benchmark Database,

NIST Stand. Ref. Database Number 101. (2022). <https://doi.org/10.18434/T47C7Z>.

- [38] F. Destyorini, Y. Irmawati, A. Hardiansyah, H. Widodo, I.N.D. Yahya, N. Indayaningsih, R. Yudianti, Y.I. Hsu, H. Uyama, Formation of nanostructured graphitic carbon from coconut waste via low-temperature catalytic graphitisation, *Eng. Sci. Technol. an Int. J.* 24 (2021) 514–523. <https://doi.org/10.1016/J.JESTCH.2020.06.011>.
- [39] P.K. Chu, L. Li, Characterization of amorphous and nanocrystalline carbon films, *Mater. Chem. Phys.* 96 (2006) 253–277. <https://doi.org/10.1016/J.MATCHEMPHYS.2005.07.048>.
- [40] R.A. Rochman, S. Wahyuningsih, A.H. Ramelan, Q.A. Hanif, Preparation of nitrogen and sulphur Co-doped reduced graphene oxide (rGO-NS) using N and S heteroatom of thiourea, *IOP Conf. Ser. Mater. Sci. Eng.* 509 (2019) 012119. <https://doi.org/10.1088/1757-899X/509/1/012119>.
- [41] X. Zhang, Y. Liu, S. Dong, Z. Ye, Y. Guo, One-step hydrothermal synthesis of a TiO₂-Ti₃C₂T_x nanocomposite with small sized TiO₂ nanoparticles, *Ceram. Int.* 43 (2017) 11065–11070. <https://doi.org/10.1016/J.CERAMINT.2017.05.151>.
- [42] N.C. Osti, M. Naguib, A. Ostadhossein, Y. Xie, P.R.C. Kent, B. Dyatkin, G. Rother, W.T. Heller, A.C.T. Van Duin, Y. Gogotsi, E. Mamontov, Effect of Metal Ion Intercalation on the Structure of MXene and Water Dynamics on its Internal Surfaces, *ACS Appl. Mater. Interfaces.* 8 (2016) 8859–8863. <https://doi.org/10.1021/acsami.6b01490>.
- [43] C. Ferrara, A. Gentile, S. Marchionna, I. Quinzeni, M. Fracchia, P. Ghigna, S. Pollastri, C. Ritter, G.M. Vanacore, R. Ruffo, The Missing Piece: The Structure of the Ti₃C₂T_xMXene and Its Behavior as Negative Electrode in Sodium Ion Batteries, *Nano Lett.* 21 (2021) 8290–8297. <https://doi.org/10.1021/ACS.NANOLETT.1C02809>.
- [44] J. Hadler-Jacobsen, F.H. Fagerli, H. Kaland, S.K. Schnell, Stacking Sequence, Interlayer Bonding, Termination Group Stability and Li/Na/Mg Diffusion in MXenes, *ACS Mater. Lett.* 3 (2021) 1369–1376. <https://doi.org/10.1021/ACSMATERIALSLETT.1C00316>.
- [45] P. Yu, G. Cao, S. Yi, X. Zhang, C. Li, X. Sun, K. Wang, Y. Ma, Binder-free 2D titanium carbide (MXene)/carbon nanotube composites for high-performance lithium-ion capacitors, *Nanoscale.* 10 (2018) 5906–5913. <https://doi.org/10.1039/C8NR00380G>.
- [46] M. Ghidui, J. Halim, S. Kota, D. Bish, Y. Gogotsi, M.W. Barsoum, Ion-Exchange and Cation Solvation Reactions in Ti₃C₂MXene, *Chem. Mater.* 28 (2016) 3507–3514. <https://doi.org/10.1021/acs.chemmater.6b01275>.

- [47] J.L. Hart, K. Hantanasirisakul, A.C. Lang, B. Anasori, D. Pinto, Y. Pivak, J.T. van Omme, S.J. May, Y. Gogotsi, M.L. Taheri, Control of MXenes' electronic properties through termination and intercalation, *Nat. Commun.* 10 (2019) 522. <https://doi.org/10.1038/s41467-018-08169-8>.
- [48] Y. Xia, L. Que, F. Yu, L. Deng, Z. Liang, Y. Jiang, M. Sun, L. Zhao, Z. Wang, Tailoring Nitrogen Terminals on MXene Enables Fast Charging and Stable Cycling Na-Ion Batteries at Low Temperature, *Nano-Micro Lett.* 2022 141. 14 (2022) 1–16. <https://doi.org/10.1007/S40820-022-00885-7>.
- [49] G. Sharma, E. Muthuswamy, M. Naguib, Y. Gogotsi, A. Navrotsky, D. Wu, Calorimetric Study of Alkali Metal Ion (K⁺, Na⁺, Li⁺) Exchange in a Clay-Like MXene, *J. Phys. Chem. C.* 121 (2017) 15145–15153. <https://doi.org/10.1021/ACS.JPCC.7B02419>.
- [50] N. Shpigel, M.D. Levi, S. Sigalov, T.S. Mathis, Y. Gogotsi, D. Aurbach, Direct Assessment of Nanoconfined Water in 2D Ti₃C₂ Electrode Interspaces by a Surface Acoustic Technique, *J. Am. Chem. Soc.* 140 (2018) 8910–8917. <https://doi.org/10.1021/JACS.8B04862>.
- [51] J. Luo, C. Fang, C. Jin, H. Yuan, O. Sheng, R. Fang, W. Zhang, H. Huang, Y. Gan, Y. Xia, C. Liang, J. Zhang, W. Li, X. Tao, Tunable pseudocapacitance storage of MXene by cation pillaring for high performance sodium-ion capacitors, *J. Mater. Chem. A.* 6 (2018) 7794–7806. <https://doi.org/10.1039/C8TA02068J>.
- [52] Tao Hu, Jiemin Wang, Hui Zhang, Zhaojin Li, Minmin Hu, Xiaohui Wang, Vibrational properties of Ti₃C₂ and Ti₃C₂T₂ (T = O, F, OH) monosheets by first-principles calculations: a comparative study, *Phys. Chem. Chem. Phys.* 17 (2015) 9997–10003. <https://doi.org/10.1039/C4CP05666C>.
- [53] H. Li, S. Chen, D.W. Boukhalov, Z. Yu, M.G. Humphrey, Z. Huang, C. Zhang, Switching the Nonlinear Optical Absorption of Titanium Carbide MXene by Modulation of the Surface Terminations, *ACS Nano.* (2022) acsnano.1c07060. <https://doi.org/10.1021/ACSNANO.1C07060>.
- [54] N.C. Osti, M. Naguib, K. Ganeshan, Y.K. Shin, A. Ostadhossein, A.C.T. Van Duin, Y. Cheng, L.L. Daemen, Y. Gogotsi, E. Mamontov, A.I. Kolesnikov, Influence of metal ions intercalation on the vibrational dynamics of water confined between MXene layers, *Phys. Rev. Mater.* 1 (2017) 065406. <https://doi.org/10.1103/PHYSREVMATERIALS.1.065406>/FIGURES/5/MEDIUM.
- [55] M.R. Lukatskaya, O. Mashtalir, C.E. Ren, Y. Dall'Agnese, P. Rozier, P.L. Taberna, M. Naguib, P. Simon, M.W. Barsoum, Y. Gogotsi, Cation intercalation and high volumetric capacitance of

two-dimensional titanium carbide, *Science* (80-.). 341 (2013) 1502–1505.
<https://doi.org/10.1126/science.1241488>.

- [56] E.S. Muckley, M. Naguib, H.W. Wang, L. Vlcek, N.C. Osti, R.L. Sacci, X. Sang, R.R. Unocic, Y. Xie, M. Tyagi, E. Mamontov, K.L. Page, P.R.C. Kent, J. Nanda, I.N. Ivanov, Multimodality of Structural, Electrical, and Gravimetric Responses of Intercalated MXenes to Water, *ACS Nano*. 11 (2017) 11118–11126. <https://doi.org/10.1021/ACS.NANO.7B05264>.
- [57] Y. Xie, Y. Dall’Agnese, M. Naguib, Y. Gogotsi, M.W. Barsoum, H.L. Zhuang, P.R.C. Kent, Prediction and characterization of mxene nanosheet anodes for non-lithium-ion batteries, *ACS Nano*. 8 (2014) 9606–9615. <https://doi.org/10.1021/nn503921j>.
- [58] J. Hadler-Jacobsen, S.K. Schnell, The Importance of Stacking and Coordination for Li, Na, and Mg Diffusion and Intercalation in Ti₃C₂T₂ MXene, *Adv. Mater. Interfaces*. (2022) 2200014. <https://doi.org/10.1002/ADMI.202200014>.
- [59] P. Bärmann, M. Winter, J. Gonzalez-Julian, T. Placke, Solvent Co-Intercalation-Induced Activation and Capacity Fade Mechanism of Few-/Multi-Layered MXenes in Lithium Ion Batteries, *Small*. (2021) 2104130. <https://doi.org/10.1002/SMLL.202104130>.
- [60] K. Prenger, Y. Sun, K. Ganeshan, A. Al-Temimy, K. Liang, C. Dun, J.J. Urban, J. Xiao, T. Petit, A.C.T. van Duin, D. Jiang, M. Naguib, Metal Cation Pre-Intercalated Ti₃C₂T_x MXene as Ultra-High Areal Capacitance Electrodes for Aqueous Supercapacitors, *ACS Appl. Energy Mater*. (2022). <https://doi.org/10.1021/ACSAEM.2C00653>.

Supplementary information

To

Bulk substitution of F-terminations from $\text{Ti}_3\text{C}_2\text{T}_x$ MXene by cation pillaring and gas hydrolysis

Frode Håskjold Fagerli,^a Per Erik Vullum,^{bc} Tor Grande,^a Zhaohui Wang,^{ab} Sverre M. Selbach,^a Kjell Wiik^a and Nils Peter Wagner^{ab*}

a. Department of Materials Science and Engineering, Norwegian University of Science and Technology, NO-7034 Trondheim, Norway.

b. SINTEF Industry, NO-7034 Trondheim, Norway.

c. Department of Physics, Norwegian University of Science and Technology, NO-7034 Trondheim, Norway.

* nils.peter.wagner@sintef.no

Additional Figures and Tables

The Figures included here present:

- Figure S1. Particle size distribution of the Ti_3AlC_2 MAX phase before and after wet milling.
- Figure S2. EDS mapping and a demonstration of how the point scan averages were obtained.
- Figure S3. Pawley fitting of X-ray diffractograms for various $\text{Ti}_3\text{C}_2\text{T}_x$ samples.
- Figure S4. X-ray diffractograms before and after etching of the Ti_3AlC_2 MAX phase.
- Figure S5. Rietveld refinement of the X-ray diffractograms for Hyd500C and Air500C.
- Figure S6. Enlarged plots on specific regions from the X-ray diffractograms presented in Figure 2a.
- Figure S7. Extended region of the FTIR spectra presented in Figure 2c.
- Figure S8. SEM micrographs of pristine $\text{Ti}_3\text{C}_2\text{T}_x$ particles before and after hydrolysis.
- Figure S9. TEM EDS mapping of the edge surface of $\text{Ti}_3\text{C}_2\text{T}_x$ particles before and after hydrolysis.
- Figure S10. XRD, Raman and EDS results from air annealing of $\text{Ti}_3\text{C}_2\text{T}_x$ at various temperatures.
- Figure S11. SEM micrographs of $\text{Ti}_3\text{C}_2\text{T}_x$ particles after air annealing at 500 °C.
- Figure S12. DFT results from five reactions showing ΔG° as a function of temperature.
- Figure S13. X-ray diffractograms of pristine $\text{Ti}_3\text{C}_2\text{T}_x$ before and after annealing in various atmospheres.
- Figure S14. FTIR spectra of pristine $\text{Ti}_3\text{C}_2\text{T}_x$ before and after annealing at 500 °C in various atmospheres.
- Figure S15. FTIR spectra of $\text{Ti}_3\text{C}_2\text{T}_x$ intercalated with K- and Mg-ions before and after hydrolysis.
- Figure S16. The complete 2θ -range of the X-ray diffractograms presented in Figure 4a.
- Figure S17. X-ray diffractograms of $\text{Ti}_3\text{C}_2\text{T}_x$, K- Ti_3C_2 , K- Ti_3C_2 -Hyd and K- Ti_3C_2 -Hyd-50h.
- Figure S18. SEM micrographs of the K- Ti_3C_2 and K- Ti_3C_2 -Hyd samples at two different magnifications.

The Tables included here present:

- Table S1. Overview over EDS point scan averages and standard deviations that are used in this article.
- Table S2. Comparison between EDS results from mapping and point scans
- Table S3. Ionic radii, hydration enthalpy and fluoride solubility for four cations (Mg^{2+} , Li^+ , Na^+ and K^+).

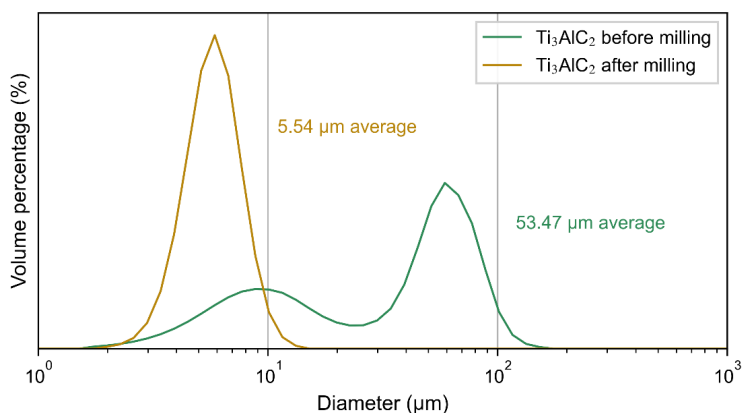


Figure S1. Particle size distribution of the Ti_3AlC_2 MAX phase before and after wet milling for 150 min in isopropanol.

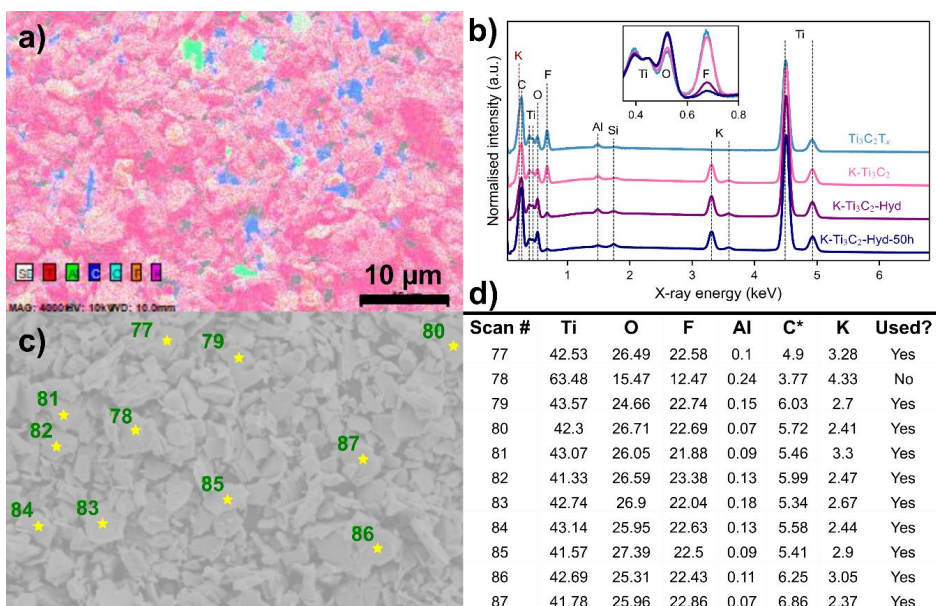


Figure S2. EDS results together with an example of how the point scan averages in Table S1 were obtained. (a) shows EDS mapping of the $\text{K-Ti}_3\text{C}_2$ sample, (c) shows the selected point scans from the same area, (d) shows the atomic percentages obtained from the analysis of the point scans in (c), and (b) shows a comparison of the normalised EDS mapping spectra for the hydrolysis of $\text{K-Ti}_3\text{C}_2$. The inset in (b) displays a comparison of the O and F peaks after normalising the plots to the Ti peaks, demonstrating a significant reduction of the F peak upon hydrolysis. As stated in (d), one spectrum (78) was omitted for the calculation of the average values for $\text{K-Ti}_3\text{C}_2$. It was omitted as the analysis software could not adjust for the high tilt, which thus resulted in an increase in the high energy components (i.e. Ti and K) versus the low energy components (i.e. O and F). The X-ray energies for the different atoms in (b) were collected from the Esprit 1.9 software, and as illustrated by the overlap of the K and C peak at ~ 0.26 keV, the calculated C content in (d) was perturbed.

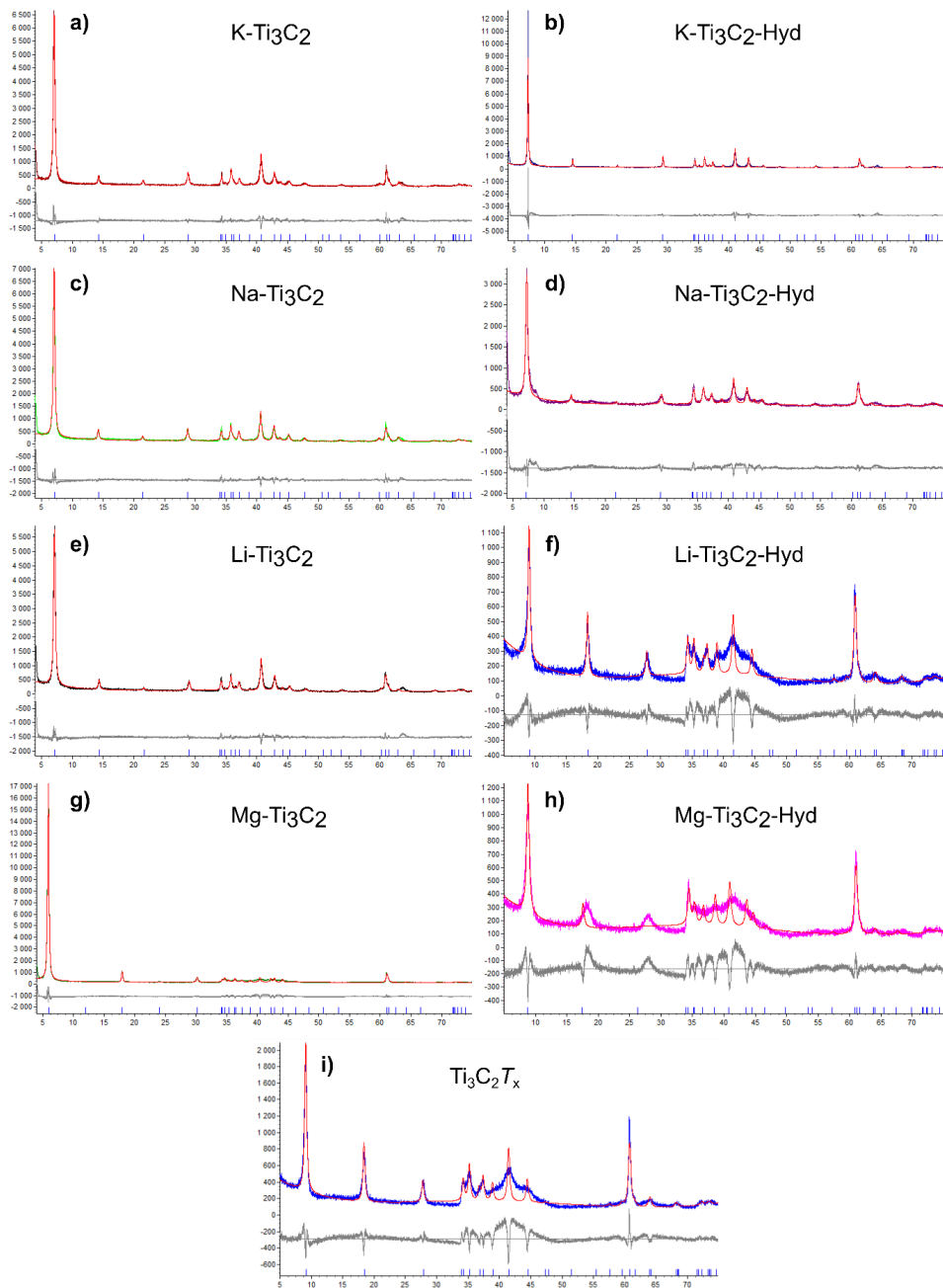


Figure S3. Pawley fitting of X-ray diffractograms for pristine $Ti_3C_2T_x$ MXene before (i) and after the intercalation of the various cations (a,c,e,g), followed by hydrolysis at 300 °C (b,d,f,h), illustrating how well the fitting matched with the experimentally obtained diffractograms. The non-intercalated samples ($Ti_3C_2T_x$, Li- Ti_3C_2 -Hyd and Mg- Ti_3C_2 -Hyd) show a higher degree of stacking faults, as they result in stronger fitting mismatches in the 35-45° 2θ region.[1]

Table S1. Overview over the EDS point scan averages and standard deviations that are used in this article. The amounts are presented relative to one formula unit of $Ti_3C_2T_x$ (or a Ti amount of 3). The C quantification of K- Ti_3C_2 is disturbed by the K and C X-rays overlapping (Figure S2b), and Li is not detectable in EDS. The results above the vertical midline represent annealing of pristine HF-etched $Ti_3C_2T_x$, where the name indicates what atmosphere and temperature is used. Below the midline are the results from the intercalation of cations into $Ti_3C_2T_x$ followed by hydrolysatation at 300 °C.

| Sample | Ti | Al | C | O | F | Mg/Na/K |
|-------------------------|----------|-------------|-------------|-------------|-------------|-------------|
| Ti_3AlC_2 | 3 ± 0.14 | 1.00 ± 0.05 | 1.97 ± 0.13 | | | |
| Ti_3C_2 | 3 ± 0.34 | 0.01 ± 0.01 | 1.57 ± 0.14 | 1.35 ± 0.11 | 1.39 ± 0.12 | |
| Hyd300C | 3 ± 0.19 | 0.01 ± 0.00 | 1.59 ± 0.05 | 1.42 ± 0.15 | 1.36 ± 0.07 | |
| Hyd400C | 3 ± 0.24 | 0.01 ± 0.00 | 1.85 ± 0.24 | 1.97 ± 0.13 | 1.21 ± 0.14 | |
| Hyd450C | 3 ± 0.15 | 0.01 ± 0.00 | 1.54 ± 0.11 | 2.09 ± 0.35 | 1.18 ± 0.18 | |
| Hyd500C | 3 ± 0.12 | 0.01 ± 0.01 | 1.38 ± 0.03 | 6.09 ± 0.26 | 0.09 ± 0.13 | |
| Vac500C | 3 ± 0.15 | 0.01 ± 0.00 | 1.61 ± 0.12 | 1.45 ± 0.08 | 1.33 ± 0.08 | |
| Ar500C | 3 ± 0.10 | 0.01 ± 0.00 | 1.65 ± 0.04 | 1.51 ± 0.08 | 1.43 ± 0.05 | |
| H ₂ /Ar-500C | 3 ± 0.17 | 0.01 ± 0.00 | 1.75 ± 0.14 | 1.30 ± 0.08 | 1.35 ± 0.06 | |
| Air300C | 3 ± 0.24 | 0.01 ± 0.00 | 1.45 ± 0.12 | 2.43 ± 0.36 | 1.29 ± 0.22 | |
| Air400C | 3 ± 0.26 | 0.01 ± 0.00 | 0.40 ± 0.37 | 5.44 ± 0.33 | 0.39 ± 0.17 | |
| Air500C | 3 ± 0.09 | 0.01 ± 0.00 | 0.36 ± 0.18 | 5.67 ± 0.23 | 0.33 ± 0.16 | |
| TBA- Ti_3C_2 | 3 ± 0.07 | 0.00 ± 0.00 | 2.77 ± 0.15 | 1.41 ± 0.08 | 1.22 ± 0.06 | |
| TBA- Ti_3C_2 -Hyd | 3 ± 0.13 | 0.01 ± 0.01 | 1.77 ± 0.10 | 1.87 ± 0.18 | 0.99 ± 0.08 | |
| K- Ti_3C_2 | 3 ± 0.05 | 0.01 ± 0.00 | 0.41 ± 0.04 | 1.85 ± 0.06 | 1.59 ± 0.03 | 0.19 ± 0.03 |
| K- Ti_3C_2 -Hyd | 3 ± 0.10 | 0.01 ± 0.00 | 0.44 ± 0.02 | 2.61 ± 0.11 | 0.51 ± 0.09 | 0.21 ± 0.04 |
| K- Ti_3C_2 -Hyd-50h | 3 ± 0.22 | 0.01 ± 0.01 | 0.47 ± 0.03 | 2.82 ± 0.22 | 0.31 ± 0.07 | 0.23 ± 0.02 |
| K- Ti_3C_2 -Ar300C | 3 ± 0.15 | 0.01 ± 0.00 | 0.00 ± 0.02 | 2.47 ± 0.15 | 1.22 ± 0.15 | 0.23 ± 0.01 |
| Mg- Ti_3C_2 * | 3 ± 0.25 | 0.01 ± 0.00 | 1.79 ± 0.14 | 2.24 ± 0.14 | 1.06 ± 0.24 | 0.18 ± 0.01 |
| Mg- Ti_3C_2 -Hyd* | 3 ± 0.28 | 0.01 ± 0.01 | 1.95 ± 0.39 | 2.10 ± 0.28 | 1.12 ± 0.21 | 0.18 ± 0.03 |
| Na- Ti_3C_2 | 3 ± 0.17 | 0.01 ± 0.01 | 1.47 ± 0.08 | 1.41 ± 0.08 | 1.13 ± 0.04 | 0.21 ± 0.07 |
| Na- Ti_3C_2 -Hyd | 3 ± 0.13 | 0.01 ± 0.00 | 1.40 ± 0.07 | 1.80 ± 0.29 | 0.77 ± 0.23 | 0.16 ± 0.01 |
| Li- Ti_3C_2 | 3 ± 0.18 | 0.01 ± 0.00 | 1.58 ± 0.10 | 1.62 ± 0.10 | 1.36 ± 0.06 | |
| Li- Ti_3C_2 -Hyd | 3 ± 0.13 | 0.01 ± 0.00 | 1.61 ± 0.07 | 1.58 ± 0.13 | 1.28 ± 0.08 | |

- No Cl peaks were detected in the Mg- Ti_3C_2 samples.

Table S2. Comparison between the chemical quantifications obtained from EDS mapping and point scans for all MXene compositions presented in this article, where the F content is highlighted with colour coding to emphasize the changes (green = low, and red = high). Apart from the unstable C content in the mapping, which is a result of extra signal from the C tape background, there are similar tendencies for both the mapping and point scan results. The amounts are presented relative to one formula unit of $Ti_3C_2T_x$ (or a Ti amount of 3). The cations are Mg, Na or K, although Al content is shown for Ti_3AlC_2 MAX phase before and after etching. Noteworthy, seeing that the EDS mapping results show similar trends as the point scan averages, the use of EDS mapping may prove to be sufficient for rough quantification of O and F content for MXenes, if the number of impurity particles in the mapped regions are consistent.

| Sample | Mapping | | | | Point scans | | | |
|-----------------------|---------|------|------|-----------|-------------|------|------|-----------|
| | C | O | F | Cation | C | O | F | Cation |
| Ti_3AlC_2 | 2.22 | | | 1.00 (Al) | 1.97 | | | 1.00 (Al) |
| Ti_3C_2 | 3.58 | 1.81 | 1.56 | 0.03 (Al) | 1.57 | 1.35 | 1.39 | 0.01 (Al) |
| Hyd300C | 2.81 | 1.87 | 1.52 | | 1.59 | 1.42 | 1.36 | |
| Hyd400C | 3.79 | 2.50 | 1.20 | | 1.85 | 1.97 | 1.21 | |
| Hyd450C | 2.36 | 2.74 | 1.13 | | 1.54 | 2.09 | 1.18 | |
| Hyd500C | 1.99 | 6.78 | 0.06 | | 1.38 | 6.09 | 0.09 | |
| Vac500C | 3.72 | 2.01 | 1.53 | | 1.61 | 1.45 | 1.33 | |
| Ar500C | 2.79 | 1.93 | 1.39 | | 1.65 | 1.51 | 1.43 | |
| $H_2/Ar500C$ | 3.11 | 1.76 | 1.53 | | 1.75 | 1.30 | 1.35 | |
| Air300C | 2.06 | 2.97 | 1.16 | | 1.45 | 2.43 | 1.29 | |
| Air400C | 1.85 | 5.85 | 0.44 | | 0.40 | 5.44 | 0.39 | |
| Air500C | 1.42 | 6.37 | 0.22 | | 0.36 | 5.67 | 0.33 | |
| TBA- Ti_3C_2 | 2.80 | 1.58 | 1.26 | | 2.77 | 1.41 | 1.22 | |
| TBA- Ti_3C_2 -Hyd | 1.53 | 1.57 | 0.71 | | 1.77 | 1.87 | 0.99 | |
| K- Ti_3C_2 | 0.47 | 1.75 | 1.27 | 0.23 | 0.41 | 1.85 | 1.59 | 0.19 |
| K- Ti_3C_2 -Hyd | 0.44 | 2.17 | 0.38 | 0.24 | 0.44 | 2.61 | 0.51 | 0.21 |
| K- Ti_3C_2 -Hyd-50h | 0.87 | 2.51 | 0.24 | 0.22 | 0.47 | 2.82 | 0.31 | 0.23 |
| K- Ti_3C_2 -Ar300C | 0.00 | 2.51 | 1.13 | 0.23 | 0.00 | 2.47 | 1.22 | 0.23 |
| Mg- Ti_3C_2 | 3.06 | 2.13 | 0.99 | 0.18 | 1.79 | 2.24 | 1.06 | 0.18 |
| Mg- Ti_3C_2 -Hyd | 8.91 | 2.74 | 0.96 | 0.16 | 1.95 | 2.10 | 1.12 | 0.18 |
| Na- Ti_3C_2 | 2.91 | 2.08 | 1.55 | 0.39 | 1.47 | 1.41 | 1.13 | 0.21 |
| Na- Ti_3C_2 -Hyd | 3.55 | 2.47 | 0.78 | 0.25 | 1.40 | 1.80 | 0.77 | 0.16 |
| Li- Ti_3C_2 | 2.06 | 1.97 | 1.48 | | 1.58 | 1.62 | 1.36 | |
| Li- Ti_3C_2 -Hyd | 7.07 | 2.34 | 1.32 | | 1.61 | 1.58 | 1.28 | |

Synthesis of $\text{Ti}_3\text{C}_2\text{T}_x$ MXene

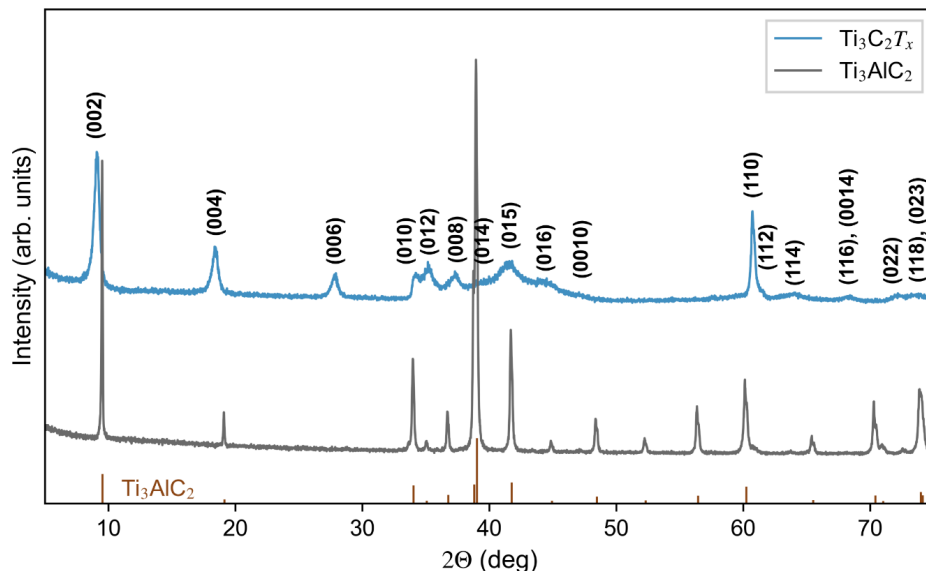


Figure S4. X-ray diffractograms before and after etching of the Ti_3AlC_2 MAX phase in 10 wt. % HF. As there are no reflections left from the MAX phase, it is assumed 100 % etching of the Al layer to form pure $\text{Ti}_3\text{C}_2\text{T}_x$ MXene. The theoretical Ti_3AlC_2 reflections are obtained from PDF 04-012-0632, and the marked (hkl) reflections of the MXene is obtained from the structureless Pawley fitting using the $P6_3/mmc$ space group.

Gas hydrolysis of pristine HF-etched $\text{Ti}_3\text{C}_2\text{T}_x$ MXene

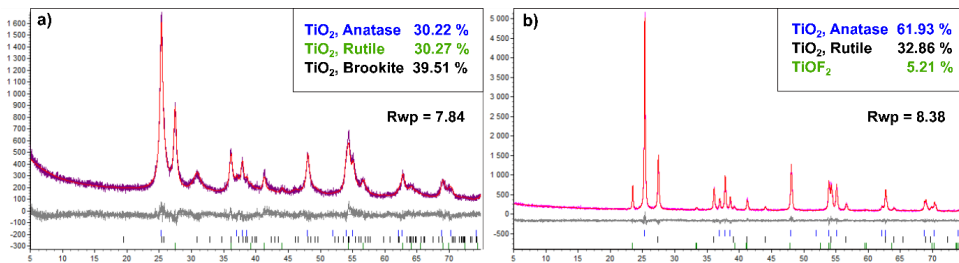


Figure S5. Rietveld refinement of the X-ray diffractograms from $\text{Ti}_3\text{C}_2\text{T}_x$ after hydrolysis (a) and air annealing (b) at 500 °C. It shows the estimated amounts of the different phases present after oxidation of the $\text{Ti}_3\text{C}_2\text{T}_x$ phase.

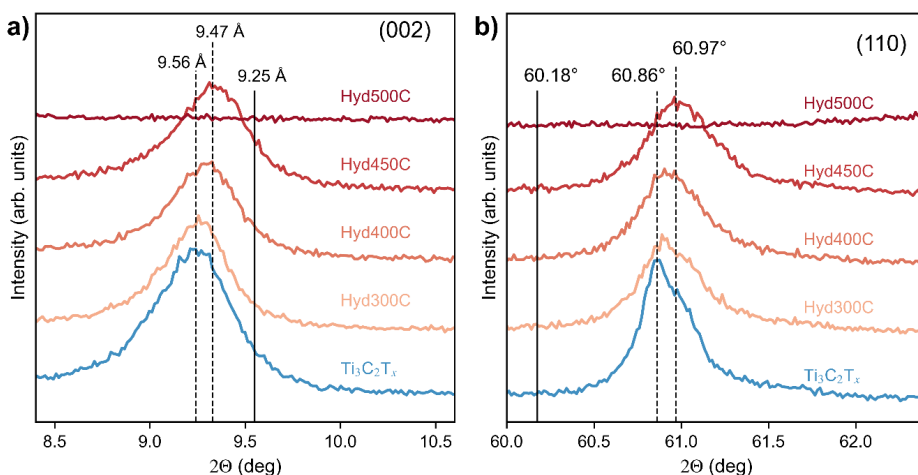


Figure S6. Specific regions from the X-ray diffractograms presented in Figure 2a indicating the shifts in the (002) reflection which gives the interlayer spacing of the $\text{Ti}_3\text{C}_2\text{T}_x$ MXene (a) and the (110) reflection which may describe changes in stacking of the MXene layers (b). The dashed lines indicate the positions of the reflections before and after hydrolysis at 450 °C, while the solid line represent positions of the same reflections for the Ti_3AlC_2 MAX phase. These plots are adjusted for sample displacement through a structureless fitting with the $\text{P6}_3/\text{mmc}$ space group.

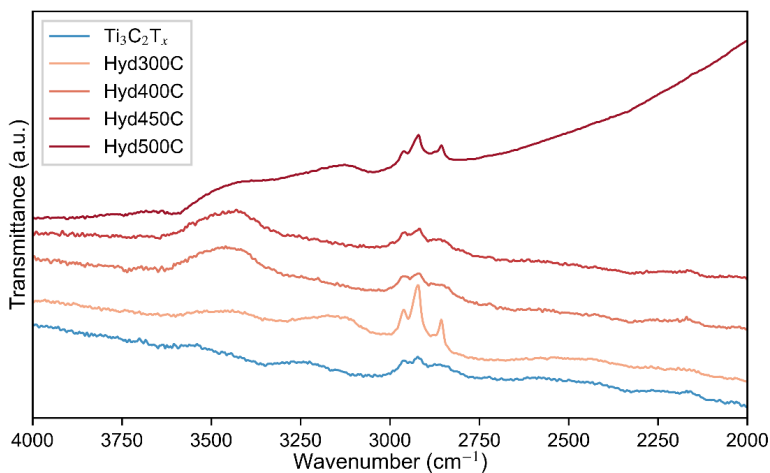


Figure S7. Extended region of the FTIR spectra presented in Figure 2c, where there are no significant transmission valleys (absorption peaks) visible in the H_2O region around 3000 cm^{-1} to 3600 cm^{-1} . Instead, transmission peaks are observed, indicating that there are some problems with the KBr reference, as the reference material may contain more water than the MXene particles. The transmission peaks at around 2900 cm^{-1} come from sp^3 C-H stretching modes which come from impurities in the instrument used.

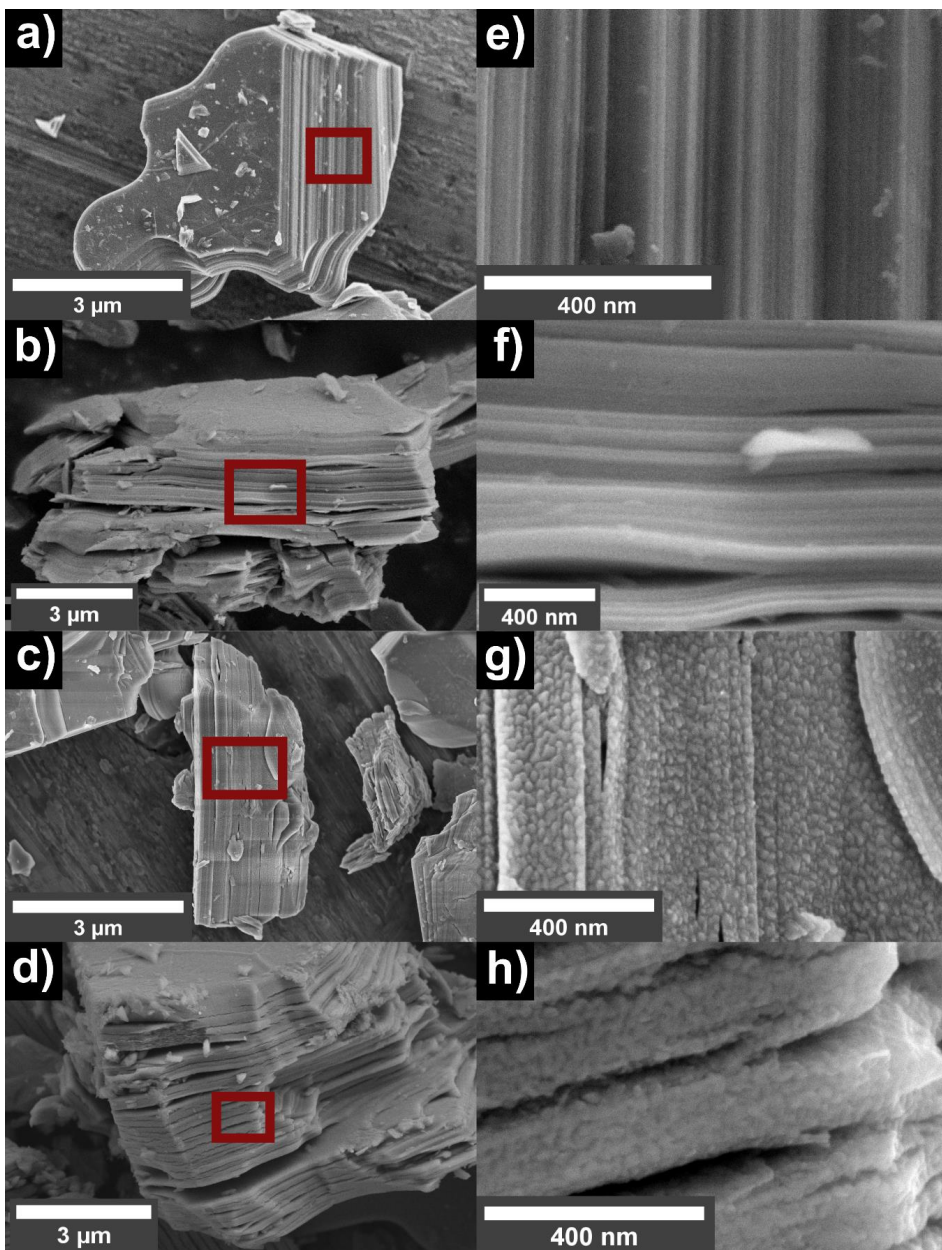


Figure S8. SEM micrographs depicting the morphology of the $\text{Ti}_3\text{C}_2\text{T}_x$ particles at low (a-d) and high (e-h) magnification, both before (a,e) and after hydrolysis at 300 °C (b,f), 400 °C (c,g) and 500 °C (d,h). It shows the formation of nanoparticles on the edge surface after hydrolysis at temperatures above 300 °C.

Characterisation of local chemical compositional changes at the edge surface

To investigate if there were any local compositional changes within the $\text{Ti}_3\text{C}_2\text{T}_x$ particles after the hydrolysis, TEM EDS mapping was performed on the particle edges before and after hydrolysis at 400 °C. The results are presented in Figure S9, showing the variation in concentration of Ti, C, O and F along a cross section of the particles. Apart from the C increase at the edge of the particle, deriving from the carbon protection layer deposited inside the FIB during TEM preparation, all other concentrations diminish outside the particle. After hydrolysis at 400 °C, the formation of TiO_2 nanoparticles is seen as a peak in the O content at the particle surface. However, as the ratio between O and F terminations remain unchanged before and after hydrolysis, and within the particles, it is concluded that the gas hydrolysis of pristine HF-etched $\text{Ti}_3\text{C}_2\text{T}_x$ does not result in any substitution of F-terminations.

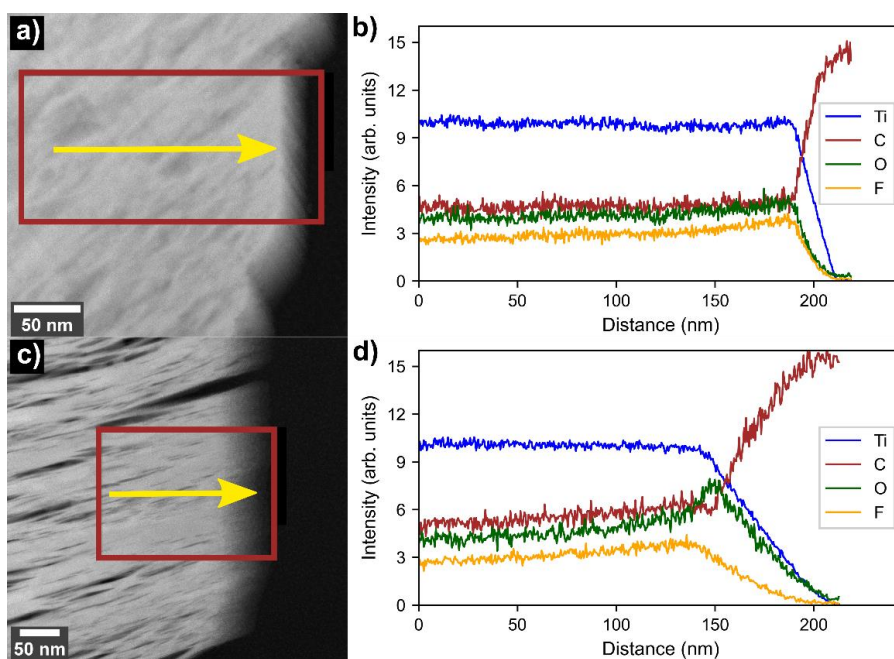


Figure S9. STEM EDS mapping of regions that include the edge surface of $\text{Ti}_3\text{C}_2\text{T}_x$ particles before (a,b) and after (c,d) hydrolysis at 400 °C. a) and c) are HAADF-STEM images where the red frames illustrate the mapped regions, while b) and d) demonstrate the intensities of Ti, C, O and F as a function of the distance from left to right in the red areas depicted in a) and c).

Comparing the thermal stability of pristine $\text{Ti}_3\text{C}_2\text{T}_x$ in various atmospheres

To compare the thermal stability of $\text{Ti}_3\text{C}_2\text{T}_x$ in humid atmosphere to other atmospheres, $\text{Ti}_3\text{C}_2\text{T}_x$ was annealed in inert (Ar), reducing (H_2/Ar) and oxidising (synthetic air) atmospheres as well as under vacuum. For annealing in air (Figure S10), it is shown that the oxidation starts at a lower temperature than for hydrolysis (300 °C compared to 400 °C) and that the MXene phase is completely oxidised to TiO_2 anatase and rutile phases after annealing at 400 °C (Figure S10 a and b). The Raman and EDS results also demonstrate how the oxidation in air drastically reduces the C content by more than 80 % (Figure S10 b and c). Comparing this to hydrolysis, where most of the C remained even after complete oxidation at 500 °C, a faster oxidation of C in the presence of O_2 gas is demonstrated. Additionally, the oxidation in air resulted in the formation of larger crystallites and did not preserve the layered morphology of the particles (Figure S11). Considering the F content upon annealing in dry air, there is a significant reduction following the oxidation of the MXene phase. However, as almost 25 % of the initial F content remains as a TiOF_2 phase even after annealing at 500 °C (Figure S5b and Table S1), air annealing demonstrates an inferior selectivity towards F removal compared to hydrolysis, where almost 100 % of the F content was removed. As similar results are reported for the oxidation in pure O_2 , [2] and seeing that the MXene oxidation by O_2 is accompanied by a high thermodynamic driving force (Figure S12), [3] annealing in oxygen is not a good alternative for F-termination substitution.

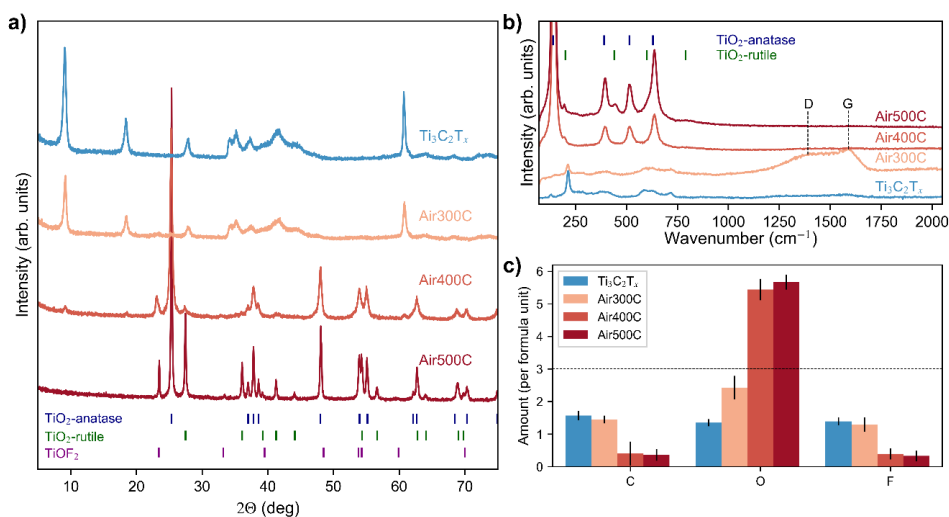


Figure S10. Results from the annealing of $\text{Ti}_3\text{C}_2\text{T}_x$ in synthetic air at different temperatures showing X-ray diffractograms (a), Raman spectra (b) and EDS average values (c). The dashed line in (c) illustrates a Ti amount of 3 and the error bars represent the standard deviation from the set of point scans used for each sample.

X-ray diffractograms, FTIR spectra and EDS quantification results from annealing of $\text{Ti}_3\text{C}_2\text{T}_x$ in inert, reducing, oxidising and vacuum environments are presented in the supplementary information (Table S1, Figure S13 and S14) and demonstrate the differences after annealing at 500 °C. As previously discussed, both the hydrolysis and air annealing of $\text{Ti}_3\text{C}_2\text{T}_x$ resulted in a complete oxidation at this temperature. However, whereas the hydrolysis preserved the C content while removing all F content, the air annealed $\text{Ti}_3\text{C}_2\text{T}_x$ shows a Ti-F shoulder at 951 cm^{-1} in the FTIR spectra and none of the C-related vibrational modes. For the MXene annealed under vacuum, inert and reducing atmospheres, only minor changes are observed. Although the XRD and FTIR results demonstrate slight decomposition into TiO_2 and C or TiF_3 phases at this temperature (Figure S13 and S14), the chemical composition of these samples remained the same (Table S1). Considering possible reaction products from F-removal, such as HF (g), F_2 (g), CF_4 (g) and F^- , HF gas would be the most likely product to leave the structure without damaging the MXene. While evaporation of F^- ions would result in a build-up of positive charge on the MXene, oxidation into F_2 gas is unattainable due to the high reduction potential of F. Additionally, the formation of carbon fluorides would depend on the decomposition of the MXene phase in order to have the required C content. Seeing that reactions with H_2O may allow for the formation of HF gas (Figure 1), a humid atmosphere (hydrolysis) is therefore expected to be the ideal annealing atmosphere for removal of F-terminations from MXenes.

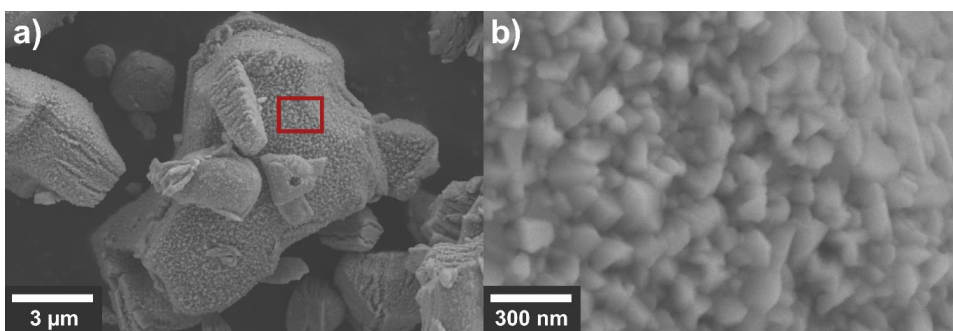


Figure S11. Low and high magnification SEM micrographs of $\text{Ti}_3\text{C}_2\text{T}_x$ particles after annealing in dry air at 500 °C, where (b) represents the region marked in red in (a).

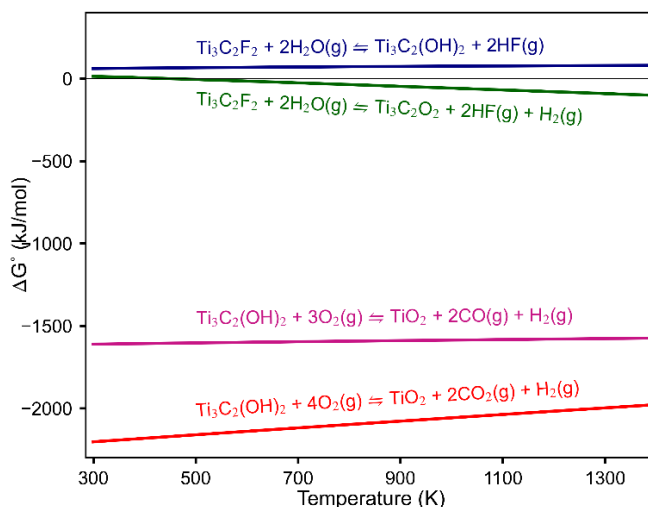


Figure S12. DFT results from four reactions showing ΔG° as a function of temperature. It demonstrates how the oxidation of $\text{Ti}_3\text{C}_2(\text{OH})_2$ is very thermodynamically favourable in O_2 atmosphere.

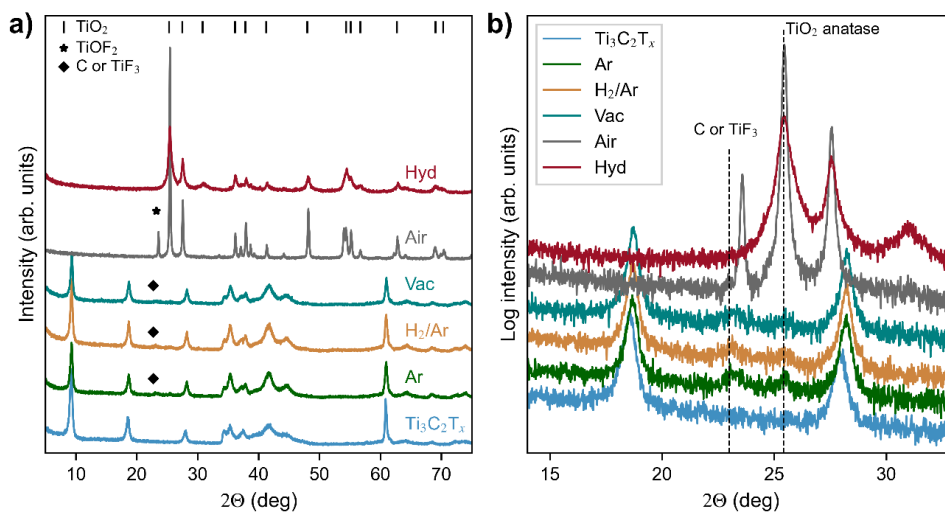


Figure S13. X-ray diffractograms of $\text{Ti}_3\text{C}_2\text{T}_x$ before and after annealing for 15 h at 500 °C in various atmospheres. (a) shows the overall spectra, whereas (b) shows logarithmic intensities from a smaller 2θ region. The names of the different samples indicate what atmospheres are used, where "Vac" represents vacuum and "Hyd" represent hydrolysis.

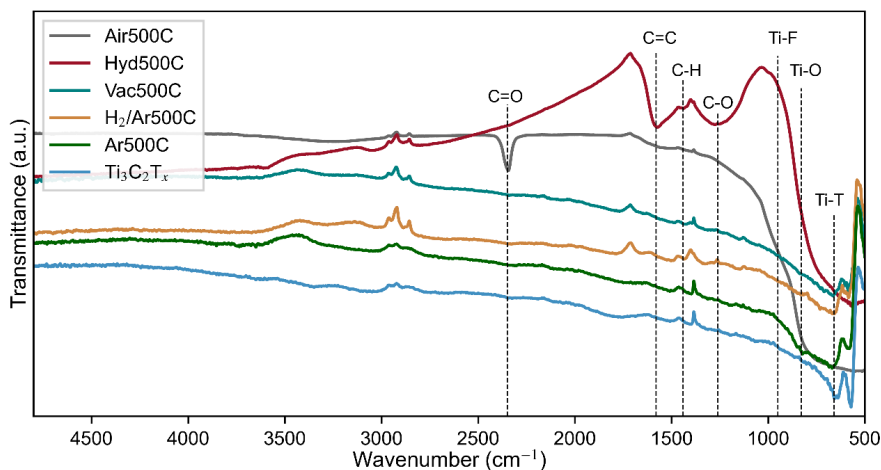


Figure S14. FTIR spectra of $\text{Ti}_3\text{C}_2\text{T}_x$ before and after annealing at $500\text{ }^\circ\text{C}$ in various atmospheres, where the names indicate which atmospheres are used. The marked transmission valleys represent the vibrations of the C=O stretching mode from CO_2 at 2351 cm^{-1} , the C=C stretching mode at 1577 cm^{-1} , the C-H bending mode at 1439 cm^{-1} , the C-O stretching mode at 1254 cm^{-1} , the Ti-F mode from the TiOF_2 phase at 951 cm^{-1} , [4] the Ti-O mode from anatase with its edge starting at around 800 cm^{-1} , [5] and the ascribed Ti-T bond between MXene Ti atoms and surface terminations T at $\sim 660\text{ cm}^{-1}$. The peaks (not valleys) presented in these plots come from instrument impurities and/or impurities in the reference. The presence of CO_2 in the Air annealed sample may come from trapped CO_2 inside the particles.

Hydrolysis of pre-intercalated $\text{Ti}_3\text{C}_2\text{T}_x$

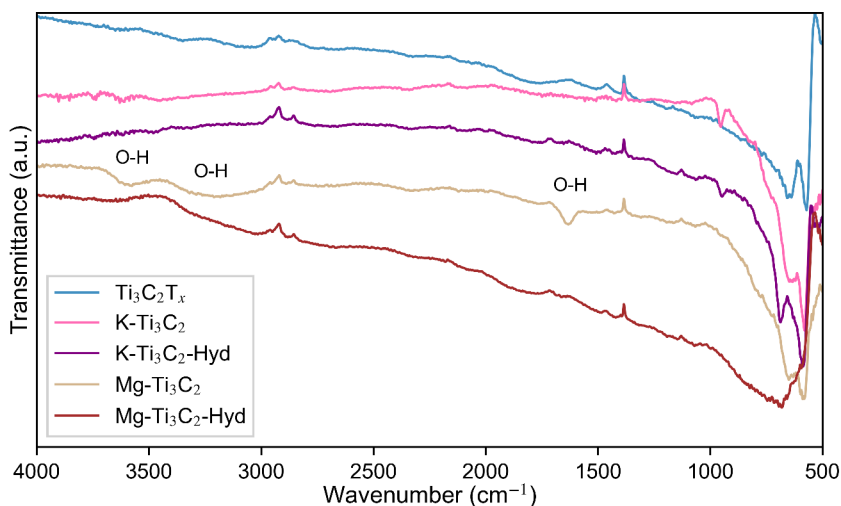


Figure S15. FTIR spectra of $\text{Ti}_3\text{C}_2\text{T}_x$ samples with the intercalation of K- and Mg-ions before and after hydrolysis at $300\text{ }^\circ\text{C}$ for 15 h. The O-H bending (1650 cm^{-1}) and stretching modes ($\sim 3300\text{ cm}^{-1}$ and 3600 cm^{-1}) indicative of water molecules are only present for the Mg-intercalated $\text{Ti}_3\text{C}_2\text{T}_x$. The peaks (not valleys) presented in these plots come from instrument impurities and/or impurities in the reference.

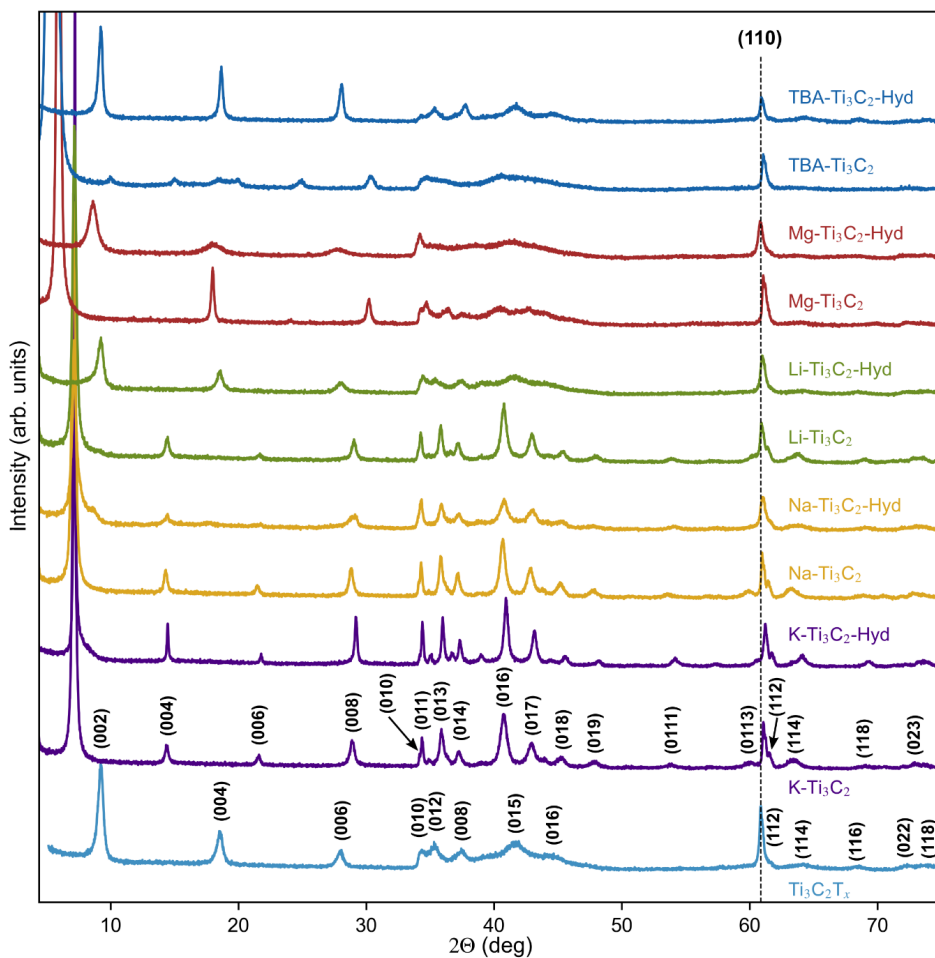


Figure S16. The whole X-ray diffractograms presented in Figure 4a, showing $\text{Ti}_3\text{C}_2\text{T}_x$ intercalated with various cations before and after hydrolysis at 300°C . It demonstrates how the diffractograms change a lot depending on the intercalated ions present, where the Na- and K-intercalated MXene as well as the Li-intercalated one before hydrolysis shows sharper reflections, and thereby a higher ordering of the structure, compared to the other samples. The dashed line marks the location of the (110) reflection of the pristine $\text{Ti}_3\text{C}_2\text{T}_x$, and illustrates the shifts in this reflection upon intercalation and hydrolysis. There are no visible reflections related to any TiO_2 phases in any of these diffractograms, indicating insignificant oxidation taking place. The (002) reflections are truncated to enhance the visibility of the other reflections, and the marked (hkl) planes are obtained from the structureless Pawley fitting of the $\text{Ti}_3\text{C}_2\text{T}_x$ and K- Ti_3C_2 phases using the $\text{P6}_3/\text{mmc}$ space group.

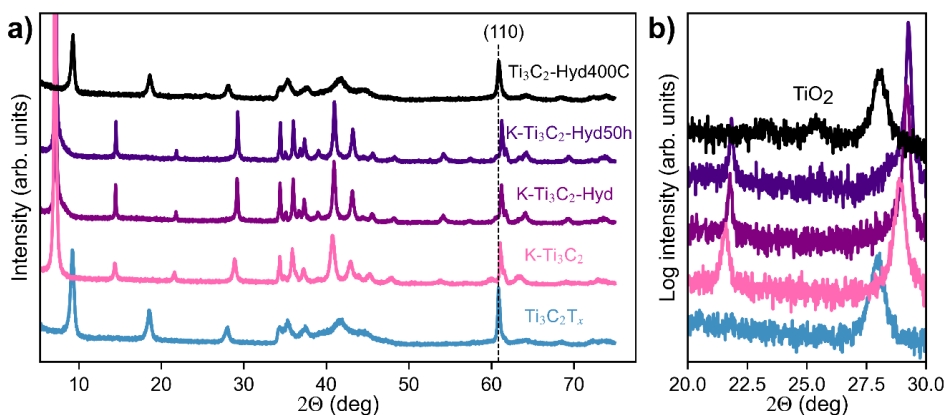


Figure S17. X-ray diffractogram of pristine $\text{Ti}_3\text{C}_2\text{T}_x$ and $\text{Ti}_3\text{C}_2\text{T}_x$ after K-intercalation and hydrolysis at $300\text{ }^\circ\text{C}$ for 15 h and 50 h, where (a) shows the overview diffractograms while (b) shows logarithmic values of a smaller region. The full height of the (002) reflections are truncated for a better presentation of the other reflections. The dashed line at 60.7 degrees represents the position of the (110) reflection of the pristine HF-etched $\text{Ti}_3\text{C}_2\text{T}_x$ and illustrates significant shifts upon intercalation and hydrolysis, attributable to stacking changes. The Hyd400C diffractogram (black) is added as a reference to demonstrate no reflections from TiO_2 at 25.3 degrees for the K-intercalated samples, even after hydrolysis for 50 h.

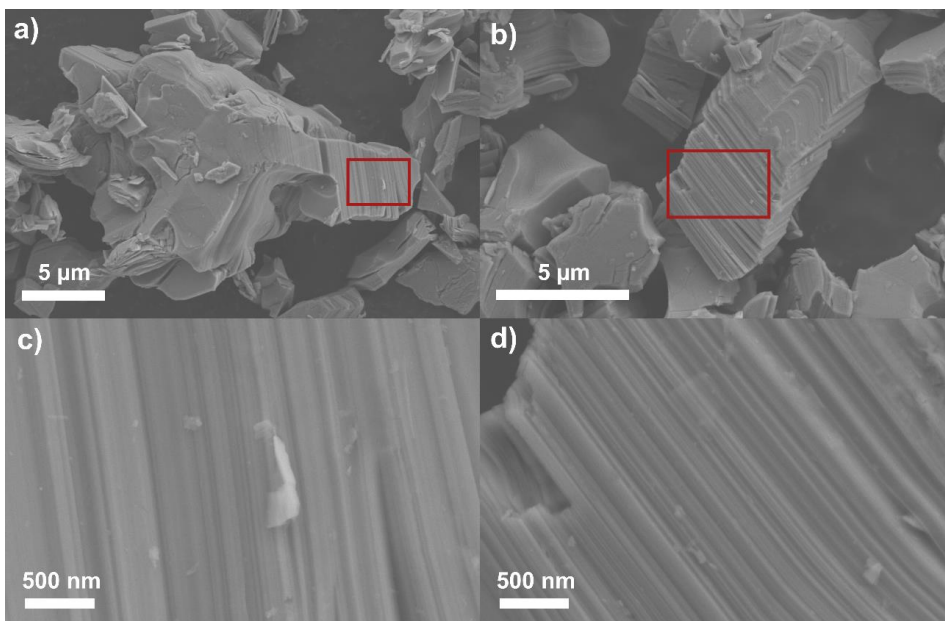


Figure S18. SEM micrographs of the $\text{K-Ti}_3\text{C}_2$ (a,c) and $\text{K-Ti}_3\text{C}_2\text{-Hyd}$ (b,d) samples at two different magnifications, where the red rectangles in a and b represent the areas depicted in c and d respectively. These micrographs show no obvious formation of TiO_2 nanoparticles on the edge surface after the intercalation of K-ions and the following hydrolysis at $300\text{ }^\circ\text{C}$.

Table S3. The ionic radii, hydration enthalpy and solubility of respective fluorides for four cations (Mg^{2+} , Li^+ , Na^+ and K^+), demonstrating how the smaller ions bond stronger to F.

| Cation | Ionic radii | Hydration Enthalpies | Solubility of fluorides in water |
|------------------|-------------|---|----------------------------------|
| | (Å)[6,7] | $-\Delta H^{\circ}_{\text{hyd}}$ (kJ/mol) [8] | (g/100 mL @ 25 °C)[6] |
| Mg^{2+} | 0.72 | 1921 | 0.013 |
| Li^+ | 0.69 | 519 | 0.13 |
| Na^+ | 1.02 | 409 | 4.1 |
| K^+ | 1.38 | 322 | 102 |

References

- [1] C. Ferrara, A. Gentile, S. Marchionna, I. Quinzeni, M. Fracchia, P. Ghigna, S. Pollastri, C. Ritter, G.M. Vanacore, R. Ruffo, The Missing Piece: The Structure of the $\text{Ti}_3\text{C}_2\text{T}_x\text{MXene}$ and Its Behavior as Negative Electrode in Sodium Ion Batteries, *Nano Lett.* 21 (2021) 8290–8297. <https://doi.org/10.1021/ACS.NANOLETT.1C02809>.
- [2] Z. Li, L. Wang, D. Sun, Y. Zhang, B. Liu, Q. Hu, A. Zhou, Synthesis and thermal stability of two-dimensional carbide MXene Ti_3C_2 , *Mater. Sci. Eng. B Solid-State Mater. Adv. Technol.* 191 (2015) 33–40. <https://doi.org/10.1016/j.mseb.2014.10.009>.
- [3] P. Zheng, X. Zhang, M. Yan, Y. Ma, Y. Jiang, H. Li, The eruption of carbon chains in the oxidation of 2D Ti_nC_n ($n = 1, 2, 3$) MXenes, *Appl. Surf. Sci.* 550 (2021) 149310. <https://doi.org/10.1016/j.apsusc.2021.149310>.
- [4] C. Hou, J. Xie, H. Yang, S. Chen, H. Liu, Preparation of $\text{Cu}_2\text{O}/\text{TiO}_2$ and its photocatalytic degradation of tetracycline hydrochloride wastewater, *RSC Adv.* 9 (2019) 37911–37918. <https://doi.org/10.1039/C9RA07999H>.
- [5] M.M. Viana, V.F. Soares, N.D.S. Mohallem, Synthesis and characterization of TiO_2 nanoparticles, *Ceram. Int.* 36 (2010) 2047–2053. <https://doi.org/10.1016/j.ceramint.2010.04.006>.
- [6] A.G. Blackman, L.R. Gahan, G.H. Aylward, T.J.V. (Tristan J.V. Findlay, Aylward and Findlay's Si chemical data, Wiley, 2013.
- [7] N. Shpigel, M.D. Levi, S. Sigalov, T.S. Mathis, Y. Gogotsi, D. Aurbach, Direct Assessment of Nanoconfined Water in 2D Ti_3C_2 Electrode Interspaces by a Surface Acoustic Technique, *J. Am. Chem. Soc.* 140 (2018) 8910–8917. <https://doi.org/10.1021/JACS.8B04862>.
- [8] D.W. Smith, Ionic hydration enthalpies, *J. Chem. Educ.* 54 (1977) 540–542. <https://doi.org/10.1021/ED054P540>.

ISBN 978-82-326-5567-0 (printed ver.)
ISBN 978-82-326-6548-8 (electronic ver.)
ISSN 1503-8181 (printed ver.)
ISSN 2703-8084 (online ver.)



NTNU

Norwegian University of
Science and Technology